Astronomy Reports, Vol. 46, No. 8, 2002, pp. 609–625. Translated from Astronomicheskiĭ Zhurnal, Vol. 79, No. 8, 2002, pp. 675–692.

Optical Monitoring of the BL Lac Object ON 231 in 1972–1990

M. K. Babadzhanyants and E. T. Belokon'

Astronomical Institute, St. Petersburg State University, St. Petersburg, Russia

Received November 30, 2001; in final form February 1, 2002

Abstract—The results of 19-year optical monitoring of ON 231 are presented. Photographic B-band observations were obtained during 123 nights from April 1972 to March 1990 as part of the quasar monitoring program carried out the Astronomical Institute of St. Petersburg State University. The new combined B-band light curve for ON 231 (1892–1999) is appreciably improved by our data, enabling us to identify a number of previously undetected high-amplitude events with time scales of weeks to months. On two nights, intraday variability with amplitudes $\sim 0\overset{m}{.}8$–$0\overset{m}{.}9$ was observed. A number of conclusions are drawn about variability components with time scales from hours to decades. There are cases when very similar behavior on time scales from several weeks to several months was observed in the presence of substantially different base brightness levels. Both the amplitudes ($\sim 1\overset{m}{.}5$) and the characteristic shapes and overall durations of these events were the same. The constancy of the amplitudes of these events in magnitudes (i.e., the proportionality of the luminosity in rapid outbursts to the underlying level of the slowly varying component) can be explained in models that associate the variability with changes in the Doppler boosting factor due to variations in the inclination of the relativistic jet to the line of sight, if the slow and rapid components of the optical variability are associated with a steady component of the relativistic jet and shock waves (superluminal components) moving in the jet, respectively. Evidence for such a connection has been found for several superluminal sources. At the same time, there is evidence that in typical IDV events for ON 231, with durations of ~ 1.5–2 hr, the amplitudes depend on the base brightness level of the objects, suggesting that the IDV events and less rapid components of the variability have different natures and/or occur in different locations in the source. © *2002 MAIK "Nauka/Interperiodica"*.

1. INTRODUCTION

The radio source ON 231 was among the first assigned to the class of BL Lac objects [1, 2], which are characterized by the absence of line emission or presence of only weak line emission in their spectra. The redshift $z = 0.102$ [3] was based on two weak emission lines belonging to the underlying galaxy [4]. ON 231 also displays other properties characteristic of BL Lac objects: high and variable polarization of the optical continuum (the relatively small amount of available data indicate that it reaches $\sim 13\%$ [5]), as well as strong variability over the entire observable spectral range, from radio to gamma-rays. However, the character of the variability is well known only in bands in which monitoring observations have been conducted over many years (for example, in the radio [6–8]).

Interest in ON 231 rose in the 1990s, when observations showed a substantial increase in its optical luminosity [9] and it was detected as a gamma-ray source at energies exceeding 300 MeV [10]. ON 231 possesses the hardest spectrum of all blazars detected as gamma-ray sources by EGRET [11]. In 1994, it was also shown that ON 231 is a superluminal source [12]—its milliarcsecond radio jet has a complex structure with several compact superluminal components [12, 13].

ON 231 is among a small group of blazars for which archival photographic plates make it possible to trace the history of its optical variability over more than 100 years. ON 231 was discovered in 1916 by Wolf [14] as the variable star 10.1916 (W Com). Observations showed that the object remained fairly bright (14^m–16^m pg) right up until the beginning of the 1970s. After the classification of ON 231 as a BL Lac object in 1971 [1, 2], it was included in several quasar optical monitoring programs [15–18]. By this time, the brightness of the object had sharply decreased, and was in the range 16^m–$17\overset{m}{.}5$ B. This may be why systematic monitoring of ON 231 was carried out only until the middle of the 1980s, after which there are only sparse observations. In the 1970s and 1980s, the object displayed brightness variations with amplitudes from several tenths to $\sim 2^m$ B on time scales of days, weeks, months, and years. On some individual nights, appreciable ($\sim 0\overset{m}{.}8$) variability on time scales of hours was observed [18].

Intensive optical observations of ON 231 were begun again in 1994 as part of several new monitoring programs carried out by observatories in Italy and Finland [9, 19]. At that time, the mean brightness

1063-7729/02/4608-0609$22.00

of the object had appreciably risen, and an absolute brightness maximum over the entire 100 years of observations (not including the data of Wolf [14]) was recorded in the spring of 1998 [19]. Detailed observations conducted in the 1990s confirmed the complex structure of the brightness variations, formed by the superposition of many flares with different amplitudes (from $\sim 0^m.2$ to $\sim 1^m.5$) and durations (from hours to months) [9].

The complex character of the variations hindered analyses, even for the best-observed, "modern" part of the light curve (after 1971), especially given the sharp decrease in the number of observations in 1985–1993 (there is only one published brightness estimate for 1991–1993 [20]). In addition, even in the comparatively well-observed interval 1972–1984, the sampling is about a factor of two to three worse than it became in the more intensive monitoring of recent years. Therefore, additional data for the modern part of the optical light curve of ON 231 could prove very fruitful for further analyses.

Here, we present B-band photometric observations of ON 231 obtained in 1972–1990 that appreciably increase the number of published data for this time interval. We have derived a new optical light curve for ON 231 that includes all B brightness estimates for this object published up until 2002. We have compared various homogeneous data sets to search for possible systematic differences between them, and have derived corrections for some data to reduce them to a common system. We discuss the results of the observations and some properties of the optical light curve of ON 231.

2. OBSERVATIONS

Photometric observations of ON 231 were carried out in the framework of the Petersburg Quasar Monitoring Program (PQMP) of the Astronomical Institute of St. Petersburg State University. All the observations were obtained at the prime focus of the 0.45-m ($F/4.5$) reflector of the Byurakan station of the Astronomical Institute using a single photographic procedure, as described in previous publications of the results of this program [21, 22]. Observations of ON 231 were conducted on 123 nights from April 1972 through March 1990, primarily in the B band (measurements were made in the V band as well only on three nights). As a rule, the brightness was determined using two to three independent estimates obtained sequentially over 20–60 minutes (for $\sim 60\%$ of the nights, two brightness estimates were obtained, and for $\sim 20\%$ of the nights, three or four brightness estimates were obtained). In all, 251 brightness estimates were obtained for the B band and five for the V band. Corrections to reduce the observations to the standard system were determined individually for each batch of the plates, and did not exceed $0^m.03$. When determining these corrections, the $B-V$ color index of ON 231 was taken from a plot of its dependence on the brightness (see Section 4.4).

All the plates were measured using a microdensitomiter with a rectangular diaphragm. Calibration curves were constructed using a large number of comparison stars to increase the accuracy and trustworthiness of the results. The primary standards were six comparison stars of Wing [23] for which photoelectric UBV magnitudes are available (an F star that proved to be variable [24, 25] was excluded). In addition, we used additional stars whose B magnitudes were obtained via photographic smoothing over a large number of plates. These were stars 1, 4, 6, and 9 of Pollock *et al.* [26], stars 2, and 10–14 of Veron and Veron [24], and 15 stars in the field of ON 231 chosen by us. All these authors used comparison stars of Wing [23] as reference stars when determining the B magnitudes of the additional comparison stars. For four stars in common to the studies conducted by these different authors, the differences between the derived magnitudes were only $0^m.01$–$0^m.05$. For these stars, we used averages of the B magnitudes.

As a rule, the calibration curves used to determine the B magnitudes of ON 231 were constructed using 21 comparison stars. Only six comparison stars of Wing [23] and the star C1 of Fiorucci and Tosti [27] were used for the V magnitudes. The rms errors of individual brightness estimates were derived from the scatter of the comparison-star data around the calibration curve, described as a smoothing cubic spline. The typical rms errors were ($0^m.05$–$0^m.15$) depending on the brightness of the object. The results of our observations are presented in Tables 1 and 2.

3. COMBINED OPTICAL LIGHT CURVE OF ON 231

Figure 1 presents a combined optical light curve for ON 231 (1892–1999), which includes all B-band and m_{pg} data published before 2002. The data are taken from 34 papers [3, 5, 9, 14–20, 23, 24, 26, 28–48] and Table 1. The data points for each individual data sets presented in this figure are nightly averages. Usually, from two to four brightness estimates were averaged, however, up to several dozen measurements were averaged in some cases [46, 48]. The resulting light curve contains 684 data points. The fact that the data sets used to make this light curve were obtained on different instruments using different methods could lead to systematic differences between them. Therefore, when it was possible, we compared

Table 1. B-band Photometry of ON 231 (PQMP data)

UT	JD 2440000+	$B \pm \sigma$	UT	JD 2440000+	$B \pm \sigma$
(1)	(2)	(3)	(1)	(2)	(3)
4/07/72	1415.303	$17^m.31 \pm 0^m.12$	5/18/74	2186.304	$16^m.76 \pm 0^m.13$
4/07/72	1415.316	17.31 0.20	5/24/74	2192.321	16.70 0.08
6/02/72	1471.321	17.05 0.13	5/24/74	2192.339	16.47 0.07
6/03/72	1472.289	16.67 0.08	5/25/74	2193.311	16.66 0.06
6/03/72	1472.312	16.68 0.14	5/25/74	2193.331	16.77 0.11
1/03/73	1685.541	16.60 0.09	6/17/74	2216.296	17.39 0.09
2/10/73	1693.434	16.76 0.10	6/22/74	2221.282	16.72 0.06
2/10/73	1693.450	16.85 0.09	6/22/74	2221.304	16.67 0.11
3/04/73	1746.382	17.18 0.10	7/14/74	2243.271	17.11 0.07
3/09/73	1751.334	16.98 0.12	7/14/74	2243.290	17.07 0.10
3/09/73	1751.350	17.29 0.08	3/08/75	2479.510	16.84 0.15
4/09/73	1782.306	16.33 0.11	3/08/75	2479.524	16.96 0.17
4/09/73	1782.319	16.33 0.08	3/15/75	2487.352	17.15 0.15
11/27/73	2013.530	16.52 0.20	3/15/75	2487.362	17.13 0.15
11/28/73	2014.535	16.88 0.08	3/19/75	2491.446	16.87 0.12
11/29/73	2015.540	16.67 0.12	3/19/75	2491.457	16.86 0.12
11/29/73	2015.554	16.59 0.13	3/31/75	2503.296	15.83 0.11
12/05/73	2021.502	16.63 0.09	3/31/75	2503.310	15.78 0.09
12/05/73	2021.517	16.53 0.07	4/04/75	2507.338	16.96 0.18
12/22/73	2039.468	17.00 0.17	4/04/75	2507.351	16.95 0.16
12/22/73	2039.482	16.96 0.10	4/05/75	2508.313	17.31 0.22
12/23/73	2040.483	16.99 0.12	4/05/75	2508.328	16.89 0.14
12/23/73	2040.499	16.74 0.18	4/08/75	2511.335	17.04 0.16
12/24/73	2041.496	17.11 0.15	4/08/75	2511.349	16.98 0.16
2/01/74	2079.552	17.0>	4/08/75	2511.362	16.84 0.10
2/01/74	2079.564	17.3>	5/04/75	2537.324	16.84 0.16
2/03/74	2081.590	17.25 0.12	5/04/75	2537.340	17.23 0.14
2/03/74	2081.610	17.31 0.12	5/04/75	2537.355	17.07 0.13
2/15/74	2094.407	17.24 0.13	6/03/75	2567.364	15.87 0.07
2/15/74	2094.430	17.18 0.16	6/03/75	2567.379	15.63 0.07
2/17/74	2096.447	17.22 0.06	12/13/75	2759.582	16.48 0.05
2/17/74	2096.469	17.21 0.14	3/26/76	2863.535	16.84 0.07
2/18/74	2097.374	17.09 0.08	3/26/76	2864.417	16.34 0.07
2/18/74	2097.396	17.03 0.13	3/26/76	2864.446	16.42 0.06
5/13/74	2181.312	16.86 0.06	3/27/76	2865.418	16.22 0.07
5/13/74	2181.335	16.86 0.06	1/25/77	3168.542	16.18 0.07
5/14/74	2182.289	16.92 0.11	1/25/77	3168.554	16.28 0.11
5/14/74	2182.304	16.81 0.17	1/25/77	3168.568	16.28 0.08
5/17/74	2185.331	16.60 0.09	2/20/77	3195.450	16.44 0.08
5/17/74	2185.350	16.68 0.11	2/20/77	3195.464	16.43 0.10
5/18/74	2186.285	16.70 0.11	4/16/77	3250.348	16.54 0.10

Table 1. (Contd.)

(1)	(2)	(3)		(1)	(2)	(3)	
4/16/77	3250.362	16.57	0.17	5/16/80	4376.250	16.91	0.10
4/16/77	3250.375	16.51	0.14	5/16/80	4376.268	16.85	0.08
5/15/77	3279.315	15.72	0.06	5/16/80	4376.287	16.98	0.14
5/15/77	3279.328	15.68	0.13	6/04/80	4395.274	16.92	0.09
5/15/77	3279.340	15.74	0.11	6/04/80	4395.290	16.82	0.07
6/09/77	3304.358	15.80	0.60	6/04/80	4395.306	16.79	0.12
6/09/77	3304.372	15.4>		6/14/80	4405.281	15.12	0.06
6/10/77	3305.308	16.27	0.16	6/14/80	4405.299	15.07	0.05
6/10/77	3305.322	16.49	0.12	6/14/80	4405.314	15.15	0.05
3/02/78	3570.408	16.73	0.15	7/03/80	4424.287	15.75	0.10
3/02/78	3570.426	17.16	0.18	12/08/80	4581.542	16.67	0.09
3/03/78	3571.397	17.35	0.20	12/09/80	4582.526	16.61	0.09
3/03/78	3571.428	17.34	0.18	1/09/81	4613.539	16.48	0.12
5/02/78	3631.365	17.00	0.13	1/09/81	4613.555	16.53	0.12
5/02/78	3631.383	17.11	0.17	1/09/81	4613.571	16.45	0.11
6/06/78	3666.257	17.05	0.10	4/06/81	4701.448	16.32	0.10
6/06/78	3666.280	17.33	0.13	4/06/81	4701.461	16.29	0.08
6/06/78	3666.303	17.37	0.12	4/06/81	4701.475	16.39	0.07
6/27/78	3687.282	17.15	0.10	5/28/81	4753.301	16.44	0.10
6/27/78	3687.301	17.22	0.16	5/28/81	4753.314	16.38	0.10
6/30/78	3690.286	17.13	0.10	5/28/81	4753.328	16.60	0.06
6/30/78	3690.309	17.09	0.12	1/05/82	4974.546	17.23	0.14
7/06/78	3696.269	16.62	0.14	1/05/82	4974.558	16.95	0.11
7/06/78	3696.293	16.56	0.10	1/05/82	4974.568	17.04	0.10
1/05/79	3878.576	16.44	0.08	1/18/82	4988.421	16.87	0.09
1/05/79	3878.609	16.50	0.11	1/18/82	4988.431	16.82	0.09
1/27/79	3900.525	16.84	0.11	1/19/82	4989.453	17.18	0.14
1/27/79	3900.554	16.73	0.10	1/23/82	4993.445	16.96	0.08
1/30/79	3903.518	17.00	0.11	1/23/82	4993.458	17.06	0.08
1/30/79	3903.549	16.81	0.12	1/23/82	4993.472	17.06	0.12
3/02/79	3935.386	16.04	0.08	1/24/82	4994.446	17.02	0.14
3/02/79	3935.410	16.07	0.07	1/24/82	4994.457	17.13	0.10
3/05/79	3938.442	16.40	0.08	1/25/82	4994.530	16.98	0.09
3/05/79	3938.464	16.42	0.06	1/25/82	4994.543	16.86	0.11
3/05/79	3938.486	16.50	0.07	2/21/82	5022.369	16.17	0.09
4/26/79	3990.363	15.90	0.08	2/21/82	5022.382	16.19	0.06
4/26/79	3990.383	15.84	0.15	2/26/82	5027.439	16.42	0.12
2/11/80	4281.378	16.04	0.06	2/26/82	5027.451	16.43	0.10
2/11/80	4281.394	16.05	0.08	3/14/82	5043.309	16.51	0.07
2/11/80	4281.411	16.04	0.06	3/14/82	5043.331	16.58	0.11
3/09/80	4308.350	16.73	0.10	3/26/82	5054.534	16.98	0.10
3/09/80	4308.366	16.56	0.07	3/26/82	5055.339	16.79	0.08
3/09/80	4308.382	16.66	0.16	3/26/82	5055.356	16.80	0.06
3/20/80	4319.378	16.68	0.10	3/27/82	5056.403	16.76	0.08
3/20/80	4319.394	16.84	0.13	3/27/82	5056.415	16.83	0.05
4/12/80	4342.301	16.69	0.09	3/28/82	5057.306	16.81	0.11
4/12/80	4342.318	16.74	0.06	3/28/82	5057.326	16.90	0.12
4/12/80	4342.334	16.79	0.11	3/28/82	5057.412	16.96	0.10

Table 1. (Contd.)

(1)	(2)	(3)		(1)	(2)	(3)	
5/05/80	4365.293	16.46	0.10	3/28/82	5057.433	16.76	0.10
5/05/80	4365.387	16.23	0.05	4/21/82	5081.358	16.83	0.12
4/21/82	5081.380	16.84	0.12	4/26/87	6912.362	16.53	0.16
4/21/82	5081.399	16.56	0.08	11/30/87	7129.572	16.48	0.20
5/20/82	5110.289	15.33	0.07	12/27/87	7156.593	15.88	0.04
5/20/82	5110.308	15.24	0.07	12/29/87	7158.592	16.11	0.08
11/15/82	5288.597	16.00	0.06	1/19/88	7179.517	16.39	0.08
11/15/82	5288.609	16.01	0.07	1/19/88	7179.543	16.52	0.15
1/12/83	5347.500	16.08	0.08	1/20/88	7180.510	16.34	0.15
1/13/83	5347.522	15.86	0.07	1/10/89	7536.539	15.87	0.08
1/16/83	5350.540	15.37	0.09	1/11/89	7537.578	15.77	0.09
1/16/83	5350.556	15.38	0.07	1/11/89	7537.592	15.86	0.06
3/07/83	5401.421	16.00	0.04	1/14/89	7540.568	15.96	0.08
3/07/83	5401.436	15.94	0.06	1/14/89	7540.586	15.87	0.09
3/19/83	5413.470	16.05	0.07	1/15/89	7541.575	15.81	0.08
3/19/83	5413.486	16.10	0.04	1/15/89	7541.591	15.71	0.07
4/15/83	5440.361	16.63	0.10	2/01/89	7559.483	15.16	0.04
5/09/83	5464.272	16.54	0.10	2/02/89	7559.504	15.17	0.09
5/09/83	5464.287	16.55	0.10	2/02/89	7560.492	15.24	0.07
5/09/83	5464.303	16.53	0.09	2/03/89	7560.509	15.24	0.07
12/15/83	5683.540	15.80	0.09	2/03/89	7561.485	15.18	0.05
12/15/83	5683.558	15.62	0.07	2/04/89	7561.501	15.24	0.14
1/03/84	5703.488	17.05	0.10	2/05/89	7563.499	15.31	0.08
1/04/84	5703.503	16.83	0.15	2/06/89	7563.516	15.26	0.09
1/04/84	5703.519	16.22	0.09	2/06/89	7564.499	14.89	0.09
2/25/84	5756.377	15.94	0.08	2/07/89	7564.515	14.91	0.04
2/25/84	5756.393	15.80	0.10	2/10/89	7567.505	14.65	0.08
2/25/84	5756.408	15.64	0.07	2/10/89	7567.521	14.71	0.10
3/30/84	5790.307	15.92	0.08	3/05/89	7591.437	15.71	0.08
3/30/84	5790.333	15.67	0.09	3/05/89	7591.454	15.86	0.12
3/30/84	5790.349	15.77	0.06	12/25/89	7885.540	16.22	0.09
4/17/85	6173.361	15.49	0.09	12/25/89	7885.556	16.13	0.07
4/17/85	6173.378	15.61	0.07	2/26/90	7949.378	16.33	0.10
7/18/85	6265.300	16.1>		2/26/90	7949.397	16.31	0.20
3/29/87	6884.382	16.46	0.18	3/20/90	7971.318	16.08	0.08
3/29/87	6884.400	16.68	0.12	3/20/90	7971.344	16.13	0.10
4/26/87	6912.342	16.76	0.09				

Table 2. V-band Photometry of ON 231 (PQMP data)

UT	JD 2440000+	$V \pm \sigma$	UT	JD 2440000+	$V \pm \sigma$
March 27, 1976	2865.449	$15^m.47 \pm 0^m.07$	March 28, 1982	5057.357	$16^m.36 \pm 0^m.07$
January 24, 1982	4994.479	16.55 0.07	March 28, 1982	5057.388	16.38 0.06
January 25, 1982	4994.506	16.41 0.02			

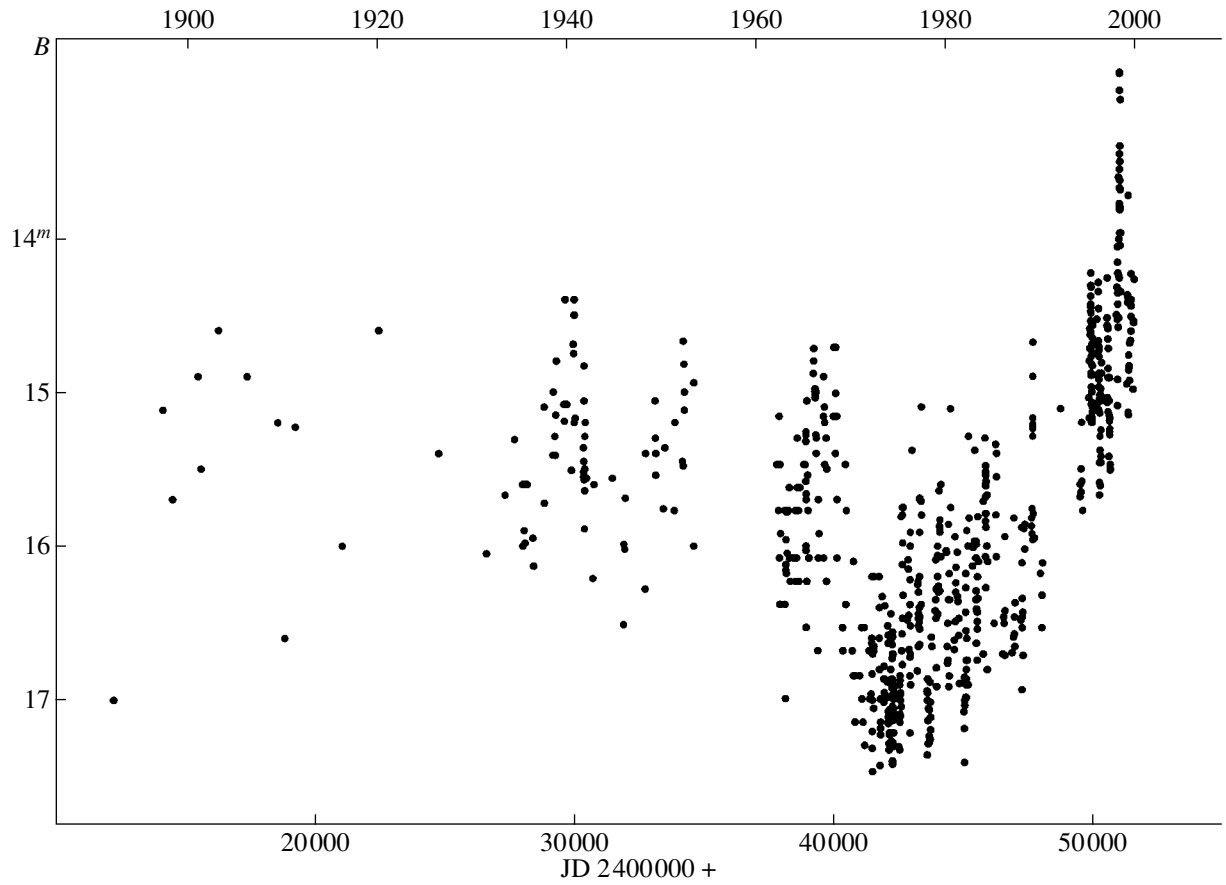

Fig. 1. Combined optical (B) light curve of ON 231 (1892–1999), based on the data of [3, 5, 9, 14–20, 23, 24, 26, 28–48] and the PQMP data (Table 1). The total number of data points is $N = 684$ (for each series of observations, the brightness estimates presented are nightly averages). We have applied corrections to reduce the brightness estimates of Wolf [14] obtained in 1892 and the data of Romano [30] to a common system (see Section 3).

homogeneous data sets to estimate possible systematic differences. This led us to apply corrections to the data of Wolf [14] and Romano [30] (see below) to reduce them to a common system.

Figure 2 presents the "historical" (before 1971) part of the combined light curve with the data of different authors denoted by different symbols. When combined light curves for ON 231 have been constructed in the past, the data of Wolf [14] ($m_{pg} = 11\overset{m}{.}5–14^m$ in 1892–1916) have usually called forth doubts, and it has been suggested more than once that they could be subject to large systematic error [9, 16, 49]. We found that all four brightness estimates in 1901–1916 published by Wolf in 1916 [14] were obtained on the same nights as four of the six brightness estimates for 1901–1916 published more than 60 years later by Zekl *et al.* [38] (without referencing the work of Wolf [14]). In addition, both works used archival plates of the same observatory (Königstuhl Sternwarte). The only difference in the dates for the two sets of published data—March 23, 1903 [14] and March 13, 1903 [38]—is likely due to a transcription error by one of these authors. In any case, there is no doubt that the four brightness estimates for 1901–1916 published by Wolf [14] and Zekl *et al.* [38] were obtained from measurements of the same plates. These two sets of measurements display a large, but fairly well determined, systematic difference of $3\overset{m}{.}0 \pm 0\overset{m}{.}3$. In this case, the results of Zekl *et al.* [38] were obtained using the photoelectric comparison stars of Wing [23], and display roughly the same brightness level for ON 231 in the 1900s as the data of Kurochkin [28] and Pollock *et al.* [26] (Fig. 2). It seems apparent that the results of Wolf [14], apart from the difference between m_{pg} and B, include a systematic error due to incorrect determination of the magnitudes of the comparison stars used.

Applying a correction ($3\overset{m}{.}0 \pm 0\overset{m}{.}3$) to the data of Wolf [14] enables us to include in the combined light curve his brightness estimate obtained on March 26, 1892 (JD 2412184.0): $B = 17\overset{m}{.}0$ [14], which is absent from the data of Zekl *et al.* [38]. This brightness estimate indicates that ON 231 may have been experiencing a brightness minimum at the end of the 19th

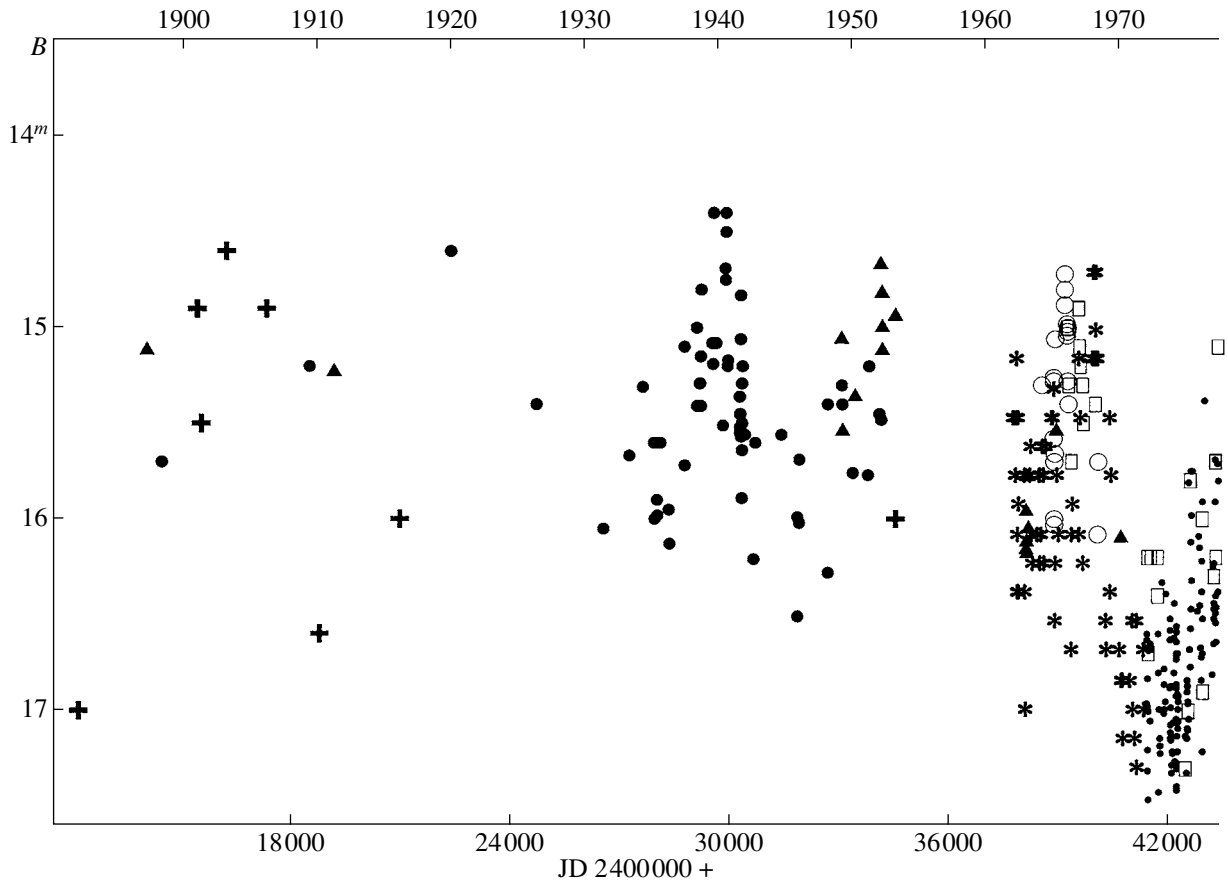

Fig. 2. Historical part of the combined light curve of ON 231. The data were taken from Wolf [14] (the brightness estimate for 1892) and Zekl *et al.* [38] (+), Kurochkin [28] (▲), Pollock *et al.* [26] (•), Markova and Fomin [33] (○), Barbieri *et al.* [16] and Barbieri and Romano [39] (□), Romano [30] (∗), and data are from the modern part of the light curve (after 1971) from [17, 23, 24, 29, 31, 32, 34–36] and Table 1 (•). Corrections were made to the data from [14, 30] (see Section 3).

century, similar to that observed in the early 1970s. In addition, there is now no doubt that the brightness estimate $B = 12^m.93$ recorded in May 1998 [19] does indeed represent an absolute brightness maximum for the entire ∼110-year interval of observations, so that the overall B-band amplitude of the variability shown by ON 231 is $4^m.5$.

We also included the photographic data of Romano [30] for 1962–1971, which make up more than 60% of all observations in the 1960s, in the combined light curve. These were obtained on a Schmidt telescope using panchromatic plates without a filter, and display appreciable systematic differences from the remaining historical data [16, 26, 28, 33, 38, 39], which are very close to B magnitudes (for example, for the data of Zekl *et al.* [38], obtained on an astrograph using orthochromatic plates, the possible systematic differences from B magnitudes are only $\sim 0^m.1$ [38]). In order to derive a correction to the data of Romano [30], we compared these data to B-band data obtained simultaneously ($\Delta T \leq 1$ day) on six nights by other authors [16, 25, 33, 39]. The magnitude of the correction depends on the brightness of the object, as expected, since the sensitivity curve of panchromatic plates is shifted toward the red and the optical color indices of ON 231 increase with decreasing brightness (see Section 4.4). We obtained the transformation equation $B = 1.52^* M_{\rm Rom} - 6.42$, which we believe is adequate to correctly transform the data of Romano [30] into B magnitudes. For most of these observations, which were obtained during the high-brightness state of the object in 1962–1968, the derived correction is in the range $+0^m.8 - +1^m.2$, which is close to the correction used by other authors from the Asiago Observatory [16] themselves when including the data of Romano [30] in their own combined light curve for ON 231. For $M_{\rm Rom} \sim 15^m - 15^m.5$ (primarily Romano's observations of 1969–1971), the transformation equation gives a correction of $\sim +1^m.5$. The same correction were independently obtained from a comparison of the data of Romano [30] and the B-band data of Erastova [25] obtained in 1969–December 1971. Both data sets (15 and 20 observations, respectively)

independently show a monotonic decrease in brightness by $0^m.7$ throughout this interval. The gradients of the brightness variations derived for each data set separately coincide, while the systematic differences between the series are $+1^m.5$. At the same time, subsequent observations of Erastova [25] obtained in 1972–1976 are in good agreement with the B-band observations of other authors ([17, 24, 31], Table 1); their systematic differences derived from 12 pairs of simultaneous ($\Delta T \leq 1$ day) observations are only $0^m.00 \pm 0^m.05$.

Due to the insufficient sampling in the historical part of the light curve, it was not possible to make a direct comparison of other homogeneous data sets based on simultaneous ($\Delta T \leq 1$ day) observations. However, Fig. 2 shows that, overall, the data of various authors are in good agreement.

The data set of Barbieri *et al.* [16] and Barbieri and Romano [39] obtained in 1966–1986 at the Asiago Observatory confirm the absence of appreciable systematic differences between the historical and modern parts of the light curve. Their observations (archival plates from the supernova search program and a quasar monitoring program) form a homogeneous data set, since they used the same telescope and reduction method. On the other hand, this data set [16, 39] does not show appreciable differences from the data of other authors [28, 33] in the historical part of the light curve, and, overall, the data are in good agreement (Fig. 2). In addition, for one night (March 20, 1966), the simultaneous ($\Delta T \leq 0.5$ day) brightness estimates of Barbieri and Romano [39] and Markova and Fomin [33] differ by only $0^m.10$ ($\sim 1\sigma$). On the other hand, the Asiago observations [16, 39] are in good agreement with other observations also in the modern part of the light curve, as follows both from a comparison of the data for the 1970s as a whole (Fig. 2) and a comparison of simultaneous ($\Delta T \leq 1$ day) observations obtained at the Asiago Observatory [16] and by other authors ([17, 36, 37] and Table 1): the systematic differences derived from data for 12 nights are only $0^m.01 \pm 0^m.06$.

The typical rms errors for observations during the historical part of the combined light curve (Fig. 2) are $\sim 0^m.1$–$0^m.3$, and we expect that systematic differences between different data set should not exceed $0^m.2$–$0^m.3$.

Figure 3 shows the modern part of the light curve of ON 231, where the overwhelming majority of observations have been obtained as part of long-term quasar monitoring programs ([9, 15–19, 21, 39, 44–47], Table 1). In the 1970s and 1980s, these programs included photographic observations with typical rms errors of $\sim 0^m.05$–$0^m.15$. We compared the main data sets obtained by various monitoring programs in the 1970s and 1980s. These are Asiago data (Asiago Observatory) [16, 39], RHO data (Florida University's Rosemary Hill Observatory) [17], and PQMP data (Astronomical Institute of St. Petersburg State University; Table 1). A pairwise comparison of these series reveals, respectively, 3, 6, and 12 pairs of simultaneous ($\Delta T \leq 1$ day) brightness estimates, which are in agreement within 1–2σ. At the same time, for three nights (JD 2443341/342, JD 2445464, and JD 45853), the difference between the brightness estimates of [16, 17] and Table 1 is $\sim 0^m.7$–$0^m.9(B)$. Without considering these three largest differences, the mean differences between the series are $0^m.01 \pm 0^m.05$ (RHO and PQMP data; $N = 12$); $0^m.02 \pm 0^m.10$ (RHO and Asiago data; $N = 6$), and $0^m.06 \pm 0^m.05$ (Asiago and PQMP data; $N = 3$). Comparison of the PQMP data (Table 1) with all the other observations yields 19 pairs of simultaneous ($\Delta T = 0.09$–0.96 day) brightness estimates including data from [16, 17, 24, 34, 44]. The systematic difference derived from these pairs is only $0^m.02 \pm 0^m.04$ ($N = 19$). Beginning in 1994, monitoring observations of ON 231 have been renewed by several monitoring programs using CCD arrays [9, 19]. The typical rms errors of these observations are $\sim 0^m.02$–$0^m.05$, and comparisons of data obtained simultaneously on several telescopes have shown that the mean differences between different homogeneous data sets are always less than one standard deviation [9].

Thus, the combined light curve of ON 231 presented in Fig. 1 does not contain appreciable systematic differences between the main homogeneous data sets; the value of such differences in both the modern and historical parts of the light curve is within the typical random observational errors characteristic of the present time.

4. DISCUSSION OF RESULTS

The addition of the 19-year (1972–1990) PQMP data set, which has the largest number of observations and is the longest homogeneous data set in the 1970s and 1980s, appreciably supplements the light curve, and reveals several large-amplitude events that were missed earlier. The PQMP data make up 38% of all data points in 1971–1990. Our data for the second half of the 1980s are especially informative, since only sporadic observations for this interval were published earlier.

In addition, the PQMP data for 1987–1990 enable us to more accurately determine the shape and beginning of the trend (a gradual growth in the mean brightness level in the 1970s–1980s) which has been noted in several earlier studies [9, 19, 48, 50]. This trend is shown by the solid line in Fig. 3, which was obtained by approximating all the observations of 1971–1999 using a smoothing cubic spline and

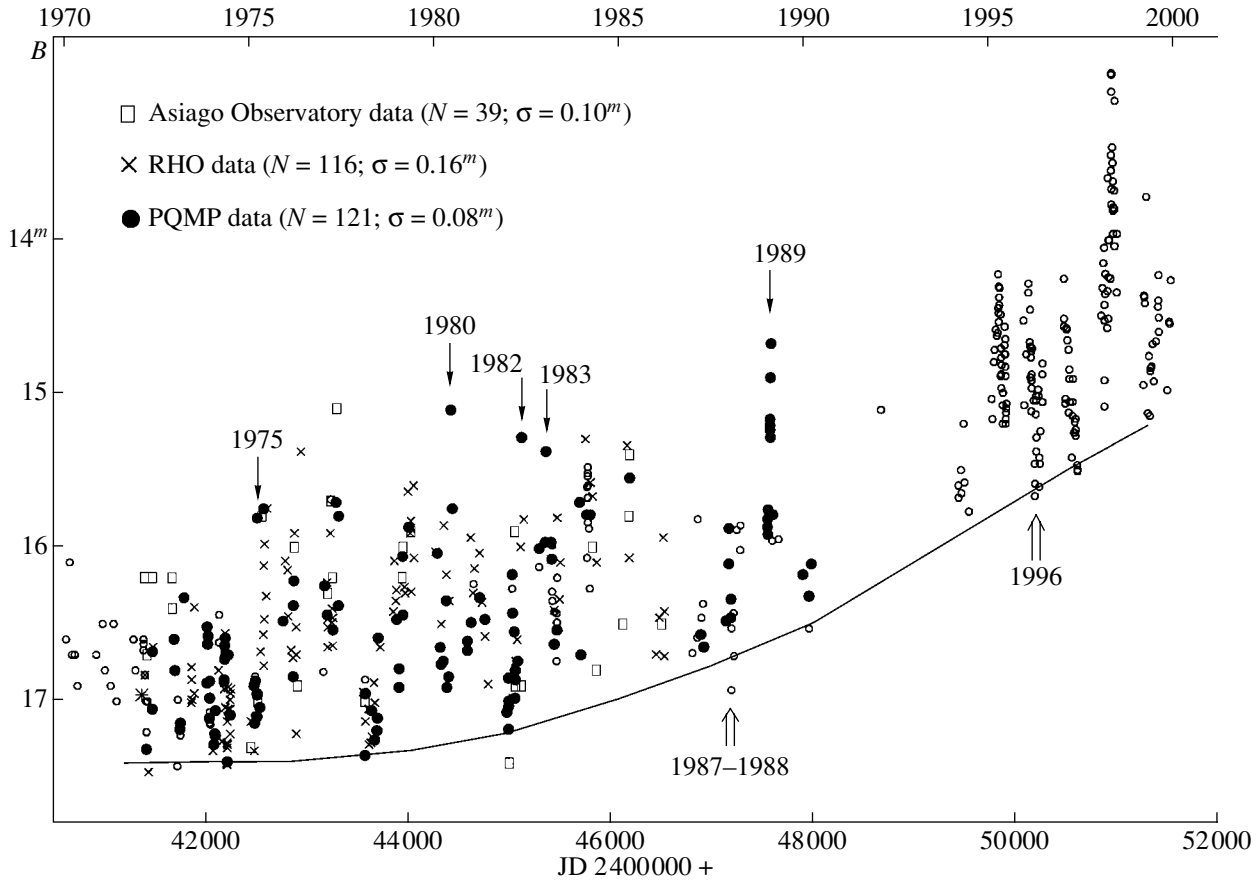

Fig. 3. Modern part of the combined light curve of ON 231, constructed using the data from [3, 5, 9, 15–20, 23, 24, 28–37, 39–48], Table 1. The data for the main homogeneous data sets ([15, 16, 17, 39], Table 1) are marked with different symbols, and the number of brightness estimates (nightly averaged) and the typical rms error of a single observation are indicated. The trend is shown by the solid line (see Section 4.2). The arrows mark large-amplitude events discussed in Section 4.1.

that was then shifted downward by $0^m.7$, in order to represent the slowly varying component as a lower envelope to the more rapid brightness variations. In the second half of the 1980s, the trend corresponds to a nearly linear growth in the mean brightness level at a rate of $\sim 0^m.1$/yr.

4.1. Events on Time Scales of Days–Months

Figures 4–6 present fragments of the combined light curve containing previously unknown large-amplitude ($\sim 1^m.3$–2^m) events on time scales of days to months, which were detected or detailed using the PQMP data (they are also marked by the arrows in Fig. 3). The same time scale is used for all the fragments, and the rms errors in the observations are shown (in some cases, they are smaller than the size of the symbols used). The most substantial and well-observed event is the flare of 1989 (Fig. 4a), whose brightness decay was also observed by Xie *et al.* [18]. This flare has a nearly symmetrical shape and an overall duration of ~50 days. Figures 4b, 4c present examples of flares with similar shapes, durations, and amplitudes in magnitudes that were observed at appreciably different base levels for the slowly varying component: $\sim 17^m.4(B)$ in 1974 and $\sim 15^m.5(B)$ in 1997. The 1997 flare [9] is presented for the V band, where the sampling is better (the brightness variations in the $BVRcIc$ bands are similar, but differ somewhat in amplitude, which grows with decreasing wavelength [19]).

Our observations reveal large-amplitude flares with durations of ~2–4 weeks in 1975 (Fig. 5a), 1980 (Fig. 6a), 1982 (Fig. 5b), and 1983 (Fig. 6b). Although we determined these brightness maxima based on observations for single nights, there is no doubt about their trustworthiness, since, in all cases, the brightness was determined independently from measurements for two to three plates, and the rms errors for the mean brightness estimates for each night were only $0^m.03$–$0^m.07$. In addition, in March 1975, 1980, and 1982, the nearest observations to the brightness maximum (within 5–20 days) also indicated a growth in brightness.

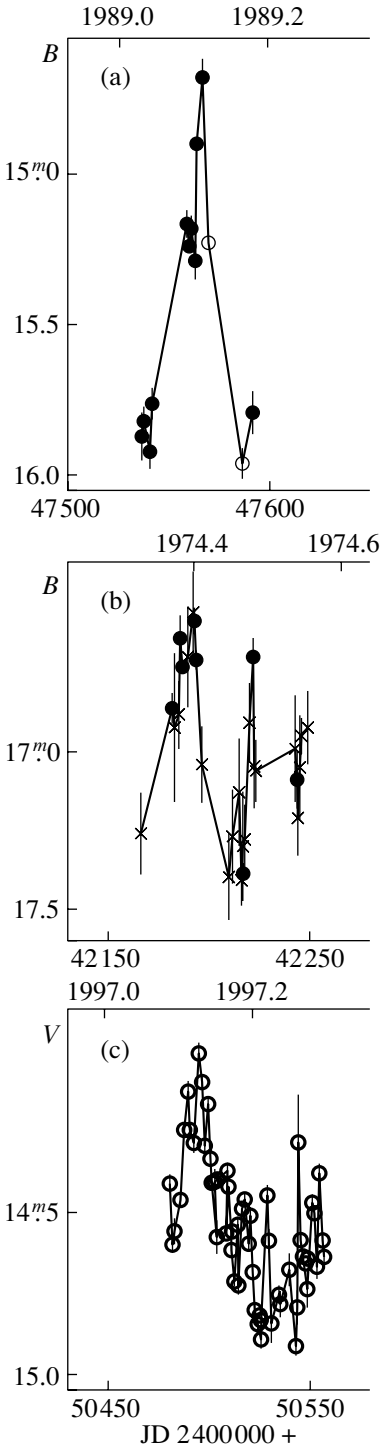

Fig. 4. Flare of ON 231 in 1989 discovered using the PQMP data and two similar flares observed in 1974 and 1997. Shown are PQMP data from Table 1 (•), RHO data [15, 17] (×), and the data of (a) Xie *et al.* [18] and (c) Tosti *et al.* [9, 19] (○). The flares were observed when the base brightness levels ranged from $\sim 17^m.4 (B)$ in 1974 to $\sim 15^m.5 (B)$ in 1997, but they had similar amplitudes in magnitudes, durations, and shapes.

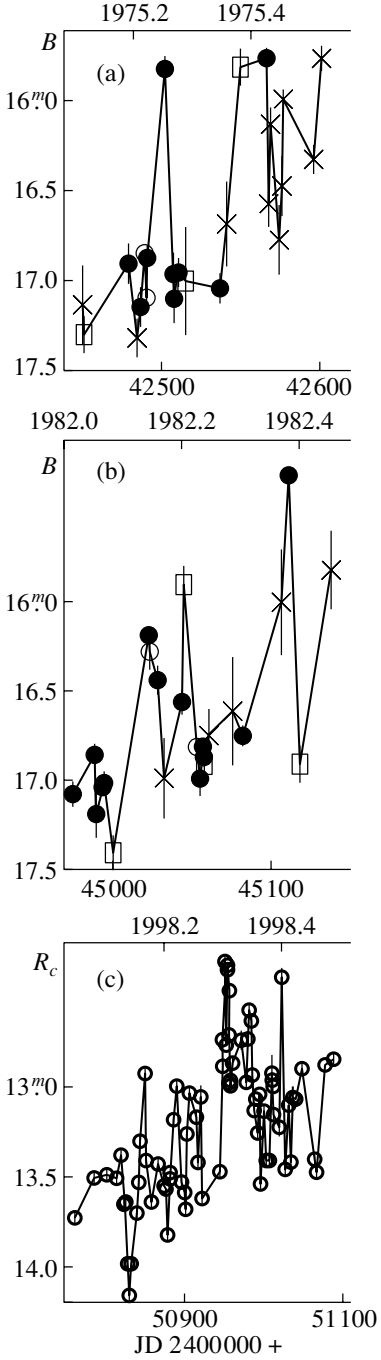

Fig. 5. (a, b) Fragments of the combined light curve of ON 231 containing large-amplitude flares revealed by the PQMP data and (c) the "extraordinary" flare of the spring of 1998 during a high ($15^m.5$ B) base brightness level (data of [5, 19]). The character of the variability in these intervals is the same: rapid brightness variations with amplitudes $\sim 1^m.5$ are superposed on slow variations (time scales of ~100 days) with amplitudes $\sim 1^m$. Shown are PQMP data from Table 1 (•), data from the Asiago Observatory [16] (□), RHO data [15, 17] (×), and the data of [34, 44] (○). The observational errors are almost always less than the size of the symbols.

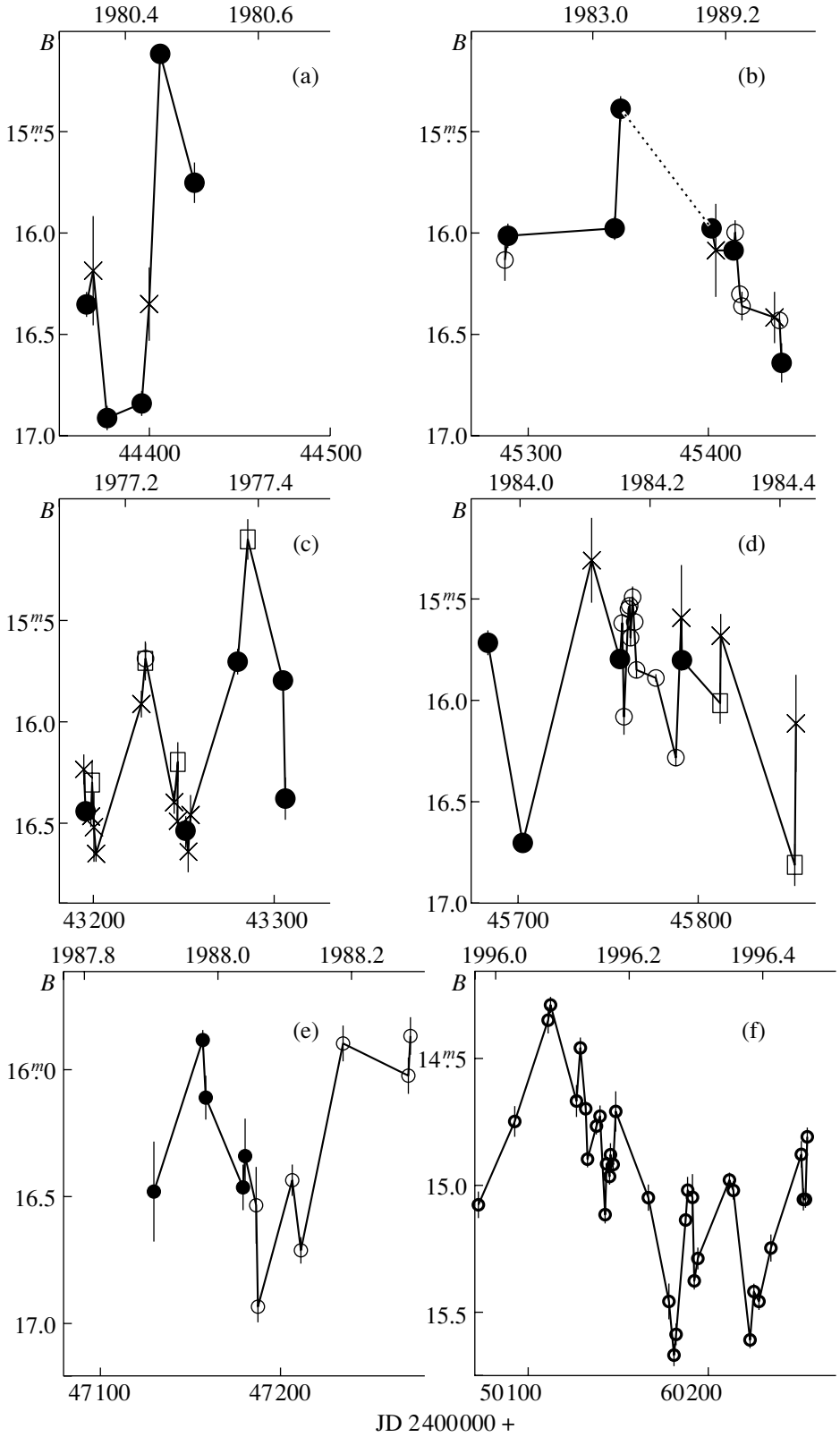

Fig. 6. (a–e) Fragments of the combined light curve of ON 231 containing large-amplitude events detected or detailed using the PQMP data. The notation for the main data sets is the same as in Fig. 5; (○) show data from [3, 34, 36, 41–44, 46]. (f) Behavior of the light curve similar with that observed in 1987–1988 (panel e), but during a high ($\sim 15^m.5(B)$) base brightness level (data of [19]). The observational errors are almost always smaller than the size of the symbols.

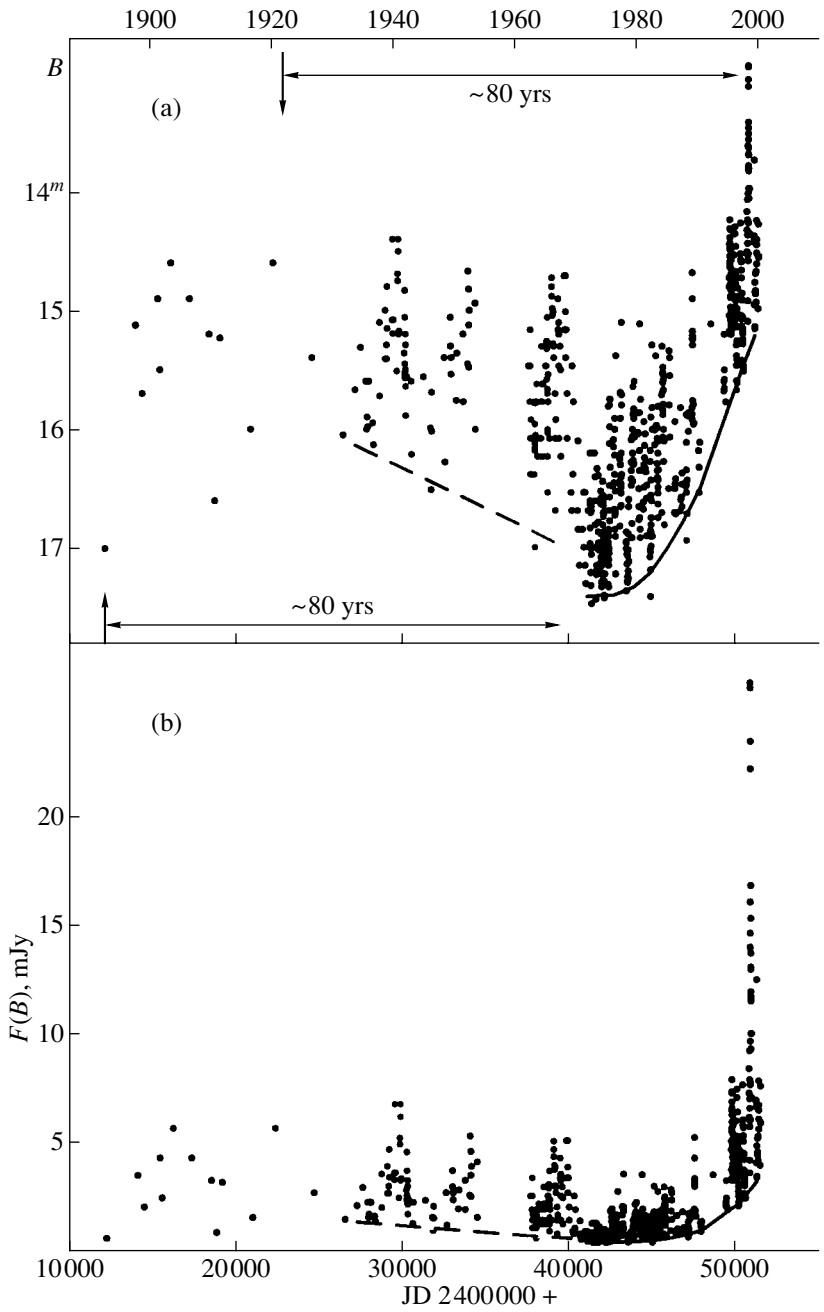

Fig. 7. (a) Combined B-band light curve for ON 231. The slow component of the 1970s–1990s (shown by the solid line), is taken from Fig. 3; the dashed line shows the slow component obtained for the data of 1933–1972 (see Section 4.2.). The arrows mark a proposed minimum and maximum of the slow component, each of which are ~80 yrs earlier than the clear minimum and maximum for this component identified in time intervals with good sampling; (b) combined light curve for ON 231 in units of flux density (without correcting for interstellar extinction, using the calibration of Smith *et al.* [67]). The same data as in Fig. 1 and panel (a) were used. The slow components are identical to those obtained for the light curve in magnitudes.

We identified two flares in 1975, with amplitudes $\sim 1^m.0$–$1^m.5$ (Fig. 5a). The overall duration of the flare of March–April 1975 was probably ~20 days (if the monotonic growth in brightness by $\sim 0^m.5$ in the interval March 12–19 corresponds to its onset). An equally high brightness level was later observed by Barbieri *et al.* [16] in May and by us in June 1975. These flares, whose maximum duration could reach ~10–30 days, were superimposed on a slower (time scale of several months) growth in the brightness with an amplitude of $\sim 1^m$. Similar behavior was observed in 1982 (Fig. 5b)—a flare with an amplitude of $\sim 1^m.5$ and a duration of ~20 days was superimposed on a

more gradual growth in brightness with an amplitude of $\sim 0\overset{m}{.}8$ on a time scale of months.

The character of these brightness variations is very close to the behavior observed for ON 231 during the "extraordinary" flare of the spring of 1998 [9, 50] (Fig.5c; observations are presented for the *Rc* band, for which the sampling is better), although the base brightness levels of ON 231 in 1975 and 1982 were roughly 2^m lower than in 1998 (Fig. 3). In spite of this substantial difference in base brightness level, the amplitudes in magnitudes of both variability components—the slow component with time scales of the order of months and superimposed rapid brightness variations with time scales of the order of weeks—remain constant (Fig. 5).

Figures 6c–6d demonstrate how the PQMP data supplementing the observations of other authors have made it possible to detail the character of the large-amplitude ($\sim 1\overset{m}{.}5$) brightness variations observed in 1977 and 1984. Figure 6e presents the local minimum observed in 1987–1988, with an amplitude of $\sim 1^m$ and an overall duration of ~3–4 months, when the brightness of ON 231 fell to the level of the slow component. Our data together with the observations of Xie *et al.* [46] enable us to follow this minimum in considerable detail. Figure 6f presents the minimum of 1996, which can be traced in detail in the observations of Tosti *et al.* [9] (the same scale was used). Both minima are also marked in Fig. 3. In spite of the appreciably different levels of the slow component ($\sim 17^m$ in 1988 and $\sim 15\overset{m}{.}6$ in 1996), the amplitudes, durations, and characters of the brightness variations in the two minima are very similar.

4.2. Variability Components with Time Scales of Years to Decades

Figure 7a presents the combined light curve of ON 231 together with the slow component of the 1970s–1990s (solid line) taken from Fig. 3. The identification of possible long-term variability components in the historical part of the light curve is made difficult by the insufficient density of the observations and presence of large gaps. Therefore, we focused on the interval 1933–1972 ($N = 189$), which is the best observed part of the historical light curve, and obtained a linear approximation to these data (dashed line), shifting it downward by $1\overset{m}{.}0$ in the same way as for the slow component derived for the 1970s–1990s. This shows that there was apparently a gradual decrease in the mean brightness level of the object in the 1930s through the 1960s. The virtual absence of observations from 1910 through the 1920s means that we cannot rule out the possibility that ON 231 had a brightness maximum in this interval, similar to that observed at the end of the 1990s (observations in 2000–2001 show a decrease in the level of the slow component [51, 52]). In this case, there could be a period of prolonged flares similar to the flare of the 1990s (the trend observed in the 1970s–1990s being its rising branch) of about ~80 yrs. It is interesting that roughly the same time interval separates the absolute brightness minimum observed at the beginning of the 1970s and the similarly deep brightness minimum reported by Wolf [14] at the beginning of the 1890s (which determines an upper limit for the level of the slow component). The possibility of periodicity in the prolonged flares of ON 231 is supported by similarities between the light curves of ON 231 (Fig. 7b) and OJ 287 (Fig. 1 of [53]), for which the presence of a 12-year periodicity in its optical flares has been very firmly established.

It was already noted earlier [19, 48, 50] that the amplitude of rapid brightness variations of ON 231 in magnitudes remains constant ($\sim 1\overset{m}{.}5$–2^m), independent of the level of the underlying slow component. Section 4.1 presents examples (Figs. 4, 5, 6e, 6f) of cases when very similar behavior on time scales from several weeks to several months was observed in the presence of substantially different (from $\sim 17\overset{m}{.}5$ to $\sim 15\overset{m}{.}5$) base brightness levels for the object. Not only were the amplitudes of these events maintained ($\sim 1\overset{m}{.}5$), but also their characteristic forms and overall durations. This constancy of the amplitude in magnitudes means that the rapid and slow components of the variability expressed in units of flux density are changing proportionally. The light curve of ON 231 in units of flux density (Fig. 7b) visually demonstrates this relation (the slow components in Fig. 7b are identical to those obtained for the light curve in magnitudes; Figs. 3, 7a). Over the last 30 years, the level of the slow component has risen by roughly a factor of seven (from 0.4 mJy in the 1970s to 3 mJy in 1999). The maximum amplitude of the superimposed rapid brightness variations increased by about the same factor.

Proportionality of the luminosity in rapid flares to the level of the underlying slow component was first noted in 1970 by Penston and Cannon [54] as a property of the optical light curve of the quasar 3C 345 (behavior which was fully confirmed by subsequent observations [55]). This property is also clearly visible in a number of active galactic nuclei whose optical light curves have large-amplitude slow components varying on time scales of the order of several years. Based on the behavior of the optical light curve of 3C 345, Penston and Cannon [54] concluded that there was a close relationship between the sources responsible for the slow and rapid components of the variability. This assertion can now be made more specific in the framework of models for blazars that link optical variability with variations in the relativistic

beaming factor due to variations in the inclination of the relativistic jet to the line of sight [56–58]. If the slow and rapid components of the optical variability are associated, respectively, with the radiation of a steady component of the relativistic jet and with shock waves (compact superluminal components) moving in the jet, their observed luminosities will vary in proportion to each other as the inclination of the jet to the line of sight varies.

This interpretation of the slow and rapid components of the optical variability is in agreement with evidence found for a number of superluminal sources (for example, 3C 345, 3C 273, 3C 120, S5 0836+710) for a connection between optical flares with time scales for their brightness variations of the order of months and the birth of new superluminal components in the parsec-scale radio jets [55, 59–64]. In addition, for 3C 120 and 3C 273, there is also evidence for an analogous connection between slow (time scales of ∼10 yrs) optical flares and more extended regions of emission in the radio jets detected on scales of the order of several tens of parsecs [60, 62].

4.3. Variability on Time Scales Less than a Day

Optical variability of ON 231 on time scales of tens of minutes to several hours with amplitudes $\sim 0^m.2$–$0^m.9 (B)$ has been noted in a number of studies [9, 18, 25, 44–47, 50, 52, 65]. In 1987–1990, a search for such intraday variability (IDV) in ON 231 was carried out by Xie *et al.* [18, 45–47], who recorded five flares with durations ∼1–2 hrs and amplitudes $\sim 0^m.8$. The presence of large-amplitude ($\sim 1^m$) variability of ON 231 on time scales of ∼1–3 hrs is independently confirmed by the data of Erastova [25], who detected several clear cases of such variability in ON 231 in 1973–1974 based on an analysis of plates taken as part of a program to search for flaring stars carried out at the Byurakan Observatory.

The PQMP data reveal two more examples of large-amplitude IDV in ON 231. For 25 nights distributed roughly uniformly in 1975–1984, the brightness of ON 231 was estimated using three to four consecutively obtained plates (the exposition for each plate was from 15 to 30 min). On two of these nights (January 3/4 and February 25, 1984), variability on a time scale of ∼1 hr is confidently detected, with the IDV detected on the first of these nights having a high amplitude. In both cases, three consecutive measurements show a nearly linear increase in brightness with amplitudes of $0^m.83$ and $0^m.3$ ($\sim 8\sigma$, 4σ). The characteristic time for the brightness increase was ∼45 min, similar to the time scale for IDV events observed in ON 231 in other studies [9, 18, 25, 45–47, 50, 52, 65].

We detected a second case of large-amplitude IDV when comparing the PQMP data with observations of other authors obtained on the same night. We made reference in Section 3 to the fact that a comparison of the three main data sets (RHO, PQMP, Asiago) indicated very good overall agreement but that there were three nights when the differences between the brightness estimates obtained by different authors separated in time by ∼5–9 h were $\sim 0^m.7$–$0^m.9$. On two nights, these discrepancies can be explained as a result of low accuracy ($\sigma \approx 0^m.25$) for the RHO data obtained on those nights [17]. However, the brightness variations on time scales of hours on April 12, 1980 (JD 2444341/342) were probably real. The separation in time between the RHO brightness estimate for this night ($B = 15^m.86 \pm 0^m.15$) [17] and our own three consecutive brightness estimates ($B = 16^m.69 \pm 0^m.09$, $16^m.74 \pm 0^m.06$, $16^m.79 \pm 0^m.11$; Table 1) is $\sim 0^m.9$ ($\sim 5.5\sigma$).

It is likely that, in addition to the events indicated above, there was also IDV with amplitudes $\sim 0^m.2$–$0^m.3$ in the 1970s and 1980s. However, the analysis of the PQMP data shows that, if such brightness variations were present, they were fairly rare, since there was suspected variability at a level of $\sim 0^m.3$ (3σ) on only ∼8% of nights (there were two to four consecutive brightness estimates for ON 231 on 100 nights, with the exposure times for each being ∼15–30 min).

In the 1990s, when the base brightness level of ON 231 became appreciably higher, flares with durations of ∼1.5–2 hrs were observed on a number of occasions; however, their maximum amplitudes did not exceed $\sim 0^m.25$. Continuous observations of ON 231 over ∼8.5 h (∼400 brightness estimates) carried out by Pollock [52, 65] on April 24/25, 1998 revealed a series of four flares with durations of ∼2 h superimposed on a nearly linear trend with an amplitude of $\sim 0^m.35$. The amplitude of the largest of these events was $0^m.24 (R)$. Five hours before the beginning of these observations, Tosti *et al.* [19] observed a similar event with an amplitude of $\sim 0^m.2 (R)$. However, on the remaining 20 nights in 1998–1999 when (according to the data by Pollock [48]) continuous monitoring was carried out over 1–5.5 h, only once did the overall variability amplitude reach $0^m.4$ [48, Table 1]. Massaro *et al.* [50] also observed variability of ON 231 on time scales of the order of several hours more than once in 1998. As an example of such brightness variations, they present an event with a duration of ∼1.5 hrs and an amplitude of $\sim 0^m.2$ superimposed on a trend with an amplitude of $\sim 0^m.2$ (the data for the B and Ic bands show the same behavior, with a small increase in the variability amplitude with decreasing wavelength [50, Fig. 3]).

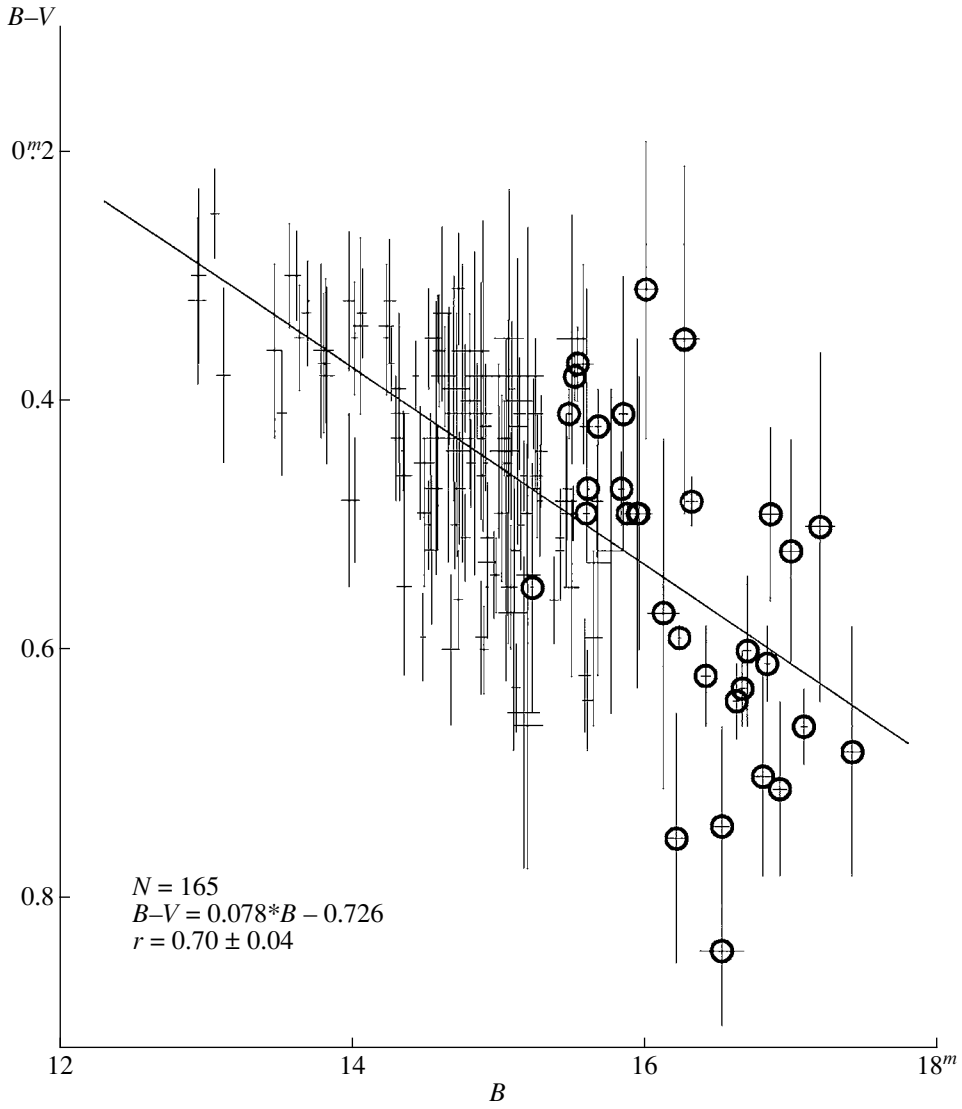

Fig. 8. Dependence of $B-V$ on B magnitude. All $B-V$ values ($N = 165$) available for ON 231 were used (data from [3, 5, 9, 18–20, 23, 29, 32, 34, 35, 40, 42–44, 46, 47], Tables 1 and 2). Errors are indicated for both variables. The data for 1972–1990 are indicated by circles. A least-squares regression line obtained taking into account the errors in $B-V$ is shown by the solid line.

In the 1970s and 1980s, when the base brightness level of the object was low, more than ten cases of IDV events with durations ∼1–2 hrs and amplitudes of $\sim n0^m.8-1^m$ were reported ([18, 25, 45–47] and the PQMP data). A number of observations of IDV were also reported in the 1990s, when the base brightness level was high, but their amplitude never exceeded $0^m.25$ [48, 50, 52, 65]; often, these events were superimposed on slower (time scales of many hours) brightness variations with amplitudes of $\sim 0^m.2-0^m.3$. Thus, in contrast to the components of the optical variability with time scales of weeks to months, the maximum amplitude (in magnitudes) of IDV events in ON 231 probably depends on the base brightness level of the object. This property suggests that the IDV events and slower variability components have a different origin and/or occur in different regions in the source.

4.4. Long-term Variations in the Colors of ON 231

Based on BVR_cI_c data obtained in 1994–1997, Tosti *et al.* [9] found a clear correlation between the spectral index of ON 231 and the flux density in the R_c band: when the brightness of the object increased, its spectrum became flatter. The correlation coefficient grew appreciably when data for each of the flares observed in 1995, 1996, and 1997 were analyzed separately [9]. A comparison of the mean spectral index for the 1994–1997 observations ($\alpha = -1.25 \pm 0.12$)

with several measurements ($\alpha \sim 1.6$) made in the 1980s, when ON 231 was roughly $1^m.5$ weaker, led Tosti *et al.* [9] to conclude that there was a systematic decrease in the slope of the optical spectrum during the increase in the mean brightness level over the last 20 years [9].

This result is confirmed by variations of the color index $B-V$, for which fairly systematic measurements are available in the 1970s and 1980s. Figure 8 shows the dependence of $B-V$ on the B brightness of the object. We have used all available measurements of $B-V$ ($N = 165$); the circles mark data for 1972–1990, which are fairly uniformly distributed in time. We used BV data obtained simultaneously ($\Delta T \leq 1$ day) by the same authors to determine the color index. The correlation is evident—the linear correlation coefficient is $R = 0.70 \pm 0.04$ (the confidence level is $p > 99.9\%$), and the Spearman ranked correlation coefficient is $R_s = 0.57$ ($p > 99.9\%$). In 1972–1990, when the base brightness level was lower, the object was, on average, redder. However, the scatter of the data is fairly large, and a more detailed analysis indicates that the dependences for individual events differ somewhat. The corresponding dependence for $V-R$ is less pronounced due to the absence of data at low brightness levels.

We also derived a conversion equation relating the R and B magnitudes required to construct the most detailed possible light curve for ON 231 (the monitoring in 1970s–1980s was carried out in B, while R has been the principal band since 1994. We used all the available simultaneous BR data and unpublished data of Pollock [52] obtained in 1999–2000. We derived the conversion equation $B = (1.145 \pm 0.037)R - (1.171 \pm 0.517)$ via a double-weighted regression fit [66], which takes into account the errors in both variables (we initially excluded two strongly deviating points). Individual flares appear to obey somewhat different dependences. The B magnitudes obtained by converting R to B with the equation used earlier [48], which had been derived based on a smaller amount of data, yields virtually the same results as our new equation for $R \sim 13^m$–15^m, and discrepancies outside this interval do not exceed $0^m.07$. Overall, uncertainty in converting R to B magnitudes should not exceed $0^m.15$ in most cases, which provides sufficient accuracy to include the converted R magnitudes in a combined B-band light curve, since the amplitudes of the events we are studying are $\sim 1^m$–$1^m.5$.

5. CONCLUSION

One of the main goals of this work was to construct a new combined light curve for ON 231 (Fig. 1) including all known B-band brightness estimates obtained up until 2002; in addition to our own PQMP data, we have used data from 34 publications for this purpose. The PQMP data for 1972–1990 presented in Table 1 substantially improve the modern part of the light curve, and enable us to detect a number of large-amplitude events that had been missed earlier. We have been able to draw a number of conclusions about the properties of the optical variability of ON 231 on time scales from $\sim$1 hr to decades.

Further, we will use the combined light curve constructed for ON 231 to search for periodic components of the variability. Our earlier analysis for data obtained in 1971–1997 showed clear evidence for the presence of a 1395-day (3.8-year) period [48]. The main unusual feature of the mean light curve of this periodic component is a flare with a complex structure, with three main peaks with amplitudes $\sim 1^m.5$–2^m. This structure appears to remain stable over at least several cycles. A more detailed analysis of the entire light curve of ON 231 will be published separately.

ACKNOWLEDGMENTS

The authors thank J.T. Pollock (Appalachian State University) for presenting observations of ON 231 obtained in December 1999–August 2000 prior to their publication and to L.K. Erastova (Byurakan Astrophysical Observatory) for the use of her data on variability of ON 231 obtained in 1969–1976. We are also sincerely grateful to J.T. Pollock and L.K. Erastova for numerous useful discussions. This work was supported by the Russian Foundation for Basic Research (project no. 00-02-16960) and the "Astronomy" State Science and Technology Program.

REFERENCES

1. F. Biraud, Nature **232**, 178 (1971).
2. I. W. A. Brown, Nature **231**, 515 (1971).
3. D. Weistrop, D. B. Shaffer, P. Hintzen, and W. Romanishin, Astrophys. J. **292**, 614 (1985).
4. R. Wurtz, J. T. Stocke, and H. K. C. Yee, Astrophys. J., Suppl. Ser. **103**, 109 (1996).
5. Yu. S. Efimov and N. M. Shakhovskoy, Blazar Data, Vol. 1, n. 3, http://bldata.pg.infn.it (1998).
6. H. D. Aller, M. F. Aller, G. E. Latimer, and P. E. Hodge, Astrophys. J., Suppl. Ser. **59**, 513 (1985).
7. H. Terasranta, M. Tornikoski, A. Mujunen, *et al.*, Astron. Astrophys., Suppl. Ser. **132**, 305 (1998).
8. M. F. Aller, H. D. Aller, P. E. Hodge, and G. E. Latimer, Astrophys. J. **512**, 601 (1999).
9. G. Tosti, M. Fiorucci, M. Luciani, *et al.*, Astron. Astrophys., Suppl. Ser. **130**, 109 (1998).
10. C. von Montigni, D. L. Bertsch, J. Chiang, *et al.*, Astrophys. J. **440**, 525 (1995).

11. P. Sreekumar, D. L. Bertsch, B. L. Dingus, *et al.*, Astrophys. J. **464**, 628 (1996).
12. D. C. Gabuzda, C. M. Mullan, T. V. Cawthorne, *et al.*, Astrophys. J. **435**, 140 (1994).
13. S. G. Jorstad, A. P. Marscher, J. R. Mattox, *et al.*, Astrophys. J., Suppl. Ser. **134**, 181 (2001).
14. M. Wolf, Astron. Nachr. **202**, 415 (1916).
15. J. T. Pollock, A. J. Pica, A. G. Smith, *et al.*, Astron. J. **84**, 1658 (1979).
16. C. Barbieri, E. Cappellaro, G. Romano, *et al.*, Astron. Astrophys., Suppl. Ser. **76**, 477 (1988).
17. J. R. Webb, A. G. Smith, R. J. Leacock, *et al.*, Astron. J. **95**, 374 (1988).
18. G. Z. Xie, K. H. Li, F. Z. Cheng, *et al.*, Astron. Astrophys., Suppl. Ser. **87**, 461 (1991).
19. G. Tosti, M. Fiorucci, M. Luciani, *et al.*, Blazar Data, Vol. 1, n. 4, http://bldata.pg.infn.it (1998).
20. E. Massaro, IAU Circ., No. 5458 (1992).
21. M. K. Babadzhanyants, V. A. Gagen-Torn, E. N. Kopatskaya, *et al.*, Tr. Astron. Obs. Leningr. Gos. Univ. **29**, 72 (1974).
22. M. K. Babadzhanyants, E. T. Belokon', and N. G. Gamm, Astron. Zh. **72**, 447 (1995) [Astron. Rep. **39**, 393 (1995)].
23. R. F. Wing, Astron. J. **78**, 684 (1973).
24. P. Veron and M. P. Veron, Astron. Astrophys. **39**, 281 (1975).
25. L. K. Erastova, private communication.
26. J. T. Pollock, D. L. Hall, C. Ambruster, and P. D. Usher, Astron. Astrophys. **30**, 41 (1974).
27. M. Fiorucci and G. Tosti, Astron. Astrophys., Suppl. Ser. **116**, 403 (1996).
28. H. E. Kurochkin, Astron. Tsirk., No. 644, 1 (1971).
29. P. A. Strittmatter, K. Serkowski, and R. Carswell, Astrophys. J. **175**, L7 (1972).
30. G. Romano, Mem. Soc. Astron. Ital. **43**, 309 (1972).
31. E. R. Craine and J. W. Warner, Astrophys. J. **179**, L53 (1973).
32. P. Battistini, A. Braccesi, and L. Formiggini, Astron. Astrophys. **35**, 93 (1974).
33. L. T. Markova and S. K. Fomin, Astron. Tsirk., No. 856, 4 (1975).
34. S. Tapia, E. R. Craine, and K. Johnson, Astrophys. J. **203**, 291 (1976).
35. F. N. Owen, R. W. Porcas, S. L. Mufson, and T. J. Moffet, Astron. J. **83**, 685 (1978).
36. S. L. O'Dell, J. J. Puschell, W. A. Stein, *et al.*, Astrophys. J. **224**, 22 (1978).
37. B. E. Schaefer, Publ. Astron. Soc. Pac. **92**, 255 (1980).
38. H. Zekl, G. Klare, and I. Appenzeller, Astron. Astrophys. **103**, 342 (1981).
39. C. Barbieri and G. Romano, Astron. Astrophys., Suppl. Ser. **44**, 159 (1981).
40. G. M. Beskin, V. M. Lyutyĭ, S. V. Neizvestnyĭ, *et al.*, Astron. Zh. **62**, 432 (1985) [Sov. Astron. **29**, 252 (1985)].
41. M. Moles, J. M. Garcia-Pelayo, J. Masegosa, and A. Aparicio, Astrophys. J., Suppl. Ser. **58**, 255 (1985).
42. D. M. Worrall, J. M. Rodrigues-Espinosa, W. Z. Wisniewski, *et al.*, Astrophys. J. **303**, 589 (1986).
43. R. Landau, B. Golisch, T. J. Jones, *et al.*, Astrophys. J. **308**, 78 (1986).
44. G. Z. Xie, R. H. Li, M. X. Bao, *et al.*, Astron. Astrophys., Suppl. Ser. **67**, 17 (1987).
45. G. Z. Xie, K. H. Li, Y. Zhou, *et al.*, Astron. J. **96**, 24 (1988).
46. G. Z. Xie, K. H. Li, F. Z. Cheng, *et al.*, Astron. Astrophys. **229**, 329 (1990).
47. G. Z. Xie, K. H. Li, F. K. Liu, *et al.*, Astrophys. J., Suppl. Ser. **80**, 683 (1992).
48. E. T. Belokon, M. K. Babadzhanyants, and J. T. Pollock, Astron. Astrophys. **356**, L21 (2000).
49. F. K. Liu, G. Z. Xie, and J. M. Bai, Astron. Astrophys. **295**, 1 (1995).
50. E. Massaro, M. Maesano, F. Montagni, *et al.*, Astron. Astrophys. **342**, L49 (1999).
51. E. Massaro, F. Mantovani, R. Fanti, *et al.*, Astron. Astrophys. **374**, L435 (2001).
52. J. T. Pollock, private communication.
53. E. Valtaola, H. Terasranta, M. Tornikoski, *et al.*, Astrophys. J. **531**, 744 (2000).
54. M. Penston and R. D. Cannon, R. Obs. Bull. **159**, 85 (1970).
55. M. K. Babadzhanyants and E. T. Belokon', Astrofizika **21**, 217 (1984).
56. J. I. Katz, Astrophys. J. **478**, 527 (1997).
57. M. K. Babadzhanyants, Yu. V. Baryshev, and E. T. Belokon, in *Variability of Blazars,* Ed. by E. Valtaoja and M. Valtonen (Cambridge Univ. Press, Cambridge, 1992), p. 45.
58. M. Villata, C. M. Raiteri, A. Sillanpaa, and L. O. Takalo, Mon. Not. R. Astron. Soc. **293**, L13 (1998).
59. M. K. Babadzhanyants and E. T. Belokon', Astrofizika **23**, 459 (1985).
60. E. T. Belokon', Astrofizika **27**, 429 (1987).
61. E. T. Belokon', Astron. Zh. **68**, 1 (1991) [Sov. Astron. **35**, 1 (1991)].
62. M. K. Babadzhanyants and E. T. Belokon', Astron. Zh. **70**, 241 (1993).
63. T. P. Krichbaum, R. S. Booth, A. J. Kus, *et al.*, Astron. Astrophys. **237**, 3 (1990).
64. K. Otterbein, T. P. Krichbaum, A. Kraus, *et al.*, Astron. Astrophys. **334**, 489 (1998).
65. J. T. Pollock, BAAS **31**, 1396 (1999).
66. F. Murtag, in *Errors, Bias, and Uncertainties in Astronomy,* Ed. by C. Jaschek and F. Murtagh (Cambridge Univ. Press, Cambridge, 1990), p. 385.
67. P. S. Smith, T. J. Balonek, R. Elston, and P. A. Heckert, Astrophys. J., Suppl. Ser. **64**, 459 (1987).

Translated by D. Gabuzda

Astronomy Reports, Vol. 46, No. 8, 2002, pp. 626–633. Translated from Astronomicheskiĭ Zhurnal, Vol. 79, No. 8, 2002, pp. 693–701.

Reconstruction of the Strip Brightness Distribution in a Quasar Accretion Disk from Gravitational Microlensing Data

M. B. Bogdanov and A. M. Cherepashchuk

Chernyshevskiĭ State University, ul. Moskovskaya 155, Saratov, 410601 Russia
Sternberg Astronomical Institute, Universitetskiĭ pr. 13, Moscow, 119992 Russia

Received October 29, 2001; in final form December 27, 2001

Abstract—A technique is proposed for the successive reconstruction of the branches of the strip brightness distribution for a quasar accretion disk via the analysis of observations of high magnification flux events in the multiple quasar images produced by a gravitational lens. The distribution branches are searched for on compact sets of nonnegative, monotonically nonincreasing, convex downward functions. The results of numerical simulations and application of the technique to real observations show that the solution obtained is stable against random noise. Analysis of the light curve of a high magnification event in image C of the gravitational lens QSO 2237+0305 observed by the OGLE group in summer 1999 has yielded the form of the strip brightness distribution in the accretion disk of the lensed quasar. The results are consistent with the hypothesis that the quasar disk was scanned by a fold caustic. The form of the strip distribution is consistent with the expected appearance of an accretion disk rotating around a supermassive black hole.

1. INTRODUCTION

Observations of so-called high magnification events in flux variations of multiple quasar images produced by a gravitational lens provide information about the brightness distribution in the accretion disk surrounding the supermassive black hole at the center of the quasar. These high magnification events are due to microlensing by stars in the lensing galaxy, and the most likely case of microlensing is when the disk image crosses a "fold" caustic. The observed lensing pattern depends only on the one-dimensional strip brightness distribution of the disk in the direction perpendicular to the caustic. Reconstructing this strip distribution from observational data involves solving an ill-posed inverse problem, and requires the use of regularization algorithms that are stable against noise. This problem was first considered by Grieger *et al.* [1], who used the regularization method of Tikhonov.

The more interesting problem of reconstructing the radial brightness distribution in the locally co-moving frame of the accretion disk was analyzed in [2, 3]. This problem is significantly more difficult, and requires, in addition to the introduction of a number of free parameters to describe the microlensing geometry, the inclusion of relativistic effects. For observations obtained in a single photometric band, it is not possible to take relativistic effects into account without a disk model that describes how the radiation intensity of a disk area element depends on direction and frequency. The attempt of Mineshige and Yonehara [4] to reconstruct the radial brightness distribution seen by an external observer was not successful in this sense, since their solution assumed circular symmetry, which will not be the case in the presence of relativistic effects.

In spite of the fundamental possibility of deriving the radial brightness distribution of an accretion disk in a locally co-moving frame, reconstructing the strip brightness distribution as seen by an external observer remains an important problem. This is true because the strip distribution can be reconstructed using minimum *a priori* information. In our analysis of observations of a star microlensed by a caustic of a binary gravitational lens [5], we showed that the form of the strip brightness distribution can be inferred without knowledge of the caustic parameters, distances to the source and lens, or the relative velocity of the source and lens. There is no need to introduce model constraints on the properties of the lensed source. However, a fundamental difficulty arises in the case of high magnification events.

Unlike the binary-lens case, in which caustics are isolated and their cross sections can be clearly fixed, microlensing by stars of a lensing galaxy produces a random field of caustics in the source plane. There have been numerous studies in which such caustic fields have been computed, and we mention here the caustic pattern reported by Shalyapin [6] as an example. Wyithe *et al.* [7] computed the typical microlensing pattern that arises when the image of

1063-7729/02/4608-0626$22.00

an accretion disk moves relative to the caustic field. The neighboring caustics also contribute to observed flux variations. Their influence can be minimized by analyzing only part of the light curve near its maximum. In this case, however, it becomes impossible to determine the initial flux level, relative to which the flux varies as additional images appear or disappear during the primary caustic crossing that led to the high magnification event; this initial flux level cannot be derived directly from the lensing curve.

At first glance, it seems that this problem has a simple solution—allowing the initial level to be a free parameter and estimating it by requiring the best model fit to the observational data. However, this approach automatically makes it impossible to apply the well-known regularization method used in [1, 2, 4] to reconstruct the brightness distribution. It is known that the function yielded by this method is the smoothest approximate solution whose lensing curve agrees with the data within the errors [8, 9]. Varying the initial level produces a family of strip brightness distributions. All functions of this family, including those having no physical meaning, will give the same goodness-of-fit to the observations. There is no criterion that can be used to select one of these functions as the best approximate solution. Requiring the brightness distribution to be nonnegative restricts the given family of functions, but does not remove the problem. In addition, regularization methods make minimum use of *a priori* information about the solution of the ill-posed problem, and therefore cannot guarantee that the solution will be good at large noise level.

Our aim here is to find a unique stable solution that best fits the data by invoking additional *a priori* information consistent with the physics of the phenomenon. We show in Section 2 that, in the analysis of optical and IR observations of a microlensed accretion disk, the branches of the strip brightness distribution corresponding to positive and negative arguments can be searched for on families of nonnegative, monotonically nonincreasing or nonnegative, monotonically nonincreasing, convex downward functions. These families of functions are compact sets, guaranteeing that the approximate solution will be stable and converge to the exact solution as the flux errors approach zero [8, 9].

In Section 3, we compute the observed strip brightness distribution for a standard model of a geometrically thin, optically thick accretion disk rotating in the prograde direction in the equatorial plane of a Kerr black hole. We use this model in Section 4 in numerical simulations of the reconstruction of the branches of the strip brightness distribution. This simulation demonstrates that the proposed technique is sufficiently stable against random noise. In Section 5, we analyze the flux variations for a high magnification event observed in image C of the gravitational lens QSO 2237+0305 in the summer of 1999 by OGLE group, and derive the form of the strip brightness distribution in the accretion disk of the lensed quasar.

2. SUCCESSIVE RECONSTRUCTION OF TWO BRANCHES OF THE STRIP-BRIGHTNESS DISTRIBUTION

Let us assume that the image of a quasar accretion disk is scanned by a fold caustic, which, in view of the small angular size of the disk, can be considered to be a straight line. Let $b(x, y)$ be the observed disk brightness distribution in a Cartesian coordinate system in the plane of the sky (x, y), with the x axis being perpendicular to the caustic and the coordinate origin coinciding with the disk center. The observed lensing curve then depends only on the one-dimensional strip brightness distribution $B(x)$, defined as

$$B(x) = \int_{-\infty}^{\infty}\int_{-\infty}^{\infty} b(\xi, y)\delta(\xi - x)d\xi dy. \qquad (1)$$

Here, $\delta(x)$ is the Dirac delta function. When the caustic crossing produces additional source images accompanied by a sharp flux increase, the lensing curve $I(x)$ is given by the convolution integral equation

$$I(x) = A(x) * B(x) = \int_{-\infty}^{\infty} A(x - \xi)B(\xi)d\xi, \quad (2)$$

whose kernel has the form [10, 11]

$$A(x - \xi) = A_0 + \frac{K}{\sqrt{x - \xi}}H(x - \xi). \qquad (3)$$

Here, $H(x - \xi)$ is the Heaviside step function, which is equal to zero and unity for negative and positive arguments, respectively. The quantity A_0 in (3) depends on the initial flux level, which is produced by all the other images and remains unchanged during the caustic crossing, and the coefficient K characterizes the amplification factor. As we said in the Introduction, the initial flux level is a free parameter of the inverse problem, and the lack of information about K means that $B(x)$ can be reconstructed only up to a constant factor.

Since the quasar accretion disk is appreciably relativistic, if the rotational axis is inclined to the line of sight, the brightness of an area element approaching the external observer should exceed the brightness of a receding area element [2, 3]. Therefore, apart from

cases where the caustic scan is directed along the rotational axis, $B(x)$ ceases to be an even function. We can now write the initial integral in (2) as a sum of two integrals taken along negative and nonnegative ξ intervals. Performing a substitution of variables in the first of these integrals, we obtain

$$I(x) = \int_0^\infty A(x+\xi)B(-\xi)d\xi + \int_0^\infty A(x-\xi)B(\xi)d\xi. \quad (4)$$

It can easily be seen that the properties of the kernel (3) for $x \in (-\infty, 0]$ imply that the second integral in (4) vanishes. It follows that only the negative branch of the strip brightness distribution contributes to the formation of the negative branch of the lensing curve, whereas both branches affect the positive branch $I(x)$ when $x \in (0, \infty)$.

We present a more detailed analysis of the form of the strip brightness distributions for relativistic accretion disks in the next section. Here, it suffices to say that, for optical and longer-wavelength fluxes outside the small region $|\xi| \le \xi_0$, which makes a negligibly small contribution to the total flux, $B(-\xi)$ for $\xi \in (-\infty, -\xi_0]$ and $B(\xi)$ for $\xi \in [\xi_0, \infty)$ are either nonnegative, monotonically nonincreasing or nonnegative, monotonically nonincreasing, convex downward functions. This *a priori* information is qualitative and imposes no rigid model constraints on the form of the strip brightness distribution but can be used when reconstructing this distribution by searching for the solution of our inverse problem on one of these compact sets of functions [8, 9].

The inverse problem we consider here depends on two additional free parameters: the initial flux level I_0 to be subtracted from the lensing curve and the time t_0 when the caustic crosses the disk center. The latter parameter determines the origin of the x axis. If the tangential velocity of the relative motion of the caustic along this axis is V_τ, then $x = V_\tau(t - t_0)$. The velocity component V_τ is, like the parameter K in (3), an unknown quantity. Setting K and V_τ equal to unity and assuming that $x - x_0 = t - t_0$, we can reconstruct only the form of the strip brightness distribution from microlensing observations [5].

The free parameters I_0 and x_0 can be found by minimizing the residual corresponding to the reconstructed function $B(\xi)$. The residual function is usually defined as the sum of the squared residuals, or χ^2_N. The set of functions on which the solution is sought is compact, guaranteeing that the resulting $B(\xi)$ contours should converge to their exact values as the flux errors tend to zero.

Given the above considerations, we have formulated the following algorithm for the successive reconstruction of the branches of the strip distribution.

(1) Specify the initial values of the free parameters I_0 and x_0.

(2) On the negative branch of the lensing curve $I(x)$ for $x \in (-\infty, 0]$, solve the inverse problem for the integral equation

$$I(x) = \int_0^\infty A(x+\xi)B(-\xi)d\xi$$

and find the negative branch $B(-\xi)$ for $\xi \in (-\infty, -\xi_0]$ on one of the compact sets of functions.

(3) Modify the positive branch of the lensing curve for $x \in (0, \infty)$ as follows:

$$\tilde{I}(x) = I(x) - \int_0^\infty A(x+\xi)B(-\xi)d\xi.$$

(4) Solve the inverse problem for the integral equation

$$\tilde{I}(x) = \int_0^\infty A(x-\xi)B(\xi)d\xi$$

for $x \in (0, \infty)$ and find the positive branch of $B(\xi)$ for $\xi \in [\xi_0, \infty)$ on the same compact set of functions.

(5) Compute the total residual function for both branches of the lensing curve.

Repeating procedures (1)–(5), we can easily find the global minimum of the residual function by exhausting all possible parameter combinations. The parameters I_0 and x_0 and the two branches of the strip brightness distribution corresponding to this minimum yield the optimal approximate solution.

A similar technique for the successive reconstruction of the branches of $B(\xi)$ can be used when a caustic crossing involves the disappearance of additional source images, resulting in an abrupt flux decrease. In this case, the argument of the kernel (3) has the opposite sign. Therefore, only the positive branch of $I(x)$ contributes to $B(\xi)$, whereas both branches of the strip distribution contribute to the formation of the negative branch of $B(\xi)$.

3. MODEL OF AN ACCRETION DISK

It follows that our technique for reconstructing the strip brightness distribution is model independent. However, it is reasonable to test the potential of this technique by applying it to a realistic model of a quasar accretion disk. The theory of disk accretion onto compact objects initially developed by Shakura [12] and Sunyaev [13] was further refined to include relativistic effects by Novikov and Thorne [14] and Page and Thorne [15]. Here, we use the conclusions of these studies and the notation of [16].

We consider a geometrically thin, optically thick accretion disk rotating in the prograde direction in the equatorial plane of a Kerr black hole with mass M and normalized angular momentum $a_*(0 \le a_* \le 1)$. Neglecting advection, we can then write for the radiation power per unit disk surface $Q(r)$ as a function of the distance r from the center

$$Q(r) = \frac{3GM\dot{M}}{4\pi r^3} R_R(x), \qquad (5)$$

where $\dot{M}$ is the accretion rate, $x = r/r_g, r_g = GM/c^2$ is the gravitational radius, and $R_R(x)$ is a factor that allows for relativistic effects. This factor can be written in the form

$$R_R(x) = \frac{C(x)}{B(x)},$$

where

$$B(x) = 1 - \frac{3}{x} + \frac{2a_*}{x^{3/2}},$$

$$C(x) = 1 - \frac{y_{ms}}{y} - \frac{3a_*}{2y}\ln\left(\frac{y}{y_{ms}}\right) - \frac{3(y_1 - a_*)^2}{yy_1(y_1 - y_2)(y_1 - y_3)}\ln\left(\frac{y - y_1}{y_{ms} - y_1}\right) - \frac{3(y_2 - a_*)^2}{yy_2(y_2 - y_1)(y_2 - y_3)}\ln\left(\frac{y - y_2}{y_{ms} - y_2}\right) - \frac{3(y_3 - a_*)^2}{yy_3(y_3 - y_1)(y_3 - y_2)}\ln\left(\frac{y - y_3}{y_{ms} - y_3}\right),$$

and $y = x^{1/2}$, y_1, y_2, and y_3 are roots of the cubic equation $y^3 - 3y + a_* = 0$, and y_{ms} corresponds to the nearest stable orbit. According to [17],

$$x_{ms} = r_{ms}/r_g = 3 + z_2 - [(3 - z_1)(3 + z_1 + 2z_2)]^{1/2},$$

where

$$z_1 = 1 + (1 - a_*^2)^{1/3}[(1 + a_*)^{1/3} + (1 - a_*)^{1/3}],$$

$$z_2 = (3a_*^2 + z_1^2)^{1/2}.$$

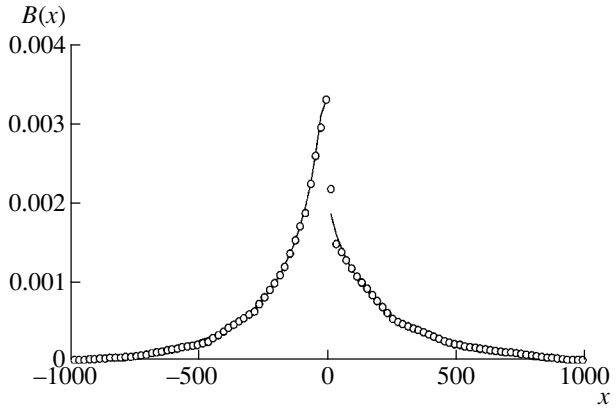

Fig. 1. Branches of the strip brightness distribution for the model of a relativistic quasar accretion disk (solid curve) and the strip distribution samples reconstructed in the numerical simulations (circles). The quantity plotted along the x axis is in units of the black-hole gravitational radius, (Gm/c^2).

The maximum normalized angular momentum of a black hole surrounded by a radiating accretion disk is $a_* = 0.998$ [18], which corresponds to the nearest stable orbit, with $x_{ms} = 1.237$.

Assuming local thermodynamic equilibrium, formula (5) can be used to determine the temperature distribution $T(r)$ in the accretion disk:

$$T(r) = [Q(r)/2\sigma]^{1/4},$$

where σ is the Stefan–Boltzmann constant. We can also determine the brightness distribution at frequency ν_e in the locally co-moving frame of the disk $b(\nu_e, r)$ by equating this result to a Planck function $B(\nu_e, T)$.

In [3], we report the brightness distributions computed for this model for the case of a typical quasar accretion disk with $M = 10^8 M_\odot$ and $a_* = 0.998$ and accretion rate $\dot{M} = 1 M_\odot/\mathrm{yr}$. These computations showed that, despite its high brightness, the central region of the disk makes only a small contribution to the total flux in the visible and IR. In the V band and at longer wavelengths, the region within $r \le 10r_g$ contributes $<1\%$ of the total flux in the locally co-moving frame.

Let i be the angle between the rotational axis of the accretion disk and the line of sight to an external observer. In the disk model considered, the disk brightness in the locally co-moving frame depends only on the distance r from the center. For an observer at $i = 0$, the disk brightness distribution would remain circularly symmetrical, albeit with a lower central brightness due to the gravitational redshift and transverse Doppler effect. When the inclination to the line of sight is not zero, the observed isophote

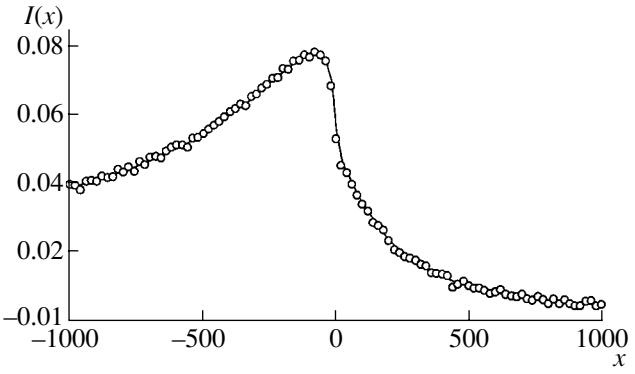

Fig. 2. Samples for a model curve of the microlensing of an accretion disk by a caustic with noise superimposed (circles) and a curve corresponding to the reconstructed strip brightness distribution. The units are the same as in Fig. 1.

pattern of a symmetrical luminous disk should have the form of embedded ellipses with equal axial ratios. A disk rotating around a Kerr black hole would appear very different from this picture. As a result of the relativistic Doppler effect, regions of the rotating disk approaching the observer appear brighter than similar regions that are receding. The brightness distribution becomes especially complex in the central region of the disk due to the gravitational focusing of radiation and bending of photon trajectories.

Let us introduce a Cartesian coordinate system (x, y) in the plane of the sky. Let $g = \nu_o/\nu_e$, where ν_e is the frequency of a photon in the locally co-moving frame of the disk and ν_o is the frequency of the same photon detected by the observer. The theorem of the conservation of phase-space volume then implies that the observed brightness distribution $b_o(\nu_o, x, y)$ should be related to the brightness distribution $b(\nu_e, r)$ in the locally co-moving frame of the disk as follows:

$$b_0(\nu_0, x, y) = g^3(x, y) b(\nu_e, r). \qquad (6)$$

To estimate the relativistic factor $g(x, y)$, together with analyzing the motion of the gas in the disk, we must determine how the angle between the velocity vector of an atom and the direction of the radiation at the chosen point in the disk is related to the inclination i and the coordinates (x, y). Furthermore, to compute the observed flux, we must know how to transform the solid angle corresponding to the given disk area element into the frame of the external observer [16]. This requires a rigorous solution of the ray-tracing problem in the strongly curved spacetime of a Kerr black hole.

This problem attracted a lot of attention due to its importance for the interpretation of X-ray observations of active galactic nuclei [19–25]. Computations of the brightness distributions in accretion disks indicates that, when the inclination angle is not too large, the effects of gravitational focusing and ray bending are manifest only in the very central part of the disk, at distances smaller than $10r_g$. This is the very region where the X-ray radiation of the strongly heated disk material originates. In particular, the profile of the iron K_α line observed in the Seyfert galaxy MCG-6-30-15 provides convincing evidence that the radiation forms in such a strongly curved region of spacetime [16].

Regular observational searches for the effects of gravitational microlensing are carried out the visible and near IR. As pointed out above, the central region of the disk contributes only a small amount of the total flux at these frequencies. Therefore, we can formally assume that the brightness is zero at $r < 10r_g$ ($b(\nu_e, r) = 0$). In [3], we estimated the factor g using exact formulas describing motion in the equatorial plane of a Kerr black hole, but assumed for simplicity that the bending of rays could be neglected outside this central disk region and that the usual formula for Euclidean space can be used to compute solid-angle elements. We also assumed that the radiation intensity emerging from a disk area element is independent of direction. We used similar approximations to compute the two-dimensional V brightness distribution $b(x, y)$ of the disk as seen by an external observer. We computed the strip brightness distribution $B(x)$ on the uniform grid $x_i = -990 + 20(i - 1)$, $i = 1, 2, \ldots M = 100$ (in units of r_g) using (1). We chose the grid step to be large enough so that the central region of the disk would not be included. We assumed that the disk material rotates counterclockwise and that the major axis of its elliptical projection onto the plane of the sky lies on the x axis.

The curve in Fig. 1 shows the strip brightness distribution of our disk model for $i = 45°$. We set the total flux emitted by the visible surface of the disk equal to unity. The negative branch $B(x)$, which corresponds to the approaching edge of the disk, is clearly brighter than the receding side. Both branches can be approximated well by convex (concave) downward, monotonically nonincreasing functions.

We would expect such a representation to be valid for a fairly broad class of quasar accretion-disk models. The radial brightness distributions for $r > 2r_g$ in the locally co-moving frame are convex downward, both when advection effects are taken into account and for geometrically thick disks with vertical temperature gradients [16]. However, this is not true of the strip distribution. Advection decreases the exponent in the denominator in (5), resulting in a slower fall-off of the disk brightness with distance from the center. Therefore, if the observed flux-variation curve cannot be described in terms of microlensing of a

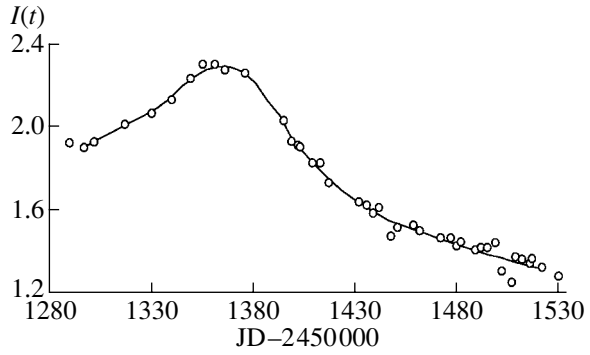

Fig. 3. Samples of the V flux-variation curve of component C of the gravitational lens QSO 2237+0305 (circles) and a curve corresponding to the reconstructed strip brightness distribution (solid line).

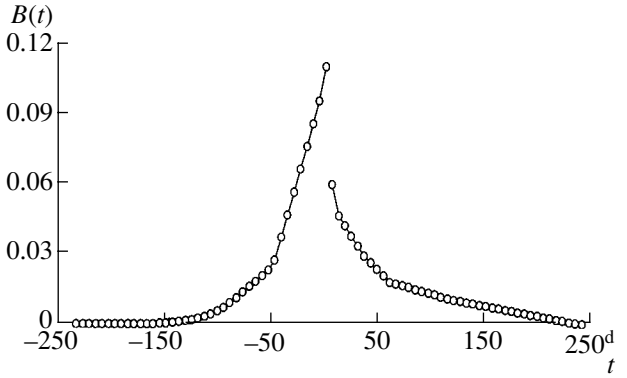

Fig. 4. Branches of the reconstructed strip brightness distribution for the quasar accretion disk whose images are produced by the gravitational lens QSO 2237+0305. The tangential velocity V_τ of the relative motion of the caustic in the x direction is set equal to unity.

source whose strip brightness distribution has the form of two branches corresponding to convex downward functions, these branches can be searched for on the compact set of nonnegative, monotonically nonincreasing functions.

4. RESULTS OF NUMERICAL SIMULATIONS

To assess the potential of our technique, we performed numerical simulations of the reconstruction of a model strip brightness distribution. Note that the main integral equation (2) has a singular kernel (3). When computing such integrals, special measures must be taken to ensure the convergence of the corresponding integral sums. In particular, attempts to compute $I(x_i)$ on a nonuniform grid x_i when $B(\xi_i)$ is defined on a uniform grid ξ_i can lead to large errors in the final results. General issues in connection with applying numerical methods to singular integral equations are considered in the monograph [26]. A simple proof of a sufficient condition for the convergence of the integral sum for the particular case of the equation (2) with the kernel (3) is given in [27]. This condition consists in a special choice of the grids forming a canonical dissection of the integration interval. Both grids are uniform, and either $\xi_i = (x_i + x_{i+1})/2$ or the grid interval $\Delta\xi$ is an integer fraction of the interval Δx, with the ξ_i being midpoints of these embedded intervals. The observed lensing curves are usually comprised of nonuniform count measurements. Therefore, before comparison with the observations, the model data must first be computed on a uniform grid and then interpolated to the observation times.

In our numerical simulations, we used the first version of the canonical dissection, with $\xi_i = (x_i + x_{i+1})/2$, $\Delta\xi = \Delta x = 20$, $\xi_i = -990 + 20(i-1)$ for $i = 1, 2, \ldots M = 100$ and $x_i = -1000 + 20(i-1)$ for $i = 1, 2, \ldots N = 101$ (in units of r_g). We assumed that the caustic crossing is accompanied by a flux decrease. We added noise in the form of a random Gaussian component with zero mean and a standard deviation equal to 1% of the maximum flux to the initial data samples $I(x_i)$ for the lensing curve computed for the V strip brightness distribution for our disk model with $i = 45°$, shown by the solid line in Fig. 1. The resulting samples for the lensing curve $I_o(x_i)$ for the values of the free parameters $I_0 = 0$ and $x_0 = 0$ are shown by the circles in Fig. 2.

We searched for the branches $B(\xi)$ on the compact set of nonnegative, monotonically nonincreasing, convex downward functions for various I_0 and x_0 values using a modified version of the PTISR code written in FORTRAN [8, 9]. To reduce the effect of roundoff errors, we transformed all real variables used in PTISR and its auxilliary subroutines into double-precision variables with 16 significant digits in their floating-point mantissas. We also used the additional *a priori* information that $B(\xi)$ is equal to zero at the ends of the domain of variation of the argument. This is equivalent to specifying the size of this interval, which is required in the solution of any ill-posed problem. Estimating the size of the domain where $B(\xi)$ takes on nonzero values does not present difficulties in practice. Initially, a domain clearly exceeding probable values for this interval is adopted, and its size is then refined iteratively via a series of successive approximations.

It is convenient to adopt the quantity

$$\chi^2_N = \sum_{i=1}^{N} [(I_o(x_i) - I_c(x_i))/\sigma_i]^2,$$

for the residual, where N is the number of data samples on the lensing curve $I_o(x_i)$, σ_i are the estimated errors of these samples, and $I_c(x_i)$ are

the fluxes corresponding to the reconstructed strip brightness distribution. The residual had its minimum for the parameter values $I_0 = 0.000 \pm 0.001$ and $x_0 = 3.0 \pm 2.0$. The samples for the corresponding reconstructed branches of the strip brightness distribution are shown by the circles in Fig. 1, and the lensing curve is shown by the curve in Fig. 2. The minimum is $\chi^2_N = 50.2$, whereas the χ^2_N value corresponding to a probability of 50% that the hypothesis in question should be adopted is 100.3 for $N = 101$ degrees of freedom. On the whole, the inferred parameter values and strip distribution branches are close to their initial specified values. Thus, the results of our numerical simulations show that the proposed technique is potentially a powerful tool.

5. OGLE OBSERVATIONS OF A HIGH MAGNIFICATION EVENT FOR COMPONENT C OF QSO 2237+0305

The gravitational lens QSO 2237+0305, also known as Huchra's Lens or the Einstein Cross, is the best known example of this class of objects. Four images of a distant ($z = 1.695$) quasar are produced by the gravitational field of a fairly nearby ($z = 0.0394$) galaxy located almost along the line of sight to the quasar. As a result, the images display time lags of less than a day, and the time scale for microlensing events is of the order of several tens of days. Uncorrelated fluctuations in different images associated with microlensing by stars of the lensing galaxy were first discovered by Irwin *et al.* [28]. Since then, various groups have monitored this object in order to record data for microlensing effects [29, 30]. The densest and most accurate observational series are those obtained by the international OGLE team [31, 32]. Their data show that, in the summer of 1999, component C exhibited a characteristic flare, such as may occur during microlensing by a fold caustic accompanied by the disappearance of additional source images. The results of their model fitting of this event led Wyithe *et al.* [33] to conclude that it may have involved a caustic cusp. We analyzed these observational data with the aim of reconstructing the strip brightness distribution.

We obtained the V magnitudes for the lensing curve and their errors via the internet from the OGLE server. We transformed these magnitudes into flux samples assuming that a unit level corresponds to $18^m\!.0$, and averaged them over each observing night. We show these samples as circles in Fig. 3 plotted as a function of time expressed in modified Julian Dates JD−2450000.0. Since the singular nature of the main integral equation (2) requires the use of grids with canonical dissections, we again adopted the first version of such grids described above and computed $I_o(t_i)$ via a linear interpolation onto a uniform grid t_i of $N = 38$ samples with a step of $\Delta t = \Delta\xi = 6^d\!.0$. We searched for the branches of the strip brightness distribution $B(\xi)$ on the grid $\xi_i = -237^d\!.0 + (i-1)\Delta\xi$, $i = 1, 2, \ldots M = 80$.

The values of the free parameters that yielded the global minimum of the residual were $I_0 = 1.020 \pm 0.005$ and $t_0 = 1392.3 \pm 0.1$. The minimum of the residual function is $\chi^2_N = 22.6$, whereas the χ^2_N value corresponding to a probability of 50% that the hypothesis in question should be adopted is 37.3 for $N = 38$ degrees of freedom. Figure 4 shows the branches of the strip brightness distribution found on the set of nonnnegative, monotonically nonincreasing, convex downward functions. The corresponding lensing curve is shown in Fig. 3, and fits the observational data well. The resulting χ^2_N indicates that the hypothesis that we have observed the lensing of a quasar accretion disk by a fold-type caustic is quite acceptable.

The form of the reconstructed strip brightness distribution agrees with our expectations for a relativistic accretion disk rotating around a supermassive black hole—its left branch is appreciably brighter than its right branch. If we adopt for the tangential velocity of the caustic its most probable value $V_\tau = 300$ km/s [32], the step size in linear units will be $\Delta\xi = 1.6 \times 10^{13}$ cm, and the total width of the $B(\xi)$ domain will be 1.2×10^{15} cm. The actual disk scale length depends on the direction of the caustic scanning. However, in any case, this value can be considered a lower limit for this size.

6. CONCLUSIONS

Our proposed technique for the successive reconstruction of the branches of the strip brightness distribution of a quasar accretion disk via analysis of observations of high magnification microlensing events makes it possible to take into account a large amount of *a priori* information that is consistent with the physics of the phenomenon. This ensures that the resulting solution is accurate and stable against random noise. Both branches of the strip brightness distribution can be derived from the lensing curve without applying any rigid model constraints. These properties are confirmed by numerical simulations and results obtained by applying the technique to real observational data.

Our analysis of a high magnification event observed in image C of the gravitational lens QSO 2237+0305 in the summer of 1999 by the international OGLE group has yielded the form of the strip brightness distribution in the accretion disk of the lensed quasar. The results are consistent with the

hypothesis that we have observed a scan of the image by a fold caustic. The form of the distribution corresponds to our expectations for a relativistic accretion disk rotating around a supermassive black hole. Further development of the proposed method and its application to the results of X-ray observations of gravitational microlensing effects for galactic nuclei and quasars obtained using the new generation of X-ray observatories (Chandra, XMM, etc.) could make it possible to reconstruct the structure of the accreting plasma near the event horizon of a black hole. These studies would be an important addition to planned future observations of the close vicinities of black holes in galactic nuclei using a future X-ray space interferometer with an angular resolution of 10^{-7} arcsec [34].

ACKNOWLEDGMENTS

We are grateful to the OGLE group members for the observational material provided. This work was partially supported by the "Astronomy" State Science and Technology Program of the Russian Federation, the Russian Foundation for Basic Research (project code 99-02-17589), the Ministry for Education of the Russian Federation, and the Program "Universities of Russia."

REFERENCES

1. B. Grieger, R. Kayser, and T. Schramm, Astron. Astrophys. **252**, 508 (1991).
2. E. Agol and J. Krolik, Astrophys. J. **524** (1), 49 (1999).
3. M. B. Bogdanov and A. M. Cherepashchuk, *Joint European and National Astronomy Meeting "JENAM-2000"* (GEOS, Moscow, 2000), p. 145.
4. S. Mineshige and A. Yonehara, Publ. Astron. Soc. Jpn. **51**, 497 (1999).
5. M. B. Bogdanov and A. M. Cherepashchuk, Astron. Zh. **77**, 842 (2000) [Astron. Rep. **44**, 745 (2000)].
6. V. N. Shalyapin, Astron. Zh. **72**, 668 (1995) [Astron. Rep. **39**, 594 (1995)].
7. J. S. B. Wyithe, R. L. Webster, E. L. Turner, and D. J. Mortlock, Mon. Not. R. Astron. Soc. **315**, 62 (2000).
8. A. N. Tikhonov, A. V. Goncharskiĭ, V. V. Stepanov, and A. G. Yagola, *Regularizing Algorithms and A Priori Information* [in Russian] (Nauka, Moscow, 1983).
9. A. V. Goncharskiĭ, A. M. Cherepashchuk, and A. G. Yagola, *Ill-posed Problems in Astrophysics* [in Russian] (Nauka, Moscow, 1985).
10. P. Schneider, J. Ehlers, and E. E. Falco, *Gravitational Lenses* (Springer-Verlag, Berlin, 1992).
11. A. F. Zakharov, *Gravitational Lenses and Microlenses* [in Russian] (Yanus-K, Moscow, 1997).
12. N. I. Shakura, Astron. Zh. **49**, 921 (1972) [Sov. Astron. **16**, 756 (1972)].
13. N. I. Shakura and R. A. Sunyaev, Astron. Astrophys. **24**, 337 (1973).
14. I. D. Novikov and K. S. Thorne, *Black Holes* (Gordon and Breach, New York, 1973), p. 343.
15. D. N. Page and K. S. Thorne, Astrophys. J. **191**, 499 (1974).
16. J. H. Krolik, *Active Galactic Nuclei* (Princeton Univ. Press, Princeton, 1999).
17. J. M. Bardeen, W. H. Press, and S. A. Teukolsky, Astrophys. J. **178**, 347 (1972).
18. K. S. Thorne, Astrophys. J. **191**, 507 (1974).
19. C. T. Cunningham, Astrophys. J. **202**, 788 (1975).
20. A. Laor, Astrophys. J. **376**, 90 (1991).
21. V. Karas, D. Vokrouhlicky, and A. G. Polnarev, Mon. Not. R. Astron. Soc. **259**, 569 (1992).
22. K. P. Rauch and R. D. Blandford, Astrophys. J. **421**, 46 (1994).
23. B. C. Bromley, K. Chen, and W. A. Miller, Astrophys. J. **475**, 57 (1997).
24. V. I. Pariev and B. C. Bromley, Astrophys. J. **508**, 590 (1998).
25. A. F. Zakharov and S. V. Repin, Astron. Zh. **76**, 780 (1999) [Astron. Rep. **43**, 705 (1999)].
26. S. M. Belotserkovskiĭ and I. K. Lifanov, *Numerical Methods in Singular Integral Equations* [in Russian] (Nauka, Moscow, 1985).
27. M. B. Bogdanov, astro-ph/0102031 (2001).
28. M. J. Irwin, R. L. Webster, P. C. Hewitt, *et al.*, Astron. J. **98**, 1989 (1989).
29. R. T. Corrigan, M. J. Irwin, J. Arnaud, *et al.*, Astron. J. **102**, 34 (1991).
30. R. Ostensen, S. Refsdal, R. Stabell, *et al.*, Astron. Astrophys. **309**, 590 (1996).
31. P. R. Wozniak, C. Alard, A. Udalski, *et al.*, Astrophys. J. **529**, 88 (2000).
32. P. R. Wozniak, A. Udalski, M. Szymanski, *et al.*, Astrophys. J. **540**, L65 (2000).
33. J. S. B. Wyithe, E. L. Turner, and R. L. Webster, Mon. Not. R. Astron. Soc. **318**, 1120 (2000).
34. N. White, Nature **407**, 146 (2000).

Translated by A. Dambis

Astronomy Reports, Vol. 46, No. 8, 2002, pp. 634–638. Translated from Astronomicheskiĭ Zhurnal, Vol. 79, No. 8, 2002, pp. 702–707.

Observations of the Flux of Very-High-Energy Gamma Rays from the Blazar 3C 66A

A. A. Stepanyan, Yu. I. Neshpor, N. A. Andreeva, O. R. Kalekin, N. A. Zhogolev, V. P. Fomin, and V. G. Shitov

Crimean Astrophysical Observatory, Nauchnyĭ, Crimea, Ukraine

Received November 15, 2001; in final form December 27, 2001

Abstract—Measurements of the flux of very-high-energy (>1 TeV) gamma rays from the blazar 3C 66A obtained over four years are presented. The mean flux over the four-year period was $(2.8 \pm 0.4) \times 10^{-11}$ cm^{-2} s^{-1}. There is a correlation between the season-averaged flux of very-high-energy gamma rays and the observed optical radiation. © *2002 MAIK "Nauka/Interperiodica".*

1. INTRODUCTION

The blazar 3C 66A was discovered in the optical in 1974 as a 15.2^m blue, point-like source near the powerful radio galaxy 3C 66B (they are separated by $6'.5$) [1]. Its radiation proved to be strongly polarized, with the degree of polarization varying over a wide range and sometimes reaching 30%. The redshift of this blazar is $z = 0.44$. The optical luminosity is also variable by at least a factor of a few, and sometimes exceeds 10^{46} erg/s. The source's X-ray emission, detected in 1979–1980, also shows large-amplitude variations that coincide with variations in the optical [2]. The X-ray luminosity of 3C 66A can reach 10^{46} erg/s [2]. Optical observations of 3C 66A have been carried out at the Crimean Astrophysical Observatory by Efimov and Shakhovskoy [3].

Our very-high-energy (VHE) gamma-ray observations of this object obtained in 1996 using the ground-based gamma-ray telescope of the Crimean Astrophysical Observatory yielded a confident detection of 3C 66A as a gamma-ray source [4]. VHE gamma rays of very high energy are absorbed by optical and infrared photons in intergalactic space. The mean free path for this absorption depends on the density of such photons, which is not accurately known. However, the distance to 3C 66A is sufficiently large that the flux of gamma rays should be substantially weakened. This fact led many astrophysicists to regard our result with skepticism.

We also observed 3C 66A in 1997 and 1998 [5]. The recorded gamma-ray flux had a low significance, although the total number of gamma rays recorded over three years yielded a high significance for detection (5.9σ). We noted that the optical luminosity of the blazar in the period of our gamma-ray observations was approximately 1^m weaker than in 1996. Note that gamma rays from 3C 66A have also been detected by EGRET on board the Compton Gamma-Ray Observatory, and this source is included in the third EGRET catalog under the name 3EG J 0222+4253 [6].

Thanks to good observing conditions, we were able to conduct more extensive observations of this object in 2000. These observations have confirmed 3C 66A as a source of VHE gamma rays.

2. BRIEF DESCRIPTION OF THE GROUND-BASED GAMMA-RAY TELESCOPE

Gamma rays with energies $E > 10^{11}$ eV were detected using a ground-based instrument based on the principle that, when VHE gamma rays interact with the nuclei of air atoms, they form so-called extensive air showers consisting of high-energy electrons and positrons, which emit optical Cherenkov radiation with opening angles of 1° in the direction of motion of the initial gamma rays. This makes it possible to determine the region from which the flux of gamma rays arrived. The area illuminated by the Cherenkov flash is large—tens of thousands of square meters—enabling the detection of small gamma-ray fluxes (approximately 10^{-11} cm^{-2} s^{-1}). The main hindrance to detecting and studying cosmic sources of VHE gamma rays of very high energy is the presence of a substantial cosmic-ray background, whose particles give rise to Cherenkov flashes in the Earth's atmosphere that are difficult to distinguish from flashes called forth by cosmic gamma rays. The application of multi-element cameras makes it possible to separate out most flashes due to charged cosmic-ray particles. The first telescope of this type began its operation in the USA in 1982 at the Whipple Observatory [7].

1063-7729/02/4608-0634$22.00

Table 1. Recorded and selected events

Selection method	Number of events on source	Number of events on background	Difference	Signal/noise (σ)
No selection	16646	16448	198	1.1
Using coordinate-independent parameters	1393	1216	177	3.5
Using coordinate-dependent parameters	436	295	141	5.2

Observations on the Crimean Astrophysics Observatory's GT-48 double telescope (mount) equipped with a multi-element camera began in 1989. We have described the GT-48 setup in a number of previous papers (see, for example, [8]); it consists of two identical altitude–azimuth mounts (sections) forming a north–south line separated by 20 m and located at an altitude of 600 m above sea level. Six telescopes, which we will call elements, are mounted on each of the two sections. The optics of each element consist of four 1.2-meter mirrors with a common focus. The four-mirror elements have a focal length of 5 m. There is a light receiver (camera) in the focal plane of each element, consisting of 37 photomultipliers (cells), used to record the images of Cherenkov flashes in the optical (300–560 nm). A conical light guide is placed in front of each photomultiplier. The outer surfaces of the light-guide windows are hexagonal in shape and abut each other, so that all the light entering the receiver falls onto the photomultiplier cathode. The field of view of the entire light receiver is 2.6°. The signals from the cells of the four elements pointed at the same region of sky are linearly added. Flashes are registered only when the amplitudes of the signals for any two of the 37 channels are coincident in time and exceed an established threshold. The time resolution for the coincidence scheme is 15 ns. The result is a digitized image of the flash. Analyses of the angular distribution of the light can be used to compare the parameters of the flashes for different events.

Two other elements with focal lengths of 3.2 m are intended for the detection of flashes of ultraviolet radiation at 200–300 nm. In this case, the light receivers are solar-blind photomultipliers. The total area for the mirrors on both mounts (sections) is 54 m^2.

The mount is moved using a control system with a pointing accuracy of $\pm 0.05°$. Observations can be carried out in both a coincidence regime for the two sections and independently for each section. The effective threshold energy for detection of the gamma rays is 1 TeV.

3. OBSERVATIONS AND REDUCTION METHOD

Observations of the blazar 3C 66A ($\alpha = 2^h22^m40^s$, $\delta = 43°02'08''$) were carried out in the two parallel oriented sections in a coincidence regime with a time resolution of 100 ns. Observations tracking the target were obtained from October 4 through November 11, 2000. The source and background were recorded alternately with a time offset of 30 minutes, with the background being observed at the same zenith angles and azimuths as the source. The duration of each tracking session was 25 minutes. In all, we carried out 50 observing sessions for both the source and the background in the indicated period. Data obtained during poor observing conditions were excluded from our analysis. This left 33 pairs of sessions, corresponding to 825 minutes of observations each of the source and the background.

We subjected the resulting data to the following reduction process. (1) Events during which we noted disruptions in the operation of the telescope guiding system (i.e., deviations of the optical axis of the telescope from the specified direction exceeded 3′) were thrown out. (2) Data in which there was saturation of the analog–digital converter (255 discrete units, or 180 photoelectrons) in at least one channel (light receiver cell) were thrown out. (3) The signal amplitudes in the channels were corrected using the appropriate calibration coefficients. (4) Flashes whose maximum amplitude was in the outer ring of light-receiver cells were thrown out. (5) We determined the parameters of the remaining flashes, namely, the first and second moments of the light distribution, from which all remaining parameters were derived. Our investigations showed that the parameters of low-energy flashes were strongly distorted. For the GT-48 gamma-ray telescope, we took flashes to have low energy if their amplitudes were less than 100 discrete units (i.e., 70 photoelectrons), and excluded such flashes from consideration. After this preliminary reduction, we were left with 16 646 events for the source and 16 448 events for the background for further analysis (Table 1).

4. SELECTION OF GAMMA RAYS

The resulting data were subjected to further reduction to enable an analysis of the digitized flash images using formal mathematical methods. We calculated the first and second moments of the brightness

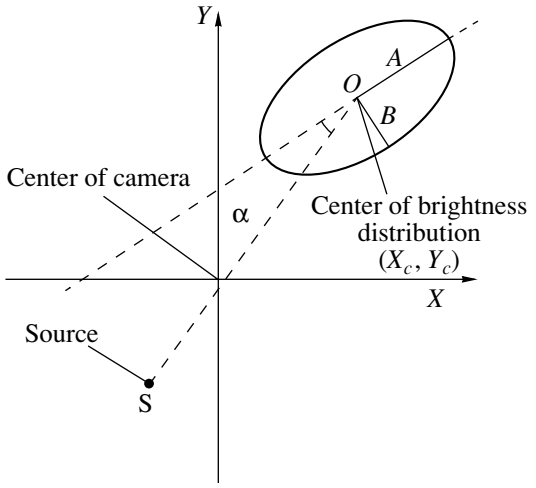

Fig. 1. Schematic of the parameters of a Cherenkov flash. A is the effective length and B the effective width of the flash image; α is the azimuthal angle.

distributions, from which we derived various parameters of the Cherenkov flashes: the coordinates of the center of the brightness distribution X_c and Y_c, the effective length A and effective width B of the flash, and the angle α between the direction toward the source from the flash center and the direction of the major axis of the flash image (Fig. 1). We calculated the moments using the data in each cell whose signal exceeded a specified threshold [9]. The letter S in Fig. 1 shows the position of the gamma-ray source in the focal plane of the camera, which we will call the source. The parameters of flashes (events) recorded simultaneously at each section were determined independently using the data for each section, so that each such event had two values for each parameter, which we denote using a 1 for the northern section and a 2 for the southern section.

The results of Monte Carlo computations indicate that flashes from charged particles have large angular sizes. In addition, they are distributed isotropically, while the images of flashes formed by gamma rays are elongated in the direction of the source. The parameter α can also be used to distinguish gamma-ray flashes. The differences between images of Cherenkov flashes associated with charged cosmic-ray particles and gamma rays enables us to separate out up to 99% of the background events while leaving an appreciable fraction of gamma-ray events. Events with parameters that do not fall in the specified range are excluded from consideration. We identified the parameter values for which the magnitude of an effect, i.e., the signal to noise ratio $N_s - N_b/\sqrt{N_s + N_b}$ in standard deviations, was maximum. Here, N_s and N_b are the number of selected gamma-ray events for observations in the direction of the source and background, respectively.

Table 2. Gamma-ray fluxes from 3C 66A in 1996–2000 (in $[10^{-11}\ \mathrm{cm}^{-2}\ \mathrm{s}^{-1}]$)

1996	1997	1998	2000
4.5 ± 1.6	1.6 ± 1.3	3.8 ± 1.8	2.7 ± 0.5

We selected the gamma-ray events using the same parameters as in the reduction of our 1996–1998 data [5]; namely, we threw out events with $A(1) > 0.33$, $A(2) > 0.33$ and with $B(1) > 0.23$, $B(2) > 0.23$. We call these coordinate-independent parameters, since their values do not depend on the angular distance between the flash center and the source. This operation separates out 93% of the background flashes (Table 1), and the difference between the numbers of source and background flashes corresponds to 3.5σ. We also used coordinate-dependent parameters to select events associated with gamma rays, namely, the parameter DIST, which is numerically equal to the angular distance between the center of the flash brightness distribution and the source (Fig. 1), and $\mathrm{MISS} = \mathrm{DIST} \times \sin\alpha$.

In this case, we selected from the Cherenkov flashes chosen according to the coordinate-independent parameters those gamma-ray-like events whose parameters satisfied all the following conditions: $0.^{\circ}3 < \mathrm{DIST}(1) < 1.^{\circ}1$, $0.^{\circ}2 < \mathrm{DIST}(2) < 1.^{\circ}1$, and $\mathrm{MISS}(1) < 0.^{\circ}16$, $\mathrm{MISS}(2) < 0.^{\circ}16$. The results of this selection are presented in the last row of Table 1 (selection using coordinate-independent parameters).

5. DISCUSSION

Our analysis of the new data for 2000 has established the presence of a flux of gamma rays from 3C 66A at the 5.2σ level. The count rate for the selected gamma rays for the 2000 data is 0.17 ± 0.033 photons/min. Since our selection procedure separated out some fraction of gamma-ray events together with the background events, we must elucidate what fraction of the gamma-ray events remained after the selection procedure taking into account the effective area of the detector if we wish to determine the actual gamma-ray flux. This can be done via theoretical Monte Carlo studies of gamma-ray showers. This method was used to numerically model the development of extensive air showers and their detection using the GT-48 gamma-ray telescope [10]. A comparison of the simulation results and the observational data showed that the average flux of gamma rays during the observing period was $(2.7 \pm 0.5) \times 10^{-11}\ \mathrm{cm}^{-2}\ \mathrm{s}^{-1}$.

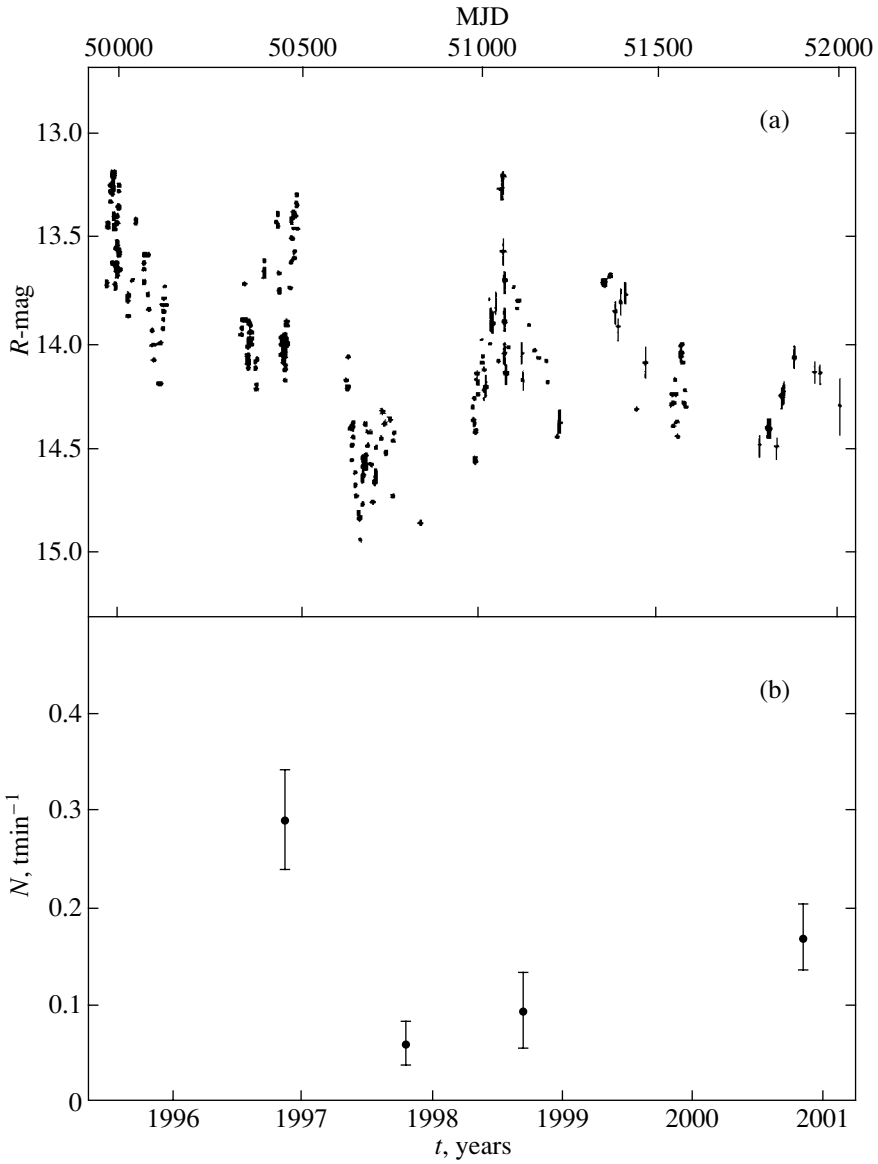

Fig. 2. (a) Time dependence of the R-band optical brightness of 3C 66A. (b) Yearly averaged very-high-energy gamma-ray flux S.

Our observations of the blazar 3C 66A carried out in 1996–2000 demonstrate that this object is a source of VHE gamma rays. Table 2 presents the yearly averaged gamma-ray fluxes.

Based on the four years of observations from 1996 to 2000, the mean gamma-ray flux was $(2.8 \pm 0.4) \times 10^{-11}$ cm^{-2} s^{-1}, and the significance of the detection of gamma rays from the direction of 3C 66A reaches 7.6σ. We see from Table 2 that the very-high-energy gamma-ray flux is variable. The statistical significance of the flux determinations for each year is low, because in determining the flux, it is not always possible to use all flash parameters within efficiently select gamma-ray photons. Monte-Carlo calculations show that the flux is determined with a larger error than the count rate of the detected selected gamma-ray photons. Therefore, we used the count rates of gamma-ray photons to analyze gamma-ray variability.

Figure 2b shows the count rates of selected gamma-ray photons in the observing period in each year. The length of the horizontal bar corresponds to the duration of observations; the vertical bars indicate errors. We see from Fig. 2 that the gamma-ray flux varies from year to year. Analysis of this variability by the χ^2 test with errors indicates that the flux is variable at 98.5% confidence.

As we seen from Fig. 2a, flux variability is also observed at optical wavelengths. Figure 2a shows the blazar magnitude, as inferred from optical measurements (in R), from late 1995 until early 2001. We

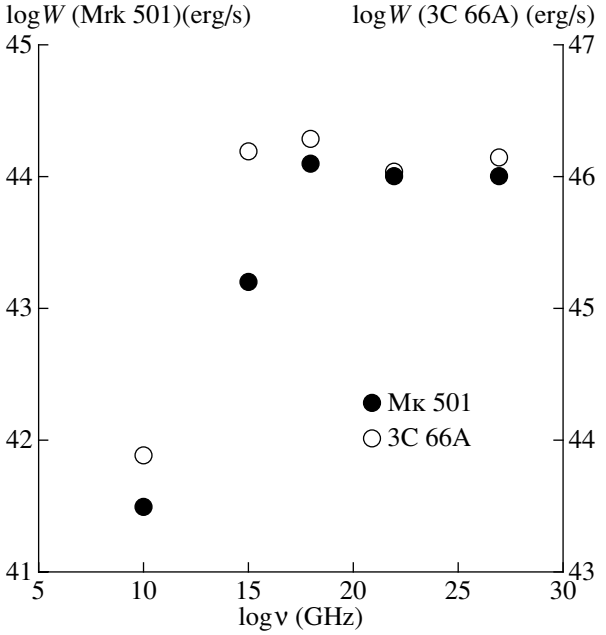

Fig. 3. Spectra of the galaxies 3C 66A and Mrk 501 [14].

obtained the optical data via the Internet, for which we are grateful to the authors who made their data available on the Internet, especially Dr. Thomas J. Balonek of Colgate University Bottom Observatory.

We can see that the optical brightness of the object varies by 2^m, or approximately a factor of six. The gamma-ray flux appears to be correlated with the optical flux. For example, there was an optical brightness minimum in 1997, when there was also a minimum in the gamma-ray flux; there was a optical brightness maximum in 1996 (see Fig. 2). The correlation coefficient between the VHE gamma-ray count rate and the optical brightness of the object was estimated to be 0.7 ± 0.2. However, the small number of data points makes this parameter unreliable, when the gamma-ray flux also had a maximum. 3C 66A was also detected in high-energy gamma rays ($>$ 100 MeV) by EGRET. The luminosity in both the optical and the gamma-ray range exceeds 10^{46} erg/s; i.e., it is two orders of magnitude higher than the luminosity of Mrk 501.

According to Lanzetti [11], the distance to the galaxy 3C 66A corresponds to $z = 0.444$ (1700 Mpc). If we suppose that the gamma radiation is emitted isotropically, its luminosity is $\approx 10^{46}$ erg/s. However, this luminosity may be severely overestimated, since the VHE gamma radiation is most likely not isotropic. At the same time, over such large distances, the flux of gamma rays with energies >1 TeV is greatly reduced due to interactions with infrared radiation in intergalactic space. It remains difficult to estimate the degree of anisotropy of the radiation. Therefore, it is not possible at the present time to make a good estimate of the intrinsic luminosity of the gamma-ray source. We note that the spectrum of 3C 66A is very similar to that of the well known galaxy Mrk 501 (see [12], Fig. 3), but the absolute magnitudes of the fluxes are two orders of magnitude higher for 3C 66A. This provides support for a common nature for these two sources, and possibly also for their radiation mechanisms.

ACKNOWLEDGMENTS

The authors thank their colleagues at the Crimean Astrophysical Observatory Z.N. Skiruta and S. Kochetkova for the large amount of work they performed in connection with the reduction of the observational data.

REFERENCES

1. B. J. Wills and D. Wills, Astrophys. J. **190**, L97 (1974).
2. L. O. Takalo, Astron. Astrophys., Suppl. Ser. **90**, 161 (1991).
3. Yu. S. Efimov and N. M. Shakovskoy, in *Proceedings of the OJ-94 Annual Meeting, Perugia, 1997,* Ed. by G. Tosti and L. Takalo, p. 24.
4. Yu. I. Neshpor, A. A. Stepanyan, O. R. Kalekin, *et al.*, Pis'ma Astron. Zh. **24** (3), 167 (1998) [Astron. Lett. **24**, 134 (1998)].
5. Yu. I. Neshpor, A. A. Stepanyan, O. R. Kalekin, *et al.*, Astron. Zh. **77** (10), 723 (2000) [Astron. Rep. **44**, 641 (2000)].
6. R. C. Hartman, D. L. Bertsch, S. D. Bloom, *et al.*, Astrophys. J., Suppl. Ser. **123**, 79 (1999).
7. M. F. Cawley, J. Clear, D. J. Fegan, *et al.*, in *Proceedings of the 18th International Cosmic Ray Conference, Bangalore, India, 1983,* Vol. 1, p. 118.
8. B. M. Vladimirskiĭ, Yu. L. Zyskin, A. A. Kornienko, *et al.*, Izv. Krym. Astrofiz. Obs. **91**, 74 (1994).
9. A. P. Kornienko, A. A. Stepanian, and Yu. L. Zyskin, Astroparticle Physics **1**, 245 (1995).
10. Yu. I. Neshpor, N. N. Chalenko, A. A. Stepanyan, *et al.*, Astron. Zh. **78** (4), 291 (2001) [Astron. Rep. **45**, 249 (2001)].
11. O. R. Kalekin, Izv. Krym. Astrofiz. Obs. **95**, 167 (1999).
12. K. M. Lanzetta, D. A. Turnsshek, and J. Sandoval, Astrophys. J., Suppl. Ser. **84**, 109 (1993).
13. F. W. Steker and O. C. De Jager, *The Kruger National Park Workshop on TeV Gamma-Ray Astrophysics, 1997*, Ed. by O.C. De Jager, p. 39.
14. J. Kataoka, J. R. Mattox, J. Quinn, *et al.*, Astropart. Phys. **11** (1–2), 149 (1999).

Translated by D. Gabuzda

Astronomy Reports, Vol. 46, No. 8, 2002, pp. 639–645. Translated from Astronomicheskiĭ Zhurnal, Vol. 79, No. 8, 2002, pp. 708–714.

An Induction Accelerator of Cosmic Rays on the Axis of an Accretion Disk

A. A. Shatskiĭ and N. S. Kardashev

Astro Space Center, Lebedev Physical Institute, Moscow, Russia

Received January 3, 2002; in final form February 1, 2002

Abstract—The structure and magnitude of the electric field created by a rotating accretion disk with a poloidal magnetic field is found for the case of a vacuum approximation along the axis. The accretion disk is modeled as a torus filled with plasma and a frozen-in magnetic field. The dimensions and location of the maximum electric field as well as the energy of the accelerated particles are found. The gravitational field is assumed to be weak. © *2002 MAIK "Nauka/Interperiodica".*

1. INTRODUCTION

Recently, there has been wide discussion of various mechanisms for accelerating particles around supermassive black holes (SMBHs) in the nuclei of galaxies and stellar-mass black holes in our Galaxy, in connection with studies of synchrotron radiation and inverse Compton scattering in the well-collimated jets observed from radio to gamma-ray wavelengths. Extremely high-angular-resolution observations obtained via radio interferometry show that these jets become very narrow (comparable to the gravitational radius) with approach to the black hole. Explanations of particle acceleration near relativistic objects (black holes and neutron stars) are usually based on two types of mechanisms: acceleration by electric fields and magnetohydrodynamical acceleration (the Blandford–Znajek mechanism [1]). Acceleration by an electric field, and the very existence of the electric field, are inseparably linked with the low density of plasma in this volume. Conditions justifying a vacuum approximation are probably realized in the magnetospheres of pulsars and in some types of SMBHs [2, 3]. In this case, it is possible to accelerate particles to extremely high energies [4]. The limiting charge densities for which the vacuum approximation remains valid are determined by the formula [5]

$$n_e < \frac{|(\Omega H)|}{2\pi ce} \simeq (1\ \text{day}/P) \times (H/10^4\ \text{G}) \times 10^{-2}\ \text{cm}^{-3}. \quad (1)$$

Here, Ω is the angular velocity of rotation, H is the characteristic magnetic-field strength, P is the rotational period, c is the velocity of light, and e is the electron charge. It is evident from this expression that we should have for typical quasars $n_e < 10^{-2}$ cm^{-3}. Note that, in intergalactic space, $n_e \simeq 10^{-6}$ cm^{-3}, and in the Galaxy, $n_e \simeq 1$ cm^{-3}. The presence of a black hole in the center of the Galaxy also leads to a decrease in n_e near the center. In addition, the magnetic fields near SMBHs can reach values of the order of 10^9 G [4]. In any case, the question of the applicability of the vacuum approximation is rather complex, and must be solved by taking into account the physics of black holes.

In this paper, we will assume that the conditions for the vacuum approximation are satisfied; this will enable us to investigate the structure of the electric field excited by a rotating accretion disk with a poloidal magnetic field. The formulation of this problem is analogous to that considered by Deutsch [6], who found the structure of the electric field created by a dipolar magnetic field frozen in a rotating star. If a conductor rotates together with a frozen-in magnetic field, then, in a rotating coordinate system in which the conductor is at rest, there must be no electric field inside the conductor. Therefore, in an inertial system, an electric field is induced inside the conductor due to the presence of the magnetic field, and this electric field gives rise to a surface charge (in the special case of a magnetic dipole with a quadrupolar distribution). This surface charge is the source of the external electric field. We will consider the analogous problem for an accretion disk.

2. CONSTRUCTION OF THE MODEL

Let us consider a stationary system consisting of a rotating accretion disk in the form of a regular torus filled with plasma and surrounded by a poloidal magnetic field. We neglect motion of the torus toward the center. The geometry of the torus is determined by the two radii a and R (Fig. 1). Due to the high conductivity of the plasma, the magnetic field is frozen

1063-7729/02/4608-0639$22.00

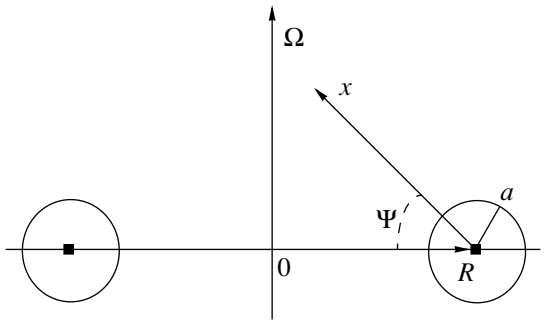

Fig. 1. Accretion disk in the form of a torus (side view).

inside the torus, and currents flow only in the toroidal direction; there is no matter outside the torus. In a coordinate system comoving with the plasma, the electric field vanishes due to the relation

$$j'_{\alpha} = \sigma' F'_{\alpha 0}, \tag{2}$$

where $j'_{\alpha} = 0$ are the poloidal components of the current density, σ' is the plasma conductivity, and $F'_{\alpha 0}$ are the covariant components of the electric field tensor in a system comoving with the plasma. We introduce the following coordinates (Fig. 1): x is the distance from an arbitrary point to the center inside the torus in the same meridional plane, ψ is the angle between the direction toward the center of the system and the direction to a given point from the center inside the torus in the same meridional plane, and φ is the position angle defining this plane. Thus, the differential coordinates dx, $d\psi$, and $d\varphi$ form a right-handed orthogonal vector triad. We can write the square of a linear element in Minkowski space for the differentials of these coordinates[1]:

$$\begin{cases} ds^2 = dt^2 - dx^2 - x^2\, d\psi^2 - (R - x\cos\psi)^2\, d\varphi^2 \\ \sqrt{-g} = x|R - x\cos\psi|. \end{cases} \tag{3}$$

Let the plasma in the torus rotate with angular velocity Ω with respect to a distant observer. Then, the coordinate transformation is given by[2]

$$dx^i = dx'^k \left(\delta^i_k + \Omega\delta^i_{\varphi}\delta^0_k\right). \tag{4}$$

We now introduce the covariant four-vector potential of the electromagnetic (EM) field A_i. Due to the axial symmetry of the system, only A_0, the potential of the electric field, and A_{φ}, the potential of the magnetic field, differ from zero. Therefore, the EM-field tensor F_{ij} has only poloidal components:

$$F_{\alpha 0} = \partial_{\alpha} A_0, \quad F_{\alpha\varphi} = \partial_{\alpha} A_{\varphi}. \tag{5}$$

[1] We take the velocity of light to be unity: $c = 1$.

[2] Where not indicated otherwise, $x^i = t$, x, ψ, φ, a $x^{\alpha} = x$, ψ.

These components transform in accordance with (4) [7, §83]:

$$F'_{\alpha 0} = F_{\alpha 0} + \Omega F_{\alpha\varphi}, \quad F'_{\alpha\varphi} = F_{\alpha\varphi}, \tag{6}$$
$$A'_0 = A_0 + \Omega A_{\varphi}, \quad A'_{\varphi} = A_{\varphi}.$$

Since $F'_{\alpha 0} = 0$ in the plasma [see (2)], we have for $x \le a$

$$F_{\alpha 0} = -\Omega F_{\alpha\varphi}. \tag{7}$$

It follows from (5) and (7) that, when $x \le a$, $A_0 = \text{const} - \Omega A_{\varphi}$. It follows from the third equation of (6) that this constant is A'_0 inside the torus.

The continuous boundary conditions for the tangential electric and normal magnetic compoments of the EM field act at the interface between the plasma and vacuum (at the surface of the torus). These components should vanish at the equator due to the axial symmetry of the system and the mirror (anti-) symmetry of the components of the EM field. Hence, the normal component of the magnetic field can be expanded in a Fourier sine series:

$$F_{\psi\varphi} = nR_n(x)\sin(\psi n). \tag{8}$$

Here and below, the summation over n is assumed, where n runs through all numbers of the natural series. It follows from (7) and (8) that the boundary condition for the tangential electric field is

$$F_{\psi 0(a,\psi)} = -\Omega n R_n(a)\sin(\psi n). \tag{9}$$

3. POTENTIAL AND STRUCTURE OF THE ELECTRIC FIELD NEAR THE TORUS

Near the torus [see formulas (30), (32), and (37) in the Appendix], the main contribution to the potential A_0 is made by the first term of the first harmonic of the Fourier series. Far from the torus, the potential dies away. The kinetic energy of a charged particle accelerated by the system is determined primarily by this part of the potential. Accordingly, we obtain the main approximation for the difference in the potentials at the torus surface between the angles $\psi = 0$ and $\psi = \tilde{\psi}$:

$$\Delta A_0 = \Omega R H_0 a \times [\ln(4/b) - 1] \times (1 - \cos\tilde{\psi})/\pi. \tag{10}$$

This same expression can also be obtained in another way [8, §63]. The corresponding invariant result has the form

$$\varepsilon \equiv U^i \Delta A_i = \int\limits_C U^i F_{ji}\, dx^j = \int\limits_0^{\tilde{\psi}} U'^{\varphi} F'_{\psi\varphi}\, d\psi. \tag{11}$$

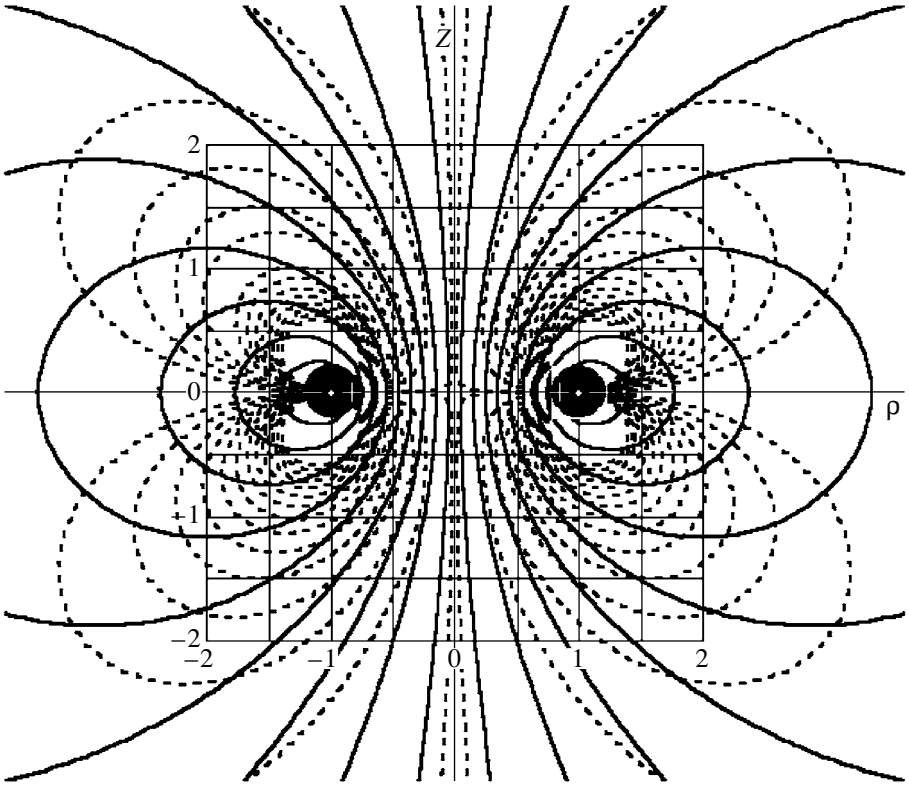

Fig. 2. Appearance of the electromagnetic field lines in the system. The solid curves show the magnetic field lines and the dashed curves the electric field lines. Z and ρ are expressed in fractions of R.

Here, U^i denotes the four-velocity of the observer[3] at the measurement point, and the contour for the integral is chosen for convenience to be on the inside surface of the torus in a reference system comoving with the torus. After substituting into this expression $U'^{\varphi} \approx \Omega$ and the expression for $F'_{\psi\varphi} = F_{\psi\varphi}$, we obtain (10).

The electric field inside the torus is zero, since the torus is conducting. In an inertial reference system, this is accomplished by the compensation of two fields: that induced by the rotation of the magnetic field and the field of the surface charge on the torus. The surface density of the electric charge on the torus is $\rho_e = -F_{x0}/(4\pi)$. F_{x0} is the normal component of the electric field on the torus surface [see (7)]. At large distances from the torus surface ($x \gg a$), these charges represent a superposition of dipoles (Fig. 2). However, at distances $x \gg R$, the field from all these dipoles has a quadrupole character. It is not difficult to obtain an expression for the dipole moment per unit angle φ:

$$d = \frac{\Omega R^2 a^2 H_0}{2\pi}\left[2 - \ln(4/b)\right]. \qquad (12)$$

[3]Who is at rest relative to the distant stars.

The electric field and its potential ϕ can be obtained by integrating all the dipoles over the angle φ [7, §40]. As a result, we obtain for the potential and components of the electric field in cylindrical coordinates the quadrature expressions

$$\phi(\rho, z) = \frac{2d}{R^2}\int_0^{\pi}\left[\frac{1 - \tilde{\rho}\cos\varphi}{(1 + \tilde{\rho}^2 + \tilde{z}^2 - 2\tilde{\rho}\tilde{z}\cos\varphi)^{3/2}}\right]d\varphi, \qquad (13)$$

$$E_\rho(\rho, z) = \frac{2d}{R^3} \qquad (14)$$

$$\times \int_0^{\pi}\left[\frac{\cos\varphi(\tilde{z}^2 - 2\tilde{\rho}^2 - 2) + 3\tilde{\rho} + \tilde{\rho}\cos^2\varphi}{(1 + \tilde{\rho}^2 + \tilde{z}^2 - 2\tilde{\rho}\tilde{z}\cos\varphi)^{5/2}}\right]d\varphi,$$

$$E_z(\rho, z) = \frac{2d}{R^3}\int_0^{\pi}\left[\frac{3\tilde{z}(1 - \tilde{\rho}\cos\varphi)}{(1 + \tilde{\rho}^2 + \tilde{z}^2 - 2\tilde{\rho}\tilde{z}\cos\varphi)^{5/2}}\right]d\varphi. \qquad (15)$$

Here, $\tilde{\rho} = \rho/R$ and $\tilde{z} = z/R$ are dimensionless cylindrical coordinates. The last three formulas are expressed in terms of derivatives of the full elliptical integrals. The result of this integration is shown in Fig. 2.

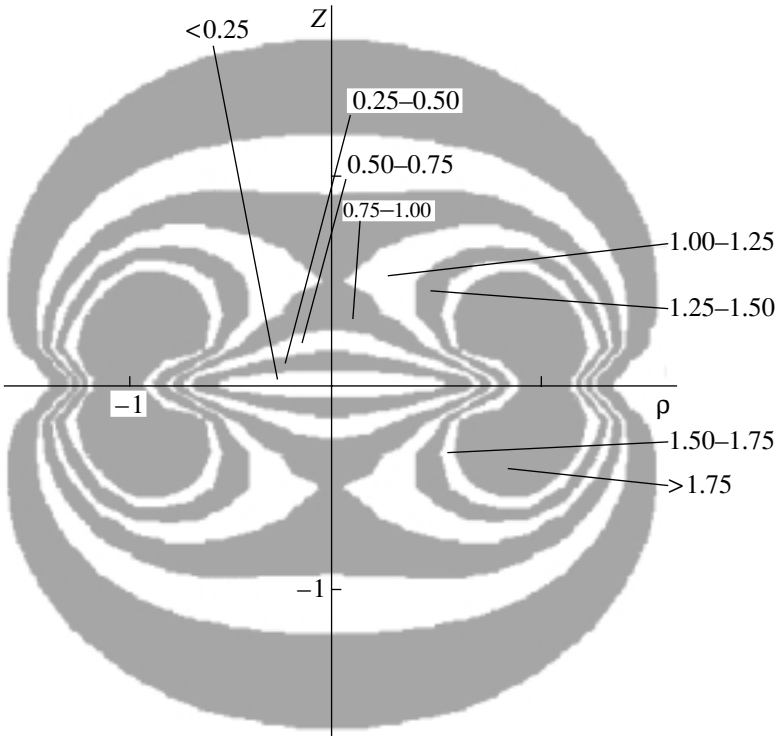

Fig. 3. Magnitude of the poloidal component of the electric field $E_\parallel(\rho/R,\ z/R)$ in units of its value at the saddle point. Z and ρ are expressed in fractions of R.

Acceleration by the electric field is associated only with the component parallel to the magnetic field. This acceleration is especially efficient on the Ω axis, where the electric and magnetic lines of force are parallel. We can readily see from (15) that the maximum electric field on the Ω axis is reached at the point $z = R/2$. However, this point is not a local maximum of the modulus of the longitudinal electric-field component $E_\parallel \equiv (\mathbf{E}\cdot\mathbf{H})/H$. Figure 3 shows the surface of the $E_\parallel$ force field, where we can see that the point $z = R/2$ on the axis is a saddle point of the distribution of $E_\parallel$. With approach to the torus, the conductivity of the medium should increase and the field should become force-free: $E_\parallel \to 0$[4].

According to (13), the potential at the saddle point is approximately 28% lower than the potential at the center of the system, and is roughly an order of magnitude lower than the maximum potential on the torus surface. The extent of the region of acceleration along the z axis (at the level of 0.5 of the value of $E_\parallel$ at the saddle point) is determined by the points $z_1 \simeq 0.25$, $z_2 \simeq 1.25$ in fractions of R. Assuming that a mass M with its corresponding gravitational radius r_g is at the center of the system, we can use (13) to estimate the energy to which particles with an elementary charge which are initially at the saddle point on the axis can be accelerated:

$$E_k \approx \left(\frac{6.5a}{R}\right)\times\left(\frac{\Omega R}{c}\right)\times\left(\frac{H_0}{10^4\ \Gamma\mathrm{c}}\right)\times\left(\frac{a}{r_g}\right) \quad (16)$$
$$\times\left(\frac{M}{10^9 M_\odot}\right)\times[\ln(4/b)-2]\times 10^{20}\ \mathrm{eV}.$$

We can see that the factors in parantheses can be ofonthe order of unity in quasars, so that the kinetic energy of particles accelerated by such a system can reach 10^{20} eV.

4. CONCLUSIONS

We can draw the following conclusions from our results.

(1) The magnetic field at large distances approaches a dipolar field, while the electric field corresponds to a quadrupolar distribution for the charge induced on the torus surface. It follows from Fig. 2 that, in the model considered here, in contrast to a Blandford–Znajek model, we find a tendency for the electric field lines to become more concentrated near the Ω axis, which can explain the observed focusing (collimation) of the accelerated relativistic particles.

[4]Note that, in a Blandford–Znajek model, the field is force-free everywhere by definition, so that efficient acceleration is not possible.

(2) The dimensions and locations of the regions of cosmic-ray acceleration we have found can be used to compare our results with observational data.

(3) Thanks to its covariance, our method for the computation of the electromagnetic field in a system with toroidal symmetry can be generalized to the case of a gravitationally curved space–time.

(4) The mechanism considered here yields accelerated-particle energies with the same order of magnitude as the Blandford–Znajek mechanism (see, for example, [1, 9, 10]).

ACKNOWLEDGMENTS

This work was supported by the Russian Foundation for Basic Research, project nos. 01-02-16812, 00-15-96698, and 01-02-17829).

APPENDICES

Finding the External Solution

Let us write Maxwell's equations for arbitrary curvilinear coordinates in the axially symmetric and stationary case [7, §90]:

$$\begin{cases} e^{\alpha\beta\varphi}\partial_\beta F_{\alpha\varphi}=0; \quad \partial_\beta\left(\sqrt{-g}g^{\alpha\beta}g^{\varphi\varphi}F_{\alpha\varphi}\right)=4\pi\sqrt{-g}j^{\varphi} \\ e^{\alpha\beta\varphi}\partial_\beta F_{\alpha 0}=0; \quad \partial_\beta\left(\sqrt{-g}g^{\alpha\beta}g^{00}F_{\alpha 0}\right)=4\pi\sqrt{-g}j^{0}. \end{cases} \tag{17}$$

Here, $e^{\alpha\beta\varphi}$ is a Levi–Civita symbol, $\sqrt{-g}$ and g^{ij} are defined by expression (3), and j^i is the current 4-vector, which is identically equal to zero when $x > a$. We obtain for the magnetic field from (8) and the first of equations (17)

$$\begin{aligned} F_{x\varphi} &= -\partial_x R_n(x)\cos(\psi n), \\ A_\varphi &= -R_n(x)\cos(\psi n). \end{aligned} \tag{18}$$

Using (9), the external solution for the electric field can be expanded in a Fourier series in the variable ψ. Then, in accordance with the third equation of (17), we obtain the solution for the electric field (for $x > a$)

$$\begin{aligned} F_{\psi 0} &= nZ_n(x)\sin(\psi n), \\ F_{x0} &= -\partial_x Z_n(x)\cos(\psi n), \\ A_0 &= -Z_n(x)\cos(\psi n). \end{aligned} \tag{19}$$

It follows from (8) and (19) that the external electric field is generated by the normal component of the magnetic field at the torus boundary.

Everywhere where the expression $R - x\cos\psi$ is positive, such as in the range $a < x < R$, we can remove the modulus signs in the second expression of (3). With this in mind, introducing the dimensionless variable $y = x/(2R)$ and denoting a derivative with respect to this variable with a prime, we substitute (19) into the fourth Maxwell equation (17) and obtain

$$\begin{aligned} y\left[y^2Z_n'' + 2yZ_n' - n(n-1)Z_n\right]\cos[(n-1)\psi] \\ - \left[y^2Z_n'' + yZ_n' - n^2Z_n\right]\cos[\psi n] + y\left[y^2Z_n''\right. \\ \left. + 2yZ_n' - n(n+1)Z_n\right]\cos[(n+1)\psi] = 0. \end{aligned} \tag{20}$$

The boundary conditions for $Z_n(y)$ when $y = b \equiv a/(2R)$ and $n > 0$ follow from (9):

$$Z_n(b) = -\Omega R_n(b) \quad (n > 0). \tag{21}$$

The necessary condition for the total electric charge in the torus to be zero can be written

$$Q = \oint F_{x0}g^{00}g^{xx}\sqrt{-g}2\pi d\psi = 0 \quad (a < x < R). \tag{22}$$

This expression follows from integration of the fourth equation of (17). We thus obtain

$$Z_0' = yZ_1'. \tag{23}$$

Setting the expressions with the same harmonics in (20) equal to zero, we obtain a recurrent system of equations for $Z_n(y)$. Equation (23) is contained in the Maxwell equation (20) with harmonic $n = 0$.

The condition that the total charge of the system be equal to zero can also be written for $x > R$. For this, we must take a contour passing around the system, so that $R - x\cos\psi$ does not change sign; i.e., the contour should be located to the right of the half-plane from the $\boldsymbol{\Omega}$ axis. We choose this contour as shown in Fig. 4. Thus, we pass by the torus along a semicircle with radius $x > a$ on the right-hand side, and we allow the contour to approach infinity at the

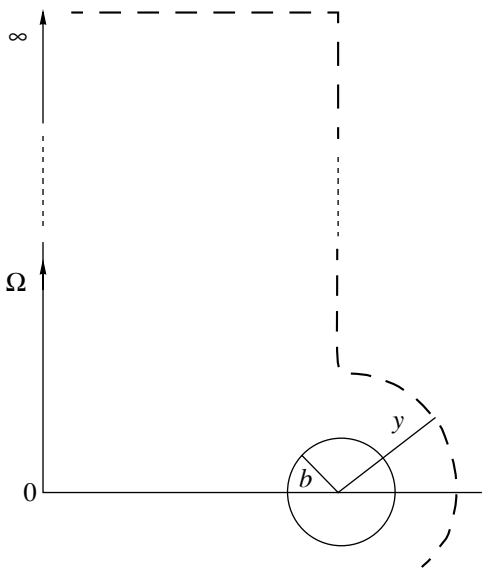

Fig. 4. Contour passing around the system, shown by the dashed line.

angles $\psi = \pi/2$ and $\psi = -\pi/2$ along half-lines parallel and antiparallel to the $\mathbf{\Omega}$ axis. The two (upper and lower) "caps" of the finite area πR^2 remain unclosed at infinity, but since the field there asymptotically approaches zero, the integrals on these caps can be neglected. We can write the surface integral over this contour in accordance with the fourth of equations (17) taking into account the mirror symmetry for the electric field in the equatorial plane:

$$Q = \int_{\pi/2}^{\pi} F_{x0} g^{00} g^{xx} \sqrt{-g} 4\pi d\psi \qquad (24)$$
$$+ \int_{x}^{\infty} F_{\psi 0} g^{00} g^{\psi\psi} \sqrt{-g} 4\pi dx \Big|_{\psi=\pi/2} = 0.$$

After straightforward but cumbersome manipulations, we obtain

$$yZ_n' \left[\pi(y\delta_n^1 - \delta_n^0) + 2y\frac{\cos(\frac{\pi n}{2})}{n^2-1} + \frac{\sin(\frac{\pi n}{2})}{n}\right] \qquad (25)$$
$$+ \sin\left(\frac{\pi n}{2}\right) \int_y^{\infty} \frac{Z_n}{y} dy = 0.$$

Let us solve this problem with accuracy to within the first three terms in the Fourier expansion (Z_0, Z_1, Z_2). In this case, taking into account (23), the last expression becomes

$$(1-2y^2) yZ_1' + \int_y^{\infty} \frac{Z_1}{y} dy \approx \frac{2}{3} y^2 Z_2'. \qquad (26)$$

Differentiating, we obtain

$$(1-2y^2)y^2 Z_1'' + (1-6y^2) yZ_1' - Z_1 \qquad (27)$$
$$\approx \frac{2}{3} y(y^2 Z_2'' + 2yZ_2').$$

We now write the Maxwell equation (20) corresponding to the harmonic $n = 1$:

$$(1-2y^2)y^2 Z_1'' + (1-6y^2) yZ_1' - Z_1 \qquad (28)$$
$$- y(y^2 Z_2'' + 2yZ_2' - 2Z_2) = 0.$$

An equation for Z_2 follows from these last two expressions:

$$y^2 Z_2'' + 2yZ_2' - 6Z_2 = 0. \qquad (29)$$

The solution vanishing at infinity has the form

$$Z_2(y) = C_2/y^3. \qquad (30)$$

The constant C_2 is found from the boundary conditions (21). We can find $Z_1(y)$ using any of equations (27) or (28):

$$(1-2y^2)y^2 Z_1'' + (1-6y^2) yZ_1' - Z_1 = 4C_2/y^2. \quad (31)$$

A partial solution of the inhomogeneous equation (31) has the form $Z_1^1 = 4C_2/(3y^2)$. However, it does not satisfy (26), of which (27) is a consequence, so that we must search for a solution of $Z_1(y)$ from (26). The substitution $\int_y^{\infty} (Z_1^{\rm o}/y) dy = f_\infty - f(y)$ brings the homogeneous equation (26) into the form $(1 - 2y^2)y(yf')' - f + f_\infty = 0$. Hence, in the limit $y \to 0$, we obtain $Z_1^{\rm o} \to C_1 y^{\pm 1}$.

In the limit $y \to \infty$, the substitution $y = \exp\xi$ reduces (26) to

$$f_{\rm o}''(\xi) + e^{-2\xi} f_{\rm o}/2 = 0,$$
$$f_{\rm n}''(\xi) + e^{-2\xi} f_{\rm n}/2 = e^{-2\xi} f_\infty/2,$$
$$f = f_{\rm o} + f_{\rm n}.$$

In the main approximation in $1/y$, the solution has the form $f(y) = \exp\left(\frac{-1}{8y^2}\right) + \frac{1}{8y^2}$. Hence, the asymptotic for $y \to \infty$ has the form $Z_1^{\rm o} \to -\frac{C_1}{32y^4}$.

$Z_0(y)$ can be found using (23) after $Z_1(y)$ is found. We present the asymptotics of these solutions for small and large y:

$$Z_0 \underset{y\to 0}{\longrightarrow} -C_1 \ln(y) + 8C_2/(3y), \qquad (32)$$
$$Z_1 \underset{y\to 0}{\longrightarrow} C_1/y + 4C_2/(3y^2),$$
$$Z_0 \underset{y\to \infty}{\longrightarrow} -(C_1 + 8C_2)/(24y^3),$$
$$Z_1 \underset{y\to \infty}{\longrightarrow} -(C_1 + 8C_2)/(32y^4).$$

Here, C_1 is the coefficient for the solution of the homogeneous equation (26); like C_2, it is determined by the specific configuration of the magnetic field from the boundary conditions.

Calculation of Coefficients for the Special Case of a Current Ring in the Torus

Let us now find the magnetic field in a simple case. Let the current in the torus be in the form of a ring along the torus axis with a delta-function distribution [7, §90]:

$$j^{\varphi} = \lim_{x_0 \to 0} J^{\varphi} \delta(x - x_0)\delta(\psi - \psi_0)/(2\pi\sqrt{-g}), \quad (33)$$
$$j^{\alpha} = 0.$$

To find the potential A_φ corresponding to this current, we introduce the physical components of vectors in accordance with the definition

$$\mathbf{H}_{\rm phys} \equiv \hat{\mathbf{H}} = \{H^{\beta}\sqrt{|g_{\alpha\beta}|}\}.$$

This is necessary because the Biot–Savart law in its usual form [7, §43] is written in physical coordinates:

$$\hat{A}^{\alpha}{}_{(x,\psi)} = \mathbf{e}^{\alpha} \oint \frac{(\hat{\tilde{j}}^{\gamma} \cdot \mathbf{e}_{\gamma})}{|\mathbf{r}-\mathbf{R}|} \sqrt{-\tilde{g}}\, d\tilde{x} d\tilde{\psi} d\tilde{\varphi}. \qquad (34)$$

Here, $\mathbf{e}^{\alpha}$ is a unit vector in the direction of the angle φ, $(\hat{\tilde{j}}^{\gamma} \cdot \hat{e}_{\gamma}) = \tilde{j}^{\varphi}\sqrt{|\tilde{g}_{\varphi\varphi}|}\cos\tilde{\varphi}$, and $|\mathbf{r}-\mathbf{R}|^2 = 2R(R - x\cos\psi)(1-\cos\tilde{\varphi}) + x^2$ is the square of the distance from the segment of current with coordinate $\tilde{\varphi}$ to the observation point.

Introducing the notation $\tilde{\varphi} = \pi + 2\phi$, $\kappa^2 = (1 - 2y \times \cos\psi)/(1 - 2y\cos\psi + y^2)$, we can tranform (34) to the form

$$A_{\varphi} = (J^{\varphi}R/\pi)\sqrt{1-2y\cos\psi} \times \kappa \times \int_0^{\pi/2} \frac{2\sin^2\phi - 1}{\sqrt{1-\kappa^2\sin^2\phi}} d\phi$$

or

$$A_{\varphi} = 2(J^{\varphi}R/\pi)\cdot\sqrt{1-2y\cos\psi} \times \left[K(\kappa)(1-\kappa^2/2) - E(\kappa)\right]/\kappa. \qquad (35)$$

Here, $K(\kappa)$ and $E(\kappa)$ are full elliptical integrals.

We can find the asymptotic of (35) as $y \to 0$ or equivalently as $\kappa \to 1$. Further, using (18), we can obtain the Fourier coefficients of the magnetic field:

$$\lim_{y\to 0} : R_0 \to \frac{J^{\varphi}R}{\pi}\left[2 - \ln(\frac{4}{y})\right], \qquad (36)$$

$$R_1 \to -\frac{J^{\varphi}R}{\pi}\left[y\left\{1 - \ln(\frac{4}{y})\right\}\right],$$

$$R_2 \to -\frac{J^{\varphi}R}{\pi}\left[y^2\left\{1 - \ln(\frac{4}{y})/4\right\}\right].$$

It is clear from the boundary conditions (21) that, according to (36), $|Z_2(b)/Z_1(b)| \sim b \to 0$ as $b \to 0$, so that we can neglect the remaining terms of the Fourier series in the case of this magnetic-field configuration. We introduce the notation $H_0 \equiv |\partial_x \hat{A}^{\varphi}|_{\{x=R,\,\psi=0\}} = J^{\varphi}/(2R)$ for the magnetic-field strength at the center of the system. We find the coefficients in this approximation from (21), (32), and (36):

$$C_1 \approx 2\Omega H_0 R^2 b^2 \left[1 - \ln(4/b)\right]/\pi, \qquad (37)$$

$$C_2 \approx 2\Omega H_0 R^2 b^5 \left[1 - \ln(4/b)/4\right]/\pi.$$

REFERENCES

1. R. D. Blandford and R. L. Znajek, Mon. Not. R. Astron. Soc. **179**, 433 (1977).
2. R. D. Blandford, astro-ph/0110396.
3. G. Barbiellini and F. Longo, astro-ph/0105464.
4. N. S. Kardashev, Mon. Not. R. Astron. Soc. **276**, 515 (1995).
5. P. Goldreich and W. H. Julian, Astrophys. J. **157**, 869 (1969).
6. J. Deutsch, Ann. Astrophys. **1** (1), 1 (1955).
7. L. D. Landau and E. M. Lifshitz, *Course of Theoretical Physics,* Vol. 2: *The Classical Theory of Fields* (Nauka, Moscow, 1988; Pergamon, Oxford, 1975).
8. L. D. Landau and E. M. Lifshitz, *Course of Theoretical Physics,* Vol. 8: *Electrodynamics of Continuous Media* (Nauka, Moscow, 1992; Pergamon, New York, 1984).
9. *Black Holes: the Membrane Paradigm,* Ed. by K. S. Thorne, R. H. Price, and D. A. Macdonald (Yale Univ. Press, New Haven, 1986; Mir, Moscow, 1988).
10. A. A. Shatskiĭ, Zh. Éksp. Teor. Fiz. **11** (2001).

Translated by D. Gabuzda

Astronomy Reports, Vol. 46, No. 8, 2002, pp. 646–655. Translated from Astronomicheskiĭ Zhurnal, Vol. 79, No. 8, 2002, pp. 715–725.

Observations of a Unique Minimum of RR Tau in the Optical and Near Infrared

V. P. Grinin[1, 2], D. N. Shakhovskoĭ[2], V. I. Shenavrin[3], A. N. Rostopchina[2], and L. V. Tambovtseva[1]

[1] *Main Astronomical Observatory, Pulkovskoe shosse 65, St. Petersburg, 196140 Russia*

[2] *Crimean Astrophysical Observatory, Nauchnyĭ, Crimea, 98409 Ukraine*

[3] *Sternberg Astronomical Institute, Universitetskiĭ pr. 13, Moscow, 119992 Russia*

Received October 25, 2001; in final form February 1, 2002

Abstract—We present observations of the UX Ori star RR Tau in the optical ($UBVRI$) and near infrared ($JHKLM$) acquired between November 2000 and April 2001. We recorded a uniquely long (about half a year) Algol-like minimum with an amplitude of $\Delta V \approx 2.9$. The dimming of RR Tau was accompanied by an increase of the linear polarization, typical of UX Ori stars and testifying to the eclipsing nature of the minimum. The J and H infrared fluxes varied synchronously with the optical variations. However, the K and L brightness changes were in the opposite sense: the flux in these two bands increased for the entire duration of the optical minimum. Our analysis suggests that the source of the K and L radiation is the dust cloud itself, moving at a distance of about 1 AU from the star. The flux increase in these bands was not due to an increase in the dust temperature, but instead to an increase in the number of emitting grains in the cloud. This could be associated either with an actual increase in the number of fine grains due to sublimation and the disruption of larger grains or with the distortion and disruption of the cloud due to tidal perturbation, permitting the star's light to penetrate and heat the densest regions of the cloud. Based on the observed L fluxes, we estimate the mass of the emitting dust in the cloud to be $\approx 10^{23}$ g. Taking into account the presence of cool dust and a gaseous component in the cloud in addition to the dust heated by the star's radiation, and adopting a ratio for the masses of the dust and gas components similar to that in the interstellar medium (1 : 100), we estimate the cloud's total mass to be $\geq 10^{25}$ g. Judging from this value and the duration of the minimum, we observed an extremely rare episode associated with a giant gas and dust cloud with a total mass on the order of 0.1 lunar mass or higher, which passed very near the young star (and may be falling onto it). © *2002 MAIK "Nauka/Interperiodica"*.

1. INTRODUCTION

The Herbig Ae star RR Tau belongs to the UX Ori subclass of young stars, distinguished by a high level of photometric activity that is manifest in the form of Algol-like minima with amplitudes of up to $2–3^m$ lasting from several days to several weeks [1–4]. Linear polarization studies of such stars [5–7] show that the polarization behaves as expected in models with variable circumstellar extinction during brightness decreases [8]. In such models, the brightness minima are the result of circumstellar gas and dust clouds passing in the vicinity of a young star and crossing the line of sight from time to time. During such events, the star's direct light is screened by the cloud, and the observer sees scattered polarized light from the protoplanetary disk—an analog of solar zodiacal light. This model is now nearly universally accepted, although there remain a number of unsolved problems (see the review [9]).

One such problem is the origin of the circumstellar dust clouds that are thought to initiate the dimming of these stars. Their chemical composition (dust-to-gas ratio) remains unknown. It is also not clear what mechanism gives rise to their orbits or whether there are periodically repeating Algol-like minima due to the same cloud crossing the line of sight. An analysis of simultaneous linear-polarization and brightness observations of UX Ori stars [7] has shown that Algol-like minima are due to the passage of clouds very near the star, which probably dissipate partially or completely in a zone of intense dust sublimation. This picture is supported by the strong fluctuations of the Stokes parameters of the radiation scattered by the circumstellar dust, revealed by long-term photometric and polarimetric monitoring of UX Ori stars. However, this important conclusion is based solely on indirect evidence, and requires confirmation.

Together with increased scattering of radiation, the passage of large dust clouds in the immediate

1063-7729/02/4608-0646$22.00

IR photometry of RR Tau

Date	JD 245...	V	J	H	K	L	M
Oct. 16/17, 2000	1834.59	11.39	9.38	8.37	7.37	6.14	
Nov. 01/02, 2000	1850.64	11.63	9.40	8.37	7.31	6.08	
Nov. 14/15, 2000	1863.51		9.75	8.52	7.35	6.04	
Nov. 16/17, 2000	1865.44	11.50	9.40	8.31	7.29	6.02	
Nov. 17/18, 2000	1866.49	11.43	9.36	8.30	7.24	6.00	
Nov. 18/19, 2000	1867.48		9.38	8.34	7.28	6.02	
Dec. 23/24, 2000	1902.45	11.30	9.15	8.10	7.07	5.85	
Jan. 15/16, 2001	1925.28	12.30	9.50	8.31	7.19	5.92	
Jan. 22/23, 2001	1932.39		9.85	8.48	7.25	5.93	
Jan. 24/25, 2001	1934.36	13.30	9.88	8.58	7.26	5.96	5.58
Jan. 10/11, 2001	1951.37	13.50		8.58		5.96	5.60
Mar. 13/14, 2001	1982.26		9.32	8.23	7.12	5.82	5.48
Apr. 03/04, 2001	2003.24	11.0.	9.02	8.07	7.02	5.72	5.47
Apr. 08/09, 2001	2008.28	10.9.	9.05	8.15	7.08	5.78	
Apr. 09/10, 2001	2009.26		9.15	8.16	7.12	5.83	
Apr. 12/13, 2001	2012.26	11.6.	9.25	8.24	7.14	5.87	

Note: The photometry of RR Tau on October 16/17, 2000 was obtained in the Astronomical Institute of the Academy of Sciences of Uzbekistan by O.V. Ezhkova (private communication).

vicinity of the star can give rise to an increase in the overall thermal emission of the protoplanetary disk in the near IR, determined by those parts of the disk that are closest to the star. Coordinated observations of UX Ori stars in the visual and near IR are required to detect this effect. However, such observations are very rare [10–12], since they require two telescopes for simultaneously observations over a fairly long time. Nevertheless, three episodes in which a star displayed a small increase in its IR flux simultaneous with a decrease in its optical flux have been recorded; two were observed by Hutchinson *et al.* [11] in South Africa and the third by Sitko *et al.* [12] in the USA.

Of course, these three episodes are not sufficient to rule out the possibility that this behavior was due to random coincidence. In addition, the result of Sitko *et al.* [12] is based on only two observations of a young star separated by twelve years. A somewhat larger number of simultaneous observations of stars in the optical and near IR are presented in [11]. However, the optical minima of the two stars observed (UX Ori and AK Sco) that displayed an anti-correlation in the variations of their optical and IR fluxes were fairly weak. In contrast, the much deeper minimum of BF Ori observed by the same authors exhibits no anti-correlation: the star dimmed simultaneously in the optical and infrared. These results demonstrate that larger numbers of such observations are sorely needed.

With this in mind, we supplemented our Crimean program of $UBVRI$ photometric monitoring of UX Ori stars with photometric observations in the near IR (the $JHKLM$ bands). We present here the first results of our coordinated optical and IR observations, which have enabled us to follow the development of a deep and long minimum of the Herbig Ae/Be star RR Tau over the wide wavelength interval from 0.35 to 3.5 μm for the first time.

2. OBSERVATIONS

Our optical observations of RR Tau were acquired with the 1.25 m telescope of the Crimean Astrophysical Observatory using the five-channel photometer and polarimeter designed by Piirola [13]. This instrument enables simultaneous observations in the $UBVRI$ bands in a photometric and polarimetric regime. We used either a 10″ or 15″ diaphragm, depending on the observing conditions. As in [6], we used HDE 245817 $=$ BD $+$ 26°885 as a comparison

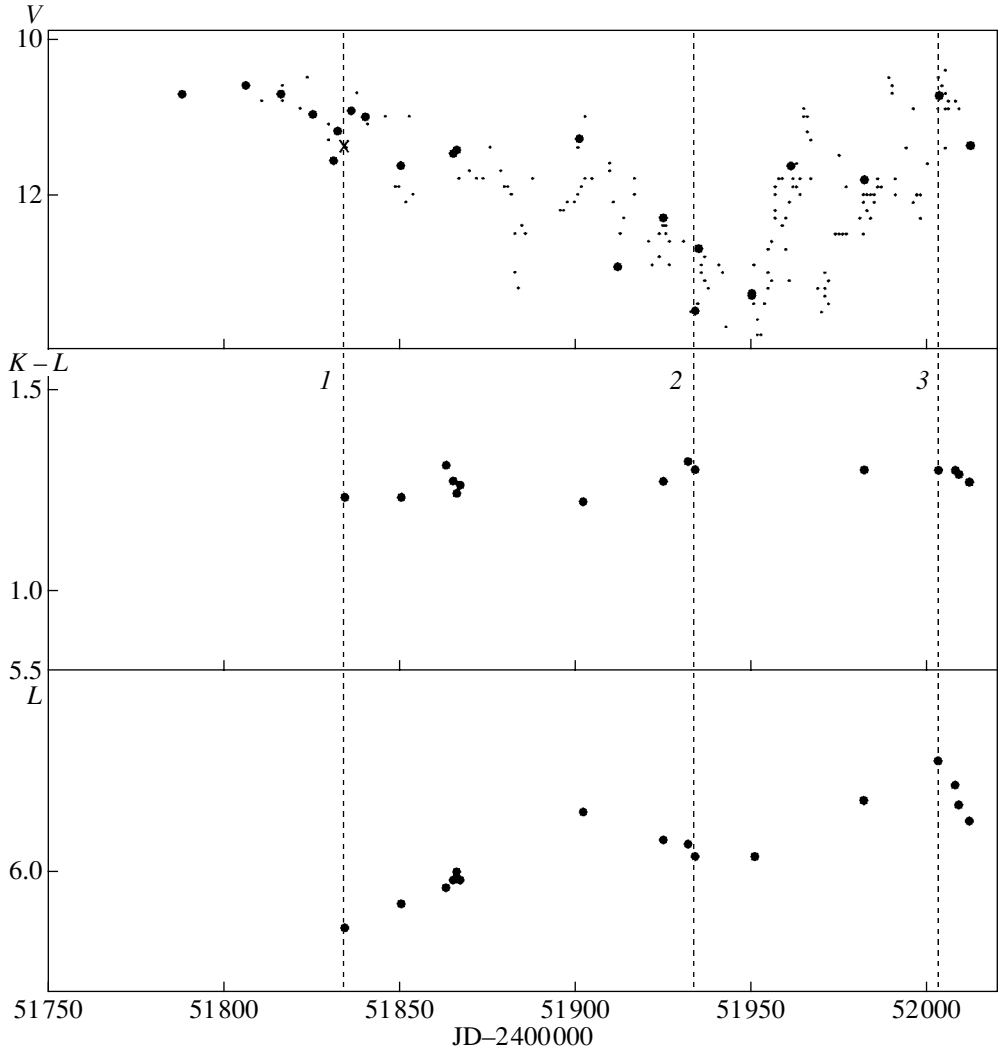

Fig. 1. Light curves of RR Tau in the V and L bands and the $K-L$ color curve from the present study (filled circles); the cross is a V brightness estimate based on Mt. Maĭdanak observations (O.V. Ezhkova, private communication). The dots are brightness estimates made by amateur astronomers, taken from the database at http//www.kusastro.kyoto-u.ac.jp/vsnet/. The numbers 1, 2, and 3 mark observations during three characteristic states of the star: in its bright state before and after the minimum, and in the deepest part of the minimum; the corresponding energy distributions are presented in Fig. 5.

star. The photometric observations were reduced to the standard photometric system. The uncertainty in the photometry was 0.02 in $U-B$ and V, and 0.01 in the other bands. The results of these observations are presented in the table and Figs. 1, 2.

Our polarimetric observations of RR Tau were obtained in the $UBVRI$ bands simultaneously with the photometric measurements. On only a few nights, the observations were limited to photometry alone. We applied the standard data-reduction techniques, including corrections for the instrumental polarization based on regular observations of polarimetric standards. Figure 3 displays the results of these observations.

Our near-IR photometry of RR Tau was obtained using the single-channel photometer of the 1.25 m telescope of the Sternberg Astronomical Institute's Crimean Laboratory. The observations were made in the standard $JHKLM$ photometric system (1.25, 1.6, 2.25, 3.4, 5.0 μm). The detector used was an InSb photodiode cooled with liquid nitrogen. A description of the photometer can be found in [14]. The comparison star used was BS 1791; the JK magnitudes of this star were taken from Johnson [15], and its HLM magnitudes were determined using formulas presented by Koornneef [16]. According to these papers, the $JHKLM$ magnitudes of BS 1791 are 1.97, 2.03, 2.05, 2.07, and 2.04, respectively. The average uncertainties in the magnitudes derived for RR Tau are about 0.02 in the $JHKL$ bands and 0.05 to 0.10 in the M band. The results of these observations are presented in the Table and in Figs. 1 and 4.

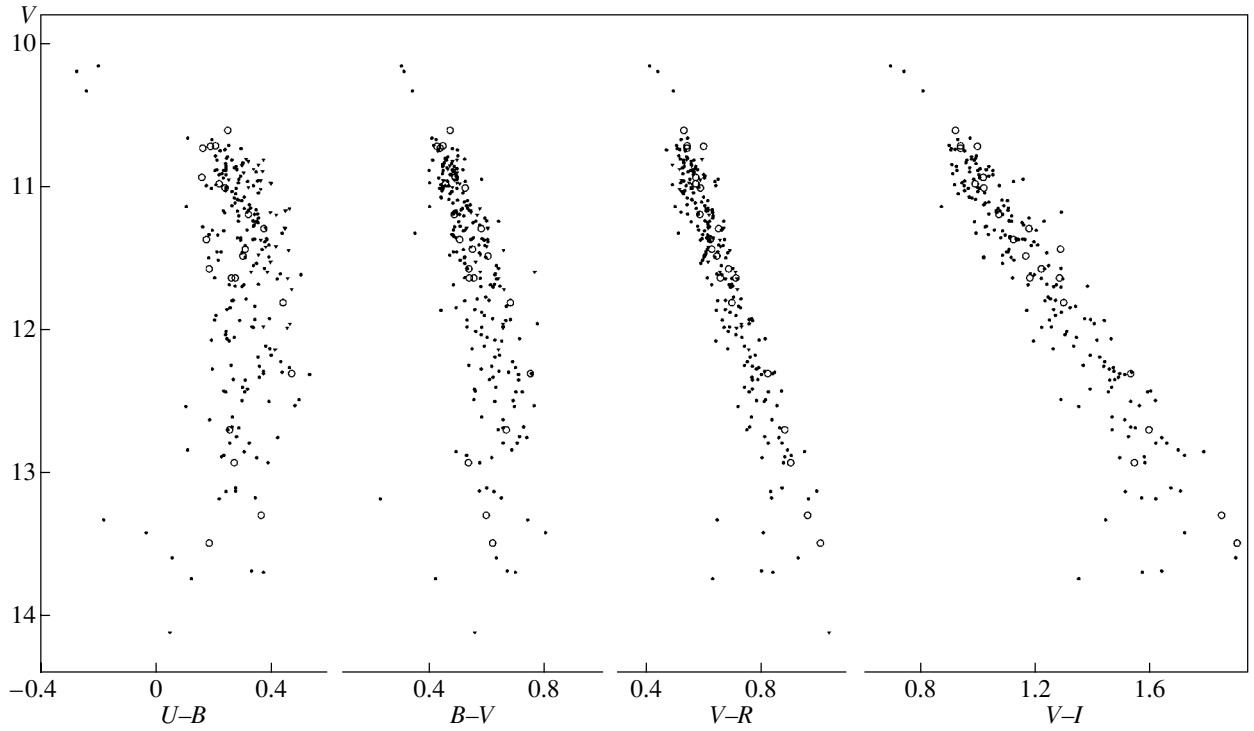

Fig. 2. Color–magnitude diagram of RR Tau based on the data presented here (open circles) and the data of [6] (dots).

3. RESULTS

3.1. Optical UBVRI Photometry

Figure 1 shows that RR Tau was rather bright at the beginning of the observing season: $V \approx 10.5$. A comparison with our earlier observations [6] and observations by other authors [17, 18] shows that this brightness level is typical of the star's bright state. Almost as soon as we started our observations, a gradual dimming of RR Tau began, which lasted almost four months and was accompanied by strong brightness fluctuations. In the deepest part of the minimum (point 2 in Fig. 1), the star's V brightness had decreased by approximately 2.9^m.

The emergence from the minimum was more rapid and lasted about two months. Figure 1 shows that strong brightness fluctuations were also observed on the ascending branch of the light curve. A comparison with earlier photometric observations of RR Tau from the database of Herbst *et al.* [3] indicates that we observed a uniquely long minimum of RR Tau, with a total duration of about half a year. A comparably long minimum of this star was observed only once before, about 20 years earlier.

Figure 2 presents color–magnitude diagrams for RR Tau. The star's brightness variations were accompanied by color-index variations that are characteristic of UX Ori stars: the star became redder as it dimmed, but, beginning with some brightness level that depends on the wavelength λ, there is a turn in the color track (the so-called "blueing effect") due to the increased contribution of stellar light scattered by the circumstellar dust [8]. As a result, the color indices decreased in the deepest part of the minimum. Comparison with our earlier observations [6] shows that the color-index variations of RR Tau during the long minimum of 2000–2001 did not differ from those observed for this star in other seasons (Fig. 2).

3.2. Polarimetry

Our polarimetric $UBVRI$ observations of RR Tau obtained simultaneously with the optical photometry revealed an anti-correlation between variations of the brightness and degree of linear polarization, characteristic of UX Ori stars and testifying to the eclipsing nature of their minima. A comparison with our earlier observations of RR Tau [6] shows that the minimum of 2000–2001 is distinguished by systematically lower levels of polarization in the polarization–brightness diagrams (Fig. 3). Thus, the minimum was not typical in terms of the observed variations of the star's linear polarization.

3.3. IR Photometry

As noted above, we obtained near-IR photometry of RR Tau in the $JHKLM$ bands. Accuracy sufficient

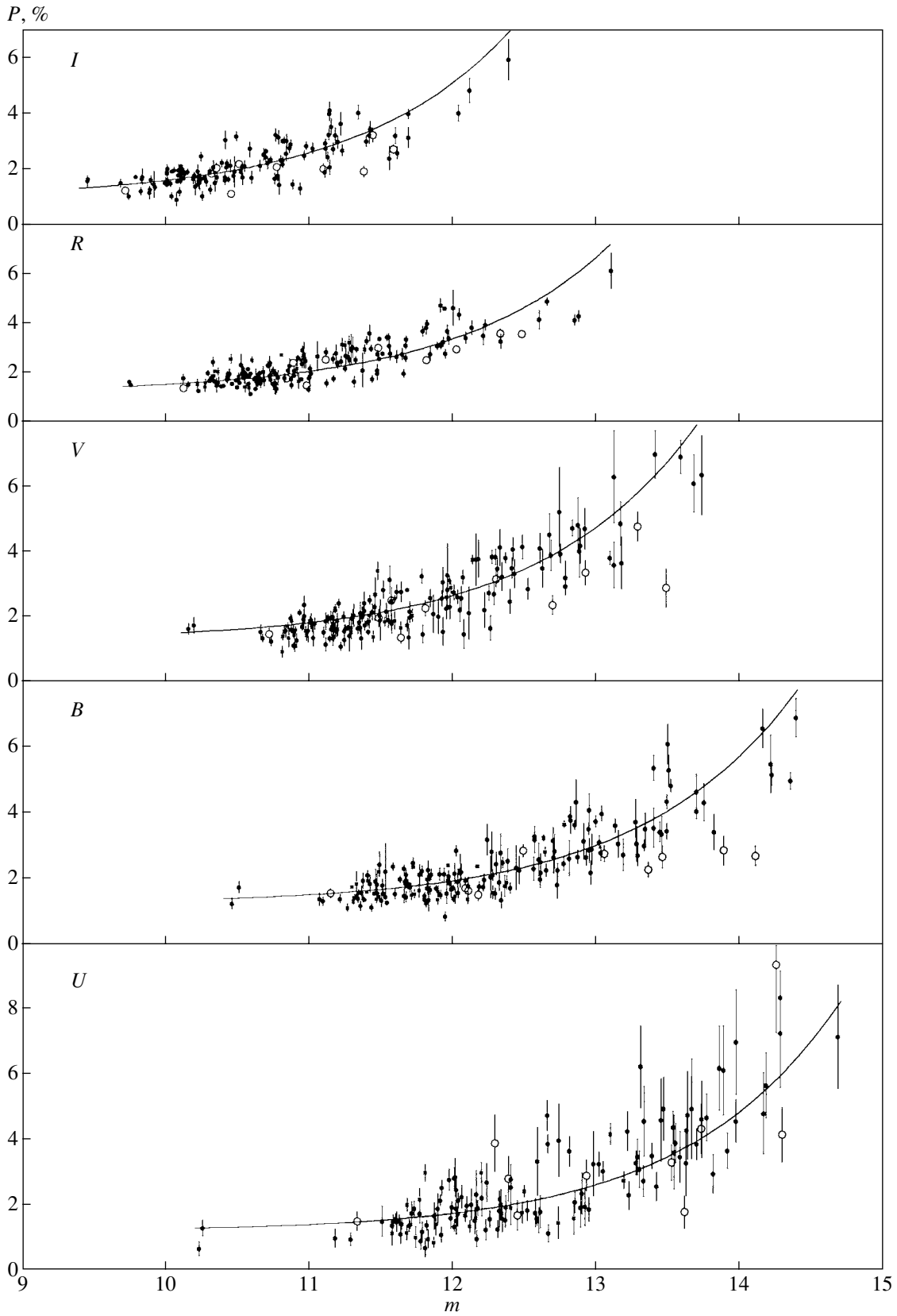

Fig. 3. Polarization–brightness relation for RR Tau based on data from the present study (open circles) and from [6] (dots). The thin curves are theoretical relations computed in [6] for the variable circumstellar extinction model of [8].

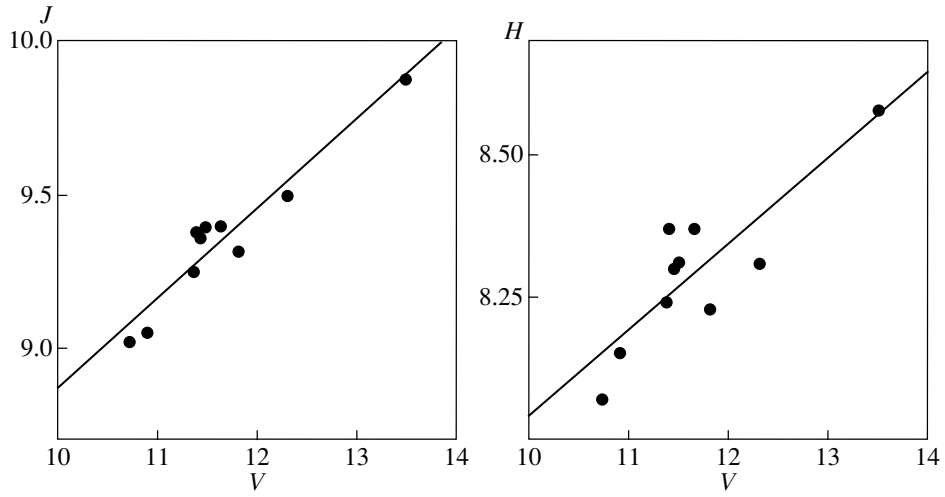

Fig. 4. Plot illustrating the simultaneity of the flux variations in the optical (V band) and near-IR (J, H bands). The correlation coefficients for the J, V and H, V bands are 0.96 and 0.89, respectively.

for reliable demonstration of IR flux variations was achieved in four bands—$JHKL$. The J and H fluxes varied synchronously with the optical brightness (see the table, Fig. 4); the correlation coefficients between the J and V magnitudes and H and V magnitudes are 0.96 and 0.89, respectively.

Quite different behavior was demonstrated by the K and L magnitudes. The Table and Fig. 1 show that the L flux *increased* as the optical brightness of RR Tau decreased. This ceased in the central part of the minimum, and a slight decrease of the IR flux was even observed during JD 2451920–2451950, but further the IR increase continued as the star emerged from the optical minimum. The L flux again decreased somewhat only at the very end of the observing season, but this measurement was recorded in the presence of growing uncertainties in the IR fluxes due to the increasing air masses and only slightly exceeded 3σ.

During these changes, the $K-L$ color index remained constant within the observational uncertainties (Fig. 1). This implies K variations synchronous with those in the L band, so that the flux ratio in these two bands was constant during the whole observation period.

4. DISCUSSION

Thus, our coordinated observations of RR Tau in the optical and near IR show that the results obtained by Hutchinson *et al.* [11] and Sitko *et al.* [12], described in the Introduction, are by no means exotic, and should not be considered random coincidences. We observed qualitatively the same behavior of the young star during its optical minimum in much more detail: a decrease in the fluxes in the $U-H$ bands (i.e., at wavelengths from 0.35 to 1.6 μm), accompanied by an increase in the fluxes in the longer wavelength K and L bands (Fig. 5). The region between the H and K infrared bands, in which RR Tau exhibited variability in opposite senses, suggests a sort of boundary in the star's spectra beyond which the thermal emission of the circumstellar dust becomes negligible compared to the radiation of the star itself. While the screening of the star by the dust cloud is still appreciable in the H band, resulting in a decrease in the observed fluxes, the dust cloud itself becomes a source of additional IR emission in the K and L bands, leading to the observed increase in the fluxes in these two bands. This abrupt transition is due to the fact that the intensity of thermal emission from dust with temperatures of the order of 10^3 K falls off rapidly with decreasing wavelength.

Thus, whereas a circumstellar dust cloud crossing the line of sight and screening the star from the observer is sufficient to explain the optical minimum of RR Tau, the cloud must pass very closely to the star if we wish to also explain the simultaneous increase of the IR radiation. Only then can the thermal emission from a single cloud, even a large one, compete with the radiation from the entire protoplanetary disk.

Another important conclusion that follows directly from our observations is that the K and L IR fluxes from RR Tau increased synchronously, so that the flux ratio in these bands remained constant within the errors (Fig. 1). This means that the dust temperature in the cloud remained unchanged during the entire observing season, so that the increase in the IR fluxes in these two bands was due to *an increase of the total mass of hot dust*.

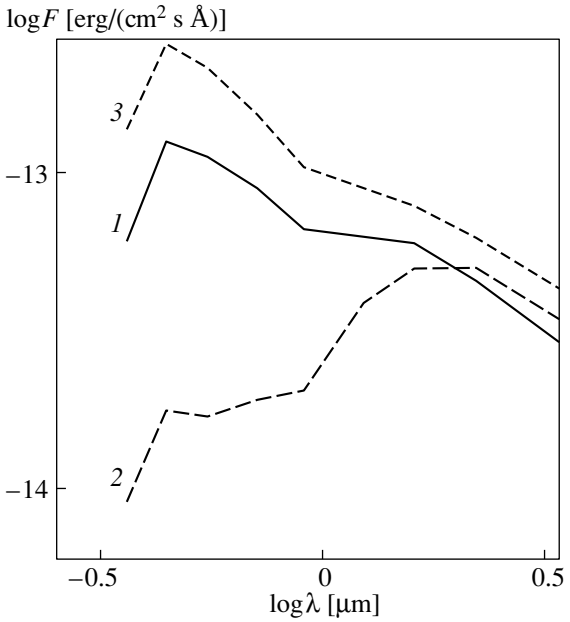

Fig. 5. Spectral energy distribution of RR Tau at 0.35–3.5 μm based on the current study for the three dates marked by dotted lines in Fig. 1: (1) bright state before the decline to the minimum, (2) deepest part of the minimum, and (3) bright state immediately after emerging from the minimum.

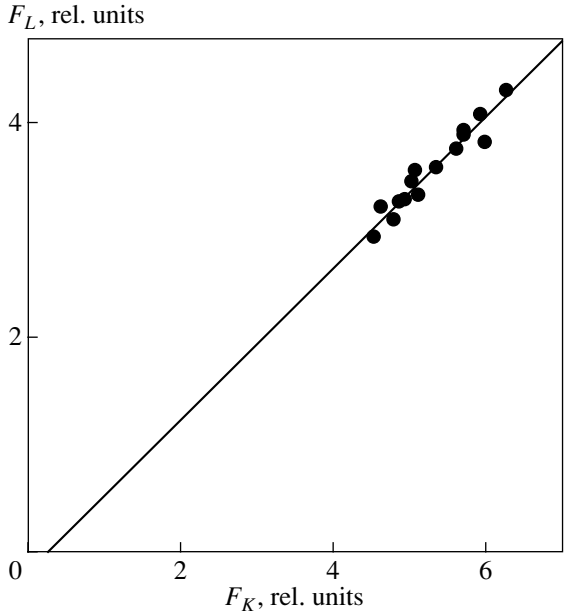

Fig. 6. Plot illustrating the synchronism of the variations in the K and L fluxes from RR Tau. Note that the minimum fluxes indicated by an extrapolation of this linear relation are virtually zero, suggesting that most of the radiation in these bands is formed in the gas and dust clouds closest to the star.

4.1. Parameters of the Circumstellar Cloud

These results enable us to estimate the main parameters of the cloud, namely, the temperature and total mass of the emitting dust, as well as the distance between the cloud and the star. To estimate the temperature, we use the K and L data. The dynamics of these flux variations (Fig. 6) suggest that, to a good approximation, nearly all the radiation from RR Tau in these two bands is due to thermal emission from the dust in the cloud. The mean $K-L$ color index was $\approx$1.25 (see Table). Using known relations to convert magnitudes into fluxes at wavelengths of 2.25 and 3.4 μm, corresponding to the maximum transmission in the K and L bands, we estimate the flux ratio in these bands to be $F_K/F_L \approx 1.7$. If the dust cloud emits as a black body, this ratio corresponds to a temperature of $T_d \approx 1300$ K. In fact, most of the cloud is already optically thin in the H band. For this reason, the resulting dust temperature is somewhat different from this value, as demonstrated below.

The fact that the star reddened as its brightness decreased (Fig. 2) provides evidence that the optical depth of the dust cloud screening the star decreases towards longer wavelrngths. We can use the upper (linear) portions of the color–magnitude diagrams (Fig. 2) to estimate the ratios of the dust cloud's optical depths at the wavelengths corresponding to the transmission maxima of the $UBVRIJH$ bands: $\tau_U : \tau_B : \tau_V : \tau_R : \tau_I : \tau_J : \tau_H =$ 1.65 : 1.21 : 1.00 : 0.84 : 0.66 : 0.29 : 0.16. Since the star's brightness decreased by $\Delta V \approx 2.9$ (corresponding to $\tau_V \approx 2.7$) in the deepest part of its minimum, the cloud's H optical depth at that time was $\tau_H \approx 0.4$. The optical depth of the cloud should be even lower in the longer-wavelength K and L bands, so that we can use an optically thin approximation for the radiating region (in the K, L bands) for our estimates.

In this case, the thermal flux from a dust cloud composed of spherical grains of radius a is:

$$F_{\rm cloud}(\lambda) = \pi \frac{a^2}{D^2} Q_{\rm abs}(\lambda, a) B_\lambda(T_d) N(a). \quad (1)$$

Here, $Q_{\rm abs}(\lambda, a)$ is the efficiency of absorption of radiation with wavelength λ by a particle of radius a, $N(a)$ is the total number of radiating grains for a cloud of the given size, and D is the distance to RR Tau (350 pc [19]).

Applying Mie theory and the optical parameters of graphite and silicates from [20, 21] (for definiteness, we selected p-obsidian), we computed $Q_{\rm abs}$ for graphite and silicate grains of various sizes. These computations show that the main contribution to the thermal emission in the considered wavelength range comes from submicron graphite grains (Fig. 7). For example, for grains with radius $a = 0.3$ μm, the observed flux ratio ($F_K/F_L \approx 1.7$) is obtained for a grain

temperature of $T_d \approx 900$ K. Solving the heat balance equation

$$\frac{1}{4\pi r^2}\int_0^\infty L_\lambda Q_{\rm abs}(a,\lambda)d\lambda = \int_0^\infty Q_{\rm abs}(a,\lambda)B_\lambda(T_d)d\lambda, \quad (2)$$

we find (Fig. 8a) that, at a distance of $r = 1$ AU from RR Tau (with its temperature $T_{\rm ef} = 9500$ K and luminosity $L_\lambda \approx 50 L_\odot$ [19]), this temperature corresponds to graphite grains with radii of ≈ 0.2 μm, close to that adopted above.

Heating leads to intense evaporation of the dust grains. The dependence of the grains' lifetime on their size and composition (graphite, silicates) is presented in Fig. 8b. We calculated these lifetimes using the same technique as in [22]. Figure 8b demonstrates that fine silicate grains evaporate rapidly 1 AU from RR Tau, whereas the lifetime of graphite grains is much longer, so that they survive with sizes as small as hundredths of a micron.

Substituting the resulting T_d value into Eq. (1) for the L flux and equating this to the maximum observed flux in this band ($F_L = 4.2 \times 10^{-14}$ erg cm^{-2} s^{-1}Å^{-1}), we find the total number of grains of the specified size to be $N \approx 10^{35}$. Thus, for grain densities of 3 g/cm^3, we obtain a total dust mass of $M_d \approx 4 \times 10^{22}$ g.

Note that this estimate gives the mass of dust emitting in the near IR star's radiation. It is independent of any assumptions about the shape and size of the circumstellar clouds, which are usually needed for similar estimates of cloud masses based on optical observations of Algol-like minima [23, 24]. Comparison with the results of [23, 24] shows that this dust mass for the RR Tau circumstellar cloud exceeds other estimates of cloud masses by about 1.5–2 orders of magnitudes and confirms the uniqueness of the event we observed.

The analogous estimate for smaller grains (for instance, $a = 0.1$ μm) yields a somewhat higher mass for the cloud's dust component: $M_d \approx 10^{23}$ g. The reddening of RR Tau during its brightness decreases indicates the presence of fine grains in the cloud, with sizes of the order of 0.1 μm [6], so that this latter estimate seems more realistic. If we adopt the same mass ratio for the cloud's gas and dust components as the average value for the interstellar medium, this dust mass should be increased by a factor of 100. In this case, the total mass of the gas and dust cloud will be $\gtrsim 10^{25}$ g.

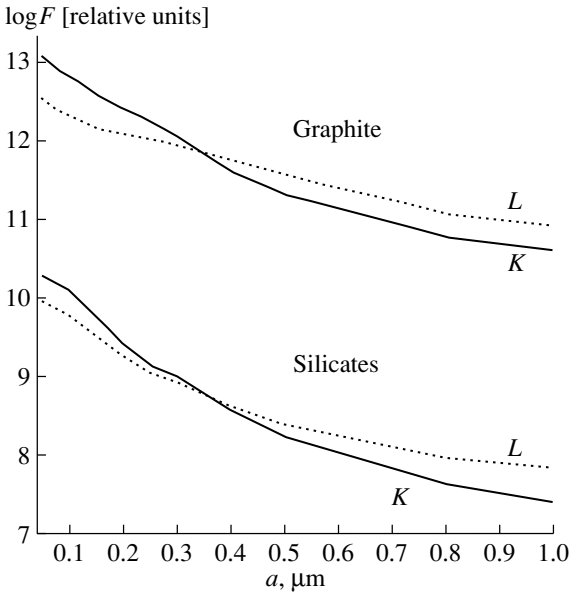

Fig. 7. A plot illustrating the K (solid) and L (dotted) emissive power for graphite and silicate grains of various sizes located at the distance of 1 AU from RR Tau. The size distribution of the grains was assumed to be the same as in the interstellar medium: $n(a) \propto a^{-3.5}$. The grain temperature was computed using Eq. (1). The vertical scale is arbitrary but is the same for the silicate and graphite grains.

4.2. Temporal Variations of the Cloud Parameters

Obviously, the increased IR radiation from RR Tau in the K and L bands during the entire optical minimum could be due to an increased total mass of fine grains in the cloud during its passage near the star. In this case, it is natural to associate this process with the thermal disruption and sublimation of larger grains and bodies that could be present in the cloud. Therefore, the analogy with solar-system comets discussed by Sitko *et al.* [12] and other authors (see the reviews [25–27]) would be appropriate.

However, a different interpretation that does not require any increase in the amount of dust in the cloud is possible. As we know from the light curve of RR Tau (Fig. 1), the central part of the cloud was opaque to the star's optical and ultraviolet radiation, so that the dust contained there was cool. During the cloud's passage near the star, tidal deformation and disruption is possible. As a result, the stellar radiation could penetrate and heat the central part of the cloud. In this situation, the increase in the number of emitting grains could be due to differing illumination conditions in the cloud, with the total amount of dust remaining the same.

Our results also enable us to draw some conclusions about the cloud's shape and orbit. First, the very fact that the cloud had a constant dust temperature and was close to the star testifies that the

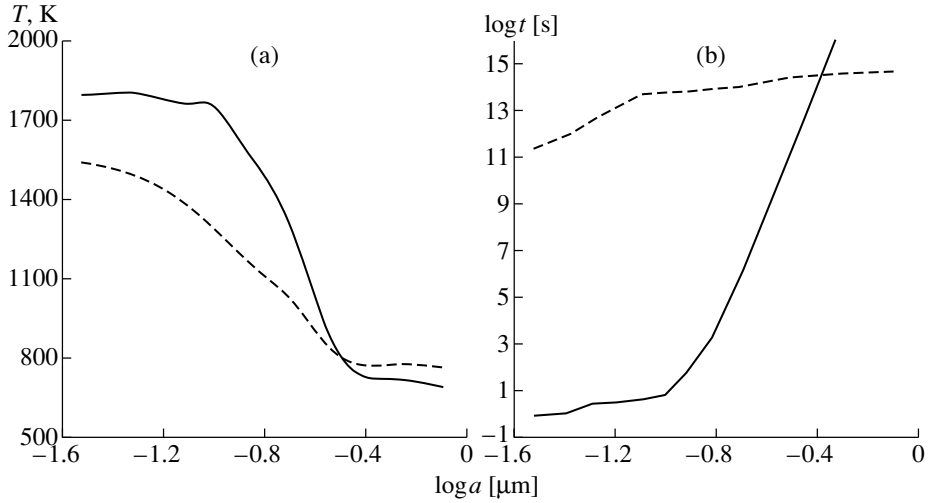

Fig. 8. (a) Temperatures (a) and (b) lifetimes of graphite and silicate (p-obsidian) grains of various sizes at a distance of 1 AU from RR Tau.

cloud passed near the periastron of its probably very eccentric orbit during the minimum. If the mass of RR Tau is 2.5 $M_\odot$ [19], the orbital period of a cloud moving around the star at a distance of 1 AU is about 7.5 months, comparable to the observed duration of the minimum. This suggests that the circumstellar cloud was strongly elongated and that, while its trailing edge was still crossing the line of sight, its front edge was already bending behind the star. In this way, the circumstellar cloud could cover a significant fraction of a 4π solid angle in its motion, giving rise to some difference of the polarization in the deepest part of the minimum compared to the results of our earlier observations of other minima of RR Tau, which were similar in depth but less prolonged [6]. This supports our earlier conclusion [7] that the strong fluctuations of the Stokes parameters of the scattered light observed for some UX Ori stars could be due to close passages of circumstellar dust clouds.

5. CONCLUSIONS

Our analysis of these new observations of RR Tau suggests that the uniquely long minimum of the star in 2000–2001 was due to a giant gas and dust cloud that appeared in the nearest vicinity of the star. Due to its high mass and proximity to the star, the cloud became the dominant source of thermal radiation in the K and L bands, resulting in an increase in the IR fluxes from RR Tau in these bands. This enabled us to estimate for the first time the temperature of grains in the cloud (about 10^3 K), distance from the star to the cloud (about 1 AU), and mass of dust emitting in the near IR (of the order of 10^{23} g). This last estimate corresponds to the dust mass in that part of the cloud heated by the star's radiation and therefore represents a lower limit for the total dust mass in the cloud. Assuming the standard mass ratio of the cloud's dust and gas components (1 : 100), the lower limit for the total mass of the cloud becomes an the order of 10^{25} g, or about 0.1 lunar mass.

This value gives us insight concerning the scale of the physical phenomena taking place near young stars, which could have occured in the vicinity of the Sun during early stages in the evolution of the solar system. It is natural to suppose that the presence of such large amounts of circumstellar material near a young star should cause strong fluctuations in the rate of gas accretion onto the star, and should be reflected by the physical characteristics of the inner layers of the accretion disk, where the stellar emission spectrum and shell components of absorption lines are formed. Such highly unstable feeding of the accretion disk may be the origin of the observed strong variations of the spectroscopic features of many young stars, including RR Tau itself [28, 29].

Within the time covered by our observations (about half a year), the mass of the emitting gas in the cloud approximately doubled, with the grain temperature remaining virtually constant. This may represent evidence for comet-like activity near RR Tau, in which large grains and bodies are disrupted during their passage close to the star, forming finer grains. An alternative explanation is that tidal forces deformed the cloud during its passage near the star, so that its densest regions became transparent to the stellar radiation, increasing the amount of heated dust.

The question arises of which processes are responsible for the formation of such massive circumstellar clouds and for their presence so close to a young star. We believe that the answer is closely related to the answer to another question: what is the origin of the large-scale photometric activity cycles of

UX Ori stars? In our papers [30–32], we propose that the existence of such cycles testifies to hidden binarity of these stars. A similar idea was also recently suggested in [33]. In connection with this, it is of considerable interest to obtain spectoscopic data for such objects that could reveal the presence of companions, as well as interferometric observations, to obtain images with high angular resolution.

ACKNOWLEDGMENTS

The authors are grateful to A. Natta for a helpful discussion and O.V. Ezhkova for providing information concerning the brightness of RR Tau on November 10, 2001. This study was supported by the Russian Foundation for Basic Research (project no. 99-02-18520) and the "Nonstationary Processes in Astrophysics" Program of the Presidium of the Russian Academy of Sciences.

REFERENCES

1. C. Hoffmeister, G. Richter, and W. Wenzel, *Variable Stars* (Springer-Verlag, Berlin, 1990).
2. G. V. Zaĭtseva, Perem. Zvezdy **19**, 63 (1973).
3. W. Herbst, D. K. Herbst, and E. A. Grossman, Astron. J. **108**, 1906 (1994).
4. P. S. Thé, in *The Nature and Evolutionary Status of Herbig Ae/Be Stars,* Ed. by S. Thé, M. R. Pérez, and P. J. van den Heuvel, Astron. Soc. Pac. Conf. Ser. **62**, 37 (1994).
5. V. P. Grinin, N. N. Kiselev, N. Kh. Minikhulov, *et al.*, Astrophys. Space Sci. **186**, 283 (1991).
6. A. N. Rostopchina, V. P. Grinin, A. Okazaki, *et al.*, Astron. Astrophys. **327**, 145 (1997).
7. V. P. Grinin, in *The Nature and Evolutionary Status of Herbig Ae/Be Stars,* Ed. by P. S. Thé, M. R. Pérez, and P. J. van den Heuvel, Astron. Soc. Pac. Conf. Ser. **62**, 63 (1994).
8. V. P. Grinin, Pis'ma Astron. Zh. **14**, 65 (1988) [Sov. Astron. Lett. **14**, 27 (1988)].
9. V. P. Grinin, in *Disk, Planetesimals and Planets,* Ed. by F. Garzon, C. Eiroa, D. de Winter, and T. J. Mahoney, Astron. Soc. Pac. Conf. Ser. **219**, 216 (2000).
10. D. Kilkenney, D. C. B. Whitted, J. K. Davies, *et al.*, S. Afr. Astron. Obs. Circ. **9**, 55 (1985).
11. M. G. Hutchinson, J. S. Albinson, P. Barrett, *et al.*, Astron. Astrophys. **285**, 883 (1994).
12. M. L. Sitko, E. M. Halbedel, G. F. Lawrence, *et al.*, Astrophys. J. **432**, 753 (1994).
13. V. Piirola, Ann. Acad. Sci. A VI **418**, 61 (1975).
14. A. E. Nadzhin, M. I. Shenavrin, and V. G. Tikhonov, Tr. Gos. Astron. Inst. Mosk. Gos. Univ. **58**, 119 (1986).
15. H. L. Johnson, R. I. Mitchell, B. Iriarte, and W. Z. Wisniewski, Commun. Lunar Planet. Lab. **4**, 99 (1966).
16. J. Koornneef, Astron. Astrophys., Suppl. Ser. **51**, 489 (1983).
17. V. I. Kardopolov and F. K. Rspaev, Kinematika Fiz. Nebesnykh Tel **5**, 50 (1989).
18. W. Herbst and V. S. Shevchenko, Astron. J. **118**, 1043 (1999).
19. A. N. Rostopchina, Astron. Zh. **76**, 136 (1999) [Astron. Rep. **43**, 113 (1999)].
20. J. B. Pollack, O. B. Toon, and B. N. Khare, Icarus **19**, 372 (1973).
21. P. L. Lamy, Icarus **34**, 68 (1978).
22. V. P. Grinin, A. Natta, and L. V. Tambovtseva, Astron. Astrophys. **313**, 857 (1996).
23. N. V. Voshchinnikov and V. P. Grinin, Astrofizika **34**, 181 (1991).
24. G. Meeus, C. Waelkens, and K. Malfait, Astron. Astrophys. **329**, 131 (1998).
25. L. B. F. M. Waters and C. Waelkens, Ann. Rev. Astron. Astrophys. **36**, 233 (1998).
26. C. A. Grady, M. L. Sitko, R. W. Russell, *et al.*, in *Protostars and Planets IV,* Ed. by V. Mannings, A. P. Boss, and S. S. Russell (The University of Arizona Press, Tucson, 2000), p. 613.
27. A. Natta, V. P. Grinin, and V. Mannings, in *Protostars and Planets IV,* Ed. by V. Mannings, A. P. Boss, and S. S. Russell (The University of Arizona Press, Tucson, 2000), p. 559.
28. B. Rodgers, D. Wooden, V. Grinin, *et al.*, Astrophys. J. (2002) (in press).
29. V. P. Grinin, O. V. Kozlova, A. Natta, *et al.*, Astron. Astrophys. (2002) (in press).
30. V. P. Grinin, A. N. Rostopchina, and D. N. Shakhovskoĭ, Pis'ma Astron. Zh. **24**, 925 (1998) [Astron. Lett. **24**, 802 (1998)].
31. A. N. Rostopchina, V. P. Grinin, and D. N. Shakhovskoĭ, Pis'ma Astron. Zh. **25**, 291 (1999) [Astron. Lett. **25**, 243 (1999)].
32. V. P. Grinin and L. V. Tambovtseva, Mon. Not. R. Astron. Soc. (2001) (in press).
33. C. Bertout, Astron. Astrophys. **363**, 984 (2000).

Note to the proofs. The recently published paper by C. Eiroa *et al.* (Astron. Astrophys., **365**, 110 (2001)) presents simultaneous photometric observations of 16 young variable stars in the optical (*UBVRI*) and near-infrared (*JHK*) bands. The 12 stars studied by these authors belong to the subclass of UX Ori stars. Each of them was observed 4 or 5 times during one week. During the observations, most of the stars were in a bright state, and their brightness varied only slightly, in the optical ($\Delta V \approx 0.1$–0.4) and infrared bands. RR Tau was also bright: $V = 10.94$–11.46, $J = 9.05$–9.24, and $K = 7.00$–7.08. Comparison with our observations indicates that approximately the same V, J, K magnitudes were observed during egress of RR Tau from the 2000/2001 minimum. The largest photometric variability was observed in RY Ori (Sp = F6 Ve); during the day, it faded in the optical ($\Delta V = 1.1$) and infrared ($\Delta K = 0.4$) wavelength ranges.

Translated by N. Samus'

Astronomy Reports, Vol. 46, No. 8, 2002, pp. 656–666. Translated from Astronomicheskiĭ Zhurnal, Vol. 79, No. 8, 2002, pp. 726–737.

The Evolutionary Status of UX CVn

V. V. Shimansky[1], N. V. Borisov[2], N. A. Sakhibullin[1], V. F. Suleĭmanov[1], and M. S. Stupalov[1]

[1] *Astronomical Observatory, Department of Astronomy, Kazan State University, ul. Lenina 18, Kazan, 420008 Tatarstan, Russia*

[2] *Special Astrophysical Observatory, Russian Academy of Sciences, Nizhniĭ Arkhyz, Karachaevo-Cherkesskaya Republic, 357169 Russia*

Received November 12, 2000; in final form November 23, 2001

Abstract—We have analyzed available spectroscopic and photometric observations of the close binary UX CVn using model atmospheres. Theoretical spectra and light curves were derived from models of a precataclysmic variable and a close binary consisting of degenerate stars. We have used the 6-m telescope of the Special Astrophysical Observatory to obtain ten moderate-resolution spectra at three orbital phases. Our analysis of the radial-velocity curve shows that the orbital period of the system has been stable over 40 yrs, and the variations of the intensities of lines of various elements at different phases and radial velocities indicates an absence of the reflection effect. As a result, we have classified UX CVn as a detached close binary consisting of a hot, low-luminosity sub-dwarf primary and a white-dwarf secondary.

1. INTRODUCTION

Pre-cataclysmic variables have recently been recognized [1] as a type of close binary system. The number of known precataclysmic variables is rapidly increasing. These are fully detached systems with orbital periods that are sufficiently small to bring about an efficient loss of the angular momenta of the components; they contain either hot, low-luminosity sub-dwarfs or white dwarfs as their primary and late-type main-sequence stars as their secondary. It has been proposed [2] that precataclysmic variables are formed when the system undergoes a common envelope stage, during which its orbital period decreases from 0.5–10 yrs to several hours or days. In its subsequent evolution, a precataclysmic variable slowly loses angular momentum due to the outflow of its magnetic stellar wind [3, 4] and the radiation of gravitational waves [5]. As a result, the system can become a cataclysmic variable for 10^7–10^8 yrs, which is a brief time interval in its overall evolution.

The most recent reviews of close binary systems [6–8] contain about 40 precataclysmic variables. It has been suggested that 15% of these objects have been erroneously classified as precataclysmic variables. Each year, an additional one or two objects are classified as precataclysmic variables, a substantial number of them being currently identified as single and binary white dwarfs and sub-dwarfs. Only for a handful of precataclysmic variables (V477 Tau, BE UMa, NN Ser) have multifaceted photometric and spectroscopic studies been carried out and reliable parameter estimates been obtained. The basic parameters of most precataclysmic variables have only been roughly estimated, and, in a number of cases, only the orbital period and evolutionary status of the objects have been determined.

Thus, quantitative studies of precataclysmic variables can be used to conclusively determine the evolutionary statuses of such systems and derive or refine their parameters. This should provide clearer insight into the physics of precataclysmic variables both as an intermediate stage between stars with common envelopes and cataclysmic binaries and as a late evolutionary stage for close binary systems as a whole. We will be devoting a series of studies to this problem.

UX CVn ≡ HZ 22 was discovered by Humason and Zwicky [9] in their search for faint blue stars at high Galactic latitudes, as a B3 object with $m_V = 12.7^m$. Its orbital period ($P_{\rm orb} = 0.573703^d$) was determined by Young *et al.* [10], who showed that the total mass of the system's components must be about 1 $M_\odot$. Brightness variations with amplitude $\approx 0.2^m$ were also detected, accompanied by negligible ($\approx 0.01^m$) variations of $U-B$ and $B-V$, and were interpreted as a consequence of the elongated shape of a primary that is close to filling its Roche lobe and its time-variable projection onto the plane of the sky. Later, Greenstein [11] derived the parameters of the primary's atmosphere from spectroscopic observations: $T_{\rm eff} = 28\,000$ K, $\log g = 4.00$. With these data, Schonberner [12] estimated the mass of the visible component to be $M_1 = 0.39 M_\odot$, based on calculated

evolutionary tracks for single hot sub-dwarfs with interior burning of helium and hydrogen [13]. A similar estimate was obtained in [14] using the technique of [15].

It has not been possible to draw unambiguous conclusions about the secondary component based on observations, since no supplementary emission or absorption features were detected and no line profile variations were seen in the spectra of UX CVn at wavelengths $\lambda\lambda$3400–6700 Å. Three hypotheses concerning the nature of the secondary were put forth: it could be either a late-type main-sequence star or a compact object—white dwarf or neutron star. The compact-object hypothesis was given preference in all the above studies, based on the argument that, since the amplitude of the brightness variations associated with the elliptically elongated star is substantial, the orbital inclination must be large, which, together with the absence of observed eclipses, provides evidence for the small size for the secondary. Young and Wentworth [16] tested the neutron-star hypothesis by searching for X-ray radiation from the system using the Einstein observatory. Since no radiation was found at the level 10^{31} erg/s, the secondary was determined not to be a neutron star. As a result, the white-dwarf hypothesis became generally accepted.

However, Ritter [1] noted that, if the system contains a white dwarf, it is a binary white dwarf that has undergone two common envelope stages, in evolutionary contradiction with the relatively long orbital period. Ritter [1] concluded that the secondary was a red dwarf, and the system itself a precataclysmic variable. Later, Ritter and De Kool [6] indicated that the evolutionary status of UX CVn remained unclear; however, in subsequent reviews of precataclysmic variables [2, 17], it was listed as precisely this type of close binary system. At the same time, the system was still classified as a hot sub-dwarf plus a white dwarf in studies of blue objects [18–21].

Thus, UX CVn may be either a precataclysmic variable or a member of the poorly understood binary white dwarf class, making it important to determine its evolutionary status. Apart from elucidating the nature of UX CVn, it is important to estimate as many parameters of the system and its components as possible, to supplement the group of precataclysmic variables or binary white dwarfs with data for another well-studied object.

Accordingly, beginning our investigations of UX CVn, we set ourselves two basic tasks: determining the evolutionary status of the system and analyzing its parameters as thoroughly as possible. In the current paper, we are concerned with the development of techniques for analyzing the observational data, new high-quality spectral observations, and the evolutionary status of the system. In Section 2, methods for modeling the radiation of UX CVn are described. Theoretical calculations carried out for two alternative models of the system are also presented and compared with the available observational data. Section 3 describes the new observations and their reduction. Section 4 contains our analysis of the observations and basic conclusions about the evolutionary status of the system.

2. MODELS OF UX CVn IN THE LIGHT OF CURRENT OBSERVATIONAL DATA

Let us consider the consistency between theoretical modeling of the radiation of UX CVn and the available observational data. Figure 1a presents a general model of the system; the secondary (with luminosity $\mathcal{L}_2$) could be either a white dwarf (Model I) or a main-sequence star (Model II). We will examine both cases.

Model I: The system consists of a hot-core primary and a low-luminosity white-dwarf secondary. It is obvious that the total brightness of the primary exceeds that of the white dwarf by a factor of 10^4 or more, and all variations of the system's radiation can be understood as a result of its asphericity. We analyzed the radiation theoretically using the ROSHE code, which models the spectrum of a star filling or close to filling its Roche lobe. This code is based on the technique suggested by Howarth and Wilson [22]. In this approach, the equipotential surface is specified in the form [23]

$$U = \frac{1}{r_s} + q(1 - 2l_s r_s + r_s^2 - l_s r_s) + F^2 r_s^2 (1+q)(1-n_s^2)/2, \quad (1)$$

where $\mathbf{r}_s$ is the radius vector directed from the center of the star, $l_s = \cos\varphi_s \sin t_s$, $n_s = \cos t_s$, and $q = M_1/M_2$ is the component mass ratio. The polar coordinate system φ_s, t_s, r_s is directed toward m_1 (Fig. 2). The unit length is taken to be the distance between the component centers. F is the ratio of the angular rotational velocity of the star and the orbital angular velocity.

The coordinate of the inner Lagrange point r_c is derived from the condition that the derivative U'_{r_s} be zero when $\varphi_s = t_s = 0$. The potential U_c at the Lagrange point specifies the shape of the critical surface of the Roche lobe [Eq. (1) is solved for r_s, for any specified φ_s, t_s, and $U = U_c$].

We assumed that the star does not fill its Roche lobe. Therefore, its surface coincides with the equipotential surface with $U_* > U_c$. The value for U_* was selected so that the average radius of the star coincided with the radius estimated from observations.

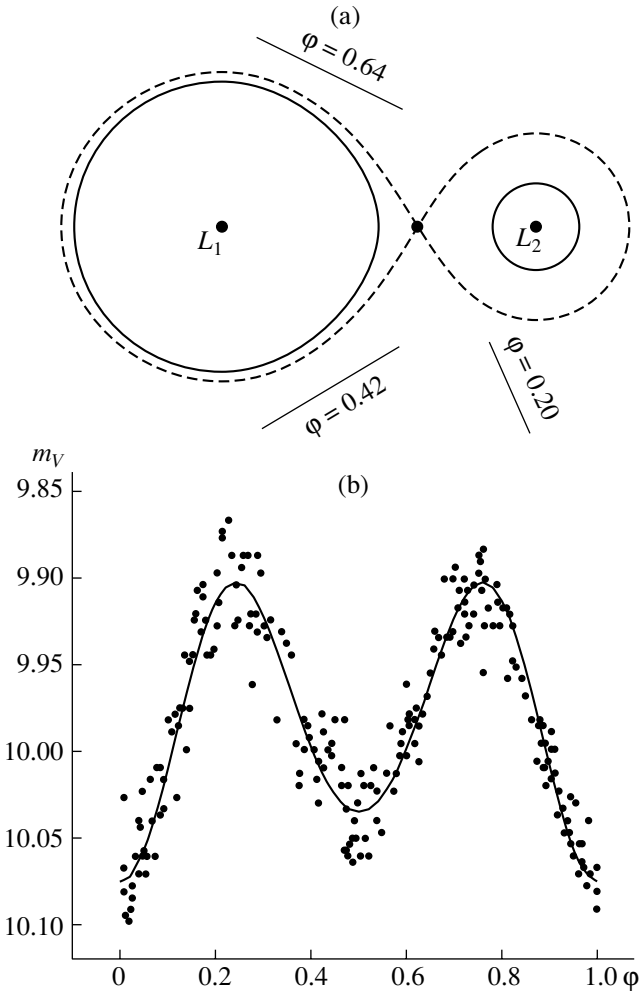

Fig. 1. (a) Model of UX CVn with observing conditions at phases $\varphi = 0.20, 0.42, 0.64$ indicated. (b) Observed (data of Young and Wentworth [16], dots) and theoretical (Model I, curve) light curves in the V band.

In the calculations, the stellar surface is divided into some number of elements (in our case, 5000; the angle φ_s was divided into 100 steps and the angle t_s into 50), with the area being given by

$$A_s = \sin t_s d\varphi_s dt_s r_s^2 / \cos\Gamma. \quad (2)$$

Here, Γ is the angle between the radius vector

$$\mathbf{r} = x\mathbf{i} + y\mathbf{j} + z\mathbf{k} \quad (3)$$

and the normal to the surface, calculated as the vector reciprocal to the gradient U:

$$\mathbf{N} = [xr_s^{-3} - q((1-x)(1-2x+r_s^2)^{-1.5} - 1) \quad (4)$$
$$- F^2(1+q)x] \cdot \mathbf{i}$$
$$+[yr_s^{-3} + q(y(1-2x+r_s^2)^{-1.5}) - F^2(1+q)y]\mathbf{j}$$
$$+[zr_s^{-3} + q(z(1-2x+r_s^2)^{-1.5})]\mathbf{k}.$$

The effective temperature of each area element is determined from the gravitational darkening law

$$T_{loc} = T_{pol}(g_{pol}/g_{loc})^b, \quad (5)$$

where T_{pol} is the effective temperature at the pole of the star, $g_{pol}/g_{loc} = |N_{pol}|/|N_{loc}|$ is the ratio of the gravitational accelerations at the pole and at the given area, and b is a constant taken in our case to be equal to 0.25.

The total spectrum of the star is combined from the spectra of the specific intensities of the area elements calculated for the angle θ to the area normal. θ is the angle between the line-of-sight vector

$$\mathbf{R} = \sin i\cos\Phi\mathbf{i} + \sin i\sin\Phi\mathbf{j} + \cos i\mathbf{k} \quad (6)$$

and the normal vector $\mathbf{N}$. Here, i is the inclination of the line of sight to the normal to the orbital plane, while Φ is the angle between the x axis, directed towards the secondary, and the projection of the line of sight onto the xy plane (Fig. 2).

For each area element on the stellar surface, we calculated the specific intensity of the emerging radiation for three basis angles θ' (with $\mu_1 = 0.11$, $\mu_2 =$

0.50, $\mu_3 = 0.89$) by solving the transfer equation using blanketed Kurucz [24] model atmospheres with parameters corresponding to the local values for the temperature, gravity, and solar chemical composition. We obtained model atmospheres with non-grid values of the parameters using the interpolation procedure [25, 26], which provides an accuracy for the electron-temperature and gas-pressure calculations no worse than 1%. When solving the transfer equation, we took into account all continuous sources of opacity tabulated in the ATLAS5 [27], STARDISK [25], and SPECTR [29] packages, as well as the strongest lines of hydrogen and helium.

Further, for each orbital phase φ, the intensity was interpolated from the three basis angles θ' for the specified angle θ and then integrated over the total surface of the star, taking into account the size of the area elements, their inclinations to the line of sight, the Doppler effect due to the orbital and rotational motions, and the condition for visibility ($\theta < \pi/2$). To calculate the theoretical light curve, we convolved the total emitted flux from UX CVn with the appropriate transmission curves, in accordance with the data from [30].

Currently, there is only one adequate light curve of UX CVn in the UBV photometric system, obtained by Nelson and Mielbrecht with the 1.3-m telescope of the Kitt Peak Observatory [16], presented here in Fig. 1b. The accuracy of a single observation is about 0.05^m; however, the large number of observations (about 175) means that the expected errors for the averaged light curve do not exceed 0.01^m. Further, we will use only the V light curve, since it is the most complete and has the smallest observational errors. Our calculations indicate that both the total observed brightness variation amplitude of about 0.17^m and the difference of the depths of the main and secondary minima can be described using the adopted model for a large number of parameter sets. Figure 1b presents one example, for the parameters $M_1 = 0.39M_\odot$, $M_2 = 0.42M_\odot$, $i = 90.^\circ0$, $A = 2.90R_\odot$, $R_1 = 1.00R_\odot$, and $T_{eff} = 28\,000$ K, adopted by Ritter and Kolb [8]. It is evident that the theoretical light curve is fully consistent with the observations within the errors. The corresponding variations of the color indices are extremely small ($\Delta(B-V) < 0.^m005$) and are not useful for quantitative analyses. Thus, Model I cannot be ruled out on the basis of the photometric data.

Variations in the spectrum of UX CVn at different phases are related to the varying conditions for observing hot and cool areas of its surface. Since the surface temperature of the primary exceeds $T_{\rm eff} = 26\,000$ K, the number of neutral hydrogen and helium atoms in its atmosphere is $<1\%$ of the number of corresponding ions. Therefore, in areas with higher temperatures, these elements will be more fully ionized, and their lines will weaken. At phases close to $\varphi = 0.25$ and $\varphi = 0.75$, the observer views hotter zones corresponding to "low tide" (i.e., the viewing angle is perpendicular to the tidal bulge between the components), and the HI and HeI lines will be weaker. At phases $\varphi = 0$ and $\varphi = 0.50$, cooler zones corresponding to "high tide" dominate (i.e., the viewing angle is along the direction of the tidal bulge), and these lines are strengthened. We obtained the corresponding line profiles for three phases using a procedure analogous to that for calculating the light curves. We used the theory of Griem [31] when calculating the Balmer HI lines, taking the oscillator strengths for the HI lines from [32, 33] and adopting broadening constants for these lines in accordance with the approximations of [34, 35]. Figure 3a illustrates the character of the line-profile variations at different phases using the H_γ line as an example. Similar profile variations are seen for the other lines, but are less prominent for weaker lines of the singlet series of helium. Overall, the profile variations occur at a level of 0.008–0.012 of the residual intensity and 1–2% of the equivalent width. Below, we will consider the availability of observations with accuracy high enough to reveal this effect.

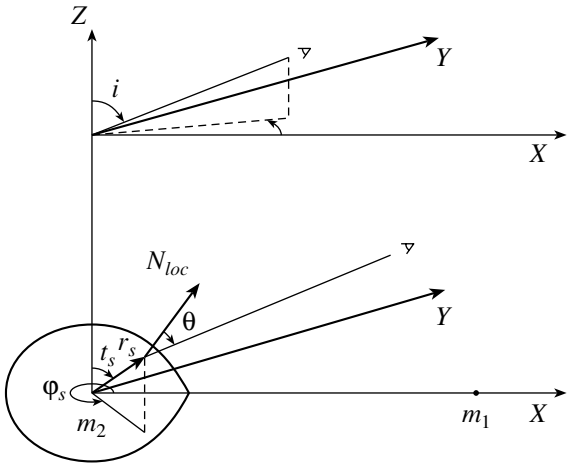

Fig. 2. Geometry of the Roche lobe model.

Model II: The system consists of a hot-core primary and a late-type red-dwarf secondary. The conditions for the absence of eclipses and accretion impose substantial constraints on the temperature and mass of the secondary. Taking into account the estimate of the primary mass $M_1 = 0.39M_\odot$ [12], we obtained limits for the dwarf's mass $M_2 = 0.60$–$0.75M_\odot$ and temperature $T_{\rm eff} = 4200$–4900 K. Under these conditions, its radiation at wavelengths $\lambda < 5500$ Å is less than 0.004 of the radiation of the blue star, i.e., it is insignificant. However, in a close binary system

with a large difference in the effective temperatures of the components, we should observe evidence of the reflection effect, when radiation from the hot star falls on the surface of the red dwarf, heating it and forming a hot spot. In this case, the total spectrum of the system will be a superposition of the individual spectra of the primary, red dwarf, and hot spot. All variations due to the ellipsoidal shape of the primary also occur in this case, but are made more complex by the reflection effect.

We studied this effect by calculating the spectra of stars with external illumination using the model stellar atmospheres of [26, 29]. The surface of the illuminated star, taken to be spherically symmetrical, is divided into rings centered on the major axis of the system; a local model for the illuminated atmosphere is calculated for each ring. The basis of this method is calculating the temperature balance between the heating and cooling functions for an atmosphere illuminated by a point-like external source and requires that a number of parameters be preliminarily specified: the effective temperature of the star T_{eff}, the surface gravititational acceleration $\log g$, the ratio of the intensity of the radiation falling on the given ring and the integrated radiation of the atmosphere $\mathrm{K}_x = H_x/H_0$, and the cosine of the angle of incidence $\mu = \cos\theta$.

In our study, the external source differs appreciably from a point source, and the incident radiation is confined within some range of angles θ, with its intensity being a complex function of μ. To take into account the finite size of the external source, we redefined the intensity of the illuminating flux on each ring to be

$$\mathrm{K}_x = \frac{L_1}{L_2}\left(\frac{R_1}{r_{1,2}}\right)^2 \frac{2}{1+\sqrt{1-\left(\frac{R_1}{r_{1,2}}\right)^2}}, \qquad (7)$$

where L_1 and L_2 are the luminosity of the primary and secondary, R_1 is the average radius of the primary, and $r_{1,2}$ is the distance from a given ring to the center of mass of the primary. We took the angle between the normal to the surface and the direction towards the center of mass of the primary to be the angle of incidence of the external radiation. Test calculations indicated that, with $T_{\text{eff}} = 4000$ and 5000 K, $\log g = 4.50$ and 5.00, and $\mathrm{K}_x = 300$, the differences between models with a single angle of incidence for the external radiation $\mu_0 = 0.50$ and with the external illumination uniformly distributed in the interval $\mu = 0.20$–0.80 were up to 1.3% for the temperature and up to 1.6% for the radiated flux. Therefore, the approximation of a point-like external source does not result in any significant loss in accuracy, and is acceptable.

We calculated the temperature distributions in the illuminated atmospheres in the semi-gray approximation suggested in [26] and modified in [36, 37]. The errors in the models for the illuminated atmospheres calculated in this approximation were up to 3–5% for the temperature and up to 7–10% for the radiated flux at optical wavelengths, for parameters of the external radiation close to those of UX CVn. Since the maximum errors occured only for certain individual rings and the total luminosity of the hot spot was only a few percent of the primary radiation, the total error due to the adopted model simplifications and inaccuracies in the calculation method did not exceed 0.3% of the total flux from the system at wavelengths $\lambda\lambda 3700$–6000 Å.

We modeled the UX CVn system by taking into account the atmospheric parameters of the primary from [11], its mass from [12], the absence of accretion and eclipses at a level higher than 0.01^m [10], and the evolutionary tracks for main-sequence stars from [38]. Finally, we adopted the effective temperature $T_{\text{eff}} = 4200$ K, radius $R_2 = 0.65R_\odot$, mass $M_2 = 0.62M_\odot$, semi-major axis of the system $A = 2.96R_\odot$, ratio of the component luminosities $L_1/L_2 = 4400$, and orbital inclination $i = 37\overset{\circ}{.}7$ for the calculations of the temperature structure of the red dwarf. Note that these parameters for the secondary are essentially extreme values, since increasing its mass to $M_2 \approx 0.80M_\odot$ would increase the radius sufficiently to overfill its Roche lobe, while decreasing the mass would increase the inclination angle, leading to eclipses in the system. We used the spectrum of a star with temperature $T_{\text{eff}} = 28\,000$ K and surface gravity $\log g = 4.00$ to specify the external illumination.

The resulting distributions of the electron temperature T_e with optical depth in the illuminated atmosphere of the red dwarf led to the following conclusions.

(1) Some layers in the atmosphere at the depth of formation of the continuum $-2.0 < \log\tau_r < 1.0$ are substantially heated. This is due to the relatively low temperature of the primary, which radiates largely in the interval 900 Å $\leq \lambda \leq$ 3000 Å. At low temperatures, the main source of absorption at these wavelengths is easily ionized atoms of metals. Therefore, when the temperature increases to $T_e = 7000$ K, the atmosphere becomes transparent at the frequencies of the external radiation, so that the incident flux penetrates to deep layers and heats them. As a result, the temperature increases to $T_e = 18\,000$ K at the depth of formation of the continuum at the center of the hot spot, making its contribution to the total luminosity of the system appreciable.

To determine this contribution, we used the procedure for calculating the spectrum of a close binary system including the reflection effect which was

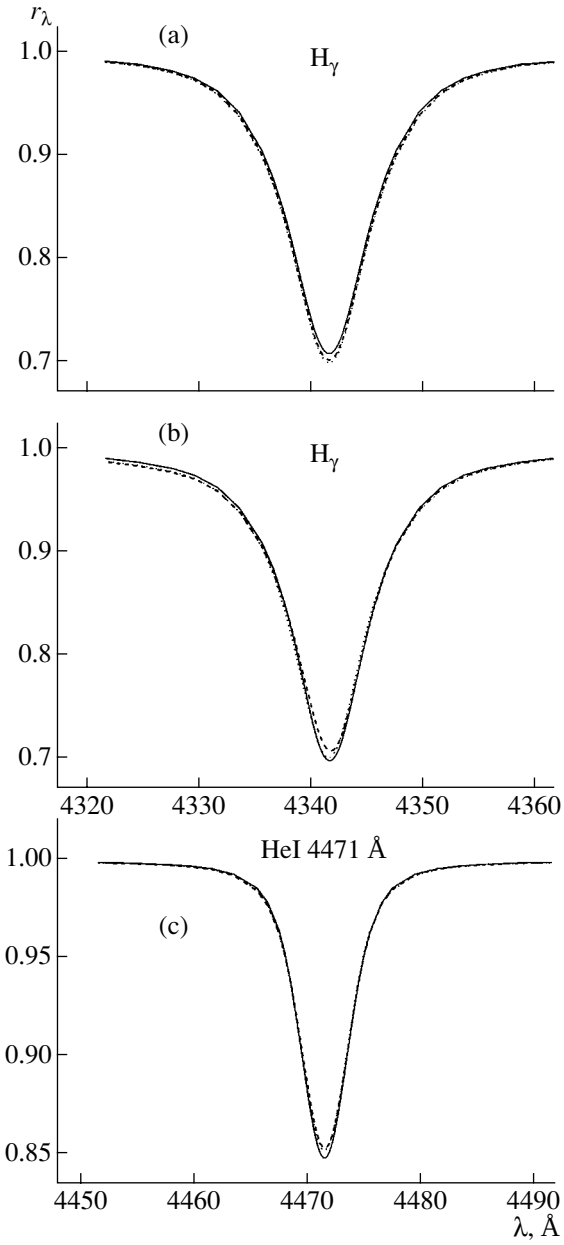

Fig. 3. Theoretical profiles for the (a, b) H_γ and (c) HeI λ4471 Å lines at three phases for (a) Model I and (b, c) Model II. Phases $\varphi = 0.20, 0.42, 0.64$ are indicated by the solid, dashed, and dotted curves, respectively.

developed in [29] and implemented in the SPECTR package. When calculating the spectra of both stars, we took into account blanketing in the strongest lines and in molecular bands in accordance with the data of Nersisyan *et al*. [39]. The total spectrum was calculated by summing the spectra of primary and secondary components with radii $R_1 = 1.00R_\odot$ and $R_2 = 0.67R_\odot$ and then convolving the resulting spectrum with the sensitivity curves for the UBV bands in accordance with the data of [30].

The reflection effect results in a monotonic increase of the brightness of UX CVn from phase $\varphi = 0$ to $\varphi = 0.5$. It should increase the difference between the depths of the main and secondary minima by 0.04^m in V, which is up to 80% of the observed value. In this case, the entire brightness variation amplitude of around 0.15^m and no more than 0.02^m of the remaining differences of the depths of the minima must be modeled as the effect of ellipsoidality of the primary. Our numerical estimates obtained with the ROSHE code and the system parameters for Model II indicate that it is possible to reproduce the specified relation between the amplitude and difference in the depths of the minima. At the same time, the impact of the reflection effect on the variations of $B - V$ and $U - B$ is insignificant (smaller than $0^m.007$). Therefore, Model II likewise cannot be ruled out based on the photometric data.

(2) A weak chromosphere is formed in the atmosphere of the red dwarf, where the temperature is 15–20% than in the photospheric layers. The physical origin of the formation of the chromosphere is the same as for the chromospheres of other precataclysmic variables, and is related to the absorption of external radiation in the region of the Lyman continuum. As a result, emission lines form in the spectrum of the secondary. When added to the absorption-line profiles of the primary, these emission lines will weaken them. Figures 3b, 3c present the resulting profiles in the total spectrum of UX CVn using the H_γ and HeI λ4471 Å lines at three phases as examples. The weakening of the lines will be maximum at phases close to $\varphi = 0.5$ and minimum at phases close to $\varphi = 0$. The total amplitude of the weakening is about 0.015 of the residual intensity of the Balmer hydrogen lines and 0.007 or lower for strong HeI lines. The corresponding equivalent-width variations for the hydrogen lines reach 3–4% and do not exceed 2% for the helium lines.

In addition, the reflection effect should result in different lines yielding different radial velocities. Since the radial velocities of the primary and secondary are not equal, the emission of the hot spot will basically weaken one of the absorption-line wings, shifting the line center. This shift can clearly be seen in Fig. 3 for H_γ at phases $\varphi = 0.42$ and $\varphi = 0.64$ (note that, in Fig. 3, the spectra are displayed in the reference frame of the primary). As a result, the radial velocities determined from the Balmer lines, strong $\lambda\lambda$4026, 4471 Å triplet helium lines, and single helium lines should increase by 22 km/s, 13 km/s, and 8 km/s, respectively. Therefore, the radial velocities determined from lines of different elements provide a supplementary criterion for the presence of the reflection effect and the determination of the evolutionary status of the system.

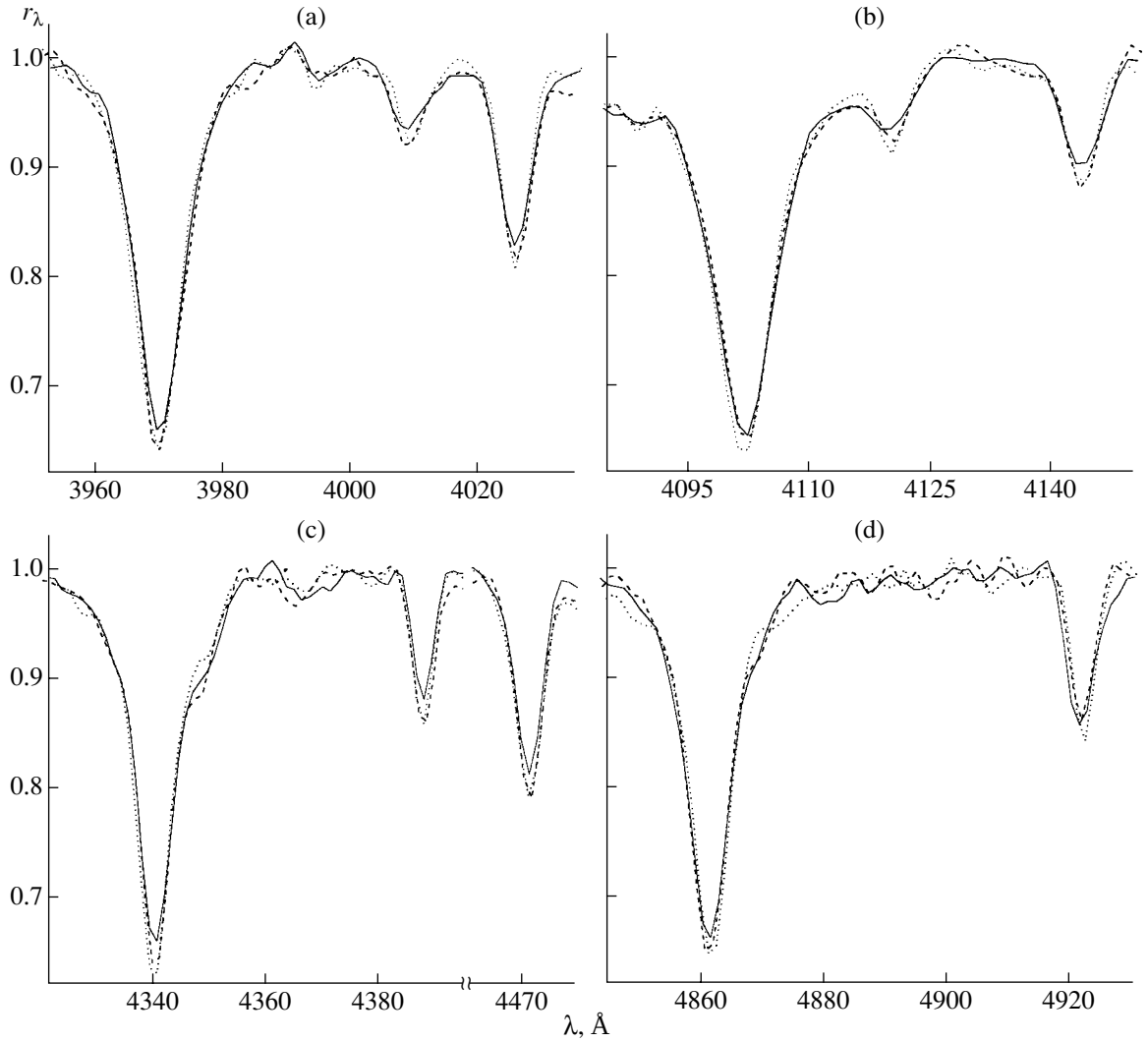

Fig. 4. Observed profiles of various lines in the spectrum of UX CVn. The notation for the curves is as in Fig. 3.

When the theoretical models of the spectra of UX CVn obtained for Models I and II are compared, it is apparent that they display opposite variations in the line profiles. In Model I, the lines of hydrogen and neutral helium are weakened at phases $\varphi = 0.25$ and $\varphi = 0.75$, whereas, for Model II, the weakening occurs around phase $\varphi = 0.5$. In both cases, the total amplitude of the variations does not exceed 0.02 for the residual intensities and 2% for the equivalent widths. Verification of these effects requires spectral data with signal-to-noise ratios ≈ 100 or higher.

Currently, two complete sets of spectroscopic observations of UX CVn at different phases have been obtained [11, 16]. In both cases, the signal-to-noise ratio for the averaged spectra at phases $\varphi = 0.25, 0.5, 0.75$ is no greater than 20–30. The error of the equivalent widths is about 10% for the HI lines and 40% for the HeI lines. Thus, existing spectroscopic data do not possess the necessary accuracy and cannot be used to distinguish between the models for UX CVn. Therefore, we concluded that we needed to conduct new spectroscopic observations adequate for all the requirements of our theoretical modeling.

3. OBSERVATIONS AND DATA PROCESSING

Our spectroscopic observations of UX CVn were carried out with the 6-m telescope of the Special Astrophysical Observatory in April 1999. The SP-124 spectrograph [40] with a PM1024 CCD (pixel size 24×24 μm) was mounted at the Nasmyth-1 focus. We used the B2 diffraction grating (1200 lines/mm), which provides a dispersion of 1.3 Å/pixel within the interval $\lambda\lambda$3920–5250 Å. The size of the stellar images was $2''$, making it possible to obtain spectra with

a two-pixel resolution of about 2.6 Å. We obtained ten individual spectrograms for UX CVn within three observing blocks from April 8–10. Table 1 presents the total distribution of the spectrograms over the blocks. For each block, we indicate the JD of the observations; the corresponding orbital phases φ and theoretical radial velocities $V_l(th)$, calculated using the ephemeris of Young *et al.* [10]; the signal-to-noise ratio for a single spectrogram s/n; the observed average radial velocities of the system $V_l(obs)$ in the blocks; and their dispersions σ.

The spectrograms were reduced using the standard procedure in the MIDAS astronomical data processing package [41]. The single white dwarf Feige 34 was used as the spectrophotometric standard for all the spectrograms [42].

The subsequent processing of the UX CVn spectra was carried out under WINDOWS using the Origin 4.0 package for numerical and graphical analysis. We added the individual spectrograms within each block to increase the signal-to-noise ratio. The resulting signal-to-noise ratios for the total spectra for the three blocks were 135, 99, and 114. This accuracy corresponds to the requirements indicated in Section 2, and we used these spectroscopic data in our subsequent analysis.

The spectra were normalized using a synthetic spectrum based on a Kurucz [24] model with $T_{\rm eff} = 29\,250$, $\log g = 4.04$, solar chemical composition, and the microturbulence velocity $\xi_{turb} = 3.0$, in accordance with the data of [20]. When calculating the spectrum, we took into account additional broadening of the lines due to the rotation of the star, which was assumed to be synchronous with the orbital period, and also due to the response function, which we approximated as a Gaussian with a half-width of 2.6 Å. The spectrum was calculated using about 500 000 lines and the data of Kurucz [24]. We chose reference intervals no narrower than 5 Å and free of any lines stronger than 10 mÅ to normalize the observed spectra. The distance between reference points did not exceed 40 Å excluding the intervals containing the Balmer lines. The normalization procedure was the same for all three spectra; Fig. 4 presents the final normalized spectra for four intervals containing the strongest lines.

The radial-velocity measurements were based on the Doppler shifts of the 15 strongest hydrogen and helium lines, with their laboratory wavelengths adopted from [43]. We averaged four to five measurements of the positions of the line centers at different intensity levels and of the centers of Gaussian or Lorentzian approximations to the lines. Table 2 presents the individual velocities obtained for various lines, as well as the mean velocities for the lines of various elements.

4. RESULTS

The data presented in Table 2 indicate that the error in the wavelengths is about 0.10–0.25 Å, which corresponds to the spectral resolution. The mean observed velocities for the first and third blocks are consistent with the theoretical estimates calculated from the ephemeris [10]. However, there is a difference for the second block of about 20 km/s. To determine possible origins of this discrepancy, we analyzed the radial-velocity curve using the results of 40 observations presented in [11] and three observations from our own study. The resulting dataset encompasses more than 30 000 orbital periods, so that the resulting accuracy in the period should be no worse than 10^{-6} day.

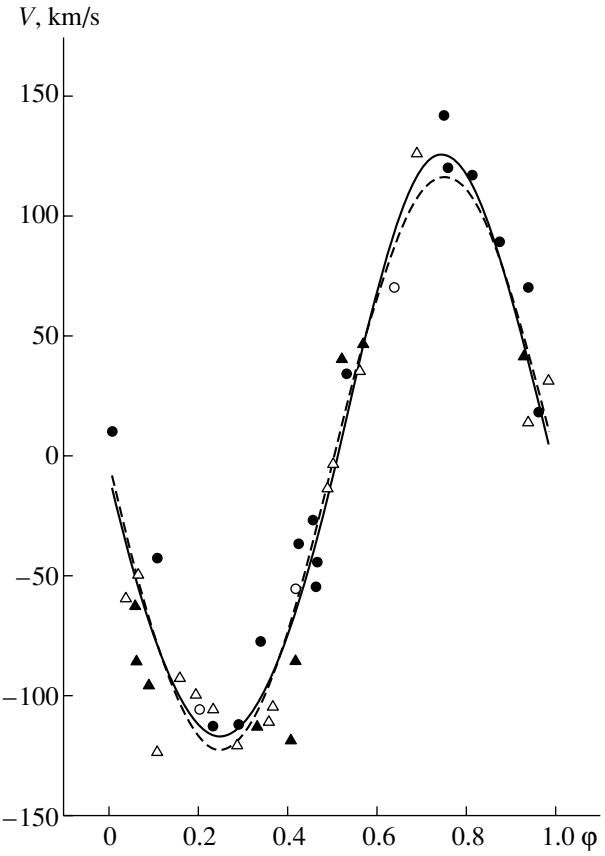

Fig. 5. Observed and theoretical radial-velocity curves for UX CVn. The hollow circles represent our data and the other symbols the data of Greenstein [23] with dispersions of 30 Å/mm (dark circles), 90 Å/mm (dark triangles), and 190 Å/mm (hollow triangles). The solid and dashed curves are the approximations for an elliptical and a circular orbit.

Table 1. Parameters of observing blocks

JD	N	s/n	φ	V_l(th), km/s	V_l(obs), km/s	σ
2451277.370	3	78	0.417	−57.5	−56.6	7.6
2451277.496	2	70	0.637	89.5	69.6	18.2
2451279.542	5	51	0.203	−109.8	−106.3	15.0

JD is the average Julian date, N the number of spectrograms inside the block, s/n the signal-to-noise ratio for a single spectrogram, φ the orbital phase, V_l(th) and V_l(obs) the theoretical and observed radial velocities for the blocks, and σ the dispersion of the velocities obtained from different lines.

We derived the orbital parameters from the radial-velocity curve using the Origin 4.0 package for mathematical and graphical data analysis. The search for the optimum parameters was conducted in a semi-automated mode using a gradient-descent method, with visual verification according to a χ^2 criterion. Calculations were carried out for both circular and elliptical orbits. Table 3 presents the orbital parameters obtained for both cases, together with those from [10], while Fig. 5 presents the observed and theoretical radial-velocity curves.È

Table 2. Radial velocities V_l for various lines in three blocks of observations

λ, Å	V_l^1, km/s	V_l^2, km/s	V_l^3, km/s
HI			
4861.33	−57.3	89.6	−101.7
4340.49	−46.0	57.7	−91.6
4101.76	−49.3	65.5	−92.5
3970.01	−56.6	56.0	−97.4
$\overline{V_l(\mathrm{HI})}$	−52.3	67.5	−95.8
σ	5.5	15.5	4.7
HeI			
4009.26	−57.6	89.0	−131.7
4026.19	−64.9	38.7	−123.0
4143.76	−51.1	81.3	−91.7
4387.93	−47.0	63.8	−101.0
4471.48	−67.5	45.5	−131.6
4921.93	−58.6	84.6	−109.6
5015.68	−66.8	94.2	−108.8
$\overline{V_l(\mathrm{HeI})}$	−59.1	71.0	−113.9
σ	7.9	22.0	15.4
HeII			
4685.63	–	69.7	−94.8

Notes: λ are the laboratory wavelengths, $\overline{V_l}$ the mean radial velocities for lines of a single element, and σ their dispersions.

Two important conclusions can be drawn on the basis of these data.

(1) The basic parameters are only weakly dependent on the adopted shape of the orbit, making it possible to derive a refined ephemeris for the system:

$$JD = 2441096.177 + 0.573704E(\pm 0.000002). \quad (8)$$

This period coincides with the result of [10] to within 10^{-6} day, which indicates that the period has been stable for the last 40 yrs. Therefore, we conclude that the effects of angular-momentum loss and mass transfer in UX CVn are extremely small, and that the components are totally detached.

(2) The use of an elliptical orbit improves the consistency with the observational data, particularly at the phases of maximum amplitude; however, the mean accuracy of the results increases only slightly. For example, the rms error remains at about 20 km/s in both cases, which corresponds to the estimated radial-velocity accuracy from [11]. In addition, the orbital eccentricity is derived mainly from observations at phases near $\varphi = 0.25$, which were made at the prime focus with a low dispersion of 190 Å/mm and have the largest errors. The radial velocities derived from these observations in the studies of Gaposhkin [44] and Greenstein [11] differ by up to $\Delta V_l = 80$ km/s. When all the data with dispersion 190 Å/mm are excluded from consideration, the eccentricity decreases by more than a factor of two, while the other orbital parameters are unchanged. At the same time, the hypothesis of an elliptical orbit gives rise to evolutionary objections, since such a large eccentricity is unlikely for a close binary system that has undergone a common-envelope stage. Therefore, we will use the solution derived for the circular orbit in our subsequent analysis. Note that most of the parameters obtained here are consistent with the data of [10] to within 10%, and the mass function is in agreement with the estimate $f(m) = 0.113$ made by Greenstein [11].

Table 3. UX CVn orbital parameters and their dispersions

Parameter	Circular orbit	Elliptical orbit	Young *et al.* [10]
P_{orb}	0.573704	0.573704	0.573703
φ_0	2441096.177	2441096.177	2441096.183
K, km/s	122.6 ± 3.5	123.0 ± 3.4	130.0 ± 3.0
γ, km/s	-3.5 ± 3.1	-8.5 ± 2.8	-1.0 ± 1.0
e		0.10 ± 0.03	0.09 ± 0.02
ω		$349° \pm 14°$	$340° \pm 12°$
$f(m)$	0.110	0.111	0.129
χ^2	406.4	378.6	

Notes: $P_{\rm orb}$ is the orbital period, φ_0 the phase of the primary minimum, K the amplitude of the radial velocity of the visual component, γ the velocity of the center of mass, e the eccentricity, ω the longitude of periastron, and $f(m)$ the mass function.

The HeI $\lambda\lambda$4026, 4471 Å triplet lines have systematically smaller radial velocities (by 10–15 km/s) compared to the average for all lines, for reasons that remain unclear. Overall, no substantial (more than 10–12 km/s) systematic differences in radial velocities are seen for the hydrogen, neutral helium, and ionized helium lines. The amplitude of the radial-velocity variations derived from the hydrogen lines is, on average, 4–8 km/s smaller than the corresponding amplitude for the helium lines. These differences do not exceed the dispersion of the velocities derived using the lines of individual elements; however, they are in unambiguous contradiction with the increase in the radial-velocity amplitudes predicted by Model II.

Thus, our radial-velocity analysis does not confirm the presence of the reflection effect, expected to be manifested as an additional line shift, as described in Section 2. The average velocities for three phases are in good agreement with both the ephemeris [10] and the results of our radial-velocity analysis. The discrepancies between the theoretical and observational data are lower than the dispersion and therefore are not significant.

A comparison of the line-intensity variations at different phases in Figs. 3 and 4 leads to the following conclusions.

(1) The line intensities at phases $\varphi = 0.42$ and $\varphi = 0.64$ are approximately the same, and the observed differences are determined by the noise level.

(2) The line intensity at phase $\varphi = 0.20$ is systematically lower than those at the other phases. The average differences in the central depths of the lines are 0.02 of the continuum level for the hydrogen lines and 0.01 for the neutral helium lines. This ratio of the line intensities at different phases is completely consistent with the theoretical calculations obtained for Model I. We have not found any signs of emission components in the profiles of strong lines of hydrogen and helium at phases $\varphi = 0.42$ and $\varphi = 0.64$ that would provide evidence for the reflection effect.

Thus, our analysis of the radial velocities at different phases and of the line-intensity ratios provides unambiguous evidence for an absence from the spectra of UX CVn of a reflection effect associated with the presence of a main-sequence secondary. Since the neutron star hypothesis has also been ruled out [16], we conclude that *UX CVn contains a low-luminosity white dwarf, and should be classified as a detached binary system with degenerate objects*.

5. CONCLUSION

Binary white dwarfs currently constitute one of the youngest and most promising classes for studies of close binary systems. Special interest in such objects is associated with the possibility that Type I supernovae can be understood in evolutionary models of binary white dwarfs [45, 46]. This idea stimulated targeted searches for such objects beginning in the middle of the 1980s, which have yielded substantial results. For example, Saffer *et al.* [47] collected data for 13 detached binary white dwarfs with periods between 0.15 and 4.8 days. As they note, only a small fraction of these systems can actually reach the supernova stage. However, determining the probability for the transformation of a specific system into a supernova proves to be extremely difficult, since the parameters of the systems remain largely unknown. The masses of both components have been estimated only for three binary white dwarfs, and the mass of the less massive star for five systems.

In this situation, the status of UX CVn as a binary white dwarf progenitor gives rise to a number of independent promising areas of investigation: determining all or most of the system's parameters, studying the chemical composition of the primary, searching for an increase of the orbital period due to deceleration of the stars under the action of tidal forces. The answers to each of these questions will provide useful information for a wide range of problems in

stellar physics, such as the physics of close binary systems with common envelopes, nuclear synthesis at late stages of evolution, and the theory of the internal structure of stars. Possibilities and prospects for further studies of UX CVn are clearly very far from being exhausted.

ACKNOWLEDGMENTS

The authors are grateful to the Committee for Time Allocation for Large Telescopes, which supported our program for the study of the spectra of close binary systems. This work was partially supported by the Russian Foundation for Basic Research, project nos. 99-02-17488 and 01-02-06065. We thank I.F. Bikmayev for numerous suggestions and advice in the course of the study, E.V. Lapina for her assistance in the data processing, and R. Kurucz for providing CD disks with the tables of spectral lines and model atmospheres.

REFERENCES

1. H. Ritter, Astron. Astrophys. **169**, 139 (1986).
2. I. J. Iben and M. Livio, Publ. Astron. Soc. Pac. **105**, 1375 (1993).
3. J. Stauffer and L. Hartmann, Astrophys. J., Suppl. Ser. **61**, 531 (1986).
4. A. G. Muslimov and M. J. Sarna, Mon. Not. R. Astron. Soc. **242**, 164 (1993).
5. M. Landini and B. C. Monsignori Fossi, Astron. Astrophys., Suppl. Ser. **82**, 229 (1990).
6. M. De Kool and H. Ritter, Astron. Astrophys. **267**, 397 (1993).
7. A. M. Cherepashchuk, N. A. Katysheva, T. S. Khruzina, and S. Y. Shugarov, *Highly Evolved Close Binary Stars. Catalog* (Gordon and Breach, Brussel, 1996), Part 1.
8. H. Ritter and U. Kolb, Astron. Astrophys., Suppl. Ser. **129**, 83 (1998).
9. M. L. Humason and F. Zwicky, Astrophys. J. **105**, 85 (1947).
10. A. Young, B. Nelson, and R. Mielbrecht, Astrophys. J. **174**, 27 (1972).
11. J. L. Greenstein, Astron. Astrophys. **23**, 1 (1973).
12. D. Schonberner, Astron. Astrophys. **70**, 451 (1978).
13. T. R. Rood, Astrophys. J. **177**, 681 (1972).
14. V. Trimble, Astron. Astrophys. **23**, 281 (1973).
15. V. Trimble and B. Paczynski, Astron. Astrophys. **22**, 9 (1973).
16. A. Young and S. T. Wentworth, Publ. Astron. Soc. Pac. **94**, 815 (1982).
17. I. J. Iben and A. Tutukov, Astrophys. J. **418**, 343 (1993).
18. J. V. Bixler, S. Bowyer, and M. Laget, Astron. Astrophys. **250**, 370 (1991).
19. N. C. Hambly, W. R. J. Rolleston, F. P. Keenan, *et al.*, Astrophys. J., Suppl. Ser. **111**, 419 (1997).
20. R. A. Saffer, F. P. Keenan, N. C. Hambly, *et al.*, Astrophys. J. **491**, 172 (1997).
21. C. Koen, J. A. Orosz, and R. A. Wade, Mon. Not. R. Astron. Soc. **300**, 695 (1998).
22. I. D. Howarth and B. Wilson, Mon. Not. R. Astron. Soc. **202**, 347 (1983).
23. Z. Kopal, *Close Binary System* (Chapman and Hall, London, 1959).
24. R. L. Kurucz, SAO CD-ROMs (Cambridge, 1994).
25. V. F. Suleĭmanov, Pis'ma Astron. Zh. **22**, 107 (1996) [Astron. Lett. **22**, 92 (1996)].
26. N. A. Sakhibullin and V. V. Shimansky, Astron. Zh. **73**, 73 (1996) [Astron. Rep. **40**, 62 (1996)].
27. R. L. Kurucz, SAO Spec. Rep. **309**, 1 (1970).
28. V. F. Suleĭmanov, Astron. Astrophys. Trans. **2**, 197 (1992).
29. N. A. Sakhibullin and V. V. Shimansky, Astron. Zh. **74**, 432 (1997) [Astron. Rep. **41**, 378 (1997)].
30. V. Straizys, *Multicolor Stellar Photometry* (Mokslas, Vil'nyus, 1977; Pachart Publ. House, Tucson, 1992).
31. H. R. Griem, Astrophys. J. **132**, 883 (1960).
32. M. J. Seaton, C. J. Zeippen, J. A. Tully, *et al.*, Rev. Mex. Astron. Astrofis. **23**, 19 (1992).
33. A. A. Radtsig and B. M. Smirnov, *Reference Data on Atoms, Molecules, and Ions* (Énergoatomizdat, Moscow, 1986; Springer-Verlag, Berlin, 1985).
34. A. J. Barnard, J. Cooper, and L. J. Shamey, Astron. Astrophys. **1**, 28 (1969).
35. D. Mihalas, A. J. Barnard, J. Cooper, and E. W. Smith, Astrophys. J. **190**, 315 (1974).
36. N. A. Sakhibullin and V. V. Shimansky, Astron. Zh. **73**, 793 (1996) [Astron. Rep. **40**, 723 (1996)].
37. D. V. Ivanova, N. A. Sakhibullin, V. V. Shimansky, Astron. Zh. **79**, 433 (2002) [Astron. Rep. **46**, 390 (2002)].
38. L. Girardi, A. Bressan, G. Bertelli, and C. Chiosi, Astron. Astrophys., Suppl. Ser. **141**, 371 (2000).
39. S. E. Nersisyan, A. V. Shavrina, and A. A. Yaremchuk, Astrofizika **30**, 247 (1989).
40. V. L. Afanas'ev, V. A. Lipovetskiĭ, V. P. Mikhaĭlov, *et al.*, Astrofiz. Issled. SAO RAN **31**, 128 (1991).
41. P. Ballester, in *Data Analysis Workshop — 4th ESO/ST-ECF Garching, 1992,* p. 177.
42. P. Massey, K. Trobel, and E. Anderson, Astrophys. J. **328**, 315 (1988).
43. A. R. Striganov and N. S. Sventitskii, *Tables of Spectral Lines of Neutral and Ionized Atoms* (Atomizdat, Moscow, 1966; Plenum, New York, 1968).
44. S. Gaposchkin, Astrophys. J. **67**, 360 (1962).
45. I. J. Iben and A. Tutukov, Astrophys. J., Suppl. Ser. **54**, 335 (1984).
46. R. Mochkovitch and M. Livio, Astron. Astrophys. **236**, 378 (1990).
47. R. A. Saffer, M. Livio, and L. R. Yungelson, Astrophys. J. **502**, 394 (1998).

Translated by K. Maslennikov

Astronomy Reports, Vol. 46, No. 8, 2002, pp. 667–683. Translated from Astronomicheskiĭ Zhurnal, Vol. 79, No. 8, 2002, pp. 738–754.

A Model for the Population of Binary Stars in the Galaxy

A. V. Tutukov and L. R. Yungelson

Institute of Astronomy, Russian Academy of Sciences, ul. Pyatnitskaya 48, Moscow, 119017 Russia

Received October 20, 2001; in final form, February 1, 2002

Abstract—A comparative investigation of the population of Galactic binary stars is performed for two modes of star formation: star formation at a constant rate over 10^{10} yrs, and a burst of star formation that reprocesses the same mass of gas into stars over 10^9 yrs. Estimates are presented for the star-formation rates and populations of about 100 types of binaries and the products of their evolution. For most close binary systems, the models depend only weakly on the common-envelope parameter α_{ce}.

1. INTRODUCTION

The objective of binary population synthesis of the Galaxy is to model the complete ensemble of binaries in a stellar system or the individual components in an ensemble. Population synthesis represents a powerful tool for developing the theory of stellar evolution via comparisons with observations and the identification of "missing links" in theoretical evolutionary sequences. Population synthesis was first applied in studies of evolutionary scenarios for high-mass close binary systems [1, 2], and was subsequently developed in numerical models for populations of pulsars [3], objects with magnetic fields in low- and moderate-mass close binaries [4], and the progenitors of cataclysmic variables [5, 6]. Its principles are described in [7–10].

Here, we study the dependence of a model for the population of binaries in the Galaxy on the star-formation history and the common-envelope parameter.

2. FORMULATION OF THE PROBLEM

Several scenarios exist for star formation in galaxies. Stars could be formed at an essentially constant rate over the entire lifetime of galaxies, or, in contrast, they could originate during relatively short bursts of star formation; a combination of an initial burst with ongoing star formation is also possible [11]. We have calculated two models for the population of binaries with ages of 10^{10} yrs. In the first, the star formation occurs at a constant rate over 10^{10} yrs, while, in the second, the same amount of matter has been reprocessed into stars during the first 10^9 yrs of the lifetime of the Galaxy.

To construct a numerical model of the population of close binary systems, we must adopt some interpretation for the "common envelope." A common envelope encompassing both components of the system is formed when a star undergoing accretion is unable to capture the infalling matter without a substantial increase in its radius. The motion of the components within the common envelope leads to its disruption. In the absence of a theory for such common envelopes, we must describe the variation of the distance between the components based on a comparison of the orbital energy of the binary and the binding energy of the donor star [12–16]. Calculations with various α_{ce} are needed to estimate errors introduced by uncertainty concerning the common-envelope parameter α_{ce}, which describes the efficiency of consumption of the system's orbital energy as the donor star is disrupted.

Basic assumptions. Binary components spend a large fraction of their lives as main-sequence (MS) stars and also as compact objects—white dwarfs (WD), neutron stars (NS), and black holes (BH). The most important evolutionary channels of close binaries from the main sequence to the final stages of evolution have been considered in our studies of the populations of white dwarfs [17–21], the cores of planetary nebulae [22], symbiotic stars [23], neutron stars and black holes [18, 24, 25], X-ray sources [26–28], cataclysmic variables [29, 30], R CrB stars [31], Wolf–Rayet stars [32], and supernovae [33–35]. These papers describe the basic assumptions used in our population synthesis code. Below, we briefly summarize those relevant to the present study.

Stars with initial masses exceeding $11.4\,M_\odot$ transform into helium stars via mass transfer. Stars with masses exceeding $40\,M_\odot$ complete their evolution as black holes with masses of $10\,M_\odot$. Objects with masses from $11.4\,M_\odot$ to $40\,M_\odot$ become neutron

1063-7729/02/4608-0667$22.00

stars with masses of 1.4 $M_\odot$. In case B of mass transfer, stars with masses from 2.5 to 9 $M_\odot$ first become helium stars and then become carbon–oxygen (CO) white dwarfs. After the helium-star stage, stars with masses from 9 to 11.4 $M_\odot$ give rise to oxygen–neon (ONe) dwarfs. Case C of mass transfer results in the formation of CO dwarfs for stars with masses from 0.8 to 9 $M_\odot$ and in the formation of ONe dwarfs for stars with masses from 9 to 11.4 $M_\odot$. Degenerate helium white dwarfs are formed from stars with masses not exceeding 2.5 $M_\odot$, in cases A and B of mass transfer. The masses of non-degenerate helium stars have a lower limit of 0.32 $M_\odot$. The masses of CO dwarfs are 0.32–1.19 $M_\odot$, of ONe-dwarfs are 1.19–1.38 $M_\odot$, and of helium dwarfs are 0.13–0.46 $M_\odot$.

We estimated the lifetime of MS stars using a formula approximating the results of evolutionary calculations [1, 36, 37]. Stars with masses $\gtrsim$0.86 $M_\odot$ evolve off the MS in 10^{10} yrs. The lifetimes of helium remnants were estimated in accordance with the results of [37, 38].

Based on studies of eclipsing, spectroscopic, and visual binaries [39–43], we took the star-formation function for binaries to have the form

$$\frac{dN}{dt} = 0.2d(\log a)\frac{dM_1}{M_1^{2.5}}f(q)dq, \qquad (1)$$

where M_1 is the mass of the initially more massive component of the system, and $f(q)$ is the distribution of the component mass ratio $q = M_2/M_1$ normalized to unity

$$f(q) = \begin{cases} 1 & \text{for close binaries} \\ 0.1055q^{-2.5} & \text{for wide binaries with } 1 \geq q \geq 0.3 \\ 2.14 & \text{for wide binaries with } 0.3 \geq q > 0. \end{cases} \qquad (2)$$

The function (1) is normalized to the formation of one binary system with $M_1 \geq 0.8\,M_\odot$ per year. We assume that all stars in the Galaxy are formed as binaries. The semimajor orbital axes of the binaries are in the range $6(M_1/M_\odot)^{1/3} \lesssim a/R_\odot \lesssim 10^6$ [39, 42]. Single stars originate due to the coalescence of close-binary components, or as a result of the disruption of systems in supernovae explosions. Assuming that the minimum mass of the binary components is 0.1 $M_\odot$ and taking into account (1) and (2), we find that the star-formation rate in our model is $\sim 8\,M_\odot$ per year. This is consistent with observational estimates for the current star-formation rate in the Galactic disk [44, 45]. Assuming that the age of the disk is 10^{10} yrs and the star-formation rate is constant, we find that the total mass reprocessed in stars should be of the order of $10^{11}\,M_\odot$, which is comparable to the mass of the Galactic disk [46].

The possibility of steady-state mass transfer in a binary system depends on the component mass ratio [47]. If the donor star has a radiative envelope, mass transfer on the nuclear timescale for the donor star is possible when $q = M_a/M_d \gtrsim 0.8$. When $0.5 \lesssim q \lesssim 0.8$, mass transfer occurs on the thermal timescale of the donor star. If the donor star is degenerate or possesses a deep convective envelope, it expands in the course of the mass loss, and stable mass transfer is possible only when $q \gtrsim 0.67$ [48]. Common envelopes develop when steady-state mass transfer is not possible.

In the case of Roche-lobe filling by a star with a non-degenerate helium core, we determined the mass of the remnant—helium star—in accordance with a formula approximating the calculation results of [37, 38]: $M_f/M_\odot = 0.066(M_i/M_\odot)^{1.54}$. If the Roche lobe is filled with a star with a degenerate helium core ($M \leq 2.5\,M_\odot$), we determined the mass of the stellar remnant after the mass transfer (the helium white dwarf) from the relation between the radius of the star and the core mass $M_{\rm He}$ [49] $R/R_\odot = 10^{3.5}(M_{\rm He}/M_\odot)^4$.

In our model, stars with masses of $\geq 50\,M_\odot$ lose their hydrogen envelopes in the MS stage due to their stellar winds, and become helium stars without undergoing a common-envelope stage. For all stars with $M \geq 50\,M_\odot$, we adopted the ratio of the final and initial masses in accordance with [50]. Mass loss for helium remnants of stars after mass transfer was described in accordance with [51]. When determining the mass-loss rate for giants formed as a result of coalescence, we assumed that the momentum of the wind is equal to that of the giant's radiation.

In the calculations of the evolution of binary systems, our program takes into account three mechanisms for the loss of orbital angular momentum by the binaries. The stellar wind carries away momentum equal to the specific momentum of the mass-losing component. Systems with MS stars with $0.3 \leq M/M_\odot \leq 1$ lose momentum due to their magnetic stellar wind [52]. For the closest systems, gravitational radiation is taken into account in accordance with [53].

3. BASIC RESULTS

We consider three models for binary populations:

Model A: Continuous star formation over 10^{10} yrs with a constant rate specified by (1). The common-envelope parameter is $\alpha_{ce} = 1$.

Model B: The star formation is as in the model **A**, but with $\alpha_{ce} = 0.5$.

Model C: The star formation occurs during the first 10^9 yrs of the Galaxy's existence, at a constant rate exceeding (1) by a factor of 10, with $\alpha_{ce} = 1$.

Models **A** and **B** can be considered as approximations for the Galactic disk, while model **C** is more appropriate for the Galactic halo or an elliptical galaxy.

The maximum radii of stars are $\sim 1000\,R_\odot$. Therefore, it follows from (1) that close systems constitute $\sim$40% of binaries with $M_1 \geq 0.8\,M_\odot$. Table 1 presents the rate of formation and numbers of close binary systems with various combinations of components in model "galaxies" for $T = 10^{10}$ yrs.

In models **A** and **B**, 40% of all close binaries formed over 10^{10} yrs with $M_1 \geq 0.8\,M_\odot$ are located on the main sequence. In model **C**, MS stars do not form at $T = 10^{10}$ yrs, but the main sequence still contains close binaries with $M_1 \lesssim 0.86\,M_\odot$. Figure 1a presents the total number of MS stars as a function of time in models **A** and **C**. In a substantial fraction of close binaries, the components coalesce, forming single stars. Such coalescence is basically due to the loss of angular momentum in the common envelopes. Coalescence of components due to momentum loss via magnetic solar wind and gravitational radiation, as well as the disruption of systems in supernova explosions, also contributes to some extent.

Let us consider some products of close-binary evolution in order of descending mass.

3.1. Black Holes

Single black holes can be formed in the final stages of several close-binary evolutionary paths, listed in Table 2. The rate of formation of black holes with MS companions is somewhat lower in model **B** than in model **A** due to the higher rate of coalescence in common envelopes. It is evident that, at the present epoch in model **C**, black holes are formed only due to the coalescence of close-binary components.

If the mass of a BH companion exceeds $\sim 10\,M_\odot$, the system may be a high-mass X-ray source. We specified the lifetime of an X-ray source in accordance with [54]. The rate of formation of X-ray sources does not depend significantly on α_{ce}, since only some fraction of their predecessors (with masses $40 \leq M_1/M_\odot \leq 50$) undergoes a common-envelope stage. In model **C**, the "X-ray epoch" coincides with the epoch of star formation.

The number of binary black holes and black holes with NS companions does not appreciably depend on the star-formation model adopted (Fig. 1b). We estimated only an upper limit for the number of systems with neutron stars, since we did not take into account the additional "kick" velocity that these stars can acquire during their formation [55], which can lead to the disruption of binaries with neutron stars. The formation of black holes is probably not accompanied by a considerable kick [56]. The number of binary black holes and black holes paired with neutron stars and the distribution of their orbital periods are of considerable interest, since coalescences of components in such systems will quite possibly be the first events to be detected by space-born gravitational-wave detectors [25, 57–59].

Non-degenerate helium stars can also be companions of black holes. For a short time, such systems can be observed as X-ray sources, if they produce sufficiently intense stellar winds. Cyg X-3 may provide an example of such stars [60].

Most helium stars that are companions of black holes have $M \lesssim 2.5\,M_\odot$ and finish their evolution as white dwarfs. After the common-envelope stage, some systems are so close that the companions of the black holes fill their Roche lobes even before the helium in their cores is burned out. This occurs due to momentum loss via gravitational-wave radiation. Such systems (BH+sdHe$\star$ in Table 1) evolve like cataclysmic variables with helium donors. In our models, the lifetime of such systems is limited to 10^9 yrs [29]. No such objects have been detected.

Relatively few black holes have WD companions. In a substantial fraction of these systems, the components coalesce due to momentum loss via gravitational-wave radiation (for this reason, their number in model **C** is lower than in **A**). The decrease of α_{ce} results in a decrease in the rate of formation of systems with white dwarfs, due to the higher frequency of coalescences.

3.2. Neutron Stars

The total current rate of formation of single neutron stars during the evolution of close binaries in models **A** and **B** depends only weakly on α_{ce}; however, α_{ce} affects the relationships between scenarios for their formation (Table 3). The main channels for their formation are the coalescence of binary components, with the formation of stars sufficiently massive for the formation of neutron stars, and the disruption of close binaries in supernovae explosions. Around 95% of disruptions occur in supernova explosions of the

Table 1. Current rate of formation of close binaries and the products of their evolution ν (yr^{-1}) and their number N in various models

Type of star or event	Model					
	A		**B**		**C**	
	ν	N	ν	N	ν	N
Main-sequence stars						
MS+MS	4.0×10^{-1}	1.6×10^{9}	4.0×10^{-1}	1.6×10^{9}	–	5.8×10^{8}
MS	7.4×10^{-2}	6.7×10^{7}	1.2×10^{-1}	1.7×10^{8}	1.9×10^{-2}	7.2×10^{7}
Systems with black holes						
BH	4.0×10^{-4}	3.3×10^{6}	4.1×10^{-4}	3.5×10^{6}	6.9×10^{-5}	4.0×10^{6}
BH+MS	6.6×10^{-2}	5.6×10^{4}	6.4×10^{-4}	4.2×10^{4}	–	2.8×10^{4}
BH+MS (XRS)	4.3×10^{-4}	5.7	4.3×10^{-4}	6.0	–	–
BH+BH	2.4×10^{-4}	2.3×10^{6}	2.4×10^{-4}	2.1×10^{6}	–	2.3×10^{6}
BH+NS	3.1×10^{-4}	3.0×10^{6}	3.0×10^{-4}	2.7×10^{6}	–	2.9×10^{6}
BH+He$\star$	5.6×10^{-4}	2.0×10^{3}	5.5×10^{-4}	1.1×10^{3}	–	–
BH+ONe wd	2.6×10^{-5}	1.6×10^{5}	1.9×10^{-5}	5.7×10^{4}	–	1.4×10^{5}
BH+CO wd	6.6×10^{-5}	5.0×10^{5}	5.2×10^{-5}	3.2×10^{5}	2.5×10^{-6}	4.8×10^{5}
BH+He wd	6.5×10^{-6}	4.9×10^{4}	5.0×10^{-6}	3.7×10^{4}	1.8×10^{-6}	5.4×10^{4}
BH+sdHe$\star$	3.4×10^{-6}	3.4×10^{3}	1.1×10^{-5}	1.1×10^{4}	–	–
Systems with neutron stars						
NS	9.9×10^{-3}	9.6×10^{7}	1.1×10^{-2}	1.0×10^{8}	1.6×10^{-4}	9.8×10^{7}
NS+MS	3.4×10^{-3}	2.7×10^{5}	2.9×10^{-3}	1.2×10^{5}	–	3.5×10^{4}
NS+MS (XRS)	2.1×10^{-3}	3.2×10^{1}	2.0×10^{-3}	3.5×10^{1}	–	–
NS+He$\star$	2.8×10^{-3}	3.5×10^{4}	1.8×10^{-3}	8.1×10^{3}	–	–
NS+sdHe$\star$	1.8×10^{-4}	6.4×10^{5}	1.5×10^{-4}	6.2×10^{5}	–	–
NS+BH	1.2×10^{-4}	8.9×10^{5}	9.9×10^{-5}	6.4×10^{5}	–	8.1×10^{5}
NS+NS	3.2×10^{-4}	2.1×10^{6}	9.9×10^{-5}	2.4×10^{5}	–	1.8×10^{6}
NS+ONe wd	2.3×10^{-4}	2.3×10^{5}	1.4×10^{-5}	4.3×10^{3}	–	1.2×10^{5}
NS+CO wd	6.6×10^{-4}	2.0×10^{6}	1.4×10^{-4}	3.7×10^{4}	–	1.2×10^{6}
NS+He wd	9.8×10^{-5}	2.7×10^{5}	9.8×10^{-5}	5.9×10^{3}	3.6×10^{-6}	2.5×10^{5}
ONe wd+NS	9.0×10^{-5}	3.0×10^{5}	7.5×10^{-6}	7.8×10^{3}	–	1.7×10^{5}
CO wd+NS	3.2×10^{-4}	2.1×10^{6}	1.3×10^{-4}	5.6×10^{5}	–	1.7×10^{6}
Systems with white dwarfs						
ONe wd	1.7×10^{-3}	1.4×10^{7}	1.7×10^{-3}	1.3×10^{7}	7.1×10^{-4}	1.8×10^{7}
ONe wd+MS	1.7×10^{-3}	5.8×10^{5}	1.2×10^{-3}	2.7×10^{5}	–	2.0×10^{5}
ONe wd+ONe wd	3.5×10^{-5}	4.9×10^{3}	–	–	–	–
ONe wd+CO wd	3.7×10^{-4}	6.5×10^{5}	3.7×10^{-5}	2.8×10^{3}	–	–
ONe wd+He wd	1.5×10^{-4}	1.6×10^{5}	8.3×10^{-5}	1.8×10^{3}	8.8×10^{-6}	1.3×10^{5}
ONe wd+He$\star$	1.1×10^{-3}	2.5×10^{4}	3.6×10^{-4}	2.1×10^{3}	–	–
ONe wd+sdHe$\star$	3.5×10^{-4}	1.3×10^{5}	1.9×10^{-4}	8.9×10^{4}	–	–
CO wd	1.4×10^{-1}	8.8×10^{8}	1.8×10^{-1}	1.2×10^{9}	5.7×10^{-2}	1.3×10^{9}
CO wd+MS	9.3×10^{-2}	3.2×10^{8}	8.7×10^{-2}	2.9×10^{8}	9.3×10^{-2}	3.2×10^{8}
CO wd+ONe wd	2.8×10^{-4}	9.9×10^{5}	5.6×10^{-5}	4.0×10^{5}	–	8.4×10^{5}
CO wd+CO wd	7.8×10^{-3}	4.9×10^{7}	2.8×10^{-3}	8.5×10^{6}	–	4.4×10^{7}
CO wd+He wd	3.6×10^{-2}	1.5×10^{8}	3.3×10^{-2}	8.5×10^{7}	1.3×10^{-2}	2.3×10^{8}
CO wd+He$\star$	1.3×10^{-2}	6.3×10^{5}	7.0×10^{-3}	7.3×10^{4}	–	–
CO wd+sdHe$\star$	9.1×10^{-3}	4.6×10^{6}	5.8×10^{-3}	2.9×10^{6}	–	–

Table 1. (Contd.)

Type of star or event	Model					
	A		**B**		**C**	
	ν	N	ν	N	ν	N
He wd	3.0×10^{-3}	8.8×10^{6}	5.3×10^{-3}	5.4×10^{6}	4.5×10^{-3}	2.2×10^{7}
He wd+MS	1.6×10^{-1}	4.4×10^{8}	1.4×10^{-1}	3.3×10^{8}	1.1×10^{-1}	7.4×10^{8}
He wd+CO wd	5.0×10^{-3}	4.0×10^{7}	5.0×10^{-3}	1.9×10^{7}	–	4.7×10^{7}
He wd+He wd	3.7×10^{-2}	8.2×10^{7}	2.7×10^{-2}	2.6×10^{7}	2.8×10^{-2}	1.7×10^{8}
He wd+He $\star$	1.5×10^{-3}	9.9×10^{3}	–	–	–	–
Systems with helium stars						
He $\star$	2.1×10^{-2}	3.7×10^{6}	2.0×10^{-2}	2.5×10^{6}	8.8×10^{-3}	1.5×10^{6}
He $\star$+MS	1.5×10^{-2}	3.8×10^{5}	1.0×10^{-2}	1.9×10^{5}	–	–
He $\star$+He $\star$	1.0×10^{-3}	9.9×10^{3}	4.6×10^{-4}	1.8×10^{3}	–	–
He $\star$+BH	9.5×10^{-7}	1.1×10^{-2}	9.5×10^{-7}	1.1×10^{-2}	–	–
He $\star$+CO wd	1.2×10^{-3}	2.9×10^{5}	7.7×10^{-4}	1.9×10^{5}	–	–
Semi-detached systems						
BH+sdMS (XRS)	5.4×10^{-7}	4.1×10^{3}	5.4×10^{-7}	4.0×10^{3}	1.1×10^{-7}	5.3×10^{3}
BH+sdSG (XRS)	6.6×10^{-6}	1.0×10^{3}	5.1×10^{-6}	9.0×10^{2}	1.8×10^{-6}	3.4×10^{2}
NS+sdMS (XRS)	8.0×10^{-6}	9.3×10^{2}	1.2×10^{-6}	1.5×10^{2}	7.9×10^{-7}	9.4×10^{1}
NS+sdSG (XRS)	4.4×10^{-6}	1.5×10^{3}	8.9×10^{-7}	1.3×10^{2}	3.2×10^{-6}	7.1×10^{2}
sdMS+MS	8.8×10^{-3}	1.6×10^{3}	7.6×10^{-3}	1.1×10^{3}	–	–
sdSG+MS	1.8×10^{-2}	3.1×10^{6}	1.6×10^{-2}	2.8×10^{6}	6.9×10^{-3}	1.6×10^{6}
ONe wd+sdMS(SXRS)	4.1×10^{-5}	2.6×10^{5}	3.7×10^{-5}	2.4×10^{5}	7.8×10^{-6}	6.3×10^{4}
CO wd+sdMS(SXRS)	2.6×10^{-3}	1.6×10^{7}	2.3×10^{-3}	1.9×10^{7}	6.3×10^{-4}	6.6×10^{6}
He wd+sdMS	2.3×10^{-3}	1.2×10^{7}	3.1×10^{-3}	1.4×10^{7}	1.8×10^{-3}	2.3×10^{7}
ONe wd+sdSG(SXRS)	3.8×10^{-6}	7.1×10^{2}	8.4×10^{-7}	1.5×10^{2}	1.8×10^{-5}	1.5×10^{3}
CO wd+sdSG(SXRS)	7.1×10^{-7}	5.2×10^{1}	7.1×10^{-7}	1.3×10^{2}	2.3×10^{-6}	1.7×10^{2}
Coalescence of components						
sdB $\star$	9.3×10^{-4}	6.9×10^{2}	3.1×10^{-3}	1.5×10^{3}	1.1×10^{-3}	5.4×10^{2}
R CrB $\star$	2.4×10^{-3}	2.1×10^{2}	6.9×10^{-3}	7.7×10^{2}	1.4×10^{-3}	1.9×10^{2}
R CrB $\star$(ONe)	5.8×10^{-4}		1.0×10^{-3}		–	–
R CrB $\star$(CO)	5.3×10^{-4}		5.0×10^{-4}		–	–
BH+R CrB $\star$	1.6×10^{-7}	3.0×10^{-4}	–	–	–	–
R CrB $\star$+MS	3.7×10^{-4}	4.3	3.4×10^{-4}	4.0		
He wd + He wd	1.9×10^{-2}		2.0×10^{-2}		8.8×10^{-3}	
CO wd + CO wd (CO $\star$)	3.4×10^{-3}	1.5×10^{2}	2.4×10^{-3}	1.1×10^{2}	1.1×10^{-3}	5.9×10^{1}
CO wd + He wd (AM CVn $\star$)	1.2×10^{-2}	8.7×10^{7}	1.5×10^{-2}	1.2×10^{8}	2.2×10^{-3}	1.2×10^{8}
Common envelopes						
HCE	0.5	4.6×10^{4}	0.4	5.7×10^{4}	0.2	3.1×10^{4}
HeCE	8.5×10^{-3}	6.9	5.3×10^{-3}	4.1		
Thorne–Żytkow Objects						
TŻ(H)	3.9×10^{-4}	2.4×10^{3}	9.7×10^{-4}	5.6×10^{3}	–	–
TŻ(He)	2.3×10^{-4}	1.5×10^{1}	4.6×10^{-4}	3.7×10^{1}	1.2×10^{-5}	1.1×10^{-1}
TŻ(CO)	9.7×10^{-4}	3.7×10^{1}	2.5×10^{-4}	9.1	9.8×10^{-5}	3.5

Table 1. (Contd.)

Type of star or event	Model					
	A		**B**		**C**	
	ν	N	ν	N	ν	N
Coalescence of relativistic objects						
BH+BH	1.2×10^{-5}		3.8×10^{-5}		8.8×10^{-6}	
BH+NS	5.8×10^{-5}		7.8×10^{-5}		1.5×10^{-5}	
NS+NS	1.5×10^{-4}		8.5×10^{-5}		3.9×10^{-5}	
Supernovae						
SNe Ia	2.1×10^{-3}		1.1×10^{-3}		4.4×10^{-4}	
SNe Ib/c	7.2×10^{-3}		5.7×10^{-3}		–	
SNe II	3.5×10^{-3}		4.9×10^{-3}		–	
Ignition of accreted He layer						
CO wd+He layer	4.6×10^{-3}		3.0×10^{-3}		–	
ONe wd+He layer	1.3×10^{-4}		8.7×10^{-5}		–	
Collapse of oxygen–neon dwarfs						
Collapse ONe wd	1.2×10^{-4}		1.3×10^{-5}		–	

Note: MS—main sequence star; BH—black hole; XRS—X-ray source; SXRS—very soft X-ray source; sd— semi-detached system; SG—subgiant (a star with a helium core and hydrogen-burning layer); He⋆—helium star; ONe, CO, He—oxygen–neon, carbon–oxygen, and helium white dwarfs; CO ⋆ —carbon–oxygen star; R CrB ⋆(CO)—R CrB star with detonating CO-core; R CrB⋆(ONe)—R CrB star with collapsing ONe core; HCE—systems with a hydrogen common envelope; HeCE—systems with a helium common envelope; TŻ— Thorne–Żytkow objects. Blank entries in the Table correspond to cases when some type of system does not appear in the model at $T = 10$ billion years.

secondaries, because we disregard the kicks received by nascent neutron stars.

Note that single neutron stars can be formed after the core collapse of R CrB stars. These stars can form due to the coalescence of CO or ONe white dwarfs with helium stars or helium white dwarfs [31]. In the course of its evolution, the mass of an ONe core can reach M_{Ch}, so that it will collapse with the formation of a neutron star. Since R CrB stars possess extended helium envelopes, such hypothetical supernovae should be classified as type Ib.

If the companion of a neutron star is close to filling its Roche lobe, the NS system can be observed as an X-ray source [NS+MS(XRS)]. We determined the lifetime of an object in the X-ray stage in accordance with [54]. We have studied the population of low-mass X-ray sources in detail in [26]. Like black holes, neutron stars can have helium companions. Some fraction of the least massive helium stars form semi-detached systems (NS+sdHE⋆), which could hypothetically be X-ray sources.

If the initial mass of both components is $\sim$ (30–40) $M_\odot$, it is possible that the first mass transfer is essentially conservative. As a result, the primary forms a neutron star, while the secondary accumulates a mass sufficient for the formation of a black hole. The number of such systems is somewhat lower in model **B** than in model **A**, since the component separations in these systems are smaller, and the components coalesce more frequently (Table 1).

Binary neutron stars are formed roughly a third as frequently in model **B** as in model **A**, due to the higher frequency of coalescence in the common envelopes, and have larger characteristic component separations in model **B**. Therefore, coalescences of binary neutron stars occur roughly twice as frequently in model **A** as in model **B**. Figure 1b presents the evolution of the number of close binary neutron stars in models **A** and **C**.

The ratios of the rates of formation of single and binary neutron stars in models **A** and **B** are $\sim$30 and $\sim$100, respectively, while only three certain cases of field binary neutron stars were found among $\sim$500 pulsars whose binarity was analyzed [61]. This discrepancy could have several origins: (1) disruption of a substantial number of systems as a result of the

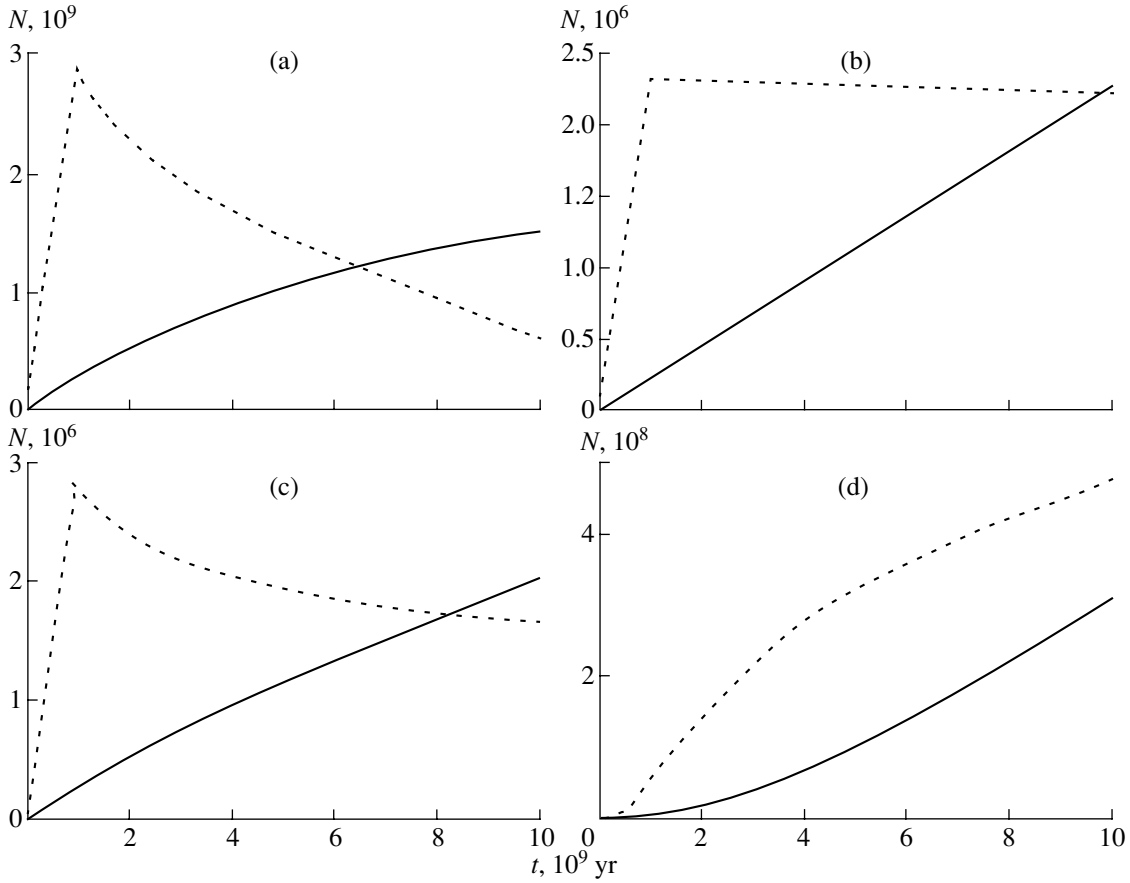

Fig. 1. Time dependence of the number (N) of some types of close binary system in models **A** (solid) and **C** (dotted) for (a) MS stars with $M_1 \geq 0.8\,M_\odot$, (b) black holes, (c) neutron stars, and (d) white dwarfs.

kick acquired by a neutron star during its birth, which we did not take into consideration [7, 58]; (2) the smearing of signals from pulsars with elliptical orbits due to the Doppler effect [62, 63]; and (3) the fact that pulsars are not always "rejuvenated" in the course of mass transfer [64].

The next family of NS companions is made up of oxygen–neon, carbon–oxygen, and helium white dwarfs. The formation of ONe and CO dwarfs—companions of old neutron star—is accompanied by the formation of common envelopes. Helium white dwarfs can be formed both via common envelopes and quasi-conservatively. This is consistent with the characteristics of millisecond pulsars, which are identified with NS+wd systems (see Table 1 in [65]): both helium and CO white dwarfs occur in short-period systems ($P_{\rm orb} \lesssim 20$ days), while only helium white dwarfs are found in long-period systems. Old neutron stars are "rejuvenated" by accretion. Observed millisecond pulsars are dominated by systems with helium companions, while they predominantly have CO companions in our model, which may indicate that the formation of systems with CO dwarfs is not accompanied by accretion sufficient to spin up old pulsars. The rate of formation of ONe dwarfs is substantially lower than that of CO dwarfs, due to the narrower mass interval for the progenitor systems. Among the known $\sim$40 rejuvenated pulsars, only PSR J1157−5112 has a companion with a mass ($\gtrsim 1.14\,M_\odot$), making it possible to conclude that it is an ONe white dwarf [66].

Another type of system in which an ONe or CO white dwarf is a companion to a neutron star is formed from systems containing a MS star with $M_{1,2} \gtrsim (6\text{–}7)\,M_\odot$, when the primary is transformed into a white dwarf and the secondary accumulates sufficient mass to form a neutron star [17]. The neutron stars in such systems are young, rather than rejuvenated, and the system orbits are elliptical. Examples of such systems include PSR B2303+46, PSR J1141−6545, and possibly PSR B1820−11 [67, 68]. Essentially all systems with a neutron star and a CO or ONe white dwarf coalesce in the course of their evolution.

3.3. White Dwarfs

Figure 1d presents the evolution of the total number of close binary white dwarfs for various star-formation models. The main channel for the formation

Table 2. Rate of formation of single black holes via different channels (yr^{-1})

Channels	Model		
	A	**B**	**C**
Disruption of binaries	1.3×10^{-4}	1.3×10^{-4}	0.0
Coalescence of black holes	1.2×10^{-5}	3.8×10^{-5}	8.8×10^{-6}
Coalescence of neutron stars and black holes	5.8×10^{-5}	$7.8 \times 10^{-}5$	1.5×10^{-5}
Coalescence of neutron stars	1.5×10^{-4}	8.5×10^{-5}	3.9×10^{-5}
Evolution of single products of the coalescence	1.1×10^{-5}	2.0×10^{-5}	0.0
Coalescence of black holes with white dwarfs	2.9×10^{-5}	5.9×10^{-5}	6.3×10^{-6}

Table 3. Current rate of formation of single neutron stars in close binaries via the main channels (yr^{-1})

Channels	Model		
	A	**B**	**C**
Disruption of binaries	3.1×10^{-3}	2.4×10^{-4}	0.0
Evolution of the single products of coalescence	3.5×10^{-3}	5.4×10^{-3}	0.0
Coalescence of white dwarfs	9.0×10^{-4}	1.3×10^{-4}	3.7×10^{-5}
Core collapse of R CrB stars	5.3×10^{-4}	5.0×10^{-4}	0.0
Coalescence of neutron stars with white dwarfs	1.2×10^{-3}	7.5×10^{-4}	1.2×10^{-4}
Coalescence of neutron stars with MS stars	3.9×10^{-4}	9.8×10^{-4}	0.0

of single ONe dwarfs ($\sim$70% in models **A** and **B**) is the coalescence of CO dwarfs when the total mass of the components is smaller than M_{Ch}. Our model assumes that the coalescence of CO dwarfs results in the formation of non-degenerate CO stars, whose cores then become ONe dwarfs. The lifetimes of CO stars are $\sim 10^5$ yrs [69]. The remaining $\sim$30% of single ONe dwarfs are produced by the disruption of binaries or remnants of single stars formed by coalescence (for example, R CrB stars). The rate of formation of ONe dwarfs in pairs with MS stars depends on α_{ce}. It rapidly decreases with α_{ce} due to the high rate of coalescence in common envelopes. Binary ONe dwarfs occur only in model **A**. In model **B**, their possible predecessors have coalesced due to their small α_{ce} values. In model **C**, all ONe+ONe pairs have already coalesced due to a loss of angular momentum. ONe white dwarfs can have helium stars as companions. The number of ONe wd+He$\star$ systems is small, due to the short lifetimes of helium stars. Roughly 40% of the ONe wd+He$\star$ pairs in models **A** and **B** are sufficiently close due to the loss of momentum to gravitational-wave radiation that the helium stars fill their Roche lobes before the He in their cores is depleted, and begin losing matter steadily. Such semidetached systems (along with systems with CO accretors) can be identified with AM CVn stars [29, 70].

Among C white dwarfs—products of the evolution of close binary systems—the most numerous objects are single stars. Essentially all of these form due to the coalescence of components. Carbon–oxygen white dwarfs with MS companions represent an intermediate stage in the evolution of systems with $2.5 \leq M_1/M_\odot \leq 9$. Roughly 30% of CO white dwarfs have companions with masses insufficient to leave the main sequence during the lifetime of the system. CO wd+ONe wd systems originate in the same general way as CO wd+NS pairs: the secondary of the initial system forms an ONe white dwarf due to the accumulation of mass in the course of quasi-conservative mass transfer. The number of such systems decreases with decreasing α_{ce} due to the high rate of coalescence in the second mass transfer.

Binary CO white dwarfs are formed relatively seldom: at T = 10^{10} yrs, they constitute $\sim$3.5, 0.5, and $\sim$2% of all systems with CO white dwarfs in models **A, B,** and **C**, respectively. This may be due to the increase of the rate of coalescence with decreasing α_{ce} and increasing age of the population. He white dwarfs are the most common evolved companions

of CO white dwarfs. They are the most numerous among all close binary white dwarfs and, naturally, also dominate among the observed systems [71, 72].

Roughly 10% of MS companions of CO white dwarfs are transformed into helium stars after filling their Roche lobes. Some of these systems are so close that the low-mass helium stars fill their Roche lobes due to the loss of momentum via gravitational-wave radiation. If the ignition of the accreted He layer does not result in the supernova explosion of the white dwarf [73, 74] and its subsequent destruction, such a system is transformed into an AM CVn star [29, 70].

In the initial stage of their existence ($\sim 10^4$ yrs), CO dwarfs are the cores of planetary nebulae. We consider the formation of binary planetary-nebula cores with various combinations of components in detail in [22].

In our models, single helium white dwarfs are formed if, after the coalescence of a white dwarf and MS star, the mass of the product is smaller than $0.46\,M_\odot$—the maximum mass of degenerate helium cores of stars[75]. Note that no observational evidence for single helium white dwarfs has been obtained [76].

The companions of the vast majority of helium white dwarfs are low-mass MS stars (Table 1). Naturally, helium white dwarfs dominate among degenerate companions. Fourteen of the known[1] 16 binary white dwarfs have observed components consisting of helium, judging from their masses. This relation is consistent with the model.

Like other close binary dwarfs, He white dwarfs can coalesce due to the emission of gravitational waves. Since, as a rule, the component mass ratios in these systems are close to unity [72], coalescence should result in the destruction of the less massive dwarf over the dynamical timescale [48, 77]. The "fate" of the resulting configuration—a core surrounded by a massive disk—depends on the rate of capture of the disk material by the core, which, in turn, depends on the disk viscosity. The accretion of helium by a helium white dwarf was considered in [78–80]. For $\dot{M} \sim 1 \times 10^{-8}\,M_\odot$/yr, helium is ignited at the center of the accretor when its mass reaches $\simeq 0.7\,M_\odot$, resulting in the destruction of the dwarf. According to the estimates of [70], the rate of such Supernova-scale events in the Galaxy is $\sim 10^{-6}$/yr. For larger $\dot{M}$ values, a thermal flare occurs in the layer of accreted helium, the burning propagates towards the center, and a helium star (subdwarf), and later a CO white dwarf, is formed. In model **C**, the formation of helium subdwarfs at the present epoch is possible only due to the "reservoir" of old helium white dwarfs.

[1] As of February, 2002.

Helium white dwarfs in pairs with helium stars are formed when primaries with masses lower than $\sim 2.5\,M_\odot$ undergo stable mass transfer that results in the accumulation of $M_2 \gtrsim 2.5\,M_\odot$ by the secondaries. After filling their Roche lobes, the latter become helium stars.

3.4. Helium Stars

The coalescence of helium white dwarfs can lead to the formation of single helium stars. In models **A** and **B**, $\sim 90\%$ of single helium stars are formed in coalescences with helium companions. All close binaries with primary masses exceeding $2.5\,M_\odot$ undergo a stage of helium stars with MS companions, provided they fill their Roche lobes prior to the ignition of He in the core. The loss of a close-binary component's envelope is the main mechanism for helium star formation. According to [81, 82], at least two thirds of helium subdwarfs near the Sun are binary. In our model, this fraction is somewhat lower: $\sim 25\%$. Any conclusions based on this comparison can be drawn only after the analysis of observational selection effects. The formation of binary helium stars (He$\star$+He$\star$) is possible only when the initial component masses are comparable. This is also a condition for the formation of rare systems in which the initially more massive component becomes a helium star, while its companion becomes a CO dwarf. Helium stars with black-hole companions are formed only in massive systems in which the Roche lobe is not filled.

3.5. Semi-Detached Systems

Low-mass X-ray systems. Companions of black holes with $M \sim M_\odot$ may fill their Roche lobes as a result of their nuclear evolution and the loss of momentum via magnetic stellar wind and/or gravitational-wave radiation. The condition of steady-state mass transfer is satisfied for small q values. Accretion disks can be unstable when $\dot{M}_\mathrm{a} \lesssim 10^{-9}\,M_\odot$/yr [83–85], and the systems can manifest themselves as transient, bright X-ray sources. Systems with stable disks may be undetectable due to their low X-ray luminosities. In model **C**, the mass-transfer rate in such systems is specified by the loss of momentum via gravitational radiation, and, in principle, they should all be transient. Semi-detached systems consisting of a black hole and a subgiant companion originate more often than those with MS companions, due to the larger interval of initial distances between the MS components (Table 1). On the other hand, their number is lower due to their shorter lifetimes. Some of these systems can also be manifested as soft X-ray transient sources [86].

Neutron stars can have MS companions with $M \sim M_\odot$, which fill their Roche lobes and give rise

to low-mass X-ray sources. Our calculations may overestimate both the rate of their formation (due to neglecting the kicks acquired during the births of neutron stars) and their number (due to neglecting the induced stellar wind [27, 87]).

Cataclysmic variable stars. Evolution of semi-detached systems with WD accretors and MS donor stars is specified by the loss of orbital angular momentum via the magnetic stellar wind when $P_{\rm orb} \gtrsim 3$ h [52, 88] and via gravitational-wave radiation when the period is shorter [89]. A large fraction of these systems have $P_{\rm orb} \approx 80$–160 min and $\dot{M}_{\rm a} \lesssim 10^{-10} M_\odot$/yr. Their lifetimes are probably limited only by the age of the Galactic disk. These stars form various types of cataclysmic variables. The variability of their brightness is due to instability of the nuclear burning within the layer of accreted matter or instability of the accretion disk. As a rule, most short-period cataclysmic systems can only be detected due to their unstable accretion disks. It is possible that tremendous outburst amplitude dwarf novae (TOADs) are precisely such systems [90]. A subgiant can also be a companion of a dwarf in a cataclysmic system, if the conditions for stable mass loss for a star with deep convective envelopes are fulfilled ($q \lesssim 0.67$).

In some semi-detached systems with accreting white dwarfs, the mass-transfer rate can correspond to the rate of steady-state hydrogen burning ($\sim 10^{-7}$–$10^{-6}\, M_\odot$/yr, depending on the mass of the dwarf). Such systems manifest themselves as soft X-ray sources [91]. White dwarfs that burn their residual hydrogen after novae bursts [28] can radiate at the same wavelengths. We considered a model for the population of cataclysmic variables and their relationship to X-ray sources in detail in [28].

If the conditions for stable mass transfer are satisfied in a system consisting of a CO or ONe dwarf and a helium dwarf or helium star, an AM CVn system can originate; these are short-period ($P_{\rm orb} \sim 10$ min) cataclysmic variables. All three models yield comparable total numbers of AM CVn stars, since the characteristic time for their formation is $\sim 3 \times 10^9$ yrs [29], while the time for their evolution is limited by the age of the Galactic disk. We consider the formation and characteristics of the population of AM CVn stars in detail in [29]. Due to uncertainties in the evolution of common envelopes, the conditions for stable mass transfer, the mass–radius relations for stars whose matter becomes degenerate in the course of their evolution, and the conditions for helium explosions at the surfaces of accreting dwarfs, the number of AM CVn stars in the Galaxy can only be estimated to order of magnitude: 10^8 (cf. [29, 70, 92, 93]).

3.6. Coalescence of Stars and Its Products

The basic reasons for the coalescence of close-binary components are the loss of angular momentum via gravitational-wave radiation and in the common envelopes. Let us consider the most important processes and products of coalescence. If the conditions for stable mass transfer are not satisfied in a system consisting of a CO dwarf and He dwarf, the components coalesce on the dynamical timescale. Three possible paths for their further evolution depend on the mass involved [94]: (a) the total mass of the object does not exceed $0.78\, M_\odot$, and the star remains compact; (b) the mass of the CO core reaches $0.78\, M_\odot$, due to the burning of He, and the envelope expands, with the star becoming a giant; (c) the mass of the initial CO core exceeds $0.78\, M_\odot$, and the star becomes a giant immediately after coalescence. Path (a) is followed by about 20% of coalesced dwarfs (Table 1). These stars are probably indistinguishable from single compact helium stars.

The expanded products of coalescence in which the masses of the CO or ONe cores exceed $0.78\, M_\odot$ can be identified with R CrB stars—rare, bright giants whose envelopes consist primarily of helium ([H/He] $\lesssim -4$) and are enriched in carbon. Single helium stars can also become R CrB stars, provided their masses are 0.8–$1.5\, M_\odot$. The evolution of R CrB stars is specified, on the one hand, by the increase of the core mass due to helium burning, and, on the other hand, by mass loss from the extended envelope. Some R CrB stars possess sufficiently massive cores that their masses reach M_{Ch} as a result of He burning. Oxygen–neon cores probably collapse with the formation of a neutron star and the partial ejection of the envelope. In the case of a carbon–oxygen core, the carbon detonates and the star is disrupted. Such a supernova should most likely display SNIa characteristics. The remaining R CrB stars give rise to single white dwarfs.

We assumed that, in all systems containing accreting CO dwarfs and non-degenerate helium donors, the accumulation by the dwarf of a helium envelope with mass $0.15\, M_\odot$ results in a double detonation (first He, then C), with a supernova explosion and destruction of the dwarf [74]. However, the conditions for double detonation are not well known. It is possible that there exists a limiting mass for a CO dwarf (0.6 or $0.8\, M_\odot$), below which the envelope undergoes thermal expansion with the formation of an R CrB star, rather than an explosion. At this time, the available data are insufficient to distinguish between this path for the formation for R CrB stars as opposed to, for example, a scenario in which these stars have undergone a planetary-nebula stage and then expanded due to a final burst of He burning [95].

Type Ia supernovae (SNIa). The formation of pairs of CO dwarfs is accompanied by a transition through two to four common-envelope stages. Therefore, a substantial fraction of these systems are very close and coalesce. In [96], we suggested that coalescing CO dwarfs with total masses exceeding M_{Ch} are SNIa progenitors. In our models (Table 1), the coalescence rate for fairly massive CO white dwarfs is, indeed, consistent with the SNIa rate in Sbc galaxies, similar to that in our Galaxy [97]. The attraction of this model is that only coalescence occurs sufficiently frequently to explain the observed SNIa rate in both young ($T \sim 10^8$ yrs) and old ($T \sim 10^{10}$ yrs) populations [18, 98]. However, the number of white dwarfs whose binarity has been investigated remains insufficient to detect such systems. Numerical modeling of WD coalescence (see, for example, [99]) indicates that the formation of a collapsing ONe dwarf is more likely than a SNIa explosion. Nonetheless, Table 1 contains the corresponding rates in the SNIa column. A detailed consideration of the present state of the SNIa problem can be found, for example, in [100].

Common envelopes. The vast majority of close binaries pass through a common-envelope stage. The rate of formation of common envelopes is somewhat higher than that of close binaries. In our models, the number of systems with hydrogen common envelopes ($\sim 10^4$) is based on the assumption that the duration of this stage is specified by the thermal timescale of the donor star. We assume that helium common envelopes exist over a time comparable to the dynamical timescale of the donor envelope. No systems with a common envelope have been identified; however, we expect they should be supergiants with intense stellar winds.

Thorne–Żytkow objects. Filling of the Roche lobe by a NS companion can result in the formation of (thus far hypothetical) stars with neutron cores, so called Thorne–Żytkow (TŻ) objects [101, 102]. TŻ objects should differ from ordinary (super)giants with hydrogen envelopes in the anomalous chemical compositions of their envelopes, due to very high-temperature hydrogen burning at the core boundary. We assumed that the lifetimes (and, hence, number) of TŻ objects are determined by mass loss via the stellar wind, which can be described by the empirical "universal formula" of Nugis [103]. Various aspects of the structure and evolution of TŻ objects with hydrogen–helium envelopes are considered, for example, in [104–110].

Neutron stars can also coalesce with helium stars, as well as with helium and CO white dwarfs. Such events have been considered as possible sources of γ-ray bursts [111]. It is possible that the dust disks, and even planets, observed around some radio pulsars [112] are remnants of companions disrupted by the tidal effects of the neutron star. If we assume that coalescence with He or CO white dwarfs results in the formation of objects with extended envelopes that lose mass in accordance with the formula of Nugis [103], the Galaxy may contain $\sim$10 such stars.

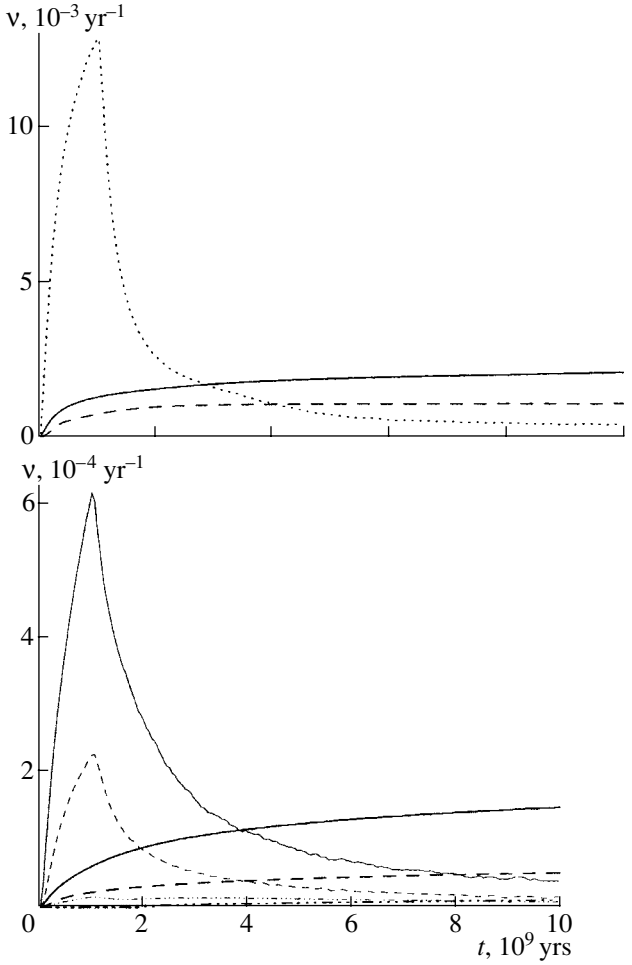

Fig. 2. Top: Time dependence of the rate of coalescence (yr^{-1}) for carbon–oxygen white dwarfs with masses exceeding M_{Ch} in models **A** (solid lines), **B** (dashed lines) and **C** (dotted lines). Bottom: Time dependence of the rate of coalescence (yr^{-1}) for binary neutron stars (solid lines), black holes (dashed lines) and black holes with neutron stars (dot–dashed lines). The thick curves represent model **A** and the thin curves model **C**.

Coalescence of relativistic objects. Black holes and neutron stars can coalesce due to momentum loss via gravitational radiation. Our estimates indicate that first-generation gravitational-wave detectors will be able to detect such events only once every $\sim$30 yrs; it is more likely that the coalescence of a binary black hole [18] will be detected first. Note that the black-hole coalescence rate in model **C** depends

only relatively weakly on time, unlike the coalescence rates for binary neutron stars and NS+BH systems (Fig. 2), since the formation of a neutron star includes numerous common-envelope stages, so that, as a rule, these systems are closer. Coalescences of neutron stars are also likely to result in bursts of γ radiation [113] and neutrino radiation, and also to enrich the interstellar medium in r-process products [114]. If the coalescence of neutron stars is accompanied by bursts of γ radiation, extrapolation of our estimates for the coalescence rate to the Metagalaxy yields a burst rate that exceeds the observed value by several orders of magnitude. This inconsistency can be resolved if the γ radiation is collimated [115].

3.7. Type II, Ib and Ic Supernovae

Type II supernovae (SNII) possess extended hydrogen envelopes. According to our assumptions, a SNII explosion can occur in a close-binary system in only two cases: due to the coalescence of MS stars in a common envelope, with the formation of a single star with mass $\gtrsim 10\,M_\odot$; or after a supernova explosion of the primary in which the pair breaks apart and the fairly massive secondary continues its evolution towards a SNII as a single object. The probability of these scenarios is low (Table 1), and SNII explode primarily in wide systems.

If the star still possesses a helium envelope by the time of the core collapse, the explosion will be observed as a SNIb. If the helium envelope has been lost, we will observe an SNIc explosion [116]. Stars with $M_0 \geq 50\,M_\odot$ lose their hydrogen envelopes via stellar winds during the MS stage [116]. Therefore, as a rule, they become helium stars without filling their Roche lobes, and always explode as SNIb/c.

3.8. Accreting Dwarfs

As discussed above, in the course of the accretion of He onto a CO white dwarf with $\dot{M} \sim 10^{-8}\,M_\odot$/yr, the detonation of helium may occur if the mass of the accumulated surface layer exceeds $\sim 0.15\,M_\odot$. The consequences of the detonation and its observational manifestations remain a subject of discussion (see [100]). It is possible that carbon detonation also occurs for certain dwarf masses and $\dot{M}$ values, observationally, such explosions may manifest themselves as SNIa [74]. The consequences of He accretion onto ONe dwarfs have not been discussed in the literature, although we expect that the detonation of He can result in the detonation of oxygen in the core of the dwarf. If He accretion results in double detonation and a SNIa explosion for any mass of a CO or ONe white dwarf, the rate of these events is sufficient to explain all SNIa in the Galaxy (Table 1).

If the mass of an ONe dwarf reaches M_{Ch} prior to detonation of the helium layer, the dwarf collapses, with the formation of a neutron star [117]. This is possible if the donor is a non-degenerate, low-mass helium star. Similar events are likely to result in SNIa bursts with anomalously low luminosities [118].

4. WIDE SYSTEMS

The components of wide binaries evolve independently, similarly to single stars. In accordance with the results of the study of visual binaries [41], we assumed that wide systems possess elliptical orbits with $e = 0.1\log(P)$, where P is the orbital period in days. The q distribution for these systems is specified by Eq. (2). Table 4 presents the main results of our calculations for wide systems.

4.1. Main-Sequence Stars

In accordance with our normalization for the star-formation function, about 60% of all currently forming binaries with $M_1 > 0.8\,M_\odot$ in model **A** are wide systems. In model **C**, star formation is already completed, but systems with $M_1 < 0.86\,M_\odot$ remain on the main sequence. In wide systems, MS stars can become single due to the disruption of binaries in supernovae explosions. In addition, we assumed that systems are disrupted when the characteristic time for the ejection of a planetary nebula by one of the components (10^4 yrs) is shorter than $P_{\rm orb}$ and the conditions for disruption are satisfied, taking into account the orbital eccentricity [119].

4.2. Black Holes

Roughly 70% of supernova explosions accompanying the formation of black holes disrupt the corresponding systems, due to the concentration of wide systems towards small q values. Wide systems that have survived the supernova explosion of the primary are virtually always disrupted if the secondary also explodes. Disruption of the system in a supernova explosion is the only path for the formation of single black holes in wide systems, while only about half of single black holes form in this way in close systems (Table 2). The secondary components in surviving systems with black holes are CO dwarfs in $\sim 90\%$ of cases. At intermediate stages, these systems exist as a black hole with an MS or (super)giant companion. Neutron stars constitute approximately 5% of black-hole companions in model **A**.

Table 4. Current rate of formation of wide binaries and products of their evolution $\nu\,(\mathrm{yr}^{-1})$ and their number N in various models

Type of star or event	Model A		Model C		Type of star or event	Model A		Model C	
	ν	N	ν	N		ν	N	ν	N
Main-sequence stars					G(He)+SG	1.8×10^{-4}	1.4×10^{4}	1.7×10^{-4}	9.1×10^{3}
MS+MS	5.9×10^{-1}	2.5×10^{9}	–	9.2×10^{8}	G(He)+G(He)	3.8×10^{-3}	1.5×10^{3}	–	
MS	2.1×10^{-2}	1.6×10^{8}	3.0×10^{-3}	1.7×10^{8}	AGB	3.8×10^{-3}	3.1×10^{3}	1.2×10^{-3}	1.2×10^{3}
Black holes					AGB+MS	4.4×10^{-1}	3.7×10^{5}	2.0×10^{-1}	2.0×10^{5}
BH	2.5×10^{-4}	2.5×10^{6}	–	2.5×10^{6}	AGB+SG	1.4×10^{-4}	1.3×10^{2}	8.5×10^{-5}	8.7×10^{1}
BH+MS	3.5×10^{-4}	3.1×10^{5}	–		AGB+G(He)	3.7×10^{-5}	2.8×10^{1}	–	
BH+BH	1.1×10^{-6}	1.1×10^{4}	–	1.1×10^{4}	Helium stars				
BH+SG	1.3×10^{-4}	5.9×10^{4}	–	9.3×10^{3}	He⋆+MS	6.4×10^{-4}	1.9×10^{2}	–	
BH+G(He)	3.4×10^{-4}	1.3×10^{4}	4.8×10^{-5}	4.8×10^{3}	He⋆	1.5×10^{-7}	3.3×10^{-2}	–	
BH+AGB	3.1×10^{-4}	1.8×10^{2}	4.8×10^{-5}	4.8×10^{1}	He⋆ + He⋆	6.5×10^{-7}	1.0×10^{-1}	–	
BH+He⋆	1.4×10^{-6}	3.4×10^{-1}	–		White dwarfs				
BH+NS	1.9×10^{-5}	1.9×10^{5}	–	1.9×10^{5}	CO wd+MS	4.1×10^{-1}	2.7×10^{9}	1.8×10^{-1}	4.0×10^{9}
BH+CO wd	3.1×10^{-4}	3.7×10^{6}	4.8×10^{-5}	3.1×10^{6}	CO wd	1.4×10^{-2}	9.9×10^{7}	4.4×10^{-3}	1.4×10^{8}
Neutron stars					CO wd+CO wd	4.7×10^{-3}	2.9×10^{7}	3.4×10^{-3}	4.8×10^{7}
NS	1.1×10^{-2}	1.1×10^{8}	–	1.1×10^{8}	CO wd+G	4.7×10^{-3}	4.4×10^{5}	3.1×10^{-3}	3.2×10^{5}
NS+MS	3.0×10^{-4}	3.2×10^{5}	–	2.8×10^{4}	CO wd+AGB	4.7×10^{-3}	4.3×10^{3}	3.4×10^{-3}	3.4×10^{3}
NS+NS	2.7×10^{-6}	2.7×10^{4}	–	2.7×10^{4}	Supernovae				
NS+SG	1.1×10^{-4}	5.6×10^{4}	4.7×10^{-5}	5.7×10^{4}	SN II	4.5×10^{-5}		–	
NS+G(He)	2.9×10^{-4}	1.0×10^{4}	2.2×10^{-5}	2.1×10^{3}	SN II+MS	1.1×10^{-2}		–	
NS+AGB	2.6×10^{-4}	1.4×10^{2}	2.0×10^{-5}	2.1×10^{1}	SN II+G(He)	2.6×10^{-6}		–	
NS+CO wd	2.6×10^{-4}	2.2×10^{6}	2.0×10^{-5}	2.6×10^{6}	SN II+NS	3.9×10^{-5}		–	
Subgiants, giants, and supergiants					SN II+BH	3.4×10^{-5}		–	
SG	3.3×10^{-3}	2.2×10^{6}	1.6×10^{-3}	3.0×10^{6}	SN Ib	1.5×10^{-7}		–	
SG+MS	4.2×10^{-1}	3.2×10^{8}	2.3×10^{-1}	4.9×10^{8}	SN Ib+MS	6.4×10^{-6}		–	
SG+SG	1.5×10^{-4}	6.2×10^{4}	1.1×10^{-4}	1.0×10^{3}	SN Ib+G(He)	7.9×10^{-8}		–	
G(He)	3.9×10^{-3}	2.9×10^{5}	1.5×10^{-3}	1.2×10^{5}	SN Ib+He⋆	6.5×10^{-7}		–	
G(He)+MS	4.7×10^{-1}	3.6×10^{7}	4.1×10^{-1}	2.1×10^{7}	SN Ib+BH	1.4×10^{-6}		–	

Note: G(He) denotes a star in the stage of core He burning, AGB denotes a star on the asymptotic giant branch, and the remaining notation is as in Table 1.

4.3. Neutron Stars

In model **A**, 90% of neutron stars are single. This is a direct consequence of the adopted q distribution for wide systems. Since the model does not take into account possible kicks during the formation of neutron stars, in our model, ∼0.01% of systems with $M_{1,2} \geq 10\,M_\odot$ are not disrupted in supernova explosions and form wide binary neutron stars. The absence of radio pulsars in wide systems may represent an argument in favor of the role of kicks that disrupt wide systems.

CO dwarfs dominate among companions of neutron stars. As in the case of black holes, the companions in intermediate stages are MS stars and (super)giants. The most interesting are systems with supergiants. Due to the accretion of material from the stellar wind, they can manifest themselves as a kind of "symbiotic star" with a neutron star in

place of a white dwarf. Single (super)giants originate from binary secondaries that have been disrupted in supernova explosions and the formation of planetary nebulae.

4.4. Helium Stars

In our model, helium stars originate from MS stars with $M \geq 50\,M_\odot$, which lose their hydrogen envelopes via their stellar winds. They should be observed as very massive Wolf–Rayet stars, and are BH progenitors. Single helium stars are former secondaries of systems that were disrupted during the formation of a black hole. About $10^{-4}\%$ of massive wide systems are capable of forming wide Wolf–Rayet binaries.

4.5. White Dwarfs

In model **A**, roughly 50% of primaries in all systems with $M_1 \geq 0.8\,M_\odot$ have completed their evolution over 10^{10} yrs with the formation of a CO dwarf. As a rule, the secondary components remain MS stars due to the concentration of companions with small q. In model **C**, the fraction of systems with white dwarfs is around two-thirds. Both components completed their evolution in $\sim 1\%$ of the systems. Due to mass loss during the ejection of planetary nebulae, several percent of all dwarfs turn out to be single. The number of systems consisting of dwarfs and evolved stars is very small due to the long lifetimes of the companions of white dwarfs.

4.6. Supernovae

Single stars and components of wide systems with $M = 10$–$50\,M_\odot$ retain their hydrogen envelopes until their SNII supernova explosions. About 70% of all SNII explode in wide systems. While it is mainly single products of coalescence that explode as SNII in close systems, as a rule, the SNII in wide systems have companions, most of them MS stars. The total rate of SNII events in model **A** is 1.48 per 100 years, which is consistent with the observational estimate [97] for the Galaxy: 1.47 ± 0.60 per 100 years.

Close binary components with $M \geq 11.4\,M_\odot$ and components of wide systems with $M > 50\,M_\odot$ complete their evolution as SNIb/c supernovae. The most massive stars explode as SNIc. SNIc spectra indicate an almost complete absence of helium (probably, due to an intense wind) and higher abundance of oxygen than in SNIb [97, 120]. A high abundance of O is characteristic of the products of He burning in the most massive stars [121]. In model **A**, the total number of SNIb/c is 0.72 per 100 years, which exceeds the observational estimate [97] of 0.24 ± 0.12 per 100 years. Since the total rate of SN(II+Ib/c) in the model does not contradict the observational data, this discrepancy may be due, for example, to overestimation of the fraction of close-binary systems, the rate of coalescence of close-binary components (underestimation of α_{ce}), or overestimation of the limit of the mass interval for stars that lose their envelopes via their stellar winds.

If SNIa explosions are due to the coalescence of white dwarfs, the model ratio of the rates of SNIa and SN(II+Ib/c) is $\sim$0.1, while the "observed" ratio for galaxies similar to the Galaxy is $\sim$0.25. This inconsistency can be removed, if, for example, during the accretion of helium onto a white dwarf, a small $\dot{M}$ also results in an SNIa (Table 1). However, such events cannot occur in old populations ($T \gtrsim 10^9$ yrs), which is consistent with the decrease of the SNIa rate for older galaxies.

5. CONCLUSION

We have considered the dependence of numerical characteristics of the population of binaries on the star-formation history and the so-called common-envelope parameter α_{ce}.

Models **A** and **B**, which have a constant rate of star formation over 10^{10} yrs, can serve as an approximation for disk galaxies, while model **C** represents an approximation for elliptical galaxies. Since essentially every spiral galaxy has a spherical component and every elliptical galaxy a disk component, our results can be used to "construct" a model for an arbitrary galaxy, provided the mass of both components is known and the star-formation function [see Eq. (1)] is universal. A comparison of the results for wide and close systems (Tables 1, 4) indicates that the existence of close binaries enriches the universe of stars in numerous objects and events that would be impossible if all stars were single objects or components of wide systems. This is primarily due to the formation of coalescing objects: close binary white dwarfs, neutron stars, and black holes. Coalescence may also generate supernovae, γ-ray bursts, neutrino radiation, and gravitational radiation.

Our calculations indicate a weak dependence of the numbers of most products of close-binary evolution on the common-envelope parameter.

Our analysis identifies problems that require particular attention: refining the star-formation function, estimating the degree of non-conservativeness of the mass and angular-momentum transfer, more accurately determining the nature of stellar remnants as a function of the initial mass and the binary parameters.

Numerical modeling of accretion in binaries and its consequences, coalescence of stars, and the evolution of coalescence products are particularly important.

ACKNOWLEDGMENTS

This work was partially supported by the State Science and Technology Project "Astronomy." The authors thank H. Heinrichs for providing us with a computer.

REFERENCES

1. A. V. Tutukov and L. R. Yungel'son, Nauchn. Inf. Astron. Sovet Akad. Nauk SSSR **27**, 70 (1973).
2. B. P. Flannery and E. P. J. van den Heuvel, Astron. Astrophys. **39**, 61 (1975).
3. R. J. Dewey and J. M. Cordes, Astrophys. J. **321**, 780 (1987).
4. V. M. Lipunov and K. A. Postnov, Astrophys. Space Sci. **145**, 1 (1988).
5. M. J. Politano, PhD Thesis (Illinois Univ., Urbana-Champaign, Savoy, 1988).
6. M. Politano and R. F. Webbink, in *IAU Colloquium 114: White Dwarfs* (Springer-Verlag, Berlin, 1989), p. 440.
7. V. M. Lipunov, K. A. Postnov, and M. E. Prokhorov, Astron. Astrophys. **310**, 489 (1996).
8. C. A. Tout, S. J. Aarseth, O. R. Pols, and P. P. Eggleton, Mon. Not. R. Astron. Soc. **291**, 732 (1997).
9. L. Yungelson and A. Tutukov, *Advances in Stellar Evolution,* Ed. by R. Rood and A. Renzini (Cambridge Univ. Press, Cambridge, 1997).
10. J. R. Hurley, C. A. Tout, and O. R. Pols, Mon. Not. R. Astron. Soc. **329**, 897 (2002).
11. A. Sandage, Astron. Astrophys. **161**, 89 (1986).
12. A. V. Tutukov and L. R. Yungelson, *Mass Loss and Evolution of O-type Stars,* Ed. by C. de Loore and P. S. Conti (Reidel, Dordrecht, 1979), p. 401.
13. R. F. Webbink, Astrophys. J. **277**, 355 (1984).
14. I. Iben, Jr. and M. Livio, Publ. Astron. Soc. Pac. **105**, 1373 (1993).
15. J. D. M. Dewi and T. M. Tauris, Astron. Astrophys. **360**, 1043 (2000).
16. T. Tauris and J. D. M. Dewi, Astron. Astrophys. **369**, 170 (2001).
17. A. V. Tutukov and L. R. Yungel'son, Astron. Zh. **69**, 526 (1992) [Sov. Astron. **36**, 266 (1992)].
18. A. V. Tutukov and L. R. Yungelson, Mon. Not. R. Astron. Soc. **268**, 871 (1994).
19. L. R. Yungelson, M. Livio, A. V. Tutukov, and R. Saffer, Astrophys. J. **420**, 336 (1994).
20. I. Iben, Jr., A. V. Tutukov, and L. R. Yungelson, Astrophys. J. **475**, 291 (1997).
21. R. A. Saffer, M. Livio, and L. R. Yungelson, Astrophys. J. **502**, 394 (1998).
22. L. R. Yungelson, A. V. Tutukov, and M. Livio, Astrophys. J. **418**, 794 (1993).
23. L. Yungelson, M. Livio, A. Tutukov, and S. J. Kenyon, Astrophys. J. **447**, 656 (1995).
24. A. V. Tutukov and L. R. Yungel'son, Astron. Zh. **70**, 812 (1993) [Astron. Rep. **37**, 411 (1993)].
25. A. V. Tutukov and L. R. Yungelson, Mon. Not. R. Astron. Soc. **260**, 675 (1993).
26. I. Iben, Jr., A. V. Tutukov, and L. R. Yungelson, Astrophys. J., Suppl. Ser. **100**, 217 (1995).
27. I. Iben, Jr., A. V. Tutukov, and L. R. Yungelson, Astrophys. J., Suppl. Ser. **100**, 233 (1995).
28. L. Yungelson, M. Livio, J. W. Truran, *et al.*, Astrophys. J. **466**, 890 (1996).
29. A. V. Tutukov and L. R. Yungelson, Mon. Not. R. Astron. Soc. **280**, 1035 (1996).
30. L. Yungelson, M. Livio, and A. Tutukov, Astrophys. J. **481**, 127 (1997).
31. I. Iben, Jr., A. V. Tutukov, and L. R. Yungelson, Astrophys. J. **456**, 750 (1996).
32. M. Vrancken, J. P. de Greve, L. Yungelson, and A. Tutukov, Astron. Astrophys. **249**, 411 (1991).
33. A. V. Tutukov, L. R. Yungelson, and I. Iben, Jr., Astrophys. J. **386**, 197 (1992).
34. L. R. Yungelson and M. Livio, Astrophys. J. **497**, 168 (1998).
35. L. R. Yungelson and M. Livio, Astrophys. J. **528**, 108 (2000).
36. J. G. Mengel, P. Demargue, A. V. Sweigart, and P. G. Gross, Astron. Astrophys., Suppl. Ser. **40**, 733 (1979).
37. I. Iben, Jr. and A. V. Tutukov, Astrophys. J., Suppl. Ser. **58**, 661 (1985).
38. A. V. Tutukov and L. R. Yungel'son, Nauchn. Inf. Astron. Soveta Akad. Nauk SSSR **27**, 3 (1973).
39. Z. T. Kraĭcheva, E. I. Popova, A. V. Tutukov, and L. R. Yungel'son, Pis'ma Astron. Zh. **7**, 488 (1981) [Sov. Astron. Lett. **7**, 269 (1981)].
40. E. I. Popova, A. V. Tutukov, and L. R. Yungelson, Astrophys. Space Sci. **88**, 55 (1982).
41. Z. T. Kraĭcheva, E. I. Popova, A. V. Tutukov, and L. R. Yungel'son, Astrofizika **22**, 105 (1985).
42. S. Vereshchagin, A. Tutukov, L. Yungelson, *et al.*, Astrophys. Space Sci. **142**, 245 (1988).
43. Z. T. Kraĭcheva, E. I. Popova, A. V. Tutukov, and L. R. Yungel'son, Astrofizika **30**, 524 (1989).
44. N. C. Rana, Annu. Rev. Astron. Astrophys. **29**, 129 (1991).
45. G. Gilmore, in *Galaxy Disks and Disk Galaxies,* Ed. by J. G. Funes and E. M. Corsini, Astron. Soc. Pac. Conf. Ser. **230**, 3 (2001).
46. W. Dehnen and J. Binney, Mon. Not. R. Astron. Soc. **294**, 429 (1998).
47. A. V. Tutukov, A. V. Fedorova, and L. R. Yungel'son, Pis'ma Astron. Zh. **8**, 365 (1982) [Sov. Astron. Lett. **8**, 198 (1982)].
48. A. V. Tutukov and L. R. Yungelson, Acta Astron. **29**, 665 (1979).
49. I. Iben, Jr. and A. V. Tutukov, Astrophys. J., Suppl. Ser. **54**, 335 (1984).
50. D. Vanbeveren, Space Sci. Rev. **56**, 249 (1991).
51. N. Langer, Astron. Astrophys. **220**, 135 (1989).
52. F. Verbunt and C. Zwaan, Astron. Astrophys. **100**, L7 (1981).

53. L. D. Landau and E. M. Lifshitz, *The Classical Theory of Fields* (Nauka, Moscow, 1973; Pergamon, Oxford, 1975).
54. A. G. Massevich, E. I. Popova, A. V. Tutukov, and L. R. Yungelson, Astrophys. Space Sci. **62**, 451 (1979).
55. I. S. Shklovskiĭ, Astron. Zh. **46**, 715 (1969) [Sov. Astron. **13**, 562 (1969)].
56. N. E. White and J. van Paradijs, Astrophys. J. **473**, L25 (1996).
57. V. M. Lipunov, K. A. Postnov, and M. E. Prokhorov, Pis'ma Astron. Zh. **23**, 563 (1997) [Astron. Lett. **23**, 492 (1997)].
58. S. F. Portegies Zwart and L. R. Yungelson, Astron. Astrophys. **332**, 173 (1998).
59. S. F. Portegies Zwart and S. L. W. McMillan, Astrophys. J. Lett. **528**, L17 (2000).
60. E. Ergma and L. R̃. Yungelson, Astron. Astrophys. **333**, 151 (1998).
61. Z. Arzoumanian, J. M. Cordes, and I. Wasserman, Astrophys. J. **520**, 696 (1999).
62. H. M. Johnston and S. R. Kulkarni, Astrophys. J. **368**, 504 (1991).
63. R. Ramachandran and S. F. Portegies Zwart, in *Abstracts of the 19th Texas Symposium on Relativistic Astrophysics and Cosmology, Paris, 1998,* Ed. by J. Paul, T. Montmerle, and E. Aubourg, p. E254.
64. K. Belczynski and V. Kalogera, Astrophys. J. Lett. **550**, L183 (2001).
65. R. E. Taam, A. R. King, and H. Ritter, Astrophys. J. **541**, 329 (2000).
66. R. T. Edwards and M. Bailes, Astrophys. J. **547**, L37 (2001).
67. S. F. Portegies Zwart and L. R. Yungelson, Mon. Not. R. Astron. Soc. **309**, 26 (1999).
68. T. M. Tauris and T. Sennels, Astron. Astrophys. **355**, 236 (2000).
69. G. Beaudet and E. E. Salpeter, Astron. J. **155**, 203 (1969).
70. G. Nelemans, S. F. Portegies Zwart, F. Verbunt, and L. R. Yungelson, Astron. Astrophys. **368**, 939 (2001).
71. L. Yungelson, G. Nelemans, S. F. Portegies Zwart, and F. Verbunt, in *The Influence of Binaries on Stellar Population Studies,* Ed. by D. Vanbeveren (Kluwer, Dordrecht, 2001), p. 349; astro-ph/0011248.
72. G. Nelemans, L. R. Yungelson, S. F. Portegies Zwart, and F. Verbunt, Astron. Astrophys. **365**, 491 (2001).
73. R. E. Taam, Astrophys. J. **242**, 749 (1980).
74. E. Livne, Astrophys. J. **354**, L53 (1990).
75. A. V. Sweigart, L. Greggio, and A. Renzini, Astrophys. J. **364**, 527 (1990).
76. T. R. Marsh, V. S. Dhillon, and S. R. Duck, Mon. Not. R. Astron. Soc. **275**, 828 (1995).
77. J. E. Pringle and R. F. Webbink, Mon. Not. R. Astron. Soc. **172**, 493 (1975).
78. K. Nomoto and D. Sugimoto, Publ. Astron. Soc. Jpn. **29**, 765 (1977).
79. H. Saio and K. Nomoto, Astrophys. J. **500**, 388 (1998).
80. H. Saio and C. S. Jeffery, Mon. Not. R. Astron. Soc. **313**, 671 (2000).
81. E. M. Green, J. Liebert, and R. A. Saffer, in *Abstracts of the 197th American Astronomical Society Meeting, 2000,* p. 4601.
82. P. F. L. Maxted, U. Heber, T. R. Marsh, and R. C. North, Mon. Not. R. Astron. Soc. **326**, 1391 (2001).
83. A. R. King, U. Kolb, and L. Burderi, Astrophys. J. **464**, L127 (1996).
84. A. R. King, U. Kolb, and E. Szuszkiewicz, Astrophys. J. **488**, 89 (1997).
85. G. Dubus, J. Lasota, J. Hameury, and P. Charles, Mon. Not. R. Astron. Soc. **303**, 139 (1999).
86. U. Kolb, Mon. Not. R. Astron. Soc. **297**, 419 (1998).
87. I. Iben, Jr., A. V. Tutukov, and A. V. Fedorova, Astrophys. J. **503**, 344 (1998).
88. H. C. Spruit and H. Ritter, Astron. Astrophys. **124**, 267 (1983).
89. R. P. Kraft, J. Mathews, and J. L. Greenstein, Astrophys. J. **136**, 312 (1962).
90. S. B. Howell, S. Rappaport, and M. Politano, Mon. Not. R. Astron. Soc. **287**, 929 (1997).
91. E. P. J. van den Heuvel, D. Bhattacharya, K. Nomoto, and S. A. Rappaport, Astron. Astrophys. **262**, 97 (1992).
92. Z. Han and R. F. Webbink, Astron. Astrophys. **349**, L17 (1999).
93. Ph. Podsiadlowski, Z. Han, and S. Rappaport, astro-ph/0109171 (2002).
94. I. Iben, Jr. and A. V. Tutukov, Astrophys. J. **342**, 430 (1989).
95. A. Renzini, in *Stars and Star Systems* (Reidel, Dordrecht, 1979), Astrophysics and Space Science Library, Vol. 75, p. 155.
96. A. V. Tutukov and L. R. Yungel'son, Nauchn. Inf. Astron. Soveta Akad. Nauk SSSR **49**, 3 (1981).
97. E. Cappellaro and M. Turatto, astro-ph/0012455 (2000).
98. D. Branch, M. Livio, L. R. Yungelson, *et al.*, Publ. Astron. Soc. Pac. **107**, 1019 (1995).
99. L. Segretain, G. Chabrier, and R. Mochkovitch, Astrophys. J. **481**, 355 (1997).
100. M. Livio, in *Type Ia Supernovae, Theory and Cosmology,* Ed. by J. C. Niemeyer and J. W. Truran (Cambridge Univ. Press, Cambridge, 2000), p. 33.
101. K. S. Thorne and A. N. Zytkow, Astrophys. J. Lett. **199**, L19 (1975).
102. K. S. Thorne and A. N. Żytkov, Astrophys. J. **212**, 832 (1977).
103. T. Nugis, Pis'ma Astron. Zh. **15**, 42 (1989) [Sov. Astron. Lett. **15**, 19 (1989)].
104. G. S. Bisnovatyĭ-Kogan and A. S. Lamzin, Astron. Zh. **61**, 323 (1984) [Sov. Astron. **28**, 187 (1984)].
105. C. Eich, M. E. Zimmermann, K. S. Thorne, and A. N. Zytkov, Astrophys. J. **346**, 277 (1989).

106. R. C. Cannon, P. P. Eggleton, A. N. Zytkow, and P. Podsiadlowski, Astrophys. J. **386**, 206 (1992).
107. R. C. Cannon, Mon. Not. R. Astron. Soc. **263**, 817 (1993).
108. P. Podsiadlowski, R. C. Cannon, and M. J. Rees, Mon. Not. R. Astron. Soc. **274**, 485 (1995).
109. C. L. Fryer, W. Benz, and M. Herant, Astrophys. J. **460**, 801 (1996).
110. M. V. Barkov, G. S. Bisnovatyĭ-Kogan, and A. S. Lamzin, Astron. Zh. **78**, 313 (2001) [Astron. Rep. **45**, 230 (2001)].
111. S. L. Fryer, S. E. Woosley, M. Herant, and M. B. Davies, Astrophys. J. **520**, 650 (1999).
112. J. S. Greaves and W. S. Holland, Mon. Not. R. Astron. Soc. **316**, L21 (2000).
113. B. Paczynski, Astrophys. J. **308**, L43 (1986).
114. D. Eichler, M. Livio, T. Piran, and D. N. Schramm, Nature **340**, 126 (1989).
115. P. Meszaros and M. J. Rees, Astrophys. J. **397**, 570 (1992).
116. L. R. Yungelson, A. G. Massevitch, and A. V. Tutukov, in *IAU Colloquium 59: Effects of Mass Loss on Stellar Evolution* (Reidel, Dordrecht, 1981), Astrophysics and Space Science Library, Vol. 89, p. 265.
117. S. A. Colgate, A. G. Petschek, and J. T. Kriese, Astrophys. J. **237**, L81 (1980).
118. C. Fryer, W. Benz, M. Herant, and S. A. Colgate, Astrophys. J. **516**, 892 (1999).
119. J. G. Hills, Astrophys. J. **267**, 322 (1983).
120. T. Matheson, A. V. Filippenko, W. Li, *et al.*, Astron. J. **121**, 1648 (2001).
121. V. I. Varshavskiĭ and A. V. Tutukov, Nauchn. Inf. Astron. Sovet Akad. Nauk SSSR **26**, 35 (1973).

Translated by K. Maslennikov

Astronomy Reports, Vol. 46, No. 8, 2002, pp. 684–690. Translated from Astronomicheskiĭ Zhurnal, Vol. 79, No. 8, 2002, pp. 755–761.

The Spectra of Hard Radiation from Radio Pulsars

I. F. Malov and G. Z. Machabeli

Astro Space Center, Lebedev Physical Institute, Russian Academy of Sciences, Leninskiĭ pr. 53, Moscow, 117924 Russia
Abastumani Astrophysical Observatory, Academy of Sciences of Georgia, Gora Kanobili, Abastumani, 383762 Georgia

Received January 9, 2002; in final form February 1, 2002

Abstract—The kinetic equation for the distribution function of relativistic electrons is solved taking into account quasi-linear interactions with waves and radiative processes. Mean values of the pitch angles ψ are calculated. If the particles of the primary beam with Lorentz factors $\gamma_b \sim 10^6$ are resonant, then the condition $\gamma_b\psi_b \lesssim 1$ is satisfied, the particle distribution is described by the function $f_\parallel(\gamma) \propto \gamma^{-4}$, and the synchrotron radiation spectrum is characterized by the spectral index $\alpha = 3/2$. On the other hand, if a cyclotron resonance is associated with particles of the high-energy tail of the secondary plasma ($\gamma_t \sim 10^5$), then $\gamma_t\psi_t \gg 1$, and the distribution function has two parts—$f_\parallel(\gamma) \propto \gamma$ and $f_\parallel(\gamma) \propto \gamma^{-2}$—which correspond to the spectral indices $\alpha_1 = +1$ and $\alpha_2 = -0.5$. This behavior is similar to that observed for the pulsar B0656+14. The predicted frequency of the maximum $\nu_m = 7.5 \times 10^{16}$ Hz coincides with the peak frequency for this pulsar. The model estimate for the total synchrotron luminosity of a typical radio pulsar with hard radiation $L_s = 3 \times 10^{33}$ erg/s is in agreement with observed values.

1. INTRODUCTION

Attempts to describe the spectra of separate radio pulsars or groups of pulsars by assuming that their radiation is generated by the synchrotron mechanism were undertaken in our earlier papers [1–7]. The transverse momentum $p_\perp$ of the relativistic electrons decreases very rapidly in the magnetic field $B \sim 10^{12}$ G near the pulsar surface due to synchrotron losses (on characteristic times $\lesssim 10^{-18}$ s). As a result, the distribution function of these particles becomes one-dimensional and takes the form presented in Fig. 1 [8], which shows the characteristic Lorentz factors of the primary beam γ_b and the secondary plasma in the maximum γ_p and tail γ_t of the distribution. Further, plasma with this anisotropic distribution function becomes unstable [9, 10], resulting in the excitation of waves in the pulsar magnetosphere. The interaction of these waves with particles produces a transverse momentum component. We used precisely this approach in [3, 5] to explain the observed optical radiation by radio pulsars in the framework of the synchrotron model, taking into account the diffusion of momentum only in the transverse direction. In the present work, we consider the influence of the generated waves on variations in the field-aligned momenta of the relativistic electrons and estimate the role of these processes in the formation of pulsar spectra.

2. DESCRIPTION OF THE MODEL

We assume here that the main origin of wave excitation in the pulsar magnetosphere is the cyclotron instability. The cyclotron resonance condition can be written in the form [11]

$$\omega - k_\varphi v_\varphi - k_x u_x \pm \frac{\omega_B}{\gamma_r} = 0, \qquad (1)$$

where $v_\varphi \approx c\left(1 - \frac{u_x^2}{c^2} - \frac{1}{2\gamma_r^2}\right)$, $k_\varphi^2 + k_\perp^2 = k^2$, $k_\perp^2 = k_x^2 + k_r^2$, and γ_r is the Lorentz factor of the resonant particles. The drift velocity of the particles due to their motion along the curved magnetic field lines is

$$u_x = \frac{c v_\varphi \gamma_r}{\rho \omega_B}, \qquad (2)$$

where ρ is the radius of curvature of the field lines and $\omega_B = \frac{eB}{mc}$ is the cyclotron frequency. The corresponding coordinate system is presented in Fig. 2. The resonance condition (1) for transverse waves with the spectrum [12]

$$\omega_t = kc(1 - \delta) \qquad (3)$$

can be written

$$\frac{1}{2\gamma_r^2} + \frac{(k_\perp/k_\varphi - u_x/c)^2}{2} + \frac{1}{2}\frac{k_r^2}{k_\varphi^2} - \delta = \pm\frac{\omega_B}{\gamma_r k_\varphi c}, \qquad (4)$$

1063-7729/02/4608-0684$22.00

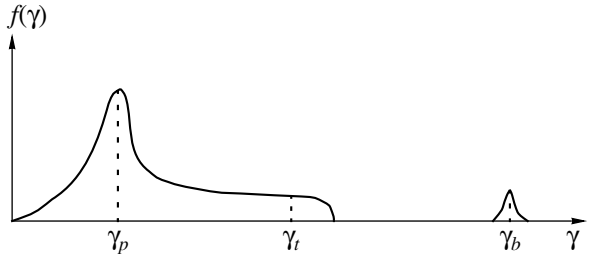

Fig. 1. Distribution function of relativistic electrons in a radio pulsar magnetosphere.

where

$$\delta = \frac{\omega_p^2}{4\omega_B^2\gamma_p^3}. \quad (5)$$

A minus sign in (4) corresponds to the excitation of waves due to the anomalous Doppler effect, and a plus sign, to their damping. Both these processes lead to a redistribution of the particle momenta due to quasi-linear diffusion.

The kinetic equation for the distribution function can be written [13]

$$\frac{\partial f}{\partial t} + \frac{\partial}{\partial p_\parallel}[(G_\parallel + F_\parallel + Q_\parallel)f] + \frac{1}{p_\parallel\psi}\frac{\partial}{\partial\psi}[\psi(G_\perp + F_\perp)f] = \frac{1}{\psi}\frac{\partial}{\partial\psi}\left[\psi\left(D_{\perp,\perp}\frac{\partial}{\partial\psi} + D_{\perp,\parallel}\frac{\partial}{\partial p_\parallel}\right)f(p_\parallel,\psi) + \frac{\partial}{\partial p_\parallel}\left(D_{\parallel,\perp}\frac{\partial}{\partial\psi} + D_{\parallel,\parallel}\frac{\partial}{\partial p_\parallel}\right)f(p_\parallel,\psi)\right], \quad (6)$$

where G is the force responsible for conservation of the adiabatic invariant $I = 3cp_\perp^2/2eB$ [14], and F is the force of deceleration by the synchrotron radiation. Unlike in [13], the force of deceleration by curvature radiation $Q_\parallel$ was taken into account in the above equation. The type of solution of (6) depends on the relationship between the forces G, F, and Q:

$$G_\perp = -\frac{mc^2}{\rho}\gamma_r\psi, \quad G_\parallel = \frac{mc^2}{\rho}\gamma_r\psi^2, \quad (7)$$

$$F_\perp = -\frac{2e^2\omega_B^2}{3c^2}\psi(1+\gamma_r^2\psi^2), \quad F_\parallel = -\alpha_s\gamma_r^2\psi^2, \quad (8)$$

$$Q_\parallel = -\frac{2}{3}\frac{e^2}{\rho^2}\gamma_r^4 = -\alpha_c\gamma^4. \quad (9)$$

The case $|G_\perp| \gg |F_\perp|$ and $|G_\parallel| \ll |F_\parallel|$ was considered in [3]. The corresponding equation for diffusion across the magnetic field takes the form

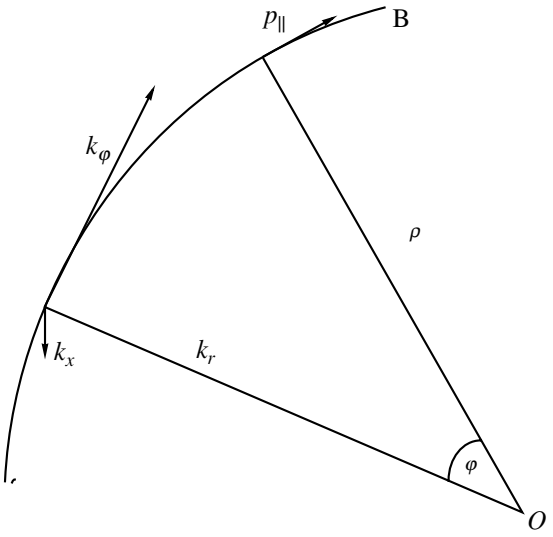

Fig. 2. Cylindrical coordinate system used.

$$\frac{\partial f^\circ}{\partial t} + \frac{1}{mc\gamma_b^2\psi}\frac{\partial}{\partial\psi}(\psi G_\perp f^\circ) + \frac{1}{mc}\frac{\partial}{\partial\gamma_b}(F_\parallel f^\circ) = \frac{1}{m^2c^2\gamma_b^2}\frac{1}{\psi}\frac{\partial}{\partial\psi}\left(\psi D_{\perp\perp}\frac{\partial f^\circ}{\partial t}\right), \quad (10)$$

where

$$D_{\perp\perp} = D\frac{\delta}{\gamma_b^2}|E_k|^2_{k=k_{\rm res}}, \quad D = \frac{\pi^2e^2}{m^2c^3}, \quad |E_k|^2 = n_k\omega_k, \quad (11)$$

and n_k is the number of plasmons. The solution of (10) gives the mean value of the pitch angle

$$\psi_0 = \frac{\sqrt{\pi}mc\gamma_b}{2\sqrt{2}eBP\gamma_p^2}. \quad (12)$$

Let us now consider (6) and write the distribution function $f_\parallel$ in the form

$$f_\parallel(p_\parallel) = \int_0^{\pi/2}\psi f(p_\parallel,\psi)d\psi. \quad (13)$$

Next, we should impose the condition

$$f\left(p_\parallel, \psi \to \frac{\pi}{2}\right) = 0, \quad (14)$$

which is similar to the usual condition $f(p_\parallel, p_\perp \to \infty) = 0$. Let us multiply both sides of (6) by ψ and integrate over ψ from 0 to $\pi/2$. As a result, the third term on the left-hand side and the first term on the right-hand side vanish. Next, using the definitions

(7)–(9), (11), and (13) and the expressions for the diffusion coefficients (see, for example, [10, 15])

$$D_{\parallel\perp} = D_{\perp\parallel} = -D\frac{\psi mc}{\gamma}|E_k|^2, \qquad (15)$$
$$D_{\parallel\parallel} = D\frac{\psi^2 m^2 c^2}{\delta}|E_k|^2,$$

we obtain

$$\frac{\partial f_\parallel}{\partial t} = \frac{\partial}{\partial p_\parallel}\left\{\left[\alpha_s\psi_0^2\left(\frac{p_\parallel}{mc}\right)^2 + \alpha_c\left(\frac{p_\parallel}{mc}\right)^4 - 2\pi^2\psi_0\frac{mc}{p_\parallel}r_e\omega_k n_k\right]f_\parallel\right\}, \qquad (16)$$

where $r_e = \dfrac{e^2}{mc^2}$.

The character of the resulting radiation spectrum depends on the form of the distribution function, which is the solution of (16). We accordingly now obtain and analyze this solution and construct possible spectra for the radiation.

3. RADIATION SPECTRUM FOR $\gamma_r\psi_0 \lesssim 1$

Quasi-linear diffusion should lead to an increasing role for nonlinear processes (such as decays, scattering, and modulation instability), resulting in the nonlinear transfer of plasmons over the spectrum. The evolution of the number of plasmons is described by the continuity equation:

$$\frac{\partial n_k}{\partial t} + \frac{\partial}{\partial k}(n_k\dot{k}) = (-\Gamma^{NCR} + \Gamma^{ACR})n_k. \qquad (17)$$

Here, $\dot{k} \simeq \Gamma_{NL}k$ is determined by nonlinear processes. We assume below that a differential transfer of energy over the spectrum (cascade) takes place. Let Γ^{ACR} be the source of plasmons with specified k and Γ^{NCR} the sink of these plasmons.

We shall seek a solution of (17) in the form

$$n_k = Ck^{-\xi}N(t). \qquad (18)$$

It is easy to shown that

$$n_k = N_0k^{-\xi}e^{-\left(1-\xi+\frac{\Gamma^{NCR}-\Gamma^{ACR}}{\Gamma_{NL}}\right)\Gamma_{NL}t}, \qquad (19)$$

where N_0 is a constant that has not yet been determined. If the quantity in parentheses in the exponent is positive, n_k decreases exponentially with time. This case in not of interest. On the other hand, if

$$\xi \gtrsim 1 + \frac{\Gamma^{NCR} - \Gamma^{ACR}}{\Gamma_{NL}}, \qquad (20)$$

the number of plasmons increases exponentially. The characteristic time for this increase (i.e., for the formation of the spectrum) cannot exceed the time for the generation of the waves:

$$\Gamma_{NL}\xi + \Gamma^{ACR} - \Gamma_{NL} - \Gamma^{NCR} > \Gamma^{ACR}, \qquad (21)$$

$$\text{or} \quad \xi \gtrsim 1 + \frac{\Gamma^{NCR}}{\Gamma_{NL}}.$$

In addition, the quantity $\left|\dfrac{\Gamma^{NCR} - \Gamma^{ACR}}{\Gamma_{NL}}\right|$ cannot exceed unity, since the increase in the amplitude of the generated wave and its maximum amplitude are determined by the equality of the linear and nonlinear increments. As a result, ξ cannot exceed two. Therefore, we conclude that there is an approximately stationary regime:

$$\xi = 1 + \frac{\Gamma^{NCR}}{\Gamma_{NL}} - \frac{\Gamma^{ACR}}{\Gamma_{NL}} \qquad (22)$$

at

$$n_k = N_0k^{-\xi} \quad \text{and} \quad 1 < \xi \lesssim 2. \qquad (23)$$

The resulting spectrum will be stationary with respect to both the pitch angles and field-aligned momenta. Taking $\dfrac{\partial f_\parallel}{\partial t} = 0$, we find from (11) that

$$f_\parallel = \frac{C_1}{\alpha_s\psi_0^2\left(\frac{p_\parallel}{mc}\right)^2 + \alpha_c\left(\frac{p_\parallel}{mc}\right)^4 - 2\pi^2 r_e\psi_0\frac{mc}{p_\parallel}\omega_k n_k}, \qquad (24)$$

where C_1 is an arbitrary constant.

Let us estimate the relative values of the three terms on the right-hand side of (16), which we denote A_I, A_{II}, and A_{III}, respectively. As can easily be seen,

$$\frac{A_{II}}{A_I} = \frac{8c^2\gamma_p^4P^2}{\pi\rho^2}, \qquad (25)$$

where P is the period of the pulsar rotation. Assuming that the radius of curvature of the field line is equal to the radius of the light cylinder, as in [3, 5],

$$\rho = r_{LC} = \frac{cP}{2\pi}, \qquad (26)$$

we find

$$\frac{A_{II}}{A_I} = 32\pi\gamma_p^4, \qquad (27)$$

which is considerably greater than unity for any Lorentz factors for the secondary plasma. After substituting the values for the constants, the ratio

$$\frac{|A_{III}|}{A_{II}} = \frac{3\pi\sqrt{\pi}m^3c^5}{32\sqrt{2}e^4B^2P\gamma_b\gamma_p^6} \qquad (28)$$

turns out to equal

$$\frac{|A_{III}|}{A_{II}} = \frac{10^8}{PB^2\gamma_b\gamma_p^6}. \qquad (29)$$

To obtain some estimates, we shall assume that the magnetic field is dipolar and that the angle between the magnetic moment and the rotational axis

of the pulsar is equal to β. If the observed radiation is generated at the periphery of the magnetosphere at the distance $r = r_{LC}/\sin\beta$, the required ratio will take the form

$$\frac{|A_{III}|}{A_{II}} = \frac{10^6 P^5}{B_{12}^2 \sin^6\beta\gamma_b\gamma_p^6}, \quad (30)$$

where $B_{12} = B_s/10^{12}$ and B_s is the magnetic field at the neutron star's surface.

The mean values of the parameters of radio pulsars whose pulsed radiation is beyond the radio band can be calculated using the data of [2]. Finally, we obtain

$$\log\bar{B}_s = 11.84, \quad \bar{P} = 0.117 \text{ s}, \quad \bar{\beta}^\circ = 19^\circ.$$

We added 0.30 to the tabulated values when calculating $\log\bar{B}_s$, so that the correct value of the dipole moment was used (see, for example, [16]). The pulsar PSR 0531+21 was not included in the calculation of $\bar{\beta}$, since the corresponding tabulated angle may be incorrect [2]. Thus, the final expression for the ratio of the third and second terms can be written

$$\frac{|A_{III}|}{A_{II}} = \frac{3.83\times10^4}{\gamma_b\gamma_p^6}. \quad (31)$$

Consequently, we obtain for the Lorentz factors $\gamma_b = 10^6$ and $\gamma_p = 3$ [17] $\dfrac{|A_{III}|}{A_{II}} \approx 5\cdot10^{-5}$. These estimates enable us to conclude that the contributions of the first and third terms in the denominator of (24) are small for most pulsars. Consequently, the main part of the spectrum will be formed by particles with the distribution function

$$f_\parallel = \mathrm{C}_2\frac{\rho^2}{e^2}\gamma^{-4}. \quad (32)$$

The spectrum will have a power-law form at large frequencies [18]:

$$I(\nu) \propto \nu^{-\alpha}, \quad (33)$$

where $\alpha = 3/2$. At the lowest frequencies, $I(\nu) \propto \nu^{5/2}$. The frequency of the maximum in the spectrum ν_m can be estimated using the data [6]. For the case under consideration, $\nu_m < 10^6$ Hz; i.e., the entire observable synchrotron spectrum should be a power law with spectral index $\alpha = 3/2$.

Let us consider again expression (30). In the case of pulsars with $P \sim 10$ ms and $B_{12} \sim 10^{-3}$, for the same values of γ_b and γ_p, the ratio $|A_{III}|/A_{II} \sim 1$ only when $\beta \approx 4^\circ$. If such angles between the rotational axis and magnetic field really exist, we should see almost continuous emission at all wavelengths and very broad pulses. However, these pulsars in fact emit pulses whose width is considerably less than their period. Therefore, the second term on the right-hand side of (16) also dominates for short-period pulsars, so that a synchrotron spectrum with $\alpha = 3/2$ should be formed.

We have carried out this analysis assuming that the cyclotron resonance is associated with particles of the primary beam. On the other hand, the resonant particles in the pulsar magnetosphere could be secondary electrons or positrons with $\gamma_r \sim 10^4$–10^5 (which correspond to the tail of the distribution function of the secondary plasma). We consider this case in the next section.

4. THE RADIATION SPECTRUM FOR $\gamma_r\psi_0 \gg 1$

Let us suppose now that $\gamma_r\psi_0 \gg 1$. It then follows from (7) and (8) that

$$G < F. \quad (34)$$

In fact, as in Section 3, $|G_\parallel| < |F_\parallel|$; however, for the ratio

$$\frac{G_\perp}{F_\perp} = \frac{3m^3c^6}{2e^4B_s^2}\frac{\gamma_r}{\rho}\left(\frac{r}{R_*}\right)^6\frac{1}{\gamma_r^2\psi^2}, \quad (35)$$

we find $G_\perp < F_\perp$ when $\gamma\psi > 10^3$. We shall assume that this condition is satisfied. (Its applicability will be evaluated after obtaining the solution.) The pitch angle ψ_0 can be found from the equation

$$\frac{\partial f^0}{\partial t} + \frac{1}{mc\gamma_r^2\psi\partial\psi}(\psi F_\perp f^\circ) + \frac{1}{mc}\frac{\partial}{\partial\gamma_b}(F_\parallel f^0) = \frac{1}{m^2c^2\gamma_r^2}\frac{1}{\psi}\frac{\partial}{\partial\psi}\left(\psi D_{\perp\perp}\frac{\partial f^0}{\partial\psi}\right). \quad (36)$$

Under the same assumptions as in [5], we obtain the pitch-angle distribution for the particles

$$\chi(\psi) = Ce^{-A\psi^4}, \quad (37)$$

where

$$A = \frac{4e^6}{3\pi^3m^5c^7}\frac{B^4P^3\gamma_p^4\gamma_r^2}{\gamma_b^3}. \quad (38)$$

The average angle ψ is [19]

$$\psi_0 = \frac{\int_0^\infty \psi e^{-A\psi^4}d\psi}{\int_0^\infty e^{-A\psi^4}d\psi} = \frac{\Gamma(0.5)}{\sqrt[4]{A}\Gamma(0.25)} \approx \frac{0.5}{\sqrt[4]{A}}. \quad (39)$$

Thus, when $\gamma_r = 10^5$,

$$\psi_0 = \frac{2.37}{BP^{3/4}} = \frac{0.26P^{9/4}}{B_{12}\sin^3\beta}. \quad (40)$$

For the average values of B, P, and β presented in Section 3, we obtain $\psi_0 = 8.87\times10^{-2}$. We can see that the inequality $\gamma_r\psi_0 > 10^3$ does indeed hold; i.e.

the solution obtained does not contradict our initial assumption.

Let us estimate the contributions of various terms on the right-hand side of (16) for the ψ_0 value from (39). Let us first compare A_I and A_{II}:

$$\frac{A_{II}}{A_I} \approx \frac{32\sqrt{\pi}e}{\sqrt{3mc^3}} \frac{\gamma_r^3\gamma_p^2}{\gamma_b^{3/2}P^{1/2}} = 10^{-10}\frac{\gamma_r^3\gamma_p^2}{\gamma_b^{3/2}P^{1/2}}. \quad (41)$$

For the parameter values specified above, this expression gives $A_{II}/A_I = 2.6 \times 10^{-3}$; i.e., the relationship between the first two terms is the opposite of that in (27).

Let us now compare A_{II} and A_{III}:

$$\frac{A_{III}}{A_{II}} = \frac{3\pi\sqrt[4]{3\pi^3}m^{13/4}c^{23/4}\gamma_b^{11/4}}{32\sqrt{2}e^{9/2}B^2P^{3/4}\gamma_p^5\gamma_r^{9/2}} \quad (42)$$

$$= 1.3\cdot 10^{14}\frac{\gamma_b^{11/4}}{B^2P^{3/4}\gamma_p^5\gamma_r^{9/2}} = 6\times 10^3\frac{P^{21/4}}{B_{12}^2\sin^6\beta}.$$

For the above parameter values, A_{III} turns out to be two orders of magnitude greater than A_{II}.

Finally, comparison of the third and first terms yields

$$\frac{A_{III}}{A_I} = \frac{3^{3/4}\pi^{9/4}c^{17/4}m^{11/4}\gamma_b^{5/4}}{\sqrt{2}e^{7/2}B^2P^{5/4}\gamma_p^3\gamma_r^{3/2}} \quad (43)$$

$$= 151\frac{\gamma_b^{5/4}P^{19/4}}{B_{12}^2\gamma_p^3\gamma_r^{3/2}\sin^6\beta},$$

so that $A_{III} \approx 0.4A_I$. Given the uncertainties in the values of γ and β, this indicates that the third and first terms are of the same order of magnitude. Therefore, as distinct from the case $\gamma_r\psi_0 \lesssim 1$ (where the second term was dominant), two other terms contribute significantly in the distribution function for $\gamma_r\psi_0 \gg 1$.

Let us now estimate the characteristic frequencies in the radiation spectrum. As follows from (4), a resonance occurs at the frequency

$$\omega \approx \frac{\omega_B}{\delta\gamma_r}, \quad (44)$$

and the generated transverse waves that propagate beyond the magnetosphere are in the range

$$\frac{\omega_B}{2\pi\delta\gamma_r} \lesssim \nu \lesssim \frac{\omega_B}{\pi}\gamma_p. \quad (45)$$

Substituting expressions for the corresponding quantities, we find

$$\frac{64\pi^4e^2}{m^2c^8}\frac{\gamma_p^4R_*^6B_s^2\sin^6\beta}{\gamma_r\gamma_bP^5} \lesssim \nu \lesssim \frac{8\pi^2e}{mc^4}\frac{B_sR_*^3\sin^3\beta\gamma_p}{P^3}; \quad (46)$$

so that, for the parameter values used here,

$$5.6\times 10^7 \text{ Hz} \lesssim \nu \lesssim 2.3\times 10^9 \text{ Hz},$$

i.e., the spectrum of the waves generated near the cyclotron resonance is in the radio.

However, a considerable fraction of the energy of the excited waves is transferred to particles possessing the above pitch-angle distribution. The peak frequency of the synchrotron spectrum of a single particle is determined by the expression [18]:

$$\nu_m \approx \frac{0.9}{4\pi}\omega_B\gamma_r^2\sin\psi. \quad (47)$$

In the particular case under consideration, this takes the form

$$\nu_m \approx \frac{3^{9/4}}{80\pi^{1/4}\sqrt{2}}\left(\frac{mc^3}{e^2}\right)^{1/4}\frac{\gamma_r^{3/2}\gamma_b^{3/4}}{P^{3/4}\gamma_p} \quad (48)$$

$$= 4.5\cdot 10^4\frac{\gamma_r^{3/2}\gamma_b^{3/4}}{P^{3/4}\gamma_p}.$$

For the values of γ and P used here, we obtain $\nu_m = 7.5\cdot 10^{16}$ Hz, which corresponds to a photon energy of ~0.3 keV. Surprisingly, this coincides with the peak frequency of the spectrum of the pulsar B0656+14 [20], suggesting an alternative to the thermal mechanism for the optical and X-ray part of the spectrum: it may be due to the combined synchrotron radiation from electrons with two distribution functions — $f_\parallel \propto \gamma$ and $f_\parallel \propto \gamma^{-2}$, with the spectral indices $\alpha_1 = +1$ and $\alpha_2 = -0.5$.

The power emitted by a single electron is given by the expression [18]

$$p \approx \frac{2e^4B^2\psi^2\gamma_r^2}{3m^2c^3}. \quad (49)$$

The ratio of the powers of the particles in the beam and tail p_b/p_t depends on the corresponding Lorentz factors and pitch angles:

$$p_b/p_t = \frac{\gamma_b^2\psi_b^2}{\gamma_t^2\psi_t^2} \quad (50)$$

or, for the values of ψ_0 obtained above,

$$p_b/p_t = \frac{e\gamma_b^{5/2}}{(3\pi c^3P)^{1/2}\gamma_p^2\gamma_t}. \quad (51)$$

For the parameter values used here, $p_b/p_t \sim 10^{-3}$. The flux excess in the spectrum of B0656+14 over an extrapolation of the power law is also about 10^3 at 5×10^{16} Hz; i.e., the observed spectrum is in satisfactory agreement with the hypothesis that it is due to the combined radiation from particles in the beam and tail.

The total expected synchrotron power can be estimated using the formula [7]:

$$L \approx \frac{16\pi^8 e^4 R_*^6 I B_s^2 \gamma_r \dot{P} \psi^2 \sin^4\beta}{m^3 c^{11} P^8}, \qquad (52)$$

where I is the moment of inertia of the neutron star. According to the above comparison, $\gamma_b\psi_b^2 \ll \gamma_t\psi_t^2$, and we will take into account only radiation by the particles in the tail when calculating the luminosity. As a result, we obtain $L = 3.3 \times 10^{33}$ erg/s for a typical radio pulsar with the observed hard radiation ($\dot{P} = 1.93 \times 10^{-13}$) [4].

A more detailed comparison and fitting of the observed optical to gamma-ray spectra of particular radio pulsars and their luminosities using the model considered here will be presented in a separate paper.

5. DISCUSSION AND CONCLUSIONS

We have presented a description of the optical and X-ray spectra of radio pulsars in the framework of the synchrotron model. This model has been used earlier to explain the spectra of pulsars at hard energies [21–26]. It has been arbitrarily assumed by most authors that the pitch angles of the radiating particles are $\psi \sim 1$. On the other hand, as we have shown in [3, 5] and the present paper, plausible mechanisms for the development of transverse momentum components can produce values $\psi \ll 1$. The synchrotron model was used recently [27] to explain the infrared, optical, and X-ray emission of the Crab pulsar, taking the Lorentz-factor distribution of the particles to be $N(\gamma) \propto \gamma^{-2}$. It was arbitrarily assumed that the radiation is produced by particles with $\gamma \sim 10^2$ and $\psi \sim 10^{-3}$. However, $\psi \sim 0.1$ is required in order to obtain agreement between the predicted and observed X-ray luminosities. Possibilities for removing this problem are not discussed in [27].

Our results make it possible to describe the most typical features of the hard emission of radio pulsars without introducing any artificial assumptions. In our opinion, the corresponding plasma processes inevitably occur in the outer parts of the pulsar magnetosphere, and should naturally result in the formation of the derived particle pitch angles and, therefore, the generation of synchrotron radiation.

Let us summarize our basic conclusions.

(1) We have written the kinetic equation for the distribution function of the relativistic electrons taking into account momentum diffusion due to quasi-linear interactions with waves and radiation processes.

(2) Solutions of this equation were obtained, and the average pitch angle ψ of the emitting electrons was calculated.

(3) If particles of the primary beam with Lorentz factors $\gamma_b \sim 10^6$ are resonant, the condition $\gamma_b\psi_b \leq 1$ is satisfied, and the energy distribution of the particles is described by the function $f_\parallel(\gamma) \propto \gamma^{-4}$. In this case, the synchrotron spectrum is a power law with spectral index $\alpha = 3/2$.

(4) If the cyclotron resonance is associated with particles in the tail of the distribution of the secondary plasma with $\gamma_t \sim 10^5$, then $\gamma_t\psi_t \gg 1$, and the distribution function of the radiating particles has two parts—$f_\parallel(\gamma) \propto \gamma$ and $f_\parallel(\gamma) \propto \gamma^{-2}$. The corresponding synchrotron intensity will initially increase as ν and then decrease as $I_\nu \propto \nu^{-0.5}$. This behavior is similar to that observed for the pulsar B0656+14. The predicted frequency of the maximum $\nu_m = 7.5 \times 10^{16}$ Hz coincides with the observed value.

(5) This form for the spectrum suggests an alternative explanation for the excess of the observed flux over a power-law dependence at optical and X-ray frequencies, which has usually been interpreted as being due to thermal radiation by the neutron star's surface. A considerable part of the spectrum can be described using the total radiation of particles of the beam and secondary plasma.

(6) We estimate the integrated synchrotron luminosity for a typical radio pulsar with hard radiation to be $L = 3 \times 10^{33}$ erg/s, in good agreement with observations [28].

Fitting of the optical to gamma-ray spectra of individual pulsars using the synchrotron model and a detailed comparison with observational data will be carried out in a subsequent paper.

ACKNOWLEDGMENTS

This work was supported by the Russian Foundation for Basic Research (project no. 00-02-17850) and the National Science Foundation (grant 00-98685). We are grateful to L.B. Potapova for help in preparation of the manuscript.

REFERENCES

1. I. F. Malov, Astron. Zh. **75**, 281 (1998) [Astron. Rep. **42**, 246 (1998)].
2. I. F. Malov, Astron. Zh. **76**, 542 (1999) [Astron. Rep. **43**, 471 (1999)].
3. I. F. Malov and G. Z. Machabeli, Astron. Zh. **76**, 788 (1999) [Astron. Rep. **43**, 691 (1999)].
4. I. F. Malov, Astron. Zh. **76**, 825 (1999) [Astron. Rep. **43**, 727 (1999)].
5. I. F. Malov and G. Z. Machabeli, Astrophys. J. **554**, 587 (2001).
6. I. F. Malov, Astron. Zh. **78**, 165 (2001) [Astron. Rep. **45**, 138 (2001)].

7. I. F. Malov, Astron. Zh. **78**, 990 (2001) [Astron. Rep. **45**, 865 (2001)].
8. J. Arons, in *Proceedings of the Varenna Summer School and Workshop on Plasma Astrophysics* (European Space Agency, Paris, 1981), p. 273.
9. R. Z. Sagdeev and V. D. Shafranov, Zh. Éksp. Teor. Fiz. **39**, 181 (1960) [Sov. Phys. JETP **12**, 130 (1960)].
10. D. G. Lominadze, G. Z. Machabeli, and A. B. Mikhaĭlovskiĭ, Fiz. Plazmy **5**, 1337 (1979) [Sov. J. Plasma Phys. **5**, 748 (1979)].
11. A. Z. Kazbegi, G. Z. Machabeli, and G. I. Melikidze, in *IAU Colloquium 128, Poland, 1990,* p. 232.
12. A. S. Volokitin, V. V. Krasnosel'skikh, and G. Z. Machabeli, Fiz. Plazmy **11**, 531 (1985) [Sov. J. Plasma Phys. **11**, 310 (1985)].
13. G. Z. Machabeli and V. V. Usov, Pis'ma Astron. Zh. **5**, 445 (1979) [Sov. Astron. Lett. **5**, 238 (1979)].
14. L. D. Landau and E. M. Lifshitz, *The Classical Theory of Fields* (Fizmatgiz, Moscow, 1967; Pergamon, Oxford, 1975).
15. D. B. Melrose, *Plasma Astrophysics: Nonthermal Processes in Diffuse Magnetized Plasmas* (Gordon and Breach, New York, 1978).
16. S. L. Shapiro and S. A. Teukolsky, *Black Holes, White Dwarfs, and Neutron Stars: the Physics of Compact Objects* (Wiley, New York, 1983; Mir, Moscow, 1985), Vol. 2.
17. G. Z. Machabeli and V. V. Usov, Pis'ma Astron. Zh. **15**, 910 (1989) [Sov. Astron. Lett. **15**, 393 (1989)].
18. A. Pacholczyk, *Radio Astrophysics. Nonthermal Processes in Galactic and Extragalactic Sources* (Freeman, San Francisco, 1970; Mir, Moscow, 1973).
19. I. M. Ryzhik and I. S. Gradshteyn, *Table of Integrals, Series, and Products* (Nauka, Moscow, 1971; Academic, New York, 1980).
20. A. B. Kopsevich, G. G. Pavlov, S. V. Zharikov, *et al.*, Astron. Astrophys. **370**, 1004 (2001).
21. V. L. Ginzburg, V. V. Zheleznyakov, and V. V. Zaĭtsev, Usp. Fiz. Nauk **98**, 201 (1969) [Sov. Phys. Usp. **12**, 378 (1969)].
22. I. S. Shklovsky, Astrophys. J. **159**, L77 (1970).
23. F. Pacini, Astrophys. J. **163**, 117 (1971).
24. V. V. Zheleznyakov and V. E. Shaposhnikov, Astrophys. Space Sci. **18**, 141 (1972).
25. F. Pacini and M. Salvati, Astrophys. J. **274**, 369 (1983).
26. F. Pacini and M. Salvati, Astrophys. J. **321**, 447 (1987).
27. A. R. Crusins-Watzel, T. Kunze, and H. Lesch, Astrophys. J. **546**, 401 (2001).
28. J. Thompson, Astron. Soc. Pac. Conf. Ser. **105**, 307 (1996).

Translated by Yu. Dumin

Astronomy Reports, Vol. 46, No. 8, 2002, pp. 691–695. Translated from Astronomicheskiĭ Zhurnal, Vol. 79, No. 8, 2002, pp. 762–767.

Formation of Planetary Systems and Brown Dwarfs around Single Stars

A. B. Tutukov

Institute of Astronomy, Russian Academy of Sciences, Pyatnitskaya ul. 48, Moscow, 109017 Russia

Received September 15, 2001; in final form November 23, 2001

Abstract—The conditions for the formation of planets and brown dwarfs around single main-sequence stars are considered in two scenarios. The formation of planets and brown dwarfs requires that the initial specific angular momentum of a solar-mass protostar be $(0.32) \times 10^{18}$ cm^2/s. The accreted matter of the protostar envelope forms a compact gas ring (disk) around the young star. If the viscosity of the matter in this ring (disk) is small, increasing its mass above a certain limit results in gravitational instability and the formation of a brown dwarf. If the viscosity of the gas is sufficiently large, the bulk of the protostar envelope material will be accreted by the young star, and the gas disk will grow considerably to the size of a protoplanetary dust disk due to the conservation of angular momentum. The formation of dust in the cool part of the extended disk and its subsequent collisional coalescence ultimately results in the formation of solar-type planetary systems. © *2002 MAIK "Nauka/Interperiodica"*.

The accuracy of stellar radial-velocity measurements has been steadily improving with time. This has led to the detection of several dozen planetary systems and more than ten brown dwarfs during the last several years, as a rule, orbiting solar-mass stars. The boundary between planets and brown dwarfs remains relative, and we take it here to be 10 Jupiter masses, in accordance with Stepinski and Black [1]. In reality, the lower limit for the masses of brown dwarfs is determined by the minimum mass of single stars with solar chemical composition born in the Galaxy. For obvious reasons, this value remains unknown, though single brown dwarfs have been found [2]. As a result, the masses of brown dwarfs are restricted to 10–100 Jupiter masses. The upper mass limit is determined by the absence of hydrogen burning in the dwarf's core. Hydrogen can be ignited in the interiors of dwarfs with masses above $0.1M_\odot$, so that they can become ordinary stars (M dwarfs). The boundary between planets and brown dwarfs in known planetary systems is relative, since the mass distribution of low-mass components with 0.5–1000 Jupiter masses appears continuous [1]. One exception may be the lack of systems with secondary-component masses of about 0.1 $M_\odot$ [3]; however, the reality of this deficiency remains uncertain [1, 4].

The total number of known planetary systems is 56 [5] and is increasing steadily. Most detected planets have masses close to the mass of Jupiter. However, we cannot exclude the possibility that we are seeing only the most massive planets of their planetary systems because of observational selection effects, and that the remaining, less massive planets have remained undetected due to insufficient sensitivity of the available observational instrumentation. This seems quite plausible, and apart from the Sun we know of at least one more example of a main-sequence star with three planets, υ And [6].

However, two important properties distinguish known examples of extrasolar planets from the planets of the solar system. Solar-system planets located inside the radius at which the ice envelopes of dust grains are vaporized have masses of about $10^{-6}M_\odot$. At the same time, the masses of extrasolar planets located at similar distances from their central stars frequently exceed the mass of Jupiter; i.e., these planets are much more massive than the Earth and Venus. Furthermore, while the orbital eccentricities of the solar system's giant planets are $\sim$0.05, the eccentricities of extrasolar planets revolving closer to their stars reach 0.63. Such large eccentricities do not fit into standard concepts about the existence of a ring-like, dissipative, gas–dust protoplanetary disk around the central star [7].

In the usual scenario for their formation, planets are the products of the collisional coalescence of various types of grains in extended, ring-like, gas–dust protoplanetary disks surrounding single stars [8–12]. This leads to small eccentricities for the planetary orbits and explains the relative positions of the terrestrial planets and giant planets in the solar system. In addition, it has been found that planets form around single solar-mass stars with initial specific angular momenta in the interval 3×10^{17}–2×10^{18} cm^2/s [13, 14]. Protostars with large angular momenta become multiple stars, while protostars with smaller angular momenta form single

1063-7729/02/4608-0691$22.00

rotating stars. The formation of binary stars probably occurs when two accreting centers appear at the beginning of the disruptive fragmentation of a protostellar cloud and are later transformed into the components of a binary. The orbits of young binary components usually have appreciable eccentricities and are circularized with time only in the closest systems with orbital periods shorter than 10–50 days, due to the viscous dissipation of orbital energy in the component interiors [1, 14].

A natural question arises: how do extrasolar planets and brown dwarfs (related to the former in many respects) that are close to their central stars acquire large orbital eccentricities? We can now propose two possible explanations for the development of large eccentricities of the orbits of these objects.

The first is connected with gravitational interactions between planets during close encounters in an unstable planetary system. In this case, it is clear that, in order for the orbital eccentricity to be large, or even for one of the planets to be lost from the system, the energy of the gravitational interaction between planets must be close to the planet's binding energy in the system. Assuming a solar mass for the central star and masses and radii of the planets equal to the mass and radius of Jupiter, we readily find that such large eccentricities can appear only for planets with orbital periods longer than one year. However, Fig. 4 of Stepinski and Black [1] demonstrates that large eccentricities occur for Jupiter-mass planets with orbital periods of 10–100 days. Since close encounters can explain large eccentricities only for long-period planets and brown dwarfs, the origin of the large eccentricities observed for close systems remains unknown.

For the other explanation, we must consider the formation of planets and brown dwarfs around single stars in some detail. As indicated above, planetary systems are the products of the evolution of protostars with initial angular momenta 3×10^{17}–2×10^{18} cm^2/s. Interestingly, estimates suggest that known systems with brown dwarfs may possess the same range of specific angular momenta, having observed orbital periods of 1.25–2600 days [1, 15]. Therefore, brown dwarfs may originate in processes similar to those occuring in the formation of planetary systems. Note that we mean here only brown dwarfs around single stars. The degree of binarity among brown dwarfs with semimajor orbital axes not exceeding 30 AU was found to coincide with that for ordinary stars [16]. For example, a simple estimate shows that the specific orbital angular momentum of the known binary brown dwarf PP1–15 [17] corresponds to those of binary stars. The origin of this system can therefore be explained by the usual scenario for binary-star formation. The masses of PP1–15's components are about 60–70 Jupiter masses, and its orbital period is 5.6 days. Single stars with such masses can also exist [18], but, according to the mass function of Najita *et al.* [19], they are rare: $f(M) \sim M^{1/2}$ for $0.015 < M/M_\odot < 0.7$.

Our purpose here is to determine the conditions required for the formation of planets and brown dwarfs around single stars. The formation of planets during the evolution of close binary stars was considered earlier in [20]. The origin of planetary systems around radio pulsars was explained as being due to the transformation of the low-mass companion in a low-mass X-ray binary system into a compact gas disk around the neutron star component. The initial mass and radius of this disk are about 0.1 $M_\odot$ and several solar radii.

The masses of the planets observed around radio pulsars indicate that they are terrestrial planets with orbit sizes reaching several astronomical units. This vividly demonstrates a plausible scheme for the evolution of protoplanetary disks around single stars. The bulk of their initial mass can be accreted by the central star, and the size of the protoplanetary disk increases considerably due to the conservation of angular momentum. Let us consider an initial solar-mass, gas–dust cloud with a specific angular momentum in the interval 3×10^{17}–2×10^{18} cm^2 s^{-1}. This angular momentum exceeds the limiting value for a single star to form, but is not sufficient to produce a close binary system; therefore, the material in the outer part of the protostellar cloud cannot directly reach the young star formed inside. This material is probably accreted into an ellipsoidal gas ring (see, for example, [21, 22]) with radius R_c, which forms around the young star. The value of R_c is determined by the initial angular momentum of the cloud, and is of the order of several solar radii. The fate of this ring is completely determined by the viscosity of the material making it up. If this viscosity is small, the accreted material will be accumulated by the compact gas ring (disk) until the onset of gravitational instability. According to Pringle [23], this is equivalent to the requirement that the ratio of the mass of the ring to the mass of the star should become greater than the ratio of the ring thickness to its radius. The ring will finally split into two or three parts, which, as a result of collisions, will produce a brown dwarf or giant planets in elliptical orbits. Cameron [24] and Pollack [25] considered a similar dynamical process for the formation of giant planets in a extended protoplanetary gas disk around the Sun. The contraction of massive planets and brown dwarfs to the final configuration was studied numerically by Chabrier and Baraffe [26]. The origin of large eccentricities of the orbits of giant planets

and brown dwarfs close to their central stars can be understood in this way.

If the viscosity of the gas ring material is sufficiently high, this ring will evolve into an extended accretion–excretion disk around the central star. In the accretion part of the disk, material losing angular momentum will be accreted by the star [27]. The ring material that accumulates the angular momentum of the accreted material will form an extended excretion gas disk around the young accreting star. The ratio of the mass of this disk M_d to the mass of the accreted material M_a can be estimated from the condition for the conservation of angular momentum: $M_d/M_a = (R_c/R_d)^{1/2}$, where R_d is the radius of the excretion disk. Adopting for the solar system $R_c = 5R_\odot$, $R_d =$ 40 AU, and the total mass of the planets 0.001 $M_\odot$, we find that the mass of the material accreted by the Sun during the formation of the extended protoplanetary disk was $\sim 0.04\,M_\odot$. This is obviously typical of brown-dwarf masses. It is possible that the formation of brown dwarfs as stellar companions is suppressed by the competing formation of solar-type planetary systems. Only those gas disks with a sufficiently low viscosity remain compact enough for the formation of a brown dwarf. The formation of planets in an excretion disk and braking of the central star by a magnetized stellar wind make it possible to understand the distinguishing feature of the solar system, namely, that the bulk of the mass is concentrated in the Sun, while the angular momentum is concentrated in the planets. The excretion disk brings about the separation of matter and angular momentum.

The size of the turbulent gas excretion disk is determined by the viscosity of the material, $R_d = (vlt)^{1/2}$, where v and l are the velocity and mean free path of turbulent elements and t is the disk life time. It is clear that, at low viscosities, the disk size will remain small. Note that standard α disks accumulate most of their material at the outer edge [27]. The gravitational instability of such compact disks will again lead to the formation of giant planets or brown dwarfs with eccentric orbits [28]. It may be that the condensation of dust grains in the expanding and cooling disk favors instability and the formation of planets, since an appreciable fraction of known extrasolar planets are located at the boundary corresponding to the vaporization of refractory grains [13].

If the viscosity of the accretion ring material is large, this facilitates the formation of extended disks, making it possible for their sizes to reach the observed values of 200–400 AU [29, 30]. Gas–dust disks are characteristic of Herbig Ae, Be stars and T Tauri stars [31, 32], and it cannot be ruled out that planetary systems are currently forming around these stars. The observed masses of the gas disks around T Tauri stars are 0.02–$0.05M_\odot$ [33–36], i.e., on the order of brown dwarf masses. Ohanesyan [37] has found that 15 of 17 A stars he studied had dust envelopes with temperatures of 70–200 K and radii of 7–400 AU. According to Sargent and Beckwith [38], about half of young stars have dust disks. The outer part of the dust disk is preserved even during the formation of planets in its inner part [38]. The formation of planets in protoplanetary disks has been studied in some detail in [8, 12, 39, 40]. The result of the evolution of protoplanetary disks is the formation of a system of planets with quasi-circular orbits.

It is interesting that gas–dust disks have also been detected in binary stars. The disk may encircle a close binary, as, for example, in BD +31°643 [42], or each of the components can have its own disk, as in UZ Tau [42]. Thus, the binarity of a star probably does not preclude the formation of planetary systems and brown dwarfs, either around each of the components or around the close binary as a whole. This problem remains only poorly studied, though a brown dwarf with a mass of $\sim 0.04M_\odot$ is known to orbit the binary V471 Tau [44].

Thus, the feature distinguishing the two scenarios for the formation of low-mass satellites around stars—brown dwarfs or giant planets (with, as a rule, large orbit eccentricities) and solar-type planetary systems (with nearly circular planetary orbits)—could be the viscosity of the material in the initial gas ring formed by the accreted material around a young star. The timescale for the gas ring to spread out into a disk due to this viscosity is $\sim R^2/\nu$ [27], where R is the ring radius; for the initial specific angular momenta we have adopted, R is several solar radii. Assuming an accretion timescale of 3×10^7 years, we can estimate an upper limit for the viscosity maintaining the gas ring during this time: $\nu < 10^8$–10^9 cm^2/s. The molecular viscosity is much smaller than this limit. The value of the turbulent viscosity, which is most likely regulated by the magnetic field, remains unclear. Therefore, it is at present impossible to prove the reality of the proposed scenario of the formation of brown dwarfs and planetary systems. Further analysis of the proposed scenario requires three-dimensional, gas dynamical numerical studies of the gravitational instability of a gas ring around a star to elucidate the overall pattern for the onset, development, and ultimate end of the gravitational instability of the ring.

It is possible that enhanced metallicity of the central star promotes the formation of planetary systems and brown dwarfs. Giménez [45] found that the heavy-element abundances of stars with planets are, on average, twice as high as that of the Sun. However, it remains unknown whether an enhanced heavy-element abundance indeed increases the probability

of the formation of planetary systems, or whether this is a consequence of observational selection effects, since stars with higher metal abundances have more narrow spectral lines suitable for analyses of radial-velocity variations aimed at searching for low-mass satellites.

Stars with known planets and brown dwarfs are concentrated in a narrow interval of primary component masses, $0.7-1.3\,M_\odot$ [1, 15]. This is a result of two observational selection effects. First, stars with masses of $0.3-1.5\ M_\odot$ have deep convective envelopes and magnetized stellar winds, reducing their equatorial rotational velocities to several km/s [14]. This simplifies the detection of radial-velocity variations when searching for low-mass satellites. Second, the apparent brightness of a main-sequence star grows with its mass up to $\sim 2M_\odot$, beyond which it begins to decrease. This is a combined effect of the stellar mass function and the mass–luminosity relationship. At the same time, a high stellar brightness is necessary to obtain the high spectral resolution used in spectroscopic searches for low-mass satellites. Naturally, stars with masses close to the solar mass are the brightest among slowly rotating stars. Therefore, most extrasolar planets and brown dwarfs have been detected around such stars, though a considerable fraction of stars with masses of $0.1-10M_\odot$ can also have planets [14]. Knowledge of the interval of initial specific angular momenta has enabled us to estimate the fraction of stars with planets and brown dwarfs to be 30–40%. The fraction of late-type young stars with extended dust disks is approximately the same [45, 46].

On the basis of the proposed scenario, it becomes clear that protostars with such angular momenta are able to produce either planetary systems or brown dwarfs as satellites of the formed stars. This reduces the rate of formation of solar-type planetary systems, but it is difficult to estimate by how much. On the other hand, it has recently been elucidated that gas–dust disks are found not only around single stars, but also around the components of wide binary stars and around close binaries. The possibility of the formation of planetary systems around these stars follows. It is clear that this circumstance increases the rate of formation of planetary systems and brown dwarfs, but again, it is not clear by how much.

We indicated above that the formation of planetary systems and circumstellar brown dwarfs is associated with the accretion by the central star of an appreciable mass possessing a large angular momentum. However, stars with deep convective envelopes and radiative cores ($0.3-1.5\,M_\odot$) have magnetized stellar winds, which help them shed excess angular momentum and remain slowly rotating. Only a small fraction of young G stars are rapid rotators [48], and it is possible that they are in an accretion phase. Stars with masses greater than $\sim 1.5\,M_\odot$ and smaller than $\sim 0.3\,M_\odot$, which cannot get rid of excess angular momentum, retain their rapid rotation for a long time, and are manifest as Be, Ae, and Me stars in young stellar aggregates. A scenario based on the formation and decay of a gas ring around the primary component can probably also be applied to the formation of binary and multiple stars with large component mass ratios. This supplements the two previously known mechanisms for the formation of binary stars: independent condensation of the components and multiple stellar encounters.

ACKNOWLEDGMENTS

The author is grateful to A.A. Boyarchuk and A.M. Fridman for useful discussions. This work was supported by the Russian Foundation for Basic Research, project no. 96-02-16351.

REFERENCES

1. T. F. Stepinski and D. C. Black, Astron. Astrophys. **356**, 903 (2000).
2. D. J. Pinfield, A. Katsyannis, C. J. Mooney, *et al.*, Ir. Astron. J. **27**, 145 (2000).
3. A. A. Tokovinin, Astron. Astrophys. **256**, 121 (1992).
4. T. Mazeh, M. Mayor, and D. V. Latham, Astrophys. J. **478**, 367 (1997).
5. A. V. Ksanfomaliti, Astron. Vestnik **35**, 1 (2001).
6. G. W. Marcy, R. P. Butler, and D. A. Fisher, BAAS **31**, 847 (1999).
7. E. B. Ford, F. A. Rasio, and A. Sills, Astrophys. J. **514**, 411 (1999).
8. V. S. Safronov, *Evolution of the Protoplanetary Cloud and Formation of the Earth and the Planets* (Moscow, 1969; Israel Program for Scientific Translations, Jerusalem, 1972).
9. T. V. Ruzmaikina and A. B. Makalkin, in *Proceedings of US-USSR Workshop on Planetary Sciences, 1991*.
10. T. Nakano, Mon. Not. R. Astron. Soc. **230**, 551 (1988).
11. T. Nakano, Mon. Not. R. Astron. Soc. **235**, 193 (1988).
12. V. S. Safronov and T. V. Ruzmaĭkina, in *Protostars and Planets,* Ed. by T. Gehrels (Univ. of Arizona Press, Tucson, 1972; Mir, Moscow, 1982).
13. A. V. Tutukov, Astron. Zh. **75**, 113 (1998) [Astron. Rep. **42**, 99 (1998)].
14. A. G. Masevich and A. V. Tutukov, *Stellar Evolution: Theory and Observations* [in Russian] (Nauka, Moscow, 1988), p. 280.
15. J. I. Halbwachs, F. Arenou, M. Mayor, *et al.*, Astron. Astrophys. **355**, 581 (2000).
16. A. Martin, Astrophys. J. **542**, 673 (2000).
17. G. Basri and A. Martin, Astron. J. **118**, 2460 (1999); astro-ph/9908015 (1999).

18. P. W. Lucas and P. F. Roche, Mon. Not. R. Astron. Soc. **314**, 858 (2000); astro-ph/0003061 (2000).
19. J. R. Najita, G. P. Tiede, and J. S. Carr, Astrophys. J. **541**, 977 (2000).
20. A. V. Tutukov, in *Modern Problems of Stellar Evolution,* Ed. by D. S. Wiebe (GEOS, Moscow, 1998), p. 16.
21. D. V. Bisikalo, A. A. Boyarchuk, O. A. Kuznetsov, and V. M. Chechetkin, Astron. Zh. **77**, 31 (2000) [Astron. Rep. **44**, 26 (2000)].
22. Yu. E. Lyubarskij, K. A. Postnov, and M. E. Prokhorov, Mon. Not. R. Astron. Soc. **268**, 586 (1994).
23. J. E. Pringle, Ann. Rev. Astron. Astrophys. **19**, 37 (1981).
24. A. G. W. Cameron, Moon Planets **18**, 5 (1978).
25. J. B. Pollack, Ann. Rev. Astron. Astrophys. **22**, 389 (1984).
26. G. Chabrier and I. Baraffe, Ann. Rev. Astron. Astrophys. **38**, 337 (2000).
27. N. I. Shakura and R. A. Sunyaev, Astron. Astrophys. **24**, 337 (1973).
28. A. P. Boss, Astrophys. J. **536**, L101 (2000).
29. J. C. Augeran, A. M. Lagrange, D. Mouillet, and F. Ménard, Astron. Astrophys. **365**, 78 (2001); astro-ph/0009496 (2000).
30. L. Testi, A. Natta, D. S. Shepherd, and D. J. Wilner, Astrophys. J. **554**, 1087 (2001); astro-ph/0102473 (2001).
31. G. Meeus, L. B. F. M. Waters, J. Bouwman, *et al.*, Astron. Astrophys. **365**, 476 (2001); astro-ph/0012295 (2000).
32. A. V. Tutukov, Astron. Zh. **72**, 397 (1995) [Astron. Rep. **39**, 351 (1995)].
33. C. D. Koresko, Astrophys. J. **507**, L145 (1998).
34. A. Natta, M. R. Meyer, and S. V. Beckwith, Astrophys. J. **534**, 838 (2000); astro-ph/9911490 (1999).
35. S. L. Skinner, A. Brown, and F. M. Walter, Astron. J. **102**, 1742 (1991).
36. M. Simon and S. Guilloteau, Astrophys. J. **397**, L47 (1992).
37. J. B. Ohanesyan, Astrophysics **40**, 237 (1997).
38. A. I. Sargent and S. V. Beckwith, Astrophys. Space Sci. **212**, 181 (1994).
39. D. E. Trilling, R. H. Brown, and A. S. Rivkin, Astrophys. J. **529**, 499 (2000).
40. S. J. Kenyon, Astron. Soc. Pac. Conf. Ser. **231**, 594 (2001); astro-ph/0010036 (2000).
41. A. B. Makalkin and V. A. Dorofeeva, Astron. Vestn. **29**, 99 (1995).
42. P. Kalas and D. Jewitt, Nature **386**, 52 (1997).
43. L. N. Jensen, D. W. Koerner, and R. D. Mathieu, Astron. J. **111**, 2431 (1996).
44. E. F. Guinan and I. Rites, Astrophys. J. **546**, L43 (2001); astro-ph/0010487 (2000).
45. A. Giménes, Astron. Astrophys. **356**, 213 (2000).
46. K. E. Haisch, E. A. Lada, and C. J. Lada, Astron. J. **121**, 2065 (2001); astro-ph/0101486 (2001).
47. H. H. Auman, Publ. Astron. Soc. Pac. **97**, 885 (1985).
48. S. A. Barnes, S. Sofia, and M. H. Pinsonneault, Astrophys. J. **548**, 1071 (2001); astro-ph/0101560 (2001).

Translated by G. Rudnitskiĭ

Astronomy Reports, Vol. 46, No. 8, 2002, p. 696. Translated from Astronomicheskiĭ Zhurnal, Vol. 79, No. 8, 2002, p. 768.

ERRATA

Erratum: "A Study of Rare-Earth Elements in the Atmospheres of Chemically Peculiar Stars. Pr III and Nd III Lines"

[*Astronomy Reports* 45, 382–388 (2001)]

T. A. Ryabchikova, I. S. Savanov, V. P. Malanushenko, and D. O. Kudryavtsev

In the paper by T.A. Ryabchikova, I.S. Savanov, V.P. Malanushenko, and D.O. Kudryavtsev entitled "A Study of Rare-Earth Elements in the Atmospheres of Chemically Peculiar Stars. Pr III and Nd III Lines," which was published in Vol. 45, no. 5, pp. 382–388, there are misprints in Table 4. Table 4 should be read as follows:

Table 4. Si, Cr, Fe, Pr, Nd, and Eu atmospheric abundances for the program stars. For Pr and Nd, the abundances are listed separately for lines of the first and second ions. The rms deviation, in fractions of the logarithm of abundance, is given in parentheses

Star	log(Si/H)	log(Cr/H)	log(Fe/H)	log(Pr/H)		log(Nd/H)		log(Eu/H)
				Pr II	Pr III	Nd II	Nd III	
HgMn stars								
HR 7775		−5.75(13)	−4.15(22)	−7.96(12)	−8.23 :	−7.85(19)	−8.07(26)	−
Am-stars								
15 Vul	−5.26	−6.33(29)	−4.80(23)	−10.06(25)	−10.60 :	−10.07(26)	−9.92(22)	−9.74
32 Aqr	−4.91	−6.03(32)	−4.45(22)	−9.98(16)	−10.36 :	−9.52(16)	−9.72 :	−10.64
Non-pulsating CP2 stars								
HR 4816	−3.80	−3.61(10)	−3.46(10)	−8.70 :	−8.76(30)	−7.90(30)	−8.06(20)	−8.36
HR 7575	−4.43	−4.21(10)	−3.98(10)	−9.00 :	−8.91(30)	−8.15(30)	−7.86(20)	−7.66
β CrB	−4.80	−4.56(10)	−4.15(10)	−9.31(30)	−9.31(20)	−8.61(20)	−8.32(05)	−8.46
HD 184471	−	−4.66(20)	−4.26(20)	−10.10(40)	$\leq$ −9.50	−9.72(30)	−9.69(25)	−9.76
HD 62140	−5.16	−4.56(20)	−4.16(15)	−8.76(25)	−7.96(30)	−7.83(30)	−6.54(15)	−8.81
HD 115708	−4.96	−5.71(10)	−4.91(10)	−10.16 :	−8.78(25)	−9.36(20)	−7.64(16)	−9.56
roAp stars								
HD 42659	−5.30	−5.15(30)	−4.56(30)	−9.10(30)	−7.76(24)	−8.65(30)	−7.58(10)	−9.56
α Cir	−4.60	−5.31(25)	−4.46(10)	−10.36(10)	−8.72(23)	−9.26(25)	−7.60(06)	−9.66
γ Equ	−4.65	−5.31(30)	−4.31(25)	−9.80(24)	−8.47(05)	−8.91(22)	−7.46(28)	−9.86
10 Aql	−4.60	−5.06(20)	−4.34(11)	−10.46(30)	−9.56(10)	−9.61(35)	−7.98(41)	−10.06
BI Mic	−4.80	−5.50(20)	−4.46(15)	−10.05(37)	−8.76(23)	−9.46(27)	−7.54(26)	−9.96
DO Eri	−5.15	−5.81(20)	−5.06(15)	−9.70(30)	−8.04(24)	−8.56(27)	−7.10(20)	−9.36

1063-7729/02/4608-0696$22.00